

ulm university universität
uulm

Enhancing magnetic resonance applications with optically polarized color centers

Dissertation

zur Erlangung des Doktorgrades Dr. rer. nat.
der Fakultät für Naturwissenschaften der Universität Ulm

vorgelegt von
Ilai Schwartz
aus Tel Aviv, Israel

2022

Amtierender Dekan: Prof. Dr. Thorsten Bernhardt

Erstgutachter: Prof. Dr. Martin Plenio

Zweitgutachter: Prof. Dr. Fedor Jelezko

Tag der Promotion: 6th of March, 2023

© 2022 - Ilai Schwartz

Contents

1 Introduction **1**

2 Nanodiamond Polarization **9**

2.1 Optically induced dynamic nuclear spin polarisation in diamond . . . 13

2.2 Robust techniques for polarization and detection of nuclear spin ensembles . . . 21

2.3 Optical hyperpolarization of ^{13}C nuclear spins in nanodiamond ensembles . . . 33

3 External molecule Polarization **55**

3.1 Resonance-inclined nuclear spin polarization of liquids in diamond structures . . . 59

3.2 Toward Hyperpolarization of Oil Molecules via Single Nitrogen Vacancy Centers in Diamond . . . 75

3.3 Robust optical polarization of nuclear spin baths using Hamiltonian engineering of nitrogen-vacancy center quantum dynamics . . . 107

4 Nanoscale Sensing **129**

4.1 Dissipatively stabilized quantum sensor based on indirect nuclear-nuclear interactions . . . 133

4.2 Blueprint for nanoscale NMR . . . 141

5 Conclusions and Outlook **155**

Bibliography **159**

List of Publications **165**

CV **167**

1 Introduction

Nuclear magnetic resonance (NMR) spectroscopy and magnetic resonance imaging (MRI) are technologies whose applications in organic chemistry, biology, medicine and material science have enabled fundamental scientific breakthroughs and continue to be drivers of scientific and technological progress [1].

NMR spectroscopy is sensitive to the precession of nuclear spins in an external magnetic field. The frequency of the oscillation depends on the magnetic field (termed the Larmor frequency) and the environment of the nuclear spin. Therefore, by analyzing the spectra of the oscillating spins, one can characterize the environment of the nuclear spins, and therefore provide insights to the structure and dynamics of the molecules.

MRI uses the same effect to image patients. Spatial information is provided by applying magnetic field gradients, thereby changing the Larmor frequency by the spatial position of the nuclear spins, and by varying the phase of the precession. The information of the tissue, i.e. the MRI contrast, is provided by changes to the nuclear spins coherence and relaxation times. This makes MRI a powerful, widespread imaging modality which is non-invasive and does not include harmful ionizing radiation.

Despite these successes, it is recognized that nuclear magnetic resonance applications has limitations due to the minute nuclear magnetization of analytes which leads to limited sensitivity in comparison to other analytic techniques such as mass spectrometry. For temperatures above the milikelvin range, the NMR signal is directly proportional to the polarization P of the molecules, which in thermal equilibrium is on the order of $P < 10^{-4}$ even for a very high magnetic field of 14 T at room temperature. Moreover, due to the low sensitivity and technical limitations, NMR spectroscopy is not feasible on the sub-micrometer scale, limiting the technique from being applicable to many exciting applications.

In order to surpass this limitation, several approaches were developed over the last decades. The most prominent approach was increasing the magnetic field. As the polarization increases linearly with the magnetic field, and the detection signal to noise ratio (SNR) increases as well by a factor of $B^{1/2}$, magnetic field significantly enhanced the NMR sensitivity. However, increasing the magnetic field greatly increases the size and cost of the magnet, and has approached saturation in the last decade.

A second main approach for increasing sensitivity is enhancing the polarization of the substrate itself. As thermal equilibrium polarization is exceedingly small, enhancing the sample polarized to 1% would result in a factor of 1,000 increase in sensitivity even for high magnetic fields.

Dynamic nuclear polarization (DNP) is an important technique that uses polarization transfer from electron to nuclear spins to achieve nuclear hyperpolarization. The electron spin coupling to the external magnetic field, and therefore its thermal polarization, is significantly larger than that of nuclear spins (660 times higher compared to 1H, 2620 times compared to 13C). Therefore, by transferring the electron polarization to the nuclear spins one can achieve a signal enhancement bounded from above by γ_e/γ_I, with γ_e denoting the electron gyromagnetic ratio and γ_I the nuclear gyromagnetic ratio. While DNP was first demonstrated already in the 1950s [1], this upper bound on the polarization enhancement limited DNP from being a widespread tool in NMR or MRI.

Recently interest in DNP has surged. In 2003 Ardenkjær-Larsen et al. demonstrated a technique termed dissolution DNP (d-DNP) [2]. The idea behind d-DNP is that at very low temperatures (< 1 K) and high magnetic fields (> 5 T) the electron thermal polarization approaches unity, and by transferring this polarization to the nuclear spins in this parameter regime, 10,000-fold polarization enhancement, compared to room temperature polarization, can be achieved. The polarization transfer is followed by a fast dissolution which brings the sample back to room temperature without a significant loss of polarization. This high polarization has demonstrated breakthrough applications in both MRI imaging and NMR spectroscopy, as shown on figure 1.1.

However, the technique still suffers from the extreme conditions that it has to operate in (temperature of 1 K, magnetic field > 5 T), including extremely costly polarizer, taking over 2 hours to polarize, and requiring room-sized equipment. This

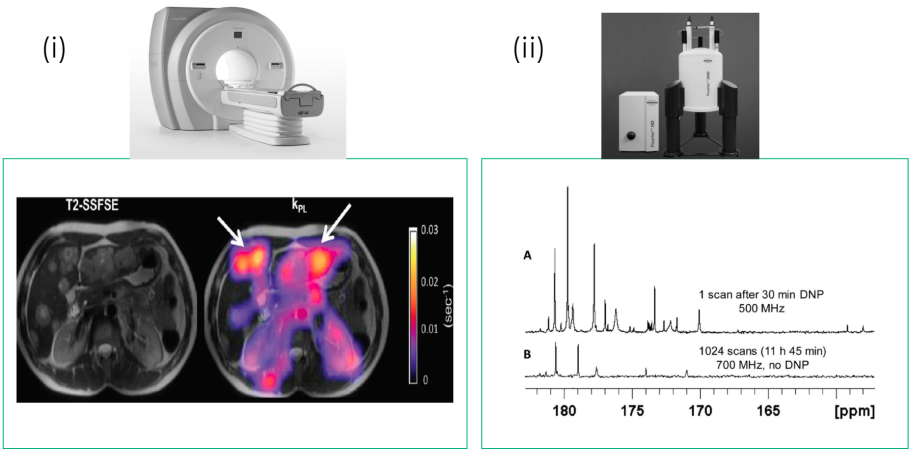


Figure 1.1: (i) Imaging of cancerous lesions in a liver using hyperpolarized metabolites in an MRI scanner. The layer of information provided by the hyperpolarized metabolites enables characterization of the tumor aggressiveness (ii) Comparison of (a) a single-shot hyperpolarized NMR signal in a tomato extract for metabolomic applications with (b) over 11 hours of thermal measurement NMR of the same sample. In addition to better signal-to-noise ratio and faster measurement, the hyperpolarized signal shows many previously unseen spectrum peaks. Reprinted with permission from Wang, Zhen J., et al. Radiology 291.2 (2019): 273-284, and Jannin, Sami, et al. Journal of Magnetic Resonance 305 (2019): 41-50.

results in significant disadvantages that severely limit the uptake of the technology and the potential impact of hyperpolarized NMR and MRI technology. Moreover, almost all molecules polarized by DNP exhibit a short hyperpolarization lifetime of 1-5 minutes, due to short T1 relaxation, limiting the technique to imaging only very fast processes, such as the metabolic process.

As the severe polarization temperatures are needed for first achieving the high electron polarization which can be transferred to the nuclear spins, the prevalent question is whether there exists an alternative, easier method for creating extremely high electron polarization which can serve as the starting point for the DNP process. The optical polarization of the electron spin in the nitrogen-vacancy center in diamond provides such an opportunity.

Diamond based polarizer for Hyperpolarized MRI technology - Due to ground-breaking progress over the last two decades, fundamental quantum science has now matured sufficiently to allow deployment in novel devices with applications to sensing and imaging. A key development in this context has been the demonstration of the quantum properties of individual nitrogen-vacancy centers (NV centers)

in diamonds [3, 4]. The NV color center in diamond consists of a substitutional nitrogen atom (N) that replaces a carbon atom and is associated with a vacancy (V) in an adjacent lattice site of the diamond crystal. Remarkably, this defects creates a localized electron spin system which has a ground state (and first excited state) corresponding to a $S = 1$ spin. This state can be manipulated by microwave or RF irradiation, and, through a transition to a metastable state, can be initialized optically to the $|m = 0 >$ state [5]. Finally, due to difference in fluorescence intensities of the different spin states, the spin state of the NV center can be inferred by an optical measurement. Thus, the NV center becomes a fully controllable, localized, quantum particle. As one application, at room temperature the electron spin native to the NV center can be initialized to the $|m = 0 >$ quantum state with an exceedingly high fidelity ($> 92\%$) by green laser irradiation [6]. This polarization can then be transferred to surrounding ^{13}C nuclear spins in the diamond, as was shown in our previous work for an individual NV center in London et al. [7].

An early motivation for this thesis was the question of what can be achieved with NV-based polarization? Synthesizing ideas we have developed throughout these research projects, we realized that by generalizing NV center-based polarization, we could envision three main endeavors:

1. Polarization of ^{13}C nuclear spins in nanodiamonds (NDs) to produce a novel MRI probe. The NV-based polarization scheme can be combined with tightly packed ^{13}C nuclei in diamonds to produce a very high magnetic resonance signal from each individual nanoparticle. This enables the imaging of only a few NDs, allowing the tracking of any attached molecule, in a standard MRI system. ND probes can exhibit hyperpolarization lifetimes reaching the range of minutes to hours [8], thus enabling long-term monitoring of molecular processes (e.g. distribution and uptake of antibodies in cancer cells) and higher imaging fidelity. Modifications of the ND surface ("functionalising the ND") will enable attachment of the ND to biomarkers or therapeutics, including antibodies, peptides, RNA, proteins and drugs [9].

2. Polarization of molecules external to the diamond (a.k.a. *The Diamond Hyperpolarizer*) - this could offer a flexible cost and time-effective solution for hyperpolarization. As the polarization can be performed at room temperature or close to it, the expensive cryostat and superconducting magnets required

in the current state-of-the-art systems will not be required, and the entire polarization system can be miniaturized.

3. The magnetic sensing capabilities of NV centers combined with their point-like nature provide a remarkable platform for nanoscale sensing, even at ambient conditions [10, 11]. A holy grail of NV-based sensing is the detection and characterization of molecules or substrates on the nanoscale (sub-micron) level. NV sensing efforts can be aided by ideas from the field of DNP, or better yet, one could combine the nanoscale sensing capabilities of NV centers with NV-based polarization to produce a device capable of sub-micron NMR detection.

We realized that the state of the art theory of DNP was insufficient to reach any of these ambitious visions. A main driving theme of this thesis work was therefore centered on figuring out how to make these ideas feasible.

In this thesis I will describe how we have developed the theory and demonstrated the proof of concept in these three main endeavors, namely using optically polarized NV centers to produce hyperpolarized nanodiamonds, polarize external molecules and optimize nanoscale sensing.

Part I

Nanodiamond polarization

2 Nanodiamond Polarization

NV centers exhibit a large zero-field splitting $D = 2.87$ GHz, which is oriented along the N-V axis. When placed in a magnetic field B, as nanodiamonds are randomly oriented, the angle between the NV axis and the magnetic field leads to a very large distribution of the NV center resonance, $D(\theta) = D[1 + 3\cos(2\theta)]/4$, with θ denoting the angle between the magnetic field and the NV axis. This can lead to deviations of hundreds of MHz to GHz in the NV resonance, see figure 2.1(a). Moreover, nanodiamonds have a short relaxation time at low magnetic fields, and a high relaxation time at high magnetic fields (magnetic fields larger than ∼0.1T). At high fields, the random orientation leads to a very inefficient polarization transfer ($\ll$ 1% of nanodiamonds involved when using a typical DNP sequence such as NOVEL).

To overcome this issue, we devised several strategies which significantly improve the polarization transfer:

- Use of a frequency sweep to produce efficient polarization transfer over a large frequency range using a modified integrated solid effect (ISE) sequence [12], therefore increasing the percentage of NV orientations which can be involved in the polarization transfer. With ISE, ranges of up to 100 MHz can be covered with sufficient efficiency. Fig. 2.1(b) depicts the polarization dynamics during the frequency sweep.

- Identifying a lambda system in the NV center at high magnetic fields which involves all three NV spin levels. This lambda system produces two dressed states which have only a small dependence on the NV axis angle to the magnetic field (the Double Quantum transition, DQT). The resonance of these two states is therefore orders of magnitude less affected by the NV orientation. For example, when $B \gg D$ a 20° angle between the magnetic field and the NV

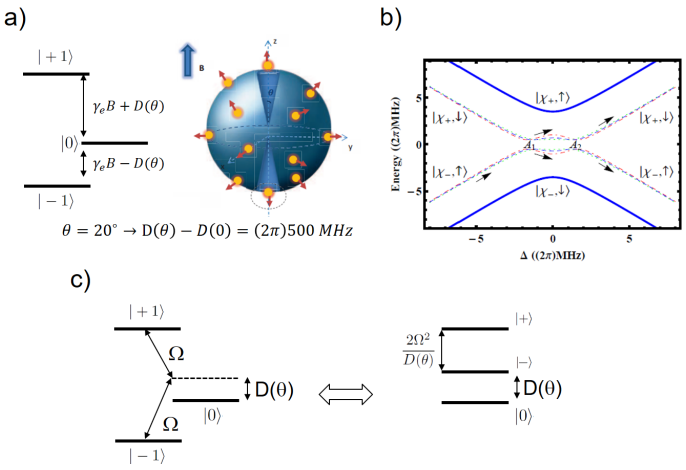


Figure 2.1: (a) Energy scheme of the NV spin states at a high magnetic field. The orientation of the NV center axis in relation to the external magnetic field B causes a deviation in the NV center resonance dependent on the angle θ. For example, a 20° angle between the magnetic field and the NV axis leads to 500 MHz detuning relative to a 0° angle. (b) A frequency sweep around the NV resonance produces two level avoided crossings at A_1, A_2. For polarization transfer via the ISE scheme, the frequency sweep needs to be non-adiabatic in these two points. (c) A lambda scheme utilizing the three NV spin states leads to protected resonance which is only weakly dependent on θ, as small θ variations of $\Omega^2/D(\theta)$ lead to resonance changes of $\Omega^2/D^2(\theta)\frac{\partial D(\theta)}{\partial\theta}\theta$. As $D(\theta) \gg \Omega$ for all points of interest, this resonance variation becomes almost negligible.

axis results in less than 1 MHz deviation. Fig. 2.1(c) illustrates the concept and provides an explanation of the decrease in resonance deviation.

- Realizing that the most efficient polarization transfer counterintuitively actually involves NV centers whose orientation is perpendicular to the magnetic field orientation. As the frequency deviation depends only on θ, a sweep between $\theta = 80°$ and $\theta = 90°$ leads to a much larger solid angle than a sweep between $\theta = 0°$ and $\theta = 10°$ (i.e. the solid angle is a ring compared to the cone shown on figure 2.1(a)).

- Temporally changing the angle of the nanodiamonds with regard to the external magnetic field, either by physical rotation of the sample holder, or preferably by placing the diamonds in a solution, thus enabling the nanodiamonds to tumble and experience Brownian rotation.

The combination of these strategies led to a very efficient polarization transfer in a nanodiamond powder, with theoretically over 20% of the NV orientations involved

in every polarization pulse. By varying the angle of the powder relatively to the magnetic field, over 20% polarization could be theoretically achieved in the entire nanodiamond powder. Our nanodiamond polarization strategy was published in Ref. [13].

We have proceeded to experimentally validate our approach by optically polarizing a bulk diamond and detecting the hyperpolarized signal, published in Ref. [14]. We collaborated in this experiment with the Institute of Quantum Optics at Ulm University, The Institut für Organische Chemie at KIT and Bruker BioSpin. In these experiments, we used the optical polarization of the NV centers and polarization transfer protocols to polarize 13C nuclear spins in an ultrapure diamond at room temperature and low magnetic fields (0.4T) in an EPR spectrometer. High polarization was built-up in the diamond which could be transferred 100m while preserving polarization and measurable in a separate NMR spectrometer. We have also validated the polarization transfer using NV centers with an axis perpendicular to the magnetic field. Figure 2.2 illustrates the experimental procedure.

In addition to demonstrating that the optical NV polarization can be used to build up a large nuclear polarization in the diamond, we have shown that using the ISE sweep we can indeed involve a large range of NV orientations in the polarization transfer.

In order to investigate the full set of strategies we have devised, we needed to identify an approach for probing the NV center 13C spin bath at the nanometer scale. We have therefore devised a new method for probing polarization on the nanometer scale using an NV center, termed Polarization Readout by Polarization Inversion (PROPI) [15]. Using this approach, we could investigate the local nuclear bath coupled to a single NV center and understand its dynamics. We showed very good agreement between simulations and experimental results in the polarization dynamics of the nuclear spin bath in a variety of polarization transfer protocols. Moreover, we were able to validate the improved polarization transfer produced by utilizing the double quantum transition.

In summary, we have devised for the first time a strategy for hyperpolarizing nanodiamonds. This polarization can be performed at a high magnetic field, where the nuclear relaxation time is highest, and the largest polarization can be achieved. We have proceeded to validate our methods in a series of experiments. For that purpose we devised several novel experimental methods, including the transfer of polarized

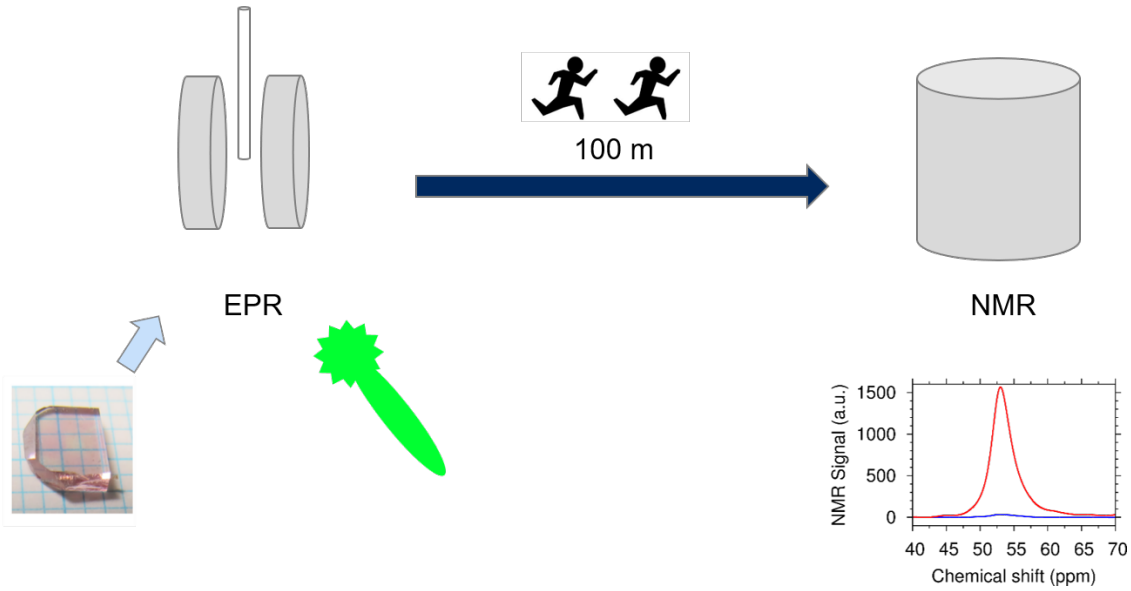


Figure 2.2: Illustration of the experiment demonstrating macroscopic diamond polarization through optically polarized NV centers. An ultrapure diamond with <100ppb NV centers was polarized in an EPR spectrometer with optical access for laser irradiation for 5 minutes. Following the polarization, the diamond was carried in a permanent magnet roughly 100m to an NMR spectrometer where the ^{13}C signal was measured. The single-shot hyperpolarized signal is in red compared to 14 hours of averages for obtaining the thermal signal in blue.

diamonds between an EPR and NMR spectrometer, and the PROPI method for the investigation of the local nuclear spin bath coupled to the NV center. Experiments combining the different strategies we devised for polarizing nanodiamonds at high magnetic fields are currently underway.

2.1 Optically induced dynamic nuclear spin polarisation in diamond

Title:	Optically induced dynamic nuclear spin polarisation in diamond
Authors:	J. Scheuer, I. Schwartz, Q. Chen, D. Schulze-Sünninghausen, P. Carl, P. Höfer, A. Retzker, H. Sumiya, J. Isoya, B. Luy, M. B. Plenio, B. Naydenov and F. Jelezko
Journal:	New Journal of Physics (New J. Phys.) 18 013040
Year:	2016
Copyright:	IOP Publishing Ltd and Deutsche Physikalische Gesellschaft. In accordance to the Creative Commons Attribution 3.0 licence, https://creativecommons.org/licenses/by/3.0/, the author has the right to reuse the full-text article in his thesis.
DOI:	https://doi.org/10.1088/1367-2630/18/1/013040

New Journal of Physics
The open access journal at the forefront of physics

Deutsche Physikalische Gesellschaft DPG
IOP Institute of Physics

Published in partnership with: Deutsche Physikalische Gesellschaft and the Institute of Physics



OPEN ACCESS

RECEIVED
29 September 2015

REVISED
20 November 2015

ACCEPTED FOR PUBLICATION
4 December 2015

PUBLISHED
18 January 2016

Original content from this work may be used under the terms of the Creative Commons Attribution 3.0 licence.

Any further distribution of this work must maintain attribution to the author(s) and the title of the work, journal citation and DOI.



PAPER

Optically induced dynamic nuclear spin polarisation in diamond

Jochen Scheuer[1,2], Ilai Schwartz[2,3], Qiong Chen[2,3], David Schulze-Sünninghausen[4], Patrick Carl[5], Peter Höfer[5], Alexander Retzker[6], Hitoshi Sumiya[7], Junichi Isoya[8], Burkhard Luy[4], Martin B Plenio[2,3], Boris Naydenov[1,2] and Fedor Jelezko[1,2]

[1] Institute of Quantum Optics, Ulm University, Albert Einstein Allee 11, D-89081 Ulm, Germany
[2] Centre for Integrated Quantum Science and Technology (IQST), Albert Einstein Allee 11, D-89081 Ulm, Germany
[3] Institute of Theoretical Physics, Ulm University, Albert Einstein Allee 11, D-89069 Ulm, Germany
[4] Institute of Organic Chemistry and Institute for Biological Interfaces 4-Magnetic Resonance, Karlsruhe Institute of Technology (KIT), Fritz-Haber-Weg 6, D-76131 Karlsruhe, Germany
[5] Bruker BioSpin GmbH, D-76287 Silberstreifen, Rheinstetten, Germany
[6] Racah Institute of Physics, The Hebrew University of Jerusalem, Jerusalem 91904, Givat Ram, Israel
[7] Sumitomo Electric Industries Ltd, Itami, 664-001, Japan
[8] Research Centre for Knowledge Communities, University of Tsukuba,Tsukuba, 305-8550, Japan

E-mail: boris.naydenov@uni-ulm.de

Keywords: nitrogen-vacancy (NV), dynamical nuclear polarisation (DNP), nuclear magnetic resonance (NMR), diamond

Supplementary material for this article is available online

Abstract

The sensitivity of magnetic resonance imaging (MRI) depends strongly on nuclear spin polarisation and, motivated by this observation, dynamical nuclear spin polarisation has recently been applied to enhance MRI protocols (Kurhanewicz *et al* 2011 *Neoplasia* **13** 81). Nuclear spins associated with the ^{13}C carbon isotope (nuclear spin $I = 1/2$) in diamond possess uniquely long spin lattice relaxation times (Reynhardt and High 2011 *Prog. Nucl. Magn. Reson. Spectrosc.* **38** 37). If they are present in diamond nanocrystals, especially when strongly polarised, they form a promising contrast agent for MRI. Current schemes for achieving nuclear polarisation, however, require cryogenic temperatures. Here we demonstrate an efficient scheme that realises optically induced ^{13}C nuclear spin hyperpolarisation in diamond at room temperature and low ambient magnetic field. Optical pumping of a nitrogen-vacancy centre creates a continuously renewable electron spin polarisation which can be transferred to surrounding ^{13}C nuclear spins. Importantly for future applications we also realise polarisation protocols that are robust against an unknown misalignment between magnetic field and crystal axis.

1. Introduction

Nuclear magnetic resonance (NMR) is one of the most powerful spectroscopic techniques with numerous applications in the life sciences, the material sciences and medicine. Long coherence times of nuclear spins allow to use this method for structural analysis of biomolecules and determination of molecular dynamics. Using highly sensitive NMR spectra combined with external magnetic field gradients nuclear magnetic moments can be imaged with high spatial resolution [1]. Both NMR spectroscopy and magnetic resonance imaging (MRI) critically depend on the polarisation of nuclear spins with which the observed signal scales linearly. At ambient conditions nuclear spins are very weakly polarised even in very high magnetic fields. Therefore significant effort was directed towards the development of protocols for enhancing nuclear spin polarisation above the thermal value.

Dynamic nuclear polarisation (DNP) protocols that use polarisation transfer from electron spins to nuclear spins have been realised and their application in imaging has been demonstrated recently [2]. It is important to note however that polarisation transfer reaches its best performance at low temperatures where electron spins are strongly polarised already in thermal equilibrium. Furthermore, owing to the long relaxation times of electron spins at these temperatures, typically a single polarisation cycle takes about a second during which a

© 2016 IOP Publishing Ltd and Deutsche Physikalische Gesellschaft

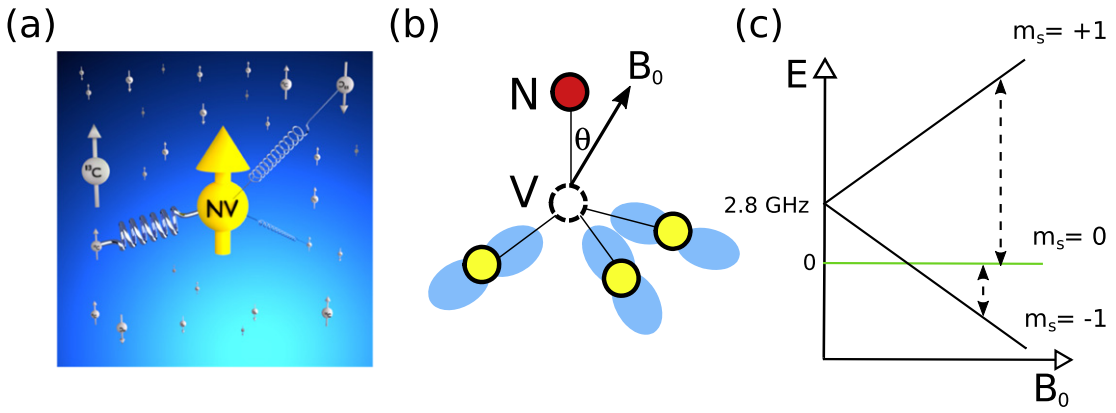


Figure 1. (a) Schematic presentation of our experiments. The electron spin of the NV is polarised with a short laser pulse. Then the polarisation is transferred to the neighbouring ^{13}C nuclei by means of a microwave induced Hartmann–Hahn resonance. The springs represent the coupling between the NV and neighbouring ^{13}C. This process is repeated many times. (b) Crystal structure of the NV centres. The magnetic field is applied usually at $\theta = 0°$. (c) Dependence of the ground state spin levels on the strength of the applied magnetic field for $\theta = 0°$. The two dashed lines show the allowed ESR transitions.

single electron spin can polarise at most a single nuclear spin. Therefore a high concentration of polarising paramagnetic agent is required to reach a high degree of nuclear spin polarisation. These limitations create a significant demand on novel polarisation protocols that allow for fast and efficient polarisation transfer ideally even at room temperature. Recently a novel mechanism for DNP based on optically pumped electron spins (optical dynamical nuclear spin polarisation (ODNP) [3, 4]) was introduced and realised in molecular crystals. However the short lifetime of the photo-excited triplet state and fast dephasing of optically active impurities at ambient conditions limit the applicability of this technique for NMR and MRI. This is the reason why the recent demonstration of diamond [5–7] as a promising ODNP platform attracted the attention of the NMR and MRI communities.

The nitrogen-vacancy (NV) centre (see figure 1(b)) in diamond exhibits a long relaxation time of its electron spins even at room temperature [8] and its electronic ground state triplet can be efficiently polarised using optical excitation [5–7]. NVs can be created in bulk diamond using electron irradiation of nitrogen rich crystals or by controlled doping of ultra-pure diamonds using nitrogen ion implantation. Their wavefunction is localised to within 1 nm of these colour centres allowing them to retain these desirable physical properties when embedded in diamond nanocrystals with sizes below 10 nm [9]. Diamond nanoparticles doped with colour centres already found their application in fluorescence microscopy as non-bleachable fluorescence markers and drug carriers [10]. Recently nanodiamonds have been considered as promising material for applications related to DNP [5–7, 11–14]. See [15] for a recent review on biomedical applications of NV centres in nanodiamonds.

The reason why diamond is attractive for DNP and MRI applications is related to the long relaxation time of ^{13}C nuclear spins and ability to polarise them quickly using optically pumped colour centres. NVs can be polarised within 200 ns by a laser pulse that induces spin-selective relaxation into the $m_s = 0$ sublevel of the ground state resulting in spin polarisation exceeding 92% [16].

In order to transfer polarisation to nuclear spins it is necessary to match the energy scale of the electron spin to that of the nuclear spin systems because the large energy mismatch between these two spins species due to the zero-field splitting ($D = 2.8$ GHz) of the spin triplet of NV centre prevents a direct polarisation exchange between the electron and nuclear spins. There are several methods to bring electron and nuclear spins in resonance. The first one is to set the static magnetic field close to the level crossing either the ground [17] or the excited state of the NV centre [18, 19]. Resonance can also be achieved by microwave driving of the electron spin of the NV with a Rabi frequency that matches the nuclear spin Larmor frequency (Hartmann–Hahn condition) [19, 20]. Furthermore it is possible to realise polarisation transfer by the solid effect (driving a forbidden double quantum transition thus inducing electron and nuclear spin flips) [5, 14]. Although the above mentioned techniques perform well for bulk diamond where NV centres have well defined orientations with respect to the static and driving fields, they do not apply directly to nanodiamond samples due to their random orientations. The strong spread of the Rabi frequencies of the microwave for chaotically oriented nanodiamonds severely reduces the probability to reach a Hartmann–Hahn resonance. Furthermore, the application of the solid effect would require an integration over a very wide range of detunings due to the large Zeeman shifts that are experienced by the NV centre. Both effects will result in a severe reduction of the total achievable nuclear spin polarisation. In this work we demonstrate the experimental realisation of a novel robust technique based on a fast sweep of the microwave driving field which induces a Landau–Zener transition [14] that has been designed

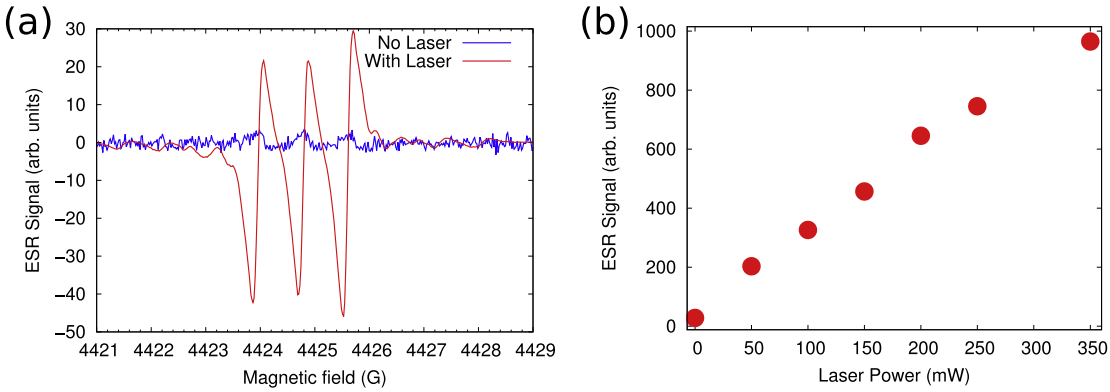


Figure 2. (a) ESR spectrum showing the NV resonance lines without (blue) and with optical pumping (red). The field was oriented along the [111] axis of the crystal coinciding with one of the four possible orientations of the NVs in the diamond. Three other orientations of NV centres have the same angle with respect to the axis of the NV centre and produce overlapping EPR lines. (b) Dependence of intensity of the ESR line as a function of the laser power. We could not observe saturation due to the limited laser power and to prevent heating of the sample.

specifically to achieve significant nuclear spin polarisation even in the presence of random orientations of nanodiamonds.

2. Experiments

The experiments reported in this paper were performed on a synthetic diamond with natural abundance of ^{13}C nuclear spins (1.1%). The crystal was grown using the high pressure high temperature technique and contains 0.5 ppm P1 centres (a paramagnetic defect which is constituted by a single substitutional nitrogen atom). About 10% of the P1 centres were converted to NV centres by high energy electron irradiation and subsequent annealing, achieving NV concentration of 0.05 ppm. Figure 1(a) shows a sketch of the DNP experiment.

The ODNP was performed on a commercial X band electron paramagnetic resonance (EPR) spectrometer (Bruker ELEXYS II) equipped with an arbitrary waveform generator and a microwave cavity allowing optical access. In order to polarise the NV centres a continuous laser beam (Laser quantum, Gem with a wavelength of 532 nm) with 3 mm diameter and 150 mW power was directed onto the crystal inside the EPR resonator. Owing to the weak NV-doping of the sample the optical density of the crystal was low (below 0.1). This allows homogeneous illumination of the sample resulting in similar polarisation conditions for the whole ensemble of NV centres. In figure 2(a) the enhancement of the EPR spectrum of NVs in diamond under continuous laser irradiation is shown.

As a first test of DNP we have performed polarisation transfer from NV centres to ^{13}C using the Hartmann Hahn resonance at room temperature. This protocol, called nuclear spin orientation via electron spin locking (NOVEL) [21], brings the electron spin of the NV centre in resonance with the surrounding nuclear spins when the driving frequency of the electron spin (Rabi frequency) equals the Larmor frequency of the nuclear spins. We have previously shown that the nuclear spin polarisation resulted in narrowing of the NV's ESR line width. Such a narrowing is related to polarisation of strongly coupled nuclear spins in its surrounding (so called 'frozen core') [19]. For experiments presented in this paper we were focusing on studies of the polarisation of bulk nuclear spins which is relevant for future applications of nanodiamonds as contrast agents in NMR and MRI. Therefore the polarisation was not measured using NV centre probes, but rather by using a conventional NMR spectrometer (Bruker Fourier 300). Figure 3(a) shows the experimental sequence for Hartmann–Hahn DNP.

It consists of an electron spin locking combined with continuous illumination of the NV centres. Note that the illumination with power density of 10 W cm^{-2} induces optical pumping at kHz rate. Therefore dephasing related to optical pumping is negligible within the duration of the spin locking pulse. The length of the latter is limited by the relaxation time of the NV electron spin in the rotating frame ($T_{1\rho} = 0.465$ ms, data not shown). In our experiments a value of 0.2 ms was used.

A single NV centre can polarise one nuclear spin within one polarisation transfer cycle. In our crystal the concentration of ^{13}C nuclear spins (1.1%) was exceeding by four orders of magnitude the concentration of NV defects. Therefore in order to achieve strong nuclear spin polarisation it was necessary to apply multiple repetitions of the Hartmann–Hahn protocol. Another important condition for efficient bulk polarisation is the ability to transfer polarisation to nuclei beyond the frozen core. This can be achieved by polarising nuclear spins at the edge of the frozen core sphere to allow for the diffusion of nuclear spin polarisation. Spin diffusion enabled

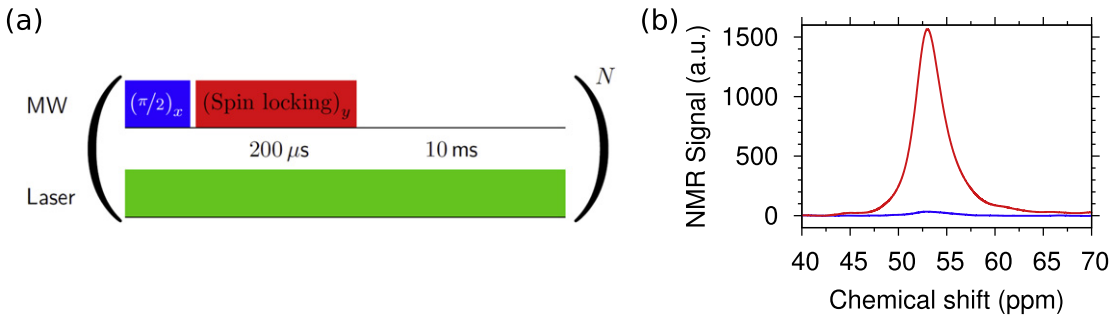


Figure 3. (a) NOVEL pulse sequence used for hyperpolarisation of the ^{13}C nuclear spins. The Rabi frequency of the spin locking pulse equals the ^{13}C Larmor frequency of 4.87 MHz. (b) NMR spectra for thermally (blue) and hyperpolarized ^{13}C nuclear spins (red). Later after a minute long probe transfer to the NMR spectrometer, an enhancement factor of about 45 is observed. Please note that for this type of sample it takes a very long time for the thermal polarisation to build up at $B = 7$ T, see also [22]; the thermal spectrum was measured after 13 h.

by dipole–dipole interaction between the nuclear spins will then lead to polarisation transfer to nuclei in the bulk. Note that the spin diffusion is slowed down by the magnetic field gradient created by the NV centres that are in the $m_s = +1$ and $m_s = -1$ state. To ameliorate conditions for diffusion we have introduced a polarisation transfer time window during which the NV centre is initialised into the $m_s = 0$ state, where there is no coupling to nuclei. During this time interval polarised nuclei in the frozen core can transfer their polarisation by diffusion to the volume outside the frozen core. The length of the spin locking pulse in the NOVEL sequence was chosen to reach nuclear spins with coupling constant of 10 kHz (situated approximately in a 2 nm radius around the NV centre). After 5 min of polarisation the sample was removed from the EPR spectrometer manually and transferred to the NMR spectrometer for measuring the ^{13}C NMR signal. During the transfer, that took about a minute time across a distance of approximately 100 m, the sample was kept in a static magnetic field (with a strength of few hundred Gauss) created by a permanent magnet. Figure 3(b) shows NMR spectra of non-polarised (blue line) and polarised (red line) nuclear spins. The former has been recorded after keeping the sample for 13 h in the spectrometer at a magnetic field of 7 T in order to let the thermal polarisation build-up. If the sample is measured directly after inserting it into the spectrometer no signal is observed in contrast to the polarised sample. Our hyperpolarisation procedure takes about 6 min, resulting in a factor of at least 130 reduction of the measurement time. Additionally we have observed a 45 fold enhancement of the signal which is in good agreement with expected polarisation enhancement (see the supplementary information for details about the simulation and measurement of the polarisation build-up). We estimate that this enhancement corresponds to a nuclear spin polarisation of 0.054%, when we assume that thermal polarisation is reached after keeping the sample 13 h in the NMR spectrometer.

A technique allowing to polarise nuclear spins in diamond is of particular interest for applications in MRI of diamond nanocrystals as labels. However, as stated earlier, in samples with random orientations, e.g. in suspensions, the Hartmann–Hahn condition is achieved only for the tiny subensemble for which the quantisation axes of NV centres are aligned with the external magnetic field. Recently, a new approach has been proposed that optimises the integrated solid effect (ISE) for randomly oriented NV centres [14].

This method is based on a quasi-adiabatic sweep of the driving field frequency and allows efficient population transfer for a wide range of misalignment angles (angle θ between the axis of the NV centre, see figure 1(b), and the external magnetic field). The pulse sequence is shown in figure 4(a).

For illustrating the basic idea, let us consider a system that is composed of a NV centre and a single ^{13}C nuclear spin in a nanodiamond of random orientation, where θ is the misalignment angle between the NV-axis and the magnetic field. In a strong magnetic field along the z-direction ($\gamma_e B \gg D$, with $\gamma_e B$ denoting the electron Larmor frequency, and D the NV centre zero-field splitting), the quantisation axis is given by the magnetic field, with the zero field splitting acting as a perturbation (see [14] and supplementary information). Focusing on the $\{|-1\rangle, |0\rangle\}$ subspace of the NV centre, we now apply a microwave driving $\sqrt{2}\,\Omega S_x \cos\omega_M t$ corresponding to the NV centre spin transitions $|-1\rangle \leftrightarrow |0\rangle$, ($\sqrt{2}\ \Omega$ is the Rabi frequency of the driving field and ω_M its frequency. In the rotating frame with the driving field frequency ω_M, the Hamiltonian can be written as

$$H_{\text{trans}} = \Omega\sigma_z + \Delta\sigma_x + B_{\text{eff}} I_z + a_z \sigma_z I_z + a_x \sigma_x I_x,$$

where $\Delta = D(\theta) - \delta(\theta) - \gamma_e B + \omega_M$ is the detuning between the driving frequency and the NV $|-1\rangle \leftrightarrow |0\rangle$, spin transition ($D(\theta)$, $\delta(\theta)$ are the angle dependent effects of the zero-field splitting, see supplementary information). $B_{\text{eff}} = \gamma_n B - A$, with γ_e, γ_n being the electron and nuclear gyromagnetic ratios,

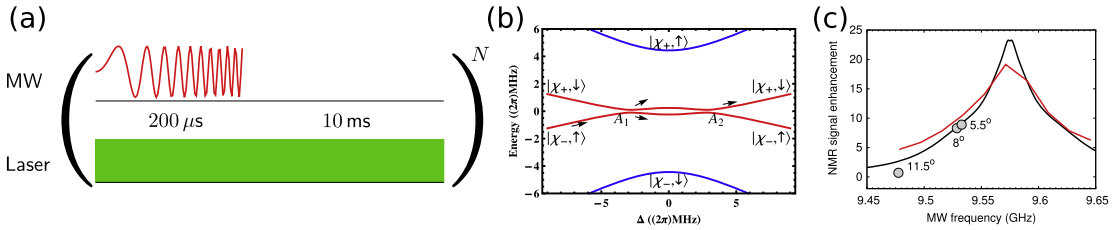


Figure 4. (a) Pulse sequence used for the ISE measurement. Instead of a spin locking sequence, the MW frequency is swept, allowing us to excite transitions at different angles θ. (b) Polarisation mechanism between the NV spin and ^{13}C nuclear spins. The solid lines depict the dependence of the eigenstates and energies on the detuning between the frequency of the microwave driving and the NV $|-1\rangle \leftrightarrow |0\rangle$ spin transition. The red lines show the states involved in the polarisation transfer, with the black arrows indicating the change of the system state in a quasi-adiabatic sweep of the microwave frequency. (c) Theoretical calculation of the nuclear spin polarisation (normalised to the thermal state) as a function of the MW frequency (black). Here we have included the bandwidth of the MW resonator (red). The circles show the enhancement of the NMR signal when we apply the ISE at different angles θ between the NV axis and the magnetic field.

and a_z, a_x are the elements of the secular and pseudo-secular hyperfine interactions respectively. $\vec{I}$ is the nuclear spin-1/2 operator and σ_z, σ_x are 1/2 times the Pauli matrices in the $|\pm\rangle = 1/\sqrt{2}\,(|0\rangle \pm |-1\rangle)$ basis.

Figure 4(b) shows the dependence of eigenstates of this Hamiltonian on the detuning, with $|\chi_\pm\rangle = \cos\zeta\,|-\rangle \pm \sin\zeta\,|+\rangle$ denoting the eigenstates, $\tan^{-1}(\zeta/2) = \Delta/\Omega$. We note two resonance points A_1 and A_2.The polarisation is transferred between the dressed state of the electron spin and the nuclear spin during a quasi-adiabatic sweep through these resonances (see supplementary information for additional details). Note that the sweep rate should be non-adiabatic compared to the dipolar coupling (typically 50–200 kHz) time constant between electron and nuclear spins, i.e. around the resonance points A_1 and A_2. The upper limit on the sweep parameter is defined by the Rabi frequency of the microwave field determining the splitting between the red and blue lines in figure 4(b). Exceeding the latter would lead to the randomisation of nuclear spin polarisation.

Owing to long sample transfer time, and the limited ^{13}C relaxation time in nanodiamonds of a few minutes [23] (we observed similar values, data not shown) compared to hours for the latter at $B = 7$ T, our demonstrations were performed on bulk diamonds rather than in nano-diamonds. In order to realise a misalignment between NV-axis and external magnetic field, experiments were performed using different orientations of the diamond crystal with respect to the external static field but without change of the polarisation protocol. In our experimental conditions the sweep rate was chosen to be 0.3 MHz μs^{-1} and the sweep range was 100 MHz This allows to cover a misalignment angle of about 10° corresponding to a ~2% fraction of colour centres for isotropic orientation of NV axes, and would result in a fast build-up of polarisation in nanodiamonds, as shown by detailed numerical simulations [14]. According to the latter it is possible to reach 20% polarisation for a nanodiamond with a spherical shape and a radius of 5 nm.

The experiment has been performed as in the case of NOVEL. We polarise the samples for 5 min. and then transfer the diamond to the NMR spectrometer where we measure the ^{13}C signal. The observed polarisation enhancement is demonstrated in figure 4(c). Note that slightly lower efficiency of polarisation transfer at strong misalignment angles is related to non-optimal drive at high detuning. In our experiments the microwave drive generated by an arbitrary waveform generator was kept at constant amplitude, but the microwave resonator bandwidth was limited to about 100 MHz half width at half maximum. Therefore at high rotation angle (corresponding to the resonance at the edge resonator band), the effective coupling by matching the resonance condition is much lower.

The theoretical expected polarisation enhancement was computed based on the calculated polarisation transfer probability of the ISE:

$$\bar{P} = 2P_{\mathrm{LZ}}\left(1 - P_{\mathrm{LZ}}\right),$$

$$P_{\mathrm{LZ}} = \mathrm{e}^{-2\pi\mu}, \quad \mu = \frac{\Omega^2 a_{x'}^2}{16\nu\left(\gamma_{\mathrm{n}}B\right)\sqrt{\left(\gamma_{\mathrm{n}}B\right)^2 - \Omega^2}}.$$

With Ω denoting the Rabi frequency, $a_{x'}$ the effective dipolar coupling, ν the frequency sweep rate, and $\gamma_{\mathrm{n}}B$ the nuclear Larmor frequency. The polarisation rate, which depends on the cycling time, is then averaged over an ensemble for a nuclear spin bath of 500 spins around the NV centre, and a steady-state polarisation depending on the ^{13}C relaxation time in the EPR magnetic field (see supplementary material stacks.iop.org/NJP/18/013040/mmedia). Nuclear spin diffusion is limited by the dipolar coupling between the ^{13}C spins (2 kHz for

next neighbours) and it does not seem to be a bottleneck of the polarisation build-up in our experiments, due to the 10 ms polarisation transfer time between cycles with the NV in the $m_s = 0$ state.

3. Conclusions

Our results show that optical nuclear spin polarisation in diamond can be performed for a wide range of orientations of NV centres at room temperature. Our protocol based on quasi-adiabatic sweep of microwave field across the resonance points makes it possible to polarise diamond nanoparticles. Such functionalised diamond nanocrystals can serve as agent for molecular imaging using MRI techniques. Our method can be in principle transferred to other nanoparticles containing electron spins that can be optically polarised.

Acknowledgments

This work was supported by the ERC Synergy grants BioQ and PoC, the EU (DIADEMS, EQUAM, SIQS), the DFG (SFB TRR/21, FOR 1493), Volkswagenstiftung, JSPS KAKENHI (No. 26246001) Bundesministerium für Bildung und Forschung (ARHES award) and an Alexander von Humboldt Professorship. BN is grateful to the Postdoc Network program of the IQST. IS acknowledges a PhD fellowship from the IQST.

References

[1] Lauterbur P C 1973 Image formation by induced local interactions—examples employing nuclear magnetic-resonance *Nature* **242** 190–1
[2] von Morze C *et al* 2014 Simultaneous multiagent hyperpolarized C-13 perfusion imaging *Magn. Reson. Med.* **72** 1599–609
[3] Sukhenko S A and Salikhov K M 1985 Calculations of optical nuclear-spin polarizations for randomly oriented molecules *Chem. Phys.* **98** 431–6
[4] Tateishi K *et al* 2014 Room temperature hyperpolarization of nuclear spins in bulk *Proc. Natl Acad. Sci. USA* **111** 7527–30
[5] London P *et al* 2013 Detecting and polarizing nuclear spins with double resonance on a single electron spin *Phys. Rev. Lett.* **111** 067601
[6] Álvarez G A *et al* 2015 Local and bulk 13C hyperpolarization in nitrogen-vacancy-centred diamonds at variable fields and orientations *Nat. Commun.* **6** 8456
[7] King J P *et al* 2015 Room-temperature *in situ* nuclear spin hyperpolarization from optically-pumped nitrogen vacancy centers in diamond *Nat. Commun.* **6** 8965
[8] Doherty M W *et al* 2013 The nitrogen-vacancy colour centre in diamond *Phys. Rep.* **528** 1–45
[9] Tisler J *et al* 2009 Fluorescence and spin properties of defects in single digit nanodiamonds *ACS Nano* **3** 1959–65
[10] Mochalin V N *et al* 2012 The properties and applications of nanodiamonds *Nat. Nanotechnology* **7** 11–23
[11] Casabianca L B *et al* 2011 Factors affecting DNP NMR in polycrystalline diamond samples *J. Phys. Chem.* C **115** 19041–8
[12] Ewa Rej T G, Boele T, Waddington D E J and Reilly D J 2015 Hyperpolarized nanodiamond with long spin relaxation times *Nat. Commun.* **6** 8459
[13] King J P, Coles P J and Reimer J A 2010 Optical polarization of C-13 nuclei in diamond through nitrogen vacancy centers *Phys. Rev.* B **81** 073201
[14] Chen Q *et al* 2015 Optical hyperpolarization of 13C nuclear spins in nanodiamond ensembles arXiv:1504.02368
[15] Wu Y *et al* 2015 Diamond quantum devices in biology *Angew. Chem. Int. Ed. Engl.* in press
[16] Waldherr G *et al* 2011 Dark states of single nitrogen-vacancy centers in diamond unraveled by single shot NMR *Phys. Rev. Lett.* **106** 157601
[17] Wang H J *et al* 2013 Sensitive magnetic control of ensemble nuclear spin hyperpolarization in diamond *Nat. Commun.* **4** 1940
[18] Jacques V *et al* 2009 Dynamic polarization of single nuclear spins by optical pumping of nitrogen-vacancy color centers in diamond at room temperature *Phys. Rev. Lett.* **102** 057403
[19] Fischer R *et al* 2013 Bulk nuclear polarization enhanced at room temperature by optical pumping *Phys. Rev. Lett.* **111** 057601
[20] Cai J-M *et al* 2013 Diamond based single molecule magnetic resonance spectroscopy *New J. Phys.* **15** 013020
[21] Henstra A *et al* 1988 Nuclear spin orientation via electron spin locking (NOVEL) *J. Magn. Reson.* **77** 389
[22] Reynhardt E C and High G L 2011 *Prog. Nucl. Magn. Reson. Spectrosc.* **38** 37
[23] Panich A M *et al* 2015 Size dependence of 13C nuclear spin-lattice relaxation in micro- and nanodiamonds *J. Phys.: Condens. Matter* **27** 072203

2.2 Robust techniques for polarization and detection of nuclear spin ensembles

Title:	Robust techniques for polarization and detection of nuclear spin ensembles
Authors:	J. Scheuer, I. Schwartz, S. Müller, Q. Chen, I. Dhand, M. B. Plenio, B. Naydenov and F. Jelezko
Journal:	Physical Review B 96, 174436
Year:	2017
Copyright:	©2017 American Physical Society. Reprinted with permission from Scheuer et al. Physical Review B 96, 174436 (2017) ©2017 by the American Physical Society
DOI:	https://doi.org/10.1103/PhysRevB.96.174436

PHYSICAL REVIEW B **96**, 174436 (2017)

Robust techniques for polarization and detection of nuclear spin ensembles

Jochen Scheuer,[1] Ilai Schwartz,[2] Samuel Müller,[1] Qiong Chen,[2] Ish Dhand,[2] Martin B. Plenio,[2] Boris Naydenov,[1,*] and Fedor Jelezko[1]

[1]*Institute for Quantum Optics and Center for Integrated Quantum Science and Technology (IQST), Albert-Einstein-Allee 11, Universität Ulm, D-89069 Ulm, Germany*

[2]*Institute of Theoretical Physics and Center for Integrated Quantum Science and Technology (IQST), Albert-Einstein-Allee 11, Universität Ulm, D-89069 Ulm, Germany*

(Received 5 June 2017; revised manuscript received 18 August 2017; published 27 November 2017)

Highly sensitive nuclear spin detection is crucial in many scientific areas including nuclear magnetic resonance spectroscopy, magnetic resonance imaging (MRI), and quantum computing. The tiny thermal nuclear spin polarization represents a major obstacle towards this goal which may be overcome by dynamic nuclear spin polarization (DNP) methods. The latter often rely on the transfer of the thermally polarized electron spins to nearby nuclear spins, which is limited by the Boltzmann distribution of the former. Here we utilize microwave dressed states to transfer the high (>92%) nonequilibrium electron spin polarization of a single nitrogen-vacancy center (NV) induced by short laser pulses to the surrounding ^{13}C carbon nuclear spins. The NV is repeatedly repolarized optically, thus providing an effectively infinite polarization reservoir. A saturation of the polarization of the nearby nuclear spins is achieved, which is confirmed by the decay of the polarization transfer signal and shows an excellent agreement with theoretical simulations. Hereby we introduce the polarization readout by polarization inversion method as a quantitative magnetization measure of the nuclear spin bath, which allows us to observe by ensemble averaging macroscopically hidden polarization dynamics like Landau-Zener-Stückelberg oscillations. Moreover, we show that using the integrated solid effect both for single- and double-quantum transitions nuclear spin polarization can be achieved even when the static magnetic field is not aligned along the NV's crystal axis. This opens a path for the application of our DNP technique to spins in and outside of nanodiamonds, enabling their application as MRI tracers. Furthermore, the methods reported here can be applied to other solid state systems where a central electron spin is coupled to a nuclear spin bath, e.g., phosphor donors in silicon and color centers in silicon carbide.

DOI: 10.1103/PhysRevB.96.174436

I. INTRODUCTION

Nuclear magnetic resonance (NMR) spectroscopy and magnetic resonance imaging (MRI) are well-established methods in chemistry, biology, and medicine. Both techniques require the detection of the low magnetic field generated by thermally polarized nuclear spins, which demand high static magnetic fields and large sample quantities. Dynamical nuclear spin polarization (DNP) has been developed to transfer the much higher thermal electron spin polarization to the nuclear spins, thus improving the NMR signal. Another important application of DNP is in the emerging field of quantum information processing and especially for the initialization of solid state quantum simulators [1,2]. The improvement factor is usually limited by the ratio of the magnetic moments of the electron and nuclear spins, which determines the ratio of equilibrium polarization levels. Although recently [3] a much larger enhancement was demonstrated using optically polarized electron spins out of thermal equilibrium, the technique relies on short-living radical triplet states, which limits its applications. A very promising DNP method is based on optically pumped nitrogen-vacancy centers in diamond (NVs), where several demonstrations have been reported [4–9], but they require very good alignment (below 1°) of the magnetic field along the NV's crystal axis. Here we report and evaluate several methods for polarizing nuclear spins using a single NV center, that are applicable at arbitrary magnetic field strengths and a wide range of orientations. Furthermore, we demonstrate a method to read out the magnetization of the nuclear spin bath – polarization readout by polarization inversion (PROPI), where we obtain the number of spin quanta transferred from the NV center to the nuclear spins.

The NV is a unique physical system which became a universal sensor for magnetic [10,11] and electric fields [12] and temperature [13,14] with nanometer spatial resolution. Single NVs can be observed and the electron spin of the triplet ground state can be optically polarized and read out. Recently it has been demonstrated that the electron spin polarization can be transferred from an ensemble of NVs to the surrounding ^{13}C nuclear spins in a bulk crystal using a specific experimental configuration, e.g., excited state level anticrossing [6], ground-state level anticrossing, or nearest neighbor ^{13}C spins [7]. We have previously demonstrated by using proper microwave driving of the NV's electron spin, that polarization transfer can be achieved at arbitrary magnetic fields both for single [5] and an ensemble of NVs [15].

One of the main goals of diamond DNP is the polarization of nanodiamonds, which due to their bio-compatibility are well suited as hyperpolarized MRI tracers. However, as detailed in Ref. [16], the polarization of nanodiamonds via NV centers requires novel approaches for DNP, due to the random orientation of the NV center axes and its large zero-field splitting. A theoretical DNP method has been proposed, combining the electron spin triplet $S = 1$ properties of the NV center, specifically its double-quantum transition (DQT), with

*boris.naydenov@uni-ulm.de

 ©2017 American Physical Society

the integrated solid effect (ISE) [17,18]. With these techniques an unprecedented level of robustness can be achieved, against misalignment of the externally applied static magnetic field with respect to the NV axis and against rotational diffusion of the NV. Usually experimental validation of DNP protocols can only be achieved in a macroscopic ensemble of nuclear spins via NMR, thus limiting the information about the dynamics due to ensemble averaging. The accessibility of a single NV, including its control and detection, makes it a unique test bed for the effect of manipulation and polarization of the surrounding nuclear spin environment and for testing of novel DNP schemes. However, the readout of the nuclear spin state and polarization remained an open challenge, due to the limited quantifiable information in methods such as linewidth narrowing [5]. Here we demonstrate methods on a single NV center, which can be used not only to polarize, but also to measure the nuclear spin bath quantitatively.

In Sec. II we present the NV's spin Hamiltonian and the general idea of our method. In Sec. III we present measurement results when using a single-quantum transition (SQT). Experimental data for polarization via the NV's double-quantum transition and for misaligned magnetic field are presented in Sec. IV.

II. CONTROLLING THE NUCLEAR SPIN BATH

The physical system consisting of a single NV and a bath of $N^{^{13}\mathrm{C}}$ ^{13}C nuclear spins can be described by the following Hamiltonian ($\hbar = 1$):

$$\hat{H} = D\hat{S}_z^2 + g\mu_B \vec{B}\cdot\vec{S} + \vec{S}\cdot\mathbf{A}^{^{14}\mathrm{N}}\cdot\vec{I}^{\,^{14}\mathrm{N}} + \sum_{j=1}^{j=N^{^{13}\mathrm{C}}} \gamma^{^{13}\mathrm{C}}|\vec{B}|\hat{I}_{jz}{}^{^{13}\mathrm{C}} + \vec{S}\cdot\sum_{j=1}^{j=N^{^{13}\mathrm{C}}} \mathbf{A_j}^{^{13}\mathrm{C}}\cdot\vec{I}_j{}^{^{13}\mathrm{C}}, \quad (1)$$

where $D/2\pi = 2.87$ GHz is the zero field splitting of the ground state, $g = 2.003$ is the Landé factor, μ_B is the Bohr magneton, $\vec{B} = B_x\vec{e}_x + B_y\vec{e}_y + B_z\vec{e}_z$ is the applied static magnetic field, $\vec{S} = \hat{S}_x + \hat{S}_y + \hat{S}_z$ and $\vec{I}^{\,^{14}\mathrm{N}} = \widehat{I}_x^{\,^{14}\mathrm{N}} + \widehat{I}_y^{\,^{14}\mathrm{N}} + \widehat{I}_z^{\,^{14}\mathrm{N}}$ are the electron and nuclear spin operators of the NV ($S = 1$ and for ^{14}N $I = 1$), and $\mathbf{A}^{^{14}\mathrm{N}}$ is the hyperfine interaction tensor of the NV. The Zeeman interaction of the ^{13}C nuclear spin bath ($I = 1/2$) is given by the second to last term in the Hamiltonian with their gyromagnetic ratio $\gamma^{^{13}\mathrm{C}} = 6.728 \times 10^7\ \mathrm{T^{-1}\,s^{-1}}$. The last term describes the hyperfine interaction between the NV and the nuclear spin bath, where $\mathbf{A_j}^{^{13}\mathrm{C}} \sim \frac{g\mu_B\gamma^{^{13}\mathrm{C}}}{r_j^3}$ with r_j^3 the distance between the NV center and the nuclear spin. For simplicity we have removed the ^{14}N nuclear spin Zeeman energy and its quadrupole interaction with the NV center. Unless otherwise stated in all experiments we set $|\vec{B}| \approx 1750$ G in order to compare the different measurements, although it should be noted that our methods can be applied at arbitrarily magnetic field strengths. The z axis is taken to be along the NV crystal axis. MW pulses are applied on the electron spin resonance transition corresponding to the NV nuclear spin state $|m_I = +1\rangle$. For the experiments presented in Secs. III and IV the magnetic field was aligned along z better than $<0.5^\circ$. Results for a misaligned field are presented in the last part of Sec. IV. We used various NV centers in different samples for our experiments, although for the results shown here the same NV center was used, in order to be able to compare quantitatively the different DNP methods. The measurements were performed on a home-built confocal microscope.

The schematic of the pulse sequence used in our experiments for polarizing the nuclear spin bath and reading out its magnetization is depicted in Fig. 1. It starts with a 3-μs-long laser pulse to polarize the NV center into the $|m_s = 0\rangle$ state, followed by a series of microwave (MW) pulses to transfer the polarization to the surrounding nuclear spins, which are coupled to the NV. The region, where this hyperfine interaction is stronger than the coupling among the nuclear spins, is often referred to as the "frozen core" and is also called the "spin diffusion barrier" [19]. We will call it the "interaction region". Theoretical simulations show that in our experiments all nuclear spins with a coupling up to about 10 kHz to the NV center become completely polarized and nuclear spins coupled from 2 to 10 kHz are partially polarized. Weakly coupled ones are not affected at all, but can be polarized via nuclear spin diffusion when the NV's electron spin is initialized into the $|m_S = 0\rangle$ state.

The pulse sequence is repeated N times, resulting in a polarization of the nuclear spin bath in the $|\uparrow\uparrow\uparrow\ldots\rangle$ state, where the states $|\uparrow\rangle$ and $|\downarrow\rangle$ are defined to be, respectively, parallel and antiparallel to the applied static magnetic field $\vec{B}$. In order to read out the nuclear spin bath, we apply another sequence, where we invert the nuclear spins into the $|\downarrow\rangle$ state; see Fig. 1 (right). By polarizing the nuclear spins in the opposite

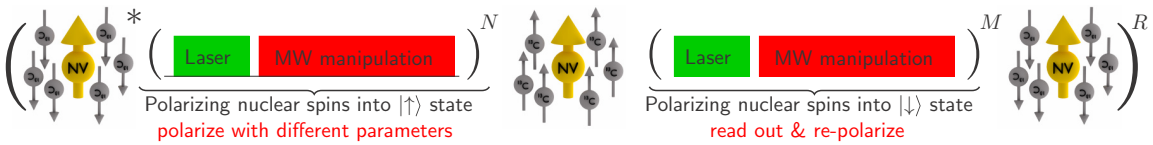


FIG. 1. Schematic representation of the experiments. The first pulse sequence is repeated N times and is used to polarize the nuclear spin bath along the static magnetic field ($|\uparrow\uparrow\uparrow\ldots\rangle$ state). By changing the MW manipulation, we can polarize the nuclear spin bath into the $|\downarrow\downarrow\downarrow\ldots\rangle$ state by repeating the sequence M times. The illustrations present the state of the spin bath around the NV center at different time instants. At the beginning the nuclear spins are polarized in the $|\downarrow\rangle$ state. After repeating the polarization sequence N times the nuclear spins are partially or fully inverted into the $|\uparrow\rangle$ state depending on N. By polarization of the nuclear spin bath during the M cycles the nuclear spin bath is both initialized and read out. Hence, M has to be set large enough, so that the nuclear spin bath is completely polarized. At the start of the experiment at $N, R = 1$ (*) the nuclear spin bath is unpolarized, but due to a larger number of repetitions of the measurements ($R = 5 \times 10^4$) the first iteration can be neglected. For most of our experiments $N = 50$ and $M = 200$. See text for more details.

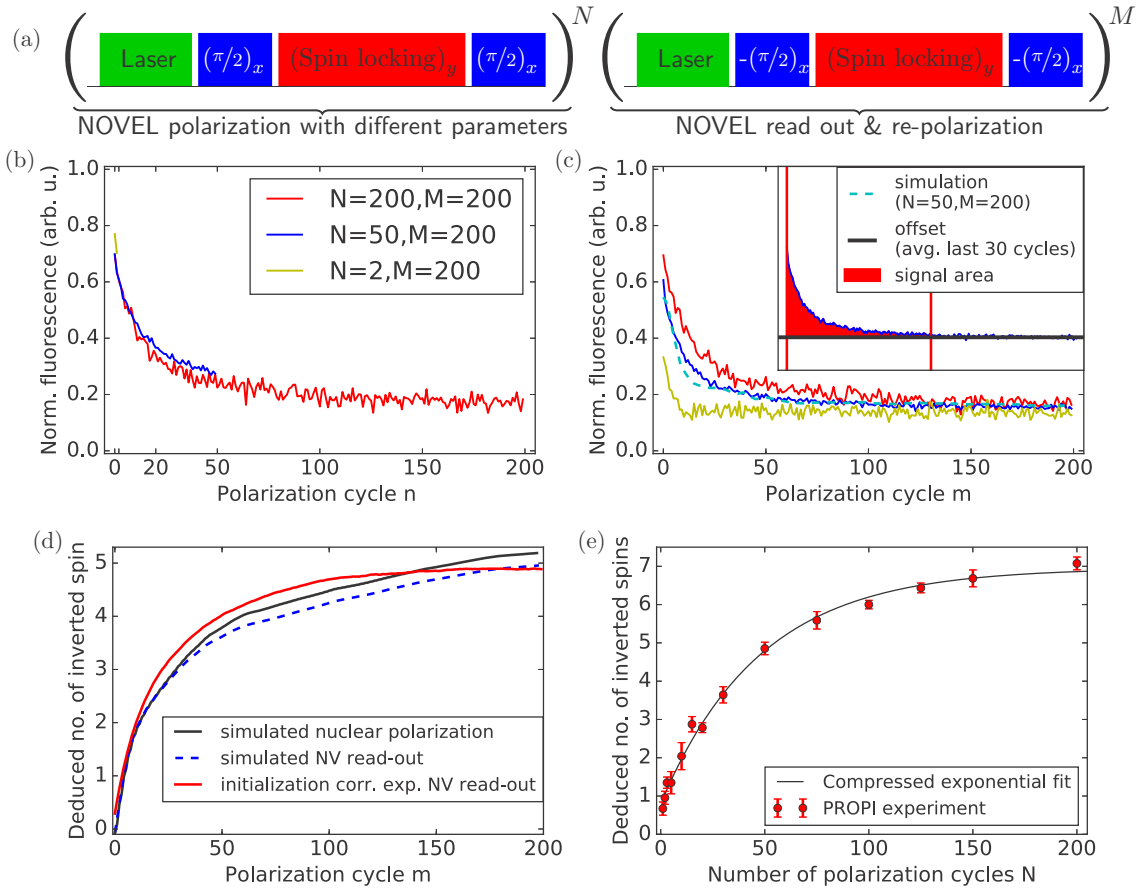


FIG. 2. (a) Pulse sequences for the NOVEL experiment. (b) Fluorescence of the NV center measured with the nth laser pulse, where $n = 0,1,...N$ for $N = 2$, (yellow), $N = 50$ (blue), and $N = 200$ (red), where $M = 200$ for all data sets; see also Fig. 1. (c) Fluorescence of the NV center measured with the mth laser pulse, where $m = 0,1,...M$. (Inset) Measurement for $N = 50$ and $M = 200$. The red colored area enclosed by the two vertical lines is the PROPI signal, which gives the number of inverted nuclear spins and is a measure of the polarization. The dashed cyan curve is a simulation of the full experiment ($N = 50$; $M = 200$). (d) Comparison between simulated nuclear polarization, simulated NV readout, and initialization corrected PROPI data (see text). (e) Nuclear spin bath polarization as a function of the number of polarization cycles N, where $M = 200$. The black line here is a fit, which serves as a guide to the eye.

direction, compared to the previous sequence and reading out the NV state optically, we are able to read out their magnetization quantitatively; see next section. In other words with the help of the NV center's electron spin we manipulate the nuclear spin environment and the back action of the latter on the NV is our signal. After normalizing the signal, we obtain the average number of spin quanta transferred from the NV to the nuclear spins, which is confirmed by theoretical simulations. We call this method polarization readout by polarization inversion, or PROPI. It is important to note, that this technique can be applied only for the readout of nondiffusing nuclear spins, e.g., spins in the crystal lattice or immobilized on the diamond surface. A typical experimental result after applying both pulse sequences is shown in Figs. 2(b) and 2(c); see also next section.

III. POLARIZATION METHODS USING SINGLE-QUANTUM TRANSITIONS

A. Nuclear spin orientation via spin locking

First we demonstrate our method using the nuclear spin orientation via electron spin locking (NOVEL) DNP technique. Here the transfer of polarization from the NV's electron spin to the nuclear spins is realized via a spin locking experiment [5,15,20]. The pulse sequence is depicted in Fig. 2(a). After initializing the NV in the $|m_s = 0\rangle$ state, we align its spin along the y axis of the Bloch sphere with a $\pi/2$ pulse, where it remains as long as the spin locking pulse is on (10 μs in our case) or until relaxation becomes important. During the spin locking pulse, the system is in the dressed state basis and the electron and nuclear spin flip-flop processes are energetically allowed. Afterwards we apply another $\pi/2$ pulse to bring the NV spin back to the $|0\rangle$, $|1\rangle$ basis, where its state is read out optically. The readout process is not part of the polarization protocol, but is used here to study the efficiency of the methods. A spin flip-flop process between the electron and nuclear spins occurs when the Hartmann-Hahn condition is fulfilled [21]:

$$\Omega_1 = \omega_0^{^{13}\mathrm{C}}, \tag{2}$$

where $\Omega_1 = g\mu_B B_1/\hbar$ is the Rabi frequency of the spin locking pulse with the magnetic field amplitude B_1 of the

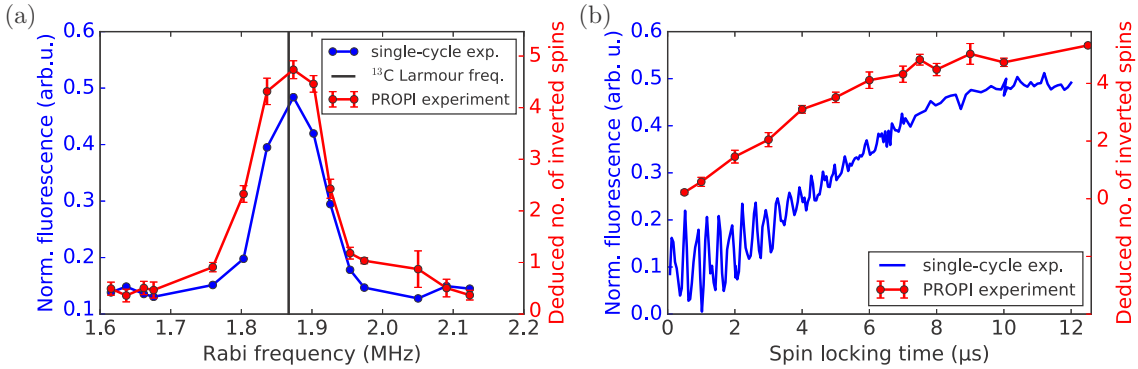


FIG. 3. (a) NOVEL experiment. Here the NV's fluorescence is observed as a function of the Rabi frequency of the spin locking pulse for a single polarization step where the nuclear spin bath is not polarized ($N = M = 1$, blue curve). The red curve is a PROPI measurement which gives the average number of nuclear spin flips after polarizing the spin bath ($N = 50$, $M = 200$). An increase of the signal is observed when the condition (2) is fulfilled, which is a signature of polarization transfer. (b) NOVEL experiment where we measure how the signal depends on the length of the spin locking pulse for $N = M = 1$ (blue curve) and $N = 50$, $M = 200$ (red curve). The oscillations in the single cycle measurement are due to coupling to the ^{14}N nuclear spin of the NV.

applied microwave. $\omega_0^{^{13}\mathrm{C}} = \gamma^{^{13}\mathrm{C}} B$ is the Larmor frequency of the ^{13}C nuclear spins; see also Eq. (1).

In the experimental data shown in Fig. 2(b) we observe that the NV's fluorescence level drops as a function of n to a certain level, where it remains constant. The phase of the $\pi/2$ pulses around the spin locking time is the same, such that a bright fluorescence level indicates a spin flip during the spin locking time. The decay of fluorescence translates to a diminishing spin flip probability (for $n \sim 200$), meaning that the NV's polarization is completely transferred to the closest nuclear spins and no further electron-nuclear spin flip-flops can be observed. Hence the loss of fluorescence is a signature that the nuclear spin bath is polarized. After that we invert this polarization by changing the phase of the $\pi/2$ pulses by 180° and run the sequence for M times. Now we again start to observe flip-flop processes, which are suppressed after $m \sim 200$ cycles as expected [see Fig. 2(c)], since the polarization transfer for both nuclear spin states must saturate for the same number of polarization cycles if we neglect spin diffusion to more distant nuclei. The area between the fluorescence signal and the offset [averaged over the last 30 points; see Fig. 2(c), inset] indicates the number of spin quanta transferred from the NV to the nuclear spins. We obtain a quantitative measure of the nuclear spin polarization by correcting for imperfect NV initialization, arising from the charge state fluctuations leading to an initialization of 70% NV^- [22], from the electron spin initialization of 92% into the $m_s = 0$ state [22] and from initialization when the NV's nuclear spin is in a different state. This measure is the deduced number of inverted spins for the buildup of polarization with different values of N as depicted in Fig. 2(e). The accuracy of our measure is confirmed by theoretical simulations with Hamiltonian (1) having a nuclear spin bath of 30 spins [Figs. 2(c) and 2(d)] and using the time-evolving block decimation (TEBD) algorithm [23–25]. The nuclear spins are randomly sampled in a diamond lattice with natural abundance of ^{13}C, the results are averaged over 30 different spin bath configurations, and we account for the above mentioned imperfect NV initialization. In Fig. 2(d) we compare the simulated polarization of the nuclear spins with the simulated NV fluorescence signal including all experimental parameters. These two together with the averaged experimental spin bath signal are in excellent agreement.

For $n = 200$ and $m = 200$ there is an offset [Figs. 2(b) and 2(c)] different from zero, which does not indicate polarization transfer. This effect can be explained by the driving of the off-resonant nitrogen hyperfine transitions. By defining the signal area between the fluorescence signal and the offset we solely observe the resonant, coherent nuclear-electron spin flip-flop process. Due to the offset correction this directly translates to polarization transfer in terms of spin flip quanta (or quanta of angular momentum transferred). Effects like decoherence, pulse imperfections, spin relaxation, and off-resonant driving will lower the efficiency of the polarization but they do not affect the accuracy of the readout. If this was the case, then they also influence the tail of the fluorescence signal and by subtracting the offset they are not observed in the signal (the area below the first 100 pulses). If the polarization is not saturated during the tail (the last 30 pulses) of the readout sequence, the offset level would be higher, meaning that the number of spin flip quanta would give a lower value than the actual transferred polarization. To avoid this in the following experiments the most effective polarization sequence (NOVEL) is chosen with a polarization cycle ratio N:M of 50:200, such that the re-polarization part of PROPI ($M = 200$ cycles) saturates the polarization to a high degree. The relaxation of the NV's electron spin in the "dressed state basis" ($T_{1\rho} > 200\,\mu$s), thermal relaxation of the nuclear spin bath (T_1 process), and diffusion of the nuclear spin polarization out of the "frozen core" are negligible at this time scale. In all experiments the NV's fluorescence signal is normalized by a separate measurement of the electron spin population inversion via a π pulse.

In Fig. 3(a) (blue curve) experimental data are shown, where the Rabi frequency Ω_1 of the spin locking pulse is varied for a single polarization cycle and the NV's fluorescence is observed.

With this measurement we determine the correct Rabi frequency for controlling the nuclear spin bath. The PROPI

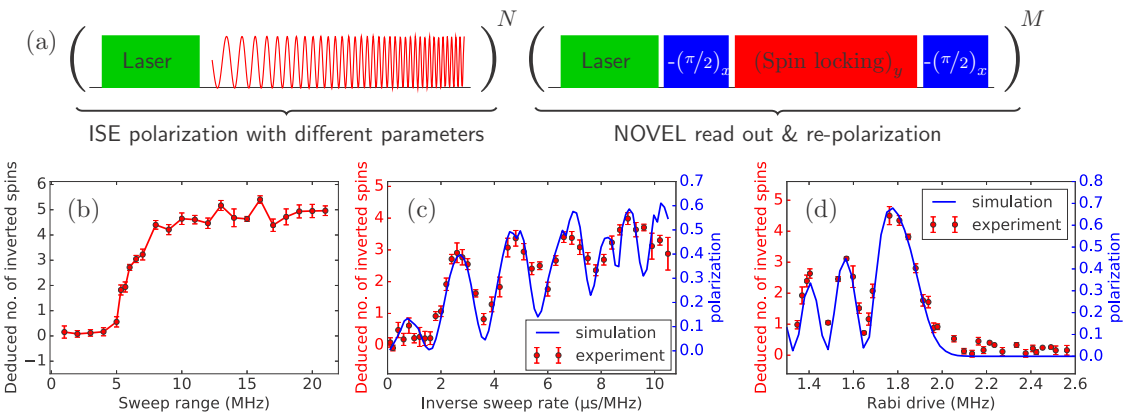


FIG. 4. DNP of the nuclear spin bath using ISE observed via PROPI. (a) Pulse sequence used in the experiments. (b) Dependence of the polarization on the sweep range of the MW. Transfer of polarization as a function of inverse sweep rate (c) and strength of the driving field (d). The red curves show the experimental data; the blue curves are simulations using three nuclear spins and without free parameters. The right axis presents the sum of the I_z of all three spins.

experiment (red curve) uses $N = 50$ cycles where one spin locking parameter is varied and afterwards $M = 200$ cycles with optimal spin locking parameters are applied. The latter 200 pulses are used to read out the magnetization and initialize the nuclear spin bath into the $|\downarrow\rangle$ state. If we repeat the polarization sequence many times, the signal becomes broader (red curve). This is due to multiple spin flip-flop processes between the NV and different nuclear spins within the N repetitions, resulting in a saturation of polarization at a broader range of Rabi frequencies. In Fig. 3(b) we plot the dependence of the NV's fluorescence on the length of the spin locking pulse, when Eq. (2) is fulfilled. The increase of the signal is again related to polarization transfer, which has a maximum at a length of the spin locking pulse of about 10 μs. Here again the blue curve represents a single polarization cycle ($N = M = 1$), while the red curve was measured using $N = 50$ and $M = 200$. For the latter we observe a faster polarization transfer, which can be explained by the multiple spin flip-flops during the repetitions of the measurement. If we continue to increase the pulse length, the signal again decreases and shows oscillations (data not shown), as reported previously [5]. The signal of the single cycle experiment shows oscillations, which are not related to the ^{13}C spins, but to hyperfine coupling to the ^{14}N nuclear spin. In all measurements the readout of the nuclear spin magnetization was performed by PROPI with the following parameters: $M = 200, \Omega_1 = \omega_0^{^{13}\mathrm{C}}$, spin locking time 10 μs. In further experiments we use the PROPI method as a benchmark to compare the efficiency of different polarization techniques.

B. Integrated solid effect

We have previously demonstrated both experimentally [15] and theoretically [16] that by using the integrated solid effect (ISE) [17] electron spin polarization from an ensemble of NVs can be transferred to the surrounding ^{13}C nuclear spins. In this technique instead of a constant MW frequency, a frequency sweep over the electron spin resonance is used, which results in transfer of polarization. The effective Hamiltonian of this experiment considering an NV center coupled to a single nuclear spin can be written as [15]

$$H_{\mathrm{trans}} = \Omega\sigma_z + \Delta\sigma_x + B_{\mathrm{eff}} I_{z'} + \sigma_z(a_{z'} I_{z'} + a_{x'} I_{x'}), \qquad (3)$$

with the effective Rabi frequency $\Omega = \Omega_M/\sqrt{2}$ and MW driving strength $\Omega_M = g\mu_B B_1/\hbar$, effective detuning $\Delta = D(\theta) - \gamma_e B - \delta(\theta) + \omega_M$ with θ the angle between the static magnetic field and the NV crystal axis and MW frequency ω_M, second-order correction $\delta(\theta)$, $\sigma_{x,z}$ and $I_{x',z'}$ the electron and nuclear spin operators in the rotated basis, and $a_{z'}$ and $a_{x'}$ the secular and nonsecular hyperfine interactions, respectively.

In the ISE experiment there are three important parameters – the sweeping range of the MW frequency f_{range}, the sweep speed $v = df/dt$, and the strength of the driving field Ω_M. To find the optimal conditions is generally a complex problem, but some considerations help to narrow the range of spectral parameters. A detailed theoretical analysis of the method [16] reveals that for effective transfer of polarization the adiabatic condition with respect to the NV states has to be fulfilled while being only semiadiabatic with respect to the flip-flop transition,

$$\frac{\Omega^2}{|v|} \gg 1. \qquad (4)$$

On the other hand v should not be too small to avoid adiabaticity for the flip-flop transition. In Fig. 4 we show how the polarization transfer depends on these parameters.

In these experiments the nuclear spin bath was polarized using the ISE pulse sequence shown in Fig. 4(a). It starts with the usual laser pulse to initialize the NV followed by an MW chirp pulse where its frequency is changed over the resonance transition. After that the polarization is measured and reinitialized by applying the NOVEL pulse sequence with optimal parameters for $M = 200$. We observe that, by increasing the sweeping range, the polarization transfer improves until a saturation for $f_{\mathrm{range}} > 10$ MHz is reached [Fig. 4(b)]. The maximum of the nuclear spin polarization is the same as in the NOVEL experiment (Fig. 3), showing that with both DNP methods similar nuclear spin polarization

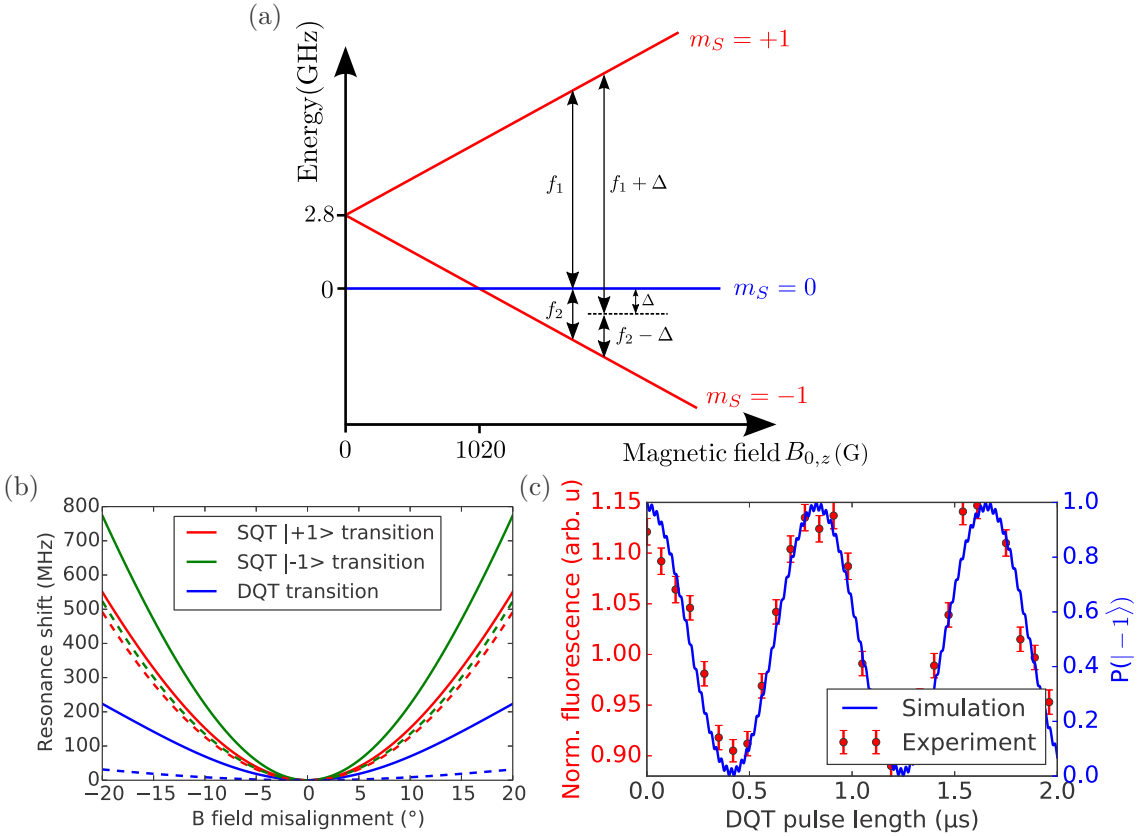


FIG. 5. (a) Energy levels of the NV's electron as a function of the strength of the applied static magnetic field $\vec{B}$ along the NV's crystal axis. The arrows indicate the two MW frequencies $f_3 = f1 + \Delta$ and $f_4 = f2 - \Delta$ which are used to drive the double-quantum transition $|-1\rangle \leftrightarrow |+1\rangle$. (b) Shift of the resonance line for the single- and double-quantum transitions as a function of the misalignment angle θ for 1770 G (solid) and for 1 T (dashed). (c) Experimental (blue markers) and theoretical [red curve, using the Hamiltonian (5)] DQT Rabi oscillations.

can be achieved. Due to the frequency sweep, ISE with the optimal parameters is about three times slower per polarization cycle than NOVEL, but it can be applied for broader spectral lines. An increase of the spin polarization transfer is also observed when the inverse sweeping rate $1/|v|$ is increased [Fig. 4(c)] and additionally the signal oscillates. A similar effect is observed when the Rabi frequency is changed; see Fig. 4(d), where the maximum polarization transfer is reached close to the Hartman-Hahn condition [Eq. (2)].

The oscillating behavior in Fig. 4(d) is attributed to Landau-Zener-Stückelberg oscillations [26,27], which is confirmed by the theoretical calculations (blue curves) using the Hamiltonian (3) with three nuclear spins, 20 polarization cycles (more cycles do not introduce changes), and no further free parameters. Such oscillations can only be observed in a single spin experiment, owing to the signal averaging in an ensemble experiment with many different nuclear spin environments.

IV. DNP USING THE DOUBLE-QUANTUM TRANSITION

One major drawback of NV centers in their application for DNP is that the electron spin polarization mechanism and its transition frequency depend on the orientation of the applied static magnetic field $\vec{B}$ with respect to the z axis (angle θ). In an ensemble of nanodiamonds each NV will have an arbitrary orientation, which may change over time and will lead both to significant broadening of the ESR line and to loss of ODMR contrast. In this case NOVEL cannot be used for DNP as it works in a narrow frequency range as shown in Fig. 3(a). Some of us have recently proposed [16] the use of DQT ($|-1\rangle \leftrightarrow |+1\rangle$) of NV centers in nanodiamonds at high magnetic fields (when $D\widehat{S}_z^2 << g\mu_B|\vec{B}|$) to reduce the sensitivity to misalignments. The DQT can be driven by applying simultaneously two MW frequencies which are detuned with Δ from the single-quantum transitions; see Fig. 5(a).

Figure 5(b) shows how the resonance frequency of SQT and DQT depends on the misalignment of $\vec{B}$. From this plot we can observe the stark difference in angle dependence between SQT and DQT. For example, for $B = 1$ T and $\theta = 20°$ the resonance shift in DQT is less than 50 MHz, compared with SQT where it is about 500 MHz. A typical experimental data set of a DQT Rabi measurement is depicted in Fig. 5(c), where the signal can be simulated using the Hamiltonian (5) explained below.

Next we describe briefly the DQT-DNP method; a more detailed description of the physics involved can be found in [16], Sec. II. Under MW irradiation with frequencies $\omega_{-1}^{\mathrm{MW}} = 2\pi f_1$, $\omega_1^{\mathrm{MW}} = 2\pi f_2$ and amplitudes (Rabi frequencies) $\sqrt{2}\,\Omega_1, \sqrt{2}\,\Omega_{-1}$, the following Hamiltonian in the

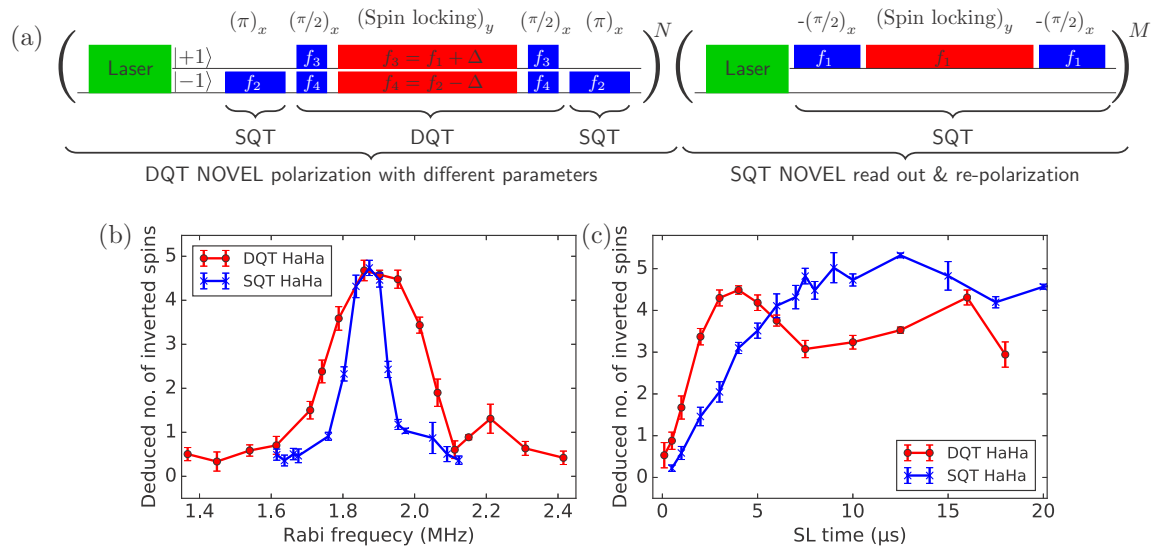


FIG. 6. (a) Pulse sequence for the DQT-NOVEL experiment. Efficiency of the transfer of polarization for SQT (blue) and DQT (red) as a function of the Rabi frequency (b) and the length of the spin locking pulse (c). All experiments are measured using PROPI with optimal NOVEL conditions.

interaction picture is obtained

$$H = \frac{\delta}{2}S_z + \Delta S_z^2 + \frac{\Omega_1}{2}(|1\rangle\langle 0| + |0\rangle\langle 1|) + \frac{\Omega_{-1}}{2}(|-1\rangle\langle 0| + |0\rangle\langle -1|) + \gamma_I B I_{z'} + S_z(a_{z'}I_{z'} + a_{x'}I_{x'}). \quad (5)$$

Defining $\Delta_1 = \omega_1 - \omega_1^{\mathrm{MW}}$, $\Delta_{-1} = \omega_{-1} - \omega_{-1}^{\mathrm{MW}}$, then $\delta = \Delta_1 + \Delta_{-1}$ is the detuning from the DQT, and $\Delta = (\Delta_1 - \Delta_{-1})/2$ is the detuning from the $|0\rangle$ state; see Fig. 5(a). As $\Delta > \Omega_1, \Omega_{-1}$, the $|0\rangle$ state is detuned from the dynamics and we obtain an effective Hamiltonian for the $\{|-1\rangle, |1\rangle\}$ subspace after adiabatic elimination of the $|0\rangle$ state,

$$H_{\mathrm{DQT}} = (\delta + \delta_{so})\sigma_z + \Omega_{\mathrm{eff}}\sigma_x + \gamma_I B I_z + 2\sigma_z(a_{z'}I_{z'} + a_{x'}I_{x'}), \quad (6)$$

where $\sigma_z = \frac{1}{2}(|1\rangle\langle 1| - |-1\rangle\langle -1|)$, $\sigma_x = \frac{1}{2}(|1\rangle\langle -1| + |-1\rangle\langle 1|)$, and $\delta_{so} = \frac{\Omega_1^2 - \Omega_{-1}^2}{4\Delta}$ is the detuning due to second-order corrections for $\Delta \gg \Omega_1, \Omega_{-1}$. The DQT Rabi frequency when $\Omega_1\Omega_{-1} = \Omega_{\mathrm{SQT}}$ and $\delta = 0$ is given by $\Omega_{\mathrm{eff}} = 1/2(\sqrt{2\alpha\Omega_{\mathrm{SQT}}^2 + \Delta^2} - \Delta)$, where typical experimental parameters are $\Omega_{\mathrm{SQT}} \approx 10\,\mathrm{MHz}$ and $\Delta = 40\,\mathrm{MHz}$. The factor α is introduced for convenient sweeping of the Rabi frequency; see Fig. 7(d).

Time evolution under the effective Hamiltonian (6) will result in polarization transfer from the NV center to a single nuclear spin. Here the effective hyperfine coupling is two times larger compared to the SQT experiments; see Eq. (3). This result is confirmed by the experiment as shown below.

A. NOVEL using DQT

The pulse sequence for the NOVEL experiment using the DQT is shown in Fig. 6(a). After the initialization of the NV in $|0\rangle$, we apply a π pulse on the $|0\rangle \leftrightarrow |-1\rangle$ transition, followed by two pulses on both transitions, which serve as a DQ $\pi/2$ pulse. Afterwards we apply a DQ spin locking pulse (90° phase shifted with respect to the $\pi/2$ pulse), during which the NV's electron spin is in the dressed state basis. Then we transform back to the $|0\rangle, |-1\rangle, |1\rangle$ basis. The magnetization of the nuclear spin bath is read out by PROPI using a SQT-NOVEL sequence with $M = 200$. In Fig. 6(b) we compare the efficiency of the polarization transfer for SQT-NOVEL (blue curves) and DQT-NOVEL (red curves) as a function of the Rabi frequency. We observe that for the DQT measurement spin flip-flop processes occur for a wider range of MW powers, compared to SQT-NOVEL. By increasing the length of the spin locking pulses, DQT reaches maximum earlier compared to SQT as shown in Fig. 6(b). Both signals show oscillations, which are caused by the ^{13}C spins with the strongest coupling (compared to the rest of the nuclear spin bath) to the NV. The DQT shows the doubled frequency (60 kHz) compared to SQT (30 kHz), as expected from the theory [see Eq. (6)] due to the twice larger magnetic dipole moment.

B. ISE using DQT

In the previous section we have shown polarization build up via the DQT-NOVEL method, but the resonance frequency range is limited [see Fig. 6(b)]. Here we implement ISE using the DQT, where both larger frequency range and robustness against misalignment of the magnetic field is expected. The pulse sequence used in the experiment is depicted in Fig. 7(a).

Again the NV is put into the $|-1\rangle$ state by a laser and a π pulse. Simultaneously two chirp pulses are applied on both NV transitions. The frequency of the pulse on the $|0\rangle \leftrightarrow |+1\rangle$ transition is increasing, while on the other one it is decreasing. Here Δ is kept constant, while δ is changed; see Eq. (5). At the end we use again a π pulse on the $|0\rangle \leftrightarrow |-1\rangle$ transition and then read out the NV state. The nuclear spin bath magnetization is read out by PROPI using a SQT-NOVEL sequence. First we compare how the polarization transfer depends on the range of the frequency sweep for DQT and SQT; Fig. 7(b). We find that for the former measurement a saturation is reached for about half of the range compared to

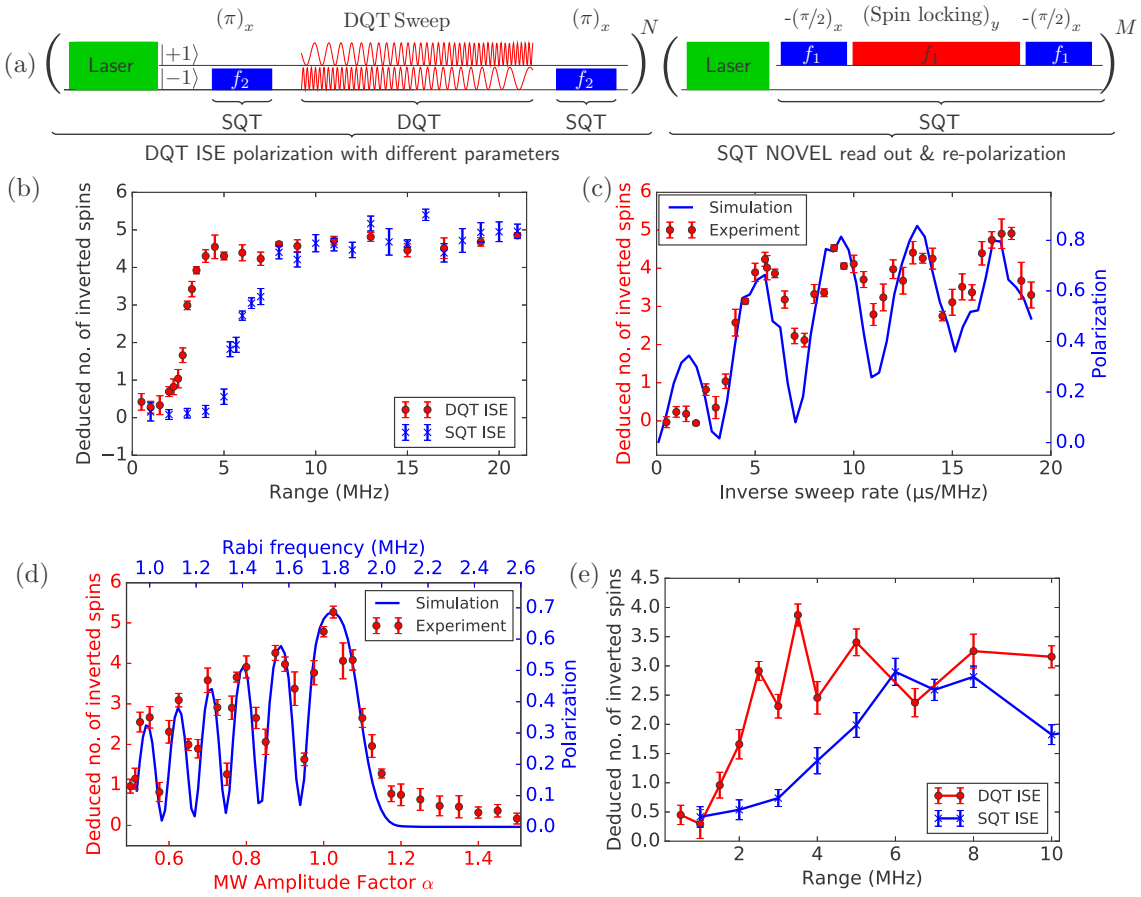


FIG. 7. (a) Pulse sequence for the DQT-ISE experiment. (b) Polarization transfer as a function of the frequency range for SQT-ISE (blue) and DQT-ISE (red). Polarization transfer dependence on the sweeping rate (c) and MW amplitude factor α proportional to the Rabi frequency (d) for DQT (red markers). The blue curves are simulations. (e) Misalignment of the external magnetic field with respect to the NV axis of 5°; performance of DQT-ISE (red) and SQT-ISE (blue) depend on the range of the sweep (here $N = 50$ and $M = 300$). Readout is performed by PROPI with Hartmann-Hahn conditions matched.

the SQT, which could be explained by the doubled effective hyperfine interaction constant to the ^{13}C nuclear spins. When we change the sweeping rate [see Fig. 7(c)], we again observe the Landau-Zehner-Stückelberg oscillations, similar to the SQT-ISE experiment [see also Fig. 4(b)]. Analogous to SQT-ISE, this is also the result of changing the DQ Rabi frequency shown in Fig. 7(d). This behavior can be reproduced with simulations [blue curves in Figs. 7(c) and 7(d)] using the Hamiltonian (6) and same parameters as in Sec. III B adding additional MW power fluctuations of ±5%.

At high magnetic fields when the magnetic field is not aligned with the NV crystal axis, both the optical polarization and contrast of the readout of the NV center are significantly reduced [4]. However, our readout method still enables the measurement of the nuclear bath polarization although with low contrast.

The misalignment shifts the NV's resonance frequency by Δ_{SQT} leading to the effective Rabi frequency $\Omega_{\mathrm{eff}} = \sqrt{\Omega_{\mathrm{SQT}}^2 + \Delta_{\mathrm{SQT}}^2}$, where the MW drive Ω_{SQT} is constant. From Fig. 3 we observe that the width of the Hartmann-Hahn resonance is approximately 100 kHz in the SQT. At the applied magnetic field of 1770 G and a misalignment angle of 5° with the NV crystal axis the electron spin resonance is shifted by $\Delta_{\mathrm{SQT}} \approx 60$ MHz, resulting in $\Omega_{\mathrm{eff}} \approx 60$ MHz since $\Omega_{\mathrm{SQT}} = 1.86$ MHz. Here we are far away from the Hartmann-Hahn condition (2).

We have performed DNP experiments with $\theta = 5°$. In Fig. 7(e) we compare SQT-ISE and DQT-ISE showing how the polarization transfer depends on the frequency sweep range, which is centered around the new, misaligned resonance condition. We observe similar behavior compared to the aligned case. Beginning from a certain range, polarization is transferred from the NV to the nuclear spins, where for DQT-ISE the required range is shorter than with SQT-ISE. In order to measure this polarization transfer PROPI is used with optimal parameters of the NOVEL sequence. The signal obtained in the experiments is rather low, compared to the signal when the magnetic field is aligned. This effect is not due to low efficiency of the polarization transfer, but rather a result of the inefficient readout of the nuclear spin bath. Owing to misalignment-induced loss of optical polarization efficiency and no nitrogen hyperfine spin state polarization [28] the ODMR contrast is ∼10-fold reduced. These lead also to lower polarization efficiency in NOVEL which means that compared to the aligned case more polarization cycles ($M = 300$) are needed to reinitialize the spin bath. Due to the low signal

the measurement time increased 100 times, thus allowing us to perform an experiment only for one off-axis angle of the magnetic field. We could not perform this measurement at higher magnetic field and at larger angle θ since the signal was too low.

In addition to requiring a shorter sweep range as in the aligned case, DQT-ISE enables covering a larger angle misalignment for the same sweep range. As shown in Fig. 5(c), in 1-T magnetic field, a 5° angle will correspond to barely a few MHz shift in the DQT resonance, compared to over 30 MHz for the SQT.

V. CONCLUSIONS

We presented a method for reading out bath's magnetization called polarization readout by polarization inversion (PROPI) providing a measure of polarization of the nearby nuclear spins. With this technique we have evaluated robust methods for controlling the nuclear spin bath (^{13}C nuclear spins) surrounding a central electron spin (single NV center). In contrast to previous reports, our polarization techniques can be applied at a wide range of magnetic fields and sample orientations. This enables the implementation of optical DNP in nanodiamonds and also in ^{13}C enriched samples with broad spectral line widths. We compare the performance of the different methods, where the experimental data are well supported by theoretical simulations. The methods demonstrated here could be applied to other promising systems like color centers in silicon carbide, where nuclear spin polarization has been also observed [29]. We believe that the results reported here will find an application in DNP NMR spectroscopy and MRI with chemically modified nanodiamonds as markers.

ACKNOWLEDGMENTS

We thank L. P. McGuinness, T. Unden, S. Schmitt, P. London, X. Kong, B. Tratzmiller, and C. Müller for fruitful discussions and technical support. We thank Jan Haase for providing code to obtain hyperfine coupling constants in the diamond lattice. This work was supported by the ERC Synergy grant BioQ, the EU (DIADEMS, HYPERDIAMOND Grant Agreement No. 667192), the DFG (SFB TR/21, FOR 1493), and the Volkswagenstiftung. B.N. is grateful to the Postdoc Network program of the IQST and to the Bundesministerium für Bildung und Forschung for receiving the ARCHES award. I.S. acknowledges a Ph.D fellowship from the IQST. I.D. acknowledges financial support from the Alexander von Humboldt-Stiftung via the Humboldt Research Fellowship for Postdoctoral Researchers.

[1] J. Cai, A. Retzker, F. Jelezko, and M. B. Plenio, Nat. Phys. **9**, 168 (2013).
[2] G. A. Álvarez, D. Suter, and R. Kaiser, Science **349**, 846 (2015).
[3] K. Tateishi, M. Negoro, S. Nishida, A. Kagawa, Y. Morita, and M. Kitagawa, Proc. Natl. Acad. Sci. USA **111**, 1599 (2014).
[4] V. Jacques, P. Neumann, J. Beck, M. Markham, D. Twitchen, J. Meijer, F. Kaiser, G. Balasubramanian, F. Jelezko, and J. Wrachtrup, Phys. Rev. Lett. **102**, 057403 (2009).
[5] P. London, J. Scheuer, J.-M. Cai, I. Schwarz, A. Retzker, M. B. Plenio, M. Katagiri, T. Teraji, S. Koizumi, J. Isoya, R. Fischer, L. P. McGuinness, B. Naydenov, and F. Jelezko, Phys. Rev. Lett. **111**, 067601 (2013).
[6] R. Fischer, C. O. Bretschneider, P. London, D. Budker, D. Gershoni, and L. Frydman, Phys. Rev. Lett. **111**, 057601 (2013).
[7] G. Alvarez, C. Bretschneider, R. Fischer, P. London, H. Kanda, S. Onoda, J. Isoya, D. Gershoni, and L. Frydman, Nat. Commun. **6**, 8456 (2015).
[8] J. P. King, K. Jeong, C. C. Vassiliou, C. C. Shin, R. H. Page, C. E. Avalos, H.-J. Wang, and A. Pines, Nat. Commun. **6**, 8965 (2015).
[9] B. L. Green, B. G. Breeze, G. J. Rees, J. V. Hanna, J.-P. Chou, V. Ivády, A. Gali, and M. E. Newton, Phys. Rev. B **96**, 054101 (2017).
[10] J. R. Maze, P. L. Stanwix, J. S. Hodges, S. Hong, J. M. Taylor, P. Cappellaro, L. Jiang, M. V. G. Dutt, E. Togan, A. S. Zibrov, A. Yacoby, R. L. Walsworth, and M. D. Lukin, Nature (London) **455**, 644 (2008).
[11] G. Balasubramanian, I. Y. Chan, R. Kolesov, M. Al-Hmoud, J. Tisler, C. Shin, C. Kim, A. Wojcik, P. R. Hemmer, A. Krueger, T. Hanke, A. Leitenstorfer, R. Bratschitsch, F. Jelezko, and J. Wrachtrup, Nature (London) **455**, 648 (2008).
[12] F. Dolde, H. Fedder, M. W. Doherty, T. Nöbauer, F. Rempp, G. Balasubramanian, T. Wolf, F. Reinhard, L. C. L. Hollenberg, F. Jelezko, and J. Wrachtrup, Nat. Phys. **7**, 459 (2011).
[13] P. Neumann, I. Jakobi, F. Dolde, C. Burk, R. Reuter, G. Waldherr, J. Honert, T. Wolf, A. Brunner, J. H. Shim, D. Suter, H. Sumiya, J. Isoya, and J. Wrachtrup, Nano Lett. **13**, 2738 (2013).
[14] G. Kucsko, P. C. Maurer, N. Y. Yao, M. Kubo, H. J. Noh, P. K. Lo, H. Park, and M. D. Lukin, Nature (London) **500**, 54 (2013).
[15] J. Scheuer, I. Schwartz, Q. Chen, D. Schulze-Sünninghausen, P. Carl, P. Höfer, A. Retzker, H. Sumiya, J. Isoya, B. Luy, M. B. Plenio, B. Naydenov, and F. Jelezko, New J. Phys. **18**, 013040 (2016).
[16] Q. Chen, I. Schwarz, F. Jelezko, A. Retzker, and M. B. Plenio, Phys. Rev. B **92**, 184420 (2015).
[17] A. Henstra, P. Dirksen, and W. Wenckebach, Phys. Lett. A **134**, 134 (1988).
[18] A. Henstra and W. Wenckebach, Mol. Phys. **112**, 1761 (2014).
[19] G. R. Khutsishvili, Sov. Phys. JETP **15**, 909 (1962).
[20] A. Henstra, P. Dirksen, J. Schmidt, and W. Wenckebach, J. Magn. Reson. **77**, 389 (1988).
[21] S. R. Hartmann and E. L. Hahn, Phys. Rev. **128**, 2042 (1962).
[22] G. Waldherr, J. Beck, M. Steiner, P. Neumann, A. Gali, T. Frauenheim, F. Jelezko, and J. Wrachtrup, Phys. Rev. Lett. **106**, 157601 (2011).

[23] J. Prior, A. W. Chin, S. F. Huelga, and M. B. Plenio, Phys. Rev. Lett. **105**, 050404 (2010).
[24] U. Schollwöck, Ann. Phys. **326**, 96 (2011).
[25] D. Suess and M. Holzaepfel, [https://github.com/dseuss/mpnum] .
[26] S. Shevchenko, S. Ashhab, and F. Nori, Phys. Rep. **492**, 1 (2010).
[27] P. Huang, J. Zhou, F. Fang, X. Kong, X. Xu, C. Ju, and J. Du, Phys. Rev. X **1**, 011003 (2011).
[28] P. Neumann, Ph.D thesis, University of Stuttgart, 2012.
[29] A. L. Falk, P. V. Klimov, V. Ivady, K. Szasz, D. J. Christle, W. F. Koehl, A. Gali, and D. D. Awschalom, Phys. Rev. Lett. **114**, 247603 (2015).

2.3 Optical hyperpolarization of ^{13}C nuclear spins in nanodiamond ensembles

Title:	Optical hyperpolarization of ^{13}C nuclear spins in nanodiamond ensembles
Authors:	Chen, Q. and Schwarz, I. and Jelezko, F. and Retzker, A. and Plenio, M. B.
Journal:	Physical Review B 92, 184420
Year:	2015
Copyright:	©2015 American Physical Society. Reprinted with permission from Chen et al. Physical Review B 92, 184420 (2015), ©2015 by the American Physical Society
DOI:	{https://doi.org/10.1103/PhysRevB.92.184420}

PHYSICAL REVIEW B **92**, 184420 (2015)

Optical hyperpolarization of ^{13}C nuclear spins in nanodiamond ensembles

Q. Chen,[1,2] I. Schwarz,[1,2] F. Jelezko,[2,3] A. Retzker,[4] and M. B. Plenio[1,2]
[1]*Institut für Theoretische Physik, Albert-Einstein-Allee 11, Universität Ulm, 89069 Ulm, Germany*
[2]*IQST, Albert-Einstein-Allee 11, Universität Ulm, 89069 Ulm, Germany*
[3]*Institut für Quantenoptik, Universität Ulm, 89073 Ulm, Germany*
[4]*Racah Institute of Physics, The Hebrew University of Jerusalem, Jerusalem 91904, Israel*
(Received 8 June 2015; revised manuscript received 8 September 2015; published 18 November 2015)

Dynamical nuclear polarization holds the key for orders of magnitude enhancements of nuclear magnetic resonance signals which, in turn, would enable a wide range of novel applications in biomedical sciences. However, current implementations of DNP require cryogenic temperatures and long times for achieving high polarization. Here we propose and analyze in detail protocols that can achieve rapid hyperpolarization of ^{13}C nuclear spins in randomly oriented ensembles of nanodiamonds at room temperature. Our protocols exploit a combination of optical polarization of electron spins in nitrogen-vacancy centers and the transfer of this polarization to ^{13}C nuclei by means of microwave control to overcome the severe challenges that are posed by the random orientation of the nanodiamonds and their nitrogen-vacancy centers. Specifically, these random orientations result in exceedingly large energy variations of the electron spin levels that render the polarization and coherent control of the nitrogen-vacancy center electron spins as well as the control of their coherent interaction with the surrounding ^{13}C nuclear spins highly inefficient. We address these challenges by a combination of an off-resonant microwave double resonance scheme in conjunction with a realization of the integrated solid effect which, together with adiabatic rotations of external magnetic fields or rotations of nanodiamonds, leads to a protocol that achieves high levels of hyperpolarization of the entire nuclear-spin bath in a randomly oriented ensemble of nanodiamonds even at room temperature. This hyperpolarization together with the long nuclear-spin polarization lifetimes in nanodiamonds and the relatively high density of ^{13}C nuclei has the potential to result in a major signal enhancement in ^{13}C nuclear magnetic resonance imaging and suggests functionalized and hyperpolarized nanodiamonds as a unique probe for molecular imaging both *in vitro* and *in vivo*.

DOI: 10.1103/PhysRevB.92.184420 PACS number(s): 76.70.Fz, 03.67.Lx, 67.30.hj, 76.90.+d

I. INTRODUCTION

Nuclear magnetic resonance (NMR) [1,2] and magnetic resonance imaging (MRI) [3] have evolved to be powerful techniques to extract molecular-level information in a wide variety of physical, chemical, and biological applications. Recently, ^{13}C based MRI has emerged as a platform enabling essentially background-free imaging of nonproton nuclei with the additional possibility for the local and permanent destruction of the signal by means of radio frequency (rf) pulses [4]. However, the low signal-to-noise ratio for ^{13}C based MRI is not sufficient for most clinical and research applications due to the combination of a relatively low gyromagnetic ratio of ^{13}C and of the low natural abundance of this nucleus. Several strategies have been proposed to enhance the sensitivity of ^{13}C based MRI. Particularly promising in this context is the hyperpolarization of the ^{13}C nuclei, i.e., the generating of a large, nonthermal ^{13}C nuclear-spin polarization. Indeed, hyperpolarized ^{13}C based MRI has shown exciting potential for *in vivo* applications, especially for metabolic imaging [5–7]. One of the most powerful methods for the generation of hyperpolarization is dynamic nuclear polarization (DNP) [8–12], in which a large polarization of electron spins is transferred to nuclear spins, resulting in an enhancement of the MRI signal by several orders of magnitude.

Over the last decade, several breakthroughs have occurred in the manufacturing, surface treatment, and use of nanoparticles for biomedical applications [13]. Biocompatible nanoparticles present an attractive platform for hyperpolarization, as they can be functionalized for molecular specificity, can exhibit long nuclear-spin-relaxation times, and contain numerous nuclear spins of a single species (e.g., carbon). Long-lived hyperpolarization has been demonstrated in silica nanoparticles [14] and nanodiamonds [15,16], using standard DNP protocols, i.e., transferring the high thermal electron spin polarization at cryogenic temperatures in a strong external magnetic field to nuclei. Nanodiamonds in particular offer exciting possibilities as novel hyperpolarized probes. In addition to excellent biocompatibility [17], the possibility for surface functionalization and nuclear-spin-relaxation time of several minutes [18], nanodiamonds contain crystal point defects with unique optical and magnetic properties. Amongst these the negatively charged nitrogen-vacancy (NV) center stands out as its electron spin can be polarized over 95% within microseconds by optical pumping while exhibiting a relaxation time in the millisecond range even at room temperature [19]. In combination with the ability for transferring this near perfect electron-spin polarization to surrounding nuclear spins by means of microwave radiation, nanodiamond optical DNP promises to overcome the severe limitations on the maximally achievable polarization at room temperature by currently available methods. This would establish the NV center electron spin as a promising candidate for achieving nanodiamond hyperpolarization at ambient conditions—room-temperature optical DNP.

Previous work has demonstrated that in bulk diamond electron-spin polarization of the NV center can be generated and subsequently be transferred via hyperfine interactions to nearby nuclei. This polarization can then be detected indirectly via the NV center [15,20–27] or directly via an NMR scanner

 ©2015 American Physical Society

[28]. To this end, in bulk diamonds a high magnetic field is aligned with the natural quantization axis of the NV center to enable optical pumping to a specific electron-spin state. Controlled interaction of the electron spin with specific nearby nuclear-spins species can then be achieved for example by the application of continuous-wave microwave (MW) radiation applied to the NV center electron spin [24]. When the Rabi frequency of the microwave driving field matches the Larmor frequency of a specific nuclear-spin species [achieving a Hartmann-Hahn (HH) resonance [29]], flip-flops can occur between the microwave dressed states of the electron spin of the NV center and the surrounding ^{13}C nuclear spins [30–32] as was recently demonstrated experimentally [24].

However, medical MRI applications require large ensembles of nanodiamonds. In such ensembles (powder or solution) the angle between the external magnetic field and the orientation of NV centers and therefore their natural quantization axis is randomly distributed. This brings about several challenges for achieving high levels of hyperpolarization that need to be addressed by means of carefully designed protocols. First, the energy levels of the NV spin are then distributed over a large energy range of possible values so that the applied microwave field will be resonantly coupled to an exceedingly small fraction of the NV spins. Second, in an external magnetic field, additional limitations concern the optical polarization of the NV spins. In particular, the NV spins will be initialized to different states relative to the laboratory frame depending on their angle with the external magnetic field, thus resulting in a small net polarization.

In this work we show how to address these challenges to achieve a radical enhancement of the hyperpolarization in a nanodiamond ensemble. To this end we use an off-resonant driving and the integrated solid effect (ISE) for the NV center spin, resulting in a robust spin-polarization transfer between the NV and nuclear spins. A very large fraction of the NV electron spins can be coherently coupled to neighboring nuclear spins. Additionally, adiabatic rotation of the magnetic fields, or the Brownian rotation of the nanodiamonds themselves (in powder or solution respectively), is proposed for extending the polarization scheme to almost the entire nanodiamond ensemble. We also discuss the effect of spin diffusion induced by the nuclear dipole-diploe interactions which will further support the polarization of large volumes.

It should be noted that the principles of optical DNP that we develop in this work can be transferred to any color center that possesses an electron spin in the ground state and admits optical pumping of this electron spin. The paper is organized as follows. In Sec. II we present the coherent coupling and polarization of a single nuclear spin near a randomly oriented NV spin. This serves the introduction of the principal challenges in nanodiamond ensemble polarization, the discussion of the robust initialization and construction of suitable dressed states for the NV center electron spin, and the realization of near resonant coupling with the nuclear spin by using off-resonant driving and the integrated solid effect. In Sec. III, we introduce mechanisms to extend our polarization protocols to the entire nanodiamond ensemble, both for nanodiamond powder and for nanodiamonds in a solution. In Sec. IV, we consider our protocol for multiple ^{13}C nuclear spins and include the effect of dipolar coupling among the nuclear spins and in particular the benefits of nuclear-spin diffusion. In Sec. V we demonstrate the applicability of our polarization schemes for another very broad range of NV center orientations. In Sec. VI we take into account the effect of depolarization processes on the efficiency of our polarization protocol. Finally, the discussion and conclusion parts are given in Secs. VII and VIII, respectively.

II. MAGNETIC MANIPULATION AND POLARIZATION OF A SINGLE NUCLEAR SPIN NEARBY A RANDOMLY ORIENTED NV SPIN

A. Difficulties from the random orientations

The nanodiamond ensembles that we are interested in are realized as powder or solutions. In both cases the spatial orientations of the nanodiamonds and therefore of the NV centers hosted in them is random and uniformly distributed across the full solid angle [see Fig. 1(a) for an illustration]. In the laboratory frame this leads to the lack of a common quantization axis for the NV centers. We begin by describing in more detail the two principal challenges that are being imposed by these random spatial orientations: (1) The direction of the natural quantization axis associated with the crystal-field

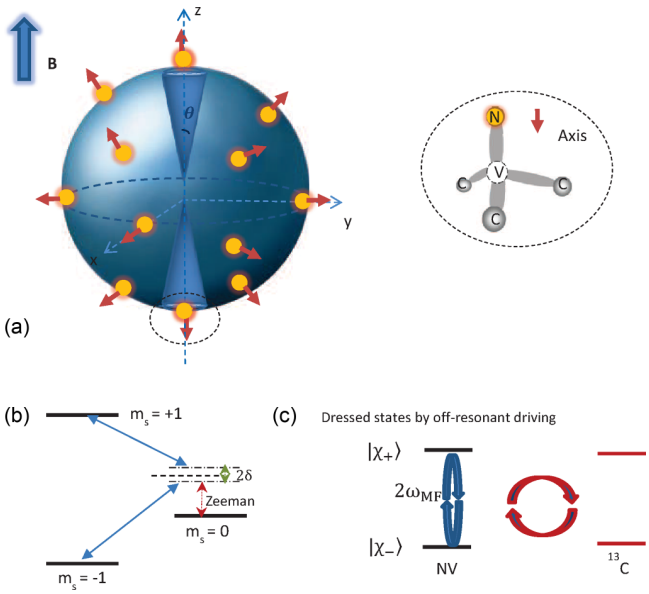


FIG. 1. (Color online) Schematic of dressed-state resonant coupling of NV spins and nuclear spins in a nanodiamond ensemble and energy-level diagrams. (a) The random orientations of the NV spins are uniformly distributed over the unit sphere. Small yellow circles represent examples with orientations indicated by red arrows which represent the unit vector pointing from the nitrogen to the vacancy of an NV center (see the example of such an NV center in the dashed circle, the axis pointing along "N-V" forms the natural quantisation axis). (b) Ground electronic spin states of an NV center in a strong external magnetic field. Microwave driving fields are applied off-resonantly achieving an effective resonant double quantum transition between the state $m_s = +1$ and $m_s = -1$ in the large detuning regime. (c) The effective coupling provides a dressed state basis which then permits energy conserving flip-flops between the dressed states and external resonant nuclear spins.

energy splitting D is not controllable, resulting in a significant variance of the energy levels in the presence of an external magnetic field, and (2) optical pumping of the NV center electron spins in an external magnetic field will not initialize all NV center electron spins to the same state.

1. Zero-field and external magnetic field distribution

The negatively charged NV center, in the following denoted for brevity as the NV center, realizes in its ground state an electronic spin triplet ($S = 1$) which exhibits a zero-field splitting of $D = (2\pi)2.87$ GHz which separates the $|m_s = 0\rangle$ state energetically from the degenerate $|m_s = \pm\rangle$ manifold. The application of an external magnetic field, in the following assumed to take the value $B = 0.36$ T, lifts this remaining degeneracy such that the state $m_s = -1$ is shifted below the $m_s = 0$ state [see Fig. 1(b)]. The zero-field splitting and the Zeemann effect due to an external magnetic field of the NV center are described by

$$H_{NV} = \vec{S}\mathbf{D}\vec{S} + \gamma_e \vec{B}\vec{S}. \tag{1}$$

Herein $\mathbf{D}$ denotes the orientation dependent zero-field splitting tensor, $\gamma_e = (2\pi)28.7$ GHz/T the gyromagnetic ratio, $\vec{S}$ the electron spin-1 vector operator [33], and $\vec{B}$ the magnetic field vector. In the principal axis system defined by the NV symmetry axes, the zero-field splitting tensor $\mathbf{D}$ is diagonal,

$$\mathbf{D} = \mathrm{diag}\left(-\tfrac{1}{3}D + E, -\tfrac{1}{3}D - E, \tfrac{2}{3}D\right). \tag{2}$$

Here E denotes the strain dependent contribution. It is worth emphasizing that in the scenario that we are considering here, the orientation of the symmetry axis of the NV center relative to the external magnetic field is uniformly distributed over the unit sphere. For the following it will be convenient to conduct the discussion in the laboratory frame whose z axis we define to take the direction of the externally applied strong magnetic field, $\gamma_e B \gg D$. In this frame, the zero-field splitting tensor $\mathbf{D}$ will have off-diagonal elements. As $\gamma_e B \gg D$ these off-diagonal elements are rapidly rotating so that their main effect will be energy shifts of the diagonal element of the Hamiltonian. The Hamiltonian can then be written as (see the Appendix for details of the derivation)

$$H''_{\mathrm{eff}} = [\gamma_e B + \delta(\theta)]S_z + D(\theta)S_z^2, \tag{3}$$

where

$$D(\theta) = \frac{D[1 + 3\cos(2\theta)] + 3E[1 - \cos(2\theta)]}{4},$$
$$\delta(\theta) = \frac{\gamma_e B|G_1|^2}{(\gamma_e B)^2 - [D(\theta)]^2} + \frac{|G_2|^2}{2\gamma_e B}, \tag{4}$$

θ is the angle between the magnetic field direction and the NV axis and the G_i are given in the Appendix. Clearly, the random orientations of the NV centers cause a variation of the zero-field splitting $D(\theta)$ across the entire interval $[-(2\pi)1.43$ GHz,$(2\pi)2.87$ GHz$]$ and $\delta(\theta)$ across the interval $[0$ MHz,$(2\pi)140$ MHz$]$ as shown in Fig. 2.

If we were to follow the scheme of Ref. [24], i.e., without the combination of off-resonant drive and ISE technique that we will present in this work, the uncertain detuning of the MW frequency from the electronic resonance can reach the order of GHz, which in turn would prevent effective polarization transfer.

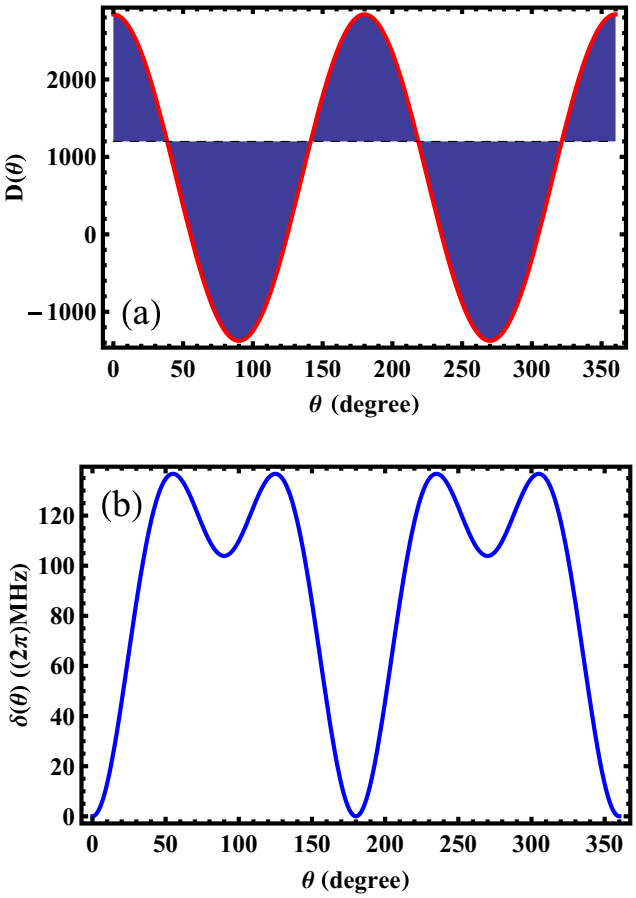


FIG. 2. (Color online) (a) Zero-field distribution $D(\theta)$ of the NV spins in nanodiamonds with $D = (2\pi)2.87$ GHz and $E = (2\pi)20$ MHz. (b) The second-order corrections which induce an energy distribution $\delta(\theta)$.

2. Optical initialization of NV spins at the high magnetic field limit

A second important difference between a randomly oriented nanodiamond ensemble and a bulk diamond concerns the optical polarization of electron spins of the NV center. For bulk diamonds, the magnetic field can be aligned with the principal axis of the NV center and the electronic spin of the NV center can be optically polarized to the state $|m_s = 0\rangle$ by illumination with a 532-nm green laser. However, for an ensemble of randomly oriented nanodiamonds, even in the limit of a strong magnetic field, the NV centers will be optically pumped to the state $|m_s = 0\rangle_\theta$ that is defined by the relative orientation of the NV center with respect to the externally applied magnetic field which defines the laboratory frame.

As discussed in the Appendix, these two coordinate systems can be transformed into each other and, employing $S_{z_\theta} = \cos\theta S_z - \sin\theta(\cos\phi S_x - \sin\phi S_y)$, we can express the eigenstate $|m_s = 0\rangle_\theta$ in terms of the eigenstates $|0\rangle, |\pm 1\rangle$ of

Eq. (3), i.e., in the laboratory frame, as

$$|0\rangle_\theta = \cos\theta|0\rangle + \frac{\sin\theta}{\sqrt{2}}(e^{i\phi}|+1\rangle - e^{-i\phi}|-1\rangle). \quad (5)$$

If θ is large, the eigenstate $|0\rangle$ of the NV center in the laboratory frame as given by Hamiltonian Eq. (3) differs significantly from the zero-field eigenstate $|0\rangle_\theta$ of the NV center. Hence optical initialization of randomly oriented NV centers lead to very different states depending on the orientation of the NV center.

Notice though that for moderate misalignment between the NV center orientation and external magnetic field, the initialization of the NV center is well approximated by $|0\rangle$. Indeed, for $\theta < 10^\circ$, $|\langle 0|0\rangle_\theta|^2 > 0.97$ and for $\theta < 20^\circ$ we find $|\langle 0|0\rangle_\theta|^2 > 0.88$ which implies significant polarization along the quantization axis defined by the external magnetic field. Therefore, for all the orientations of the NV centers that fall into two spherical sectors whose cone angle is 2θ, i.e., the two blue spherical sectors in Fig. 1(a), significant optical polarization can be achieved. From now on, we define a deviation by θ to imply that the symmetry axis of the NV spins falls within these two spherical cones.

B. The main ideas

The main idea that we will develop in this section consists of three main ingredients, namely (i) the generation of an energy gap between electronic states that is relatively robust with respect to variations in the relative orientation between the NV center and an external magnetic field, and at the same time (ii) a strong coupling between these electronic states and nuclear spins. Finally, (iii) the integrated solid effect is employed to achieve additional robustness against imperfections. All this is achieved by the use of dressed states in a ladder-type configuration in which the single quantum transitions are far detuned and the double quantum transition is nearly resonant (see Fig. 3).

In such a setting, that is for a detuning on the single quantum transition $D(\theta)$, the effective Rabi frequency and

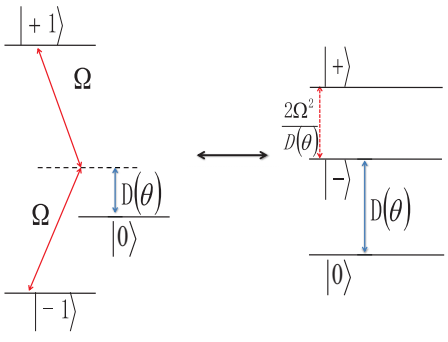


FIG. 3. (Color online) The level structure of the three-level Hartmann-Hann. A gap is created between the $|+\rangle = \frac{1}{\sqrt{2}}(|+1\rangle + |-1\rangle)$ and the $|-\rangle = \frac{1}{\sqrt{2}}(|+1\rangle - |-1\rangle)$ states. This gap is robust to changes in the one photon detuning $[D(\theta)]$ and is also robust to small changes in the two-photon detuning $[\delta(\theta)]$. Due to the fact that the coupling to the nuclei is via the dressed states $(|+\rangle,|-\rangle)$ and not the bare states, the coupling is not decreased due to the off resonant drivings.

thus the energy splitting on the double quantum transition is proportional to $\Omega^2/D(\theta)$, in which Ω is related to the Rabi frequency of the applied microwave field and defined later. In leading order in θ, this suffers a variation that is of the order of $\Omega^2/D^2(\theta)\frac{\partial D(\theta)}{\partial\theta}\theta$. This contrasts with the case of the detuned driving single quantum transition only. In that case the effective energy gap is proportional to $\sqrt{D^2(\theta)+\Omega^2}$ which, if $D(\theta) \gg \Omega$, suffers a variation that is of order $\frac{\partial D(\theta)}{\partial\theta}\theta$. Therefore the variation in the former is suppressed by a factor of $\Omega^2/D^2(\theta)$ compared to the latter. This makes it much easier to achieve and maintain a Hartmann-Hahn resonance.

The second crucial ingredient is related to the fact that the coupling between the electron spin and the nuclear spins is mediated by terms of the form $S_z \otimes I_z$. In a far-detuned single quantum transition the eigenstates involved in the Hartmann-Hahn resonance are $|m_s = 0\rangle + \frac{\Omega}{D(\theta)}|m_s = +1\rangle$ and $|m_s = +1\rangle - \frac{\Omega}{D(\theta)}|m_s = 0\rangle$. As these states are close to being eigenstates of S_z they hardly couple and in consequence the electron-nuclear coupling is suppressed by a factor proportional to $\frac{\Omega}{D(\theta)}$ when compared to the coupling between states with equally weighted superpositions $|m_s = 0\rangle \pm |m_s = +1\rangle$ which one would have obtained for resonant driving. Crucially, thanks to the small detuning on the double quantum transition we obtain $|m_s = -1\rangle \pm |m_s = +1\rangle$ which leads to a strong coupling between electron and nuclear spins if a Hartmann-Hahn resonance is realized (see right-hand side of Fig. 3). The latter is relatively robust thanks to the strong detuning on the single quantum transitions.

So far we have ignored additional energy shifts on the double quantum transition $\delta(\theta)$ which will lead to a loss of the Hartmann-Hahn resonance. In order to confer additional robustness to our scheme, rather than aiming to maintain a fixed Hartmann-Hahn resonance, we consider an adiabatic sweep of the external magnetic field on the double quantum transition where start and endpoint of the sweep are chosen such that intermittent Hartmann-Hahn resonances are guaranteed. This technique, the integrated solid effect, allows polarization transfer from a large fraction of the NV electron spins to their surrounding nuclear spins.

Therefore, the resonant double quantum transition that is mediated by far-detuned single quantum transitions combines robustness with strong electron-nuclear coupling. It is this idea and its combination with the integrated solid effect that we are going to develop and analyze in detail for realistic experimental parameters and various imperfections in this section.

1. Double quantum transition

For illustration of the basic idea, let us first consider a system that is composed of an NV center and a single ^{13}C nuclear spin in a nanodiamond of random orientation. In the laboratory frame the applied magnetic field defines the z axis, the NV is placed at the origin of the coordinate system, and the ^{13}C nuclear spin, placed near the NV center, is situated at position $\vec{r}$. A microwave (MW) field of frequency ω_M is applied as off-resonant drive of the spin transitions $|-1\rangle \leftrightarrow |0\rangle$ and $|0\rangle \leftrightarrow |+1\rangle$ while approximately satisfying a double resonance condition, that is $2\omega_M \cong E_{|+\rangle} - E_{|-\rangle}$. We chose circular polarization but linear polarization would suffice. The

Hamiltonian of the whole system is then

$$H = \Omega_M(S_x \cos\omega_M t + S_y \sin\omega_M t) + [\gamma_e B + \delta(\theta)]S_z + D(\theta)S_z^2 + g[\vec{S}\vec{I} - 3(\vec{S}\cdot\vec{e}_r)(\vec{I}\cdot\vec{e}_r)] + \gamma_n B I_z, \quad (6)$$

in which $g = \frac{\mu_0}{4\pi}\frac{\gamma_e\gamma_n}{r^3}$ with $r = |\vec{r}|$ denoting the distance from the NV spin to the nuclear spin and $\vec{e}_r = \vec{r}/r$. $\vec{I}$ is the spin-$\frac{1}{2}$ vector operator of the nuclear spin with the gyromagnetic ratio γ_n and $\Omega_M = \sqrt{2}\Omega$ is the Rabi frequency of the driving field. Assuming a point-dipole interaction and neglecting the contact term we obtain

$$H_e \simeq \Omega_M(S_x \cos\omega_M t + S_y \sin\omega_M t) + [\gamma_e B + \delta(\theta)]S_z + D(\theta)S_z^2 + \gamma_n B I_z - g S_z\{3e_r^z(e_r^x I_x + e_r^y I_y) + [3(e_r^z)^2 - 1]I_z\}. \quad (7)$$

In the interaction picture with respect to $H_0 = \omega_M S_z$, the Hamiltonian is given by

$$H' = \Omega(|-1\rangle\langle 0| + |0\rangle\langle +1| + \text{H.c.}) + \gamma_n B I_z + D(\theta)S_z^2 + \Delta S_z + S_z\cdot\mathbf{A}\cdot\vec{I}, \quad (8)$$

in which $\mathbf{A} = g\sqrt{1+3(e_r^z)^2}\vec{h} = A\vec{h}$ is the hyperfine interaction tensor for the nuclear spin, with $\vec{h}$ determined by e_r: $h_x = 3e_r^x e_r^z/\sqrt{1+3(e_r^z)^2}$, $h_y = 3e_r^y e_r^z/\sqrt{1+3(e_r^z)^2}$, and $h_z = [3(e_r^z)^2 - 1]/\sqrt{1+3(e_r^z)^2}$. The detuning Δ is given by

$$\Delta = \gamma_e B + \delta(\theta) - \omega_M, \quad (9)$$

which is a function of the NV orientation due to the second-order energy correction $\delta(\theta)$.

Since the nuclear coordinate system is arbitrary, we can redefine it by following the method in Ref. [24]. The z axis is chosen to coincide with the external magnetic field, and we define the y axis to be perpendicular to both magnetic field direction and $\vec{h}$. In the new nuclear coordinate system, the Hamiltonian is given by

$$H'' = \Omega(|-1\rangle\langle 0| + |0\rangle\langle +1| + \text{H.c.}) + D(\theta)S_z^2 + \Delta S_z + \gamma_n B I_{z'} + S_z(a_{x'}I_{x'} + a_{z'}I_{z'}) \quad (10)$$

where $I_z = I_{z'}$ and $a_{z'}$ and $a_{x'}$ are the elements of the secular and pseudosecular hyperfine interactions, respectively.

In what follows we assume that (i) $|D(\theta)| \gg \Delta$ which implies that the microwave driving field tends to be far detuned from the single quantum transitions $|-1\rangle \leftrightarrow |0\rangle$ and $|0\rangle \leftrightarrow |+1\rangle$, and (ii) $|D(\theta)| \gg \Omega$ such that the Rabi frequency is significantly smaller than the detuning [see Fig. 1(b)]. This will allow us to remove level $|0\rangle$ adiabatically from the dynamics to achieve a simplified effective Hamiltonian, Eq. (16).

To this end, we consider the dominant parts of Eq. (10) by neglecting the nuclear spins as well as ΔS_z. In the basis $\{|+1\rangle, |0\rangle, |-1\rangle\}$ we therefore consider

$$H_{NV} = \begin{pmatrix} D(\theta) & \Omega & 0 \\ \Omega & 0 & \Omega \\ 0 & \Omega & D(\theta) \end{pmatrix}. \quad (11)$$

The eigenstates and eigenenergies of H_{NV} are

$$|\mu_\mp\rangle = \frac{1}{\sqrt{2 + X_\pm^2}}(|+1\rangle + |-1\rangle - X_\pm|0\rangle), \quad (12)$$

$$\omega_{\mu_\pm} = \frac{1}{2}[D(\theta) \pm \sqrt{8\Omega^2 + D^2(\theta)}] \quad (13)$$

and

$$|\lambda\rangle = \frac{1}{\sqrt{2}}(|+1\rangle - |-1\rangle), \quad (14)$$

$$\omega_\lambda = D(\theta) \quad (15)$$

with

$$X_\pm(D(\theta),\Omega) = \frac{D(\theta) \pm \sqrt{8\Omega^2 + D^2(\theta)}}{2\Omega}.$$

For $|D(\theta)| \gg \Omega$ we have two cases: $D(\theta) > 0$ leads to $X_-(D(\theta),\Omega) \sim 0$ and $X_+(D(\theta),\Omega) \gg 1$, while $D(\theta) < 0$ results in $X_+(D(\theta),\Omega) \sim 0$ and $X_-(D(\theta),\Omega) \gg 1$.

In both cases, two of the eigenstates are approximately given by $|\pm\rangle = \frac{1}{\sqrt{2}}(|-1\rangle \pm |+1\rangle)$ and form an effective two-level system while the state $|0\rangle$ does not participate in the dynamics because for $|D(\theta)| \gg \Omega$ it is far detuned. We will now focus attention on these two states $|\pm\rangle$ and write the Hamiltonian Eq. (10) in the subspace spanned by $\{|+\rangle, |-\rangle\}$ to find

$$H_\pm \simeq \pm\Omega_{\text{eff}}\sigma_z + 2\Delta\sigma_x + \gamma_n B I_{z'} + 2\sigma_x(a_{x'}I_{x'} + a_{z'}I_{z'}) \quad (16)$$

in which H_+ and H_- correspond to the cases $D(\theta) > 0$ and $D(\theta) < 0$, respectively. Here

$$\Omega_{\text{eff}} = \tfrac{1}{2}[-|D(\theta)| + \sqrt{8\Omega^2 + D^2(\theta)}]$$

and $\sigma_z = \frac{1}{2}(|+\rangle\langle +| - |-\rangle\langle -|)$, $\sigma_x = \frac{1}{2}(|+\rangle\langle -| + |-\rangle\langle +|)$, $I_{z'} = \frac{1}{2}(|\uparrow\rangle\langle\uparrow| - |\downarrow\rangle\langle\downarrow|)$, and $I_{x'} = \frac{1}{2}(|\uparrow\rangle\langle\downarrow| + |\downarrow\rangle\langle\uparrow|)$. Furthermore $|\downarrow\rangle$ and $|\downarrow\rangle$ denote the ground and excited states of the nuclear spin.

For the final step, we now restrict attention to the case where $\theta \in [0^\circ, 20^\circ]$ in which case $D(\theta) > 0$ and we consider Hamiltonian H_+. In matrix notation, the electronic part of the Hamiltonian Eq. (16) then takes the form

$$H_\Delta = \begin{pmatrix} \frac{\Omega_{\text{eff}}}{2} & \Delta \\ \Delta & -\frac{\Omega_{\text{eff}}}{2} \end{pmatrix}. \quad (17)$$

The eigenstates and eigenenergies are

$$|\chi_-\rangle = \cos\frac{\zeta}{2}|-\rangle - \sin\frac{\zeta}{2}|+\rangle,$$
$$|\chi_+\rangle = \cos\frac{\zeta}{2}|+\rangle + \sin\frac{\zeta}{2}|-\rangle, \quad (18)$$
$$\omega_{\text{eff}} = \pm\sqrt{\Delta^2 + \frac{\Omega_{\text{eff}}^2}{4}},$$

in which $\arctan\zeta = \frac{-\Delta}{\Omega_{\text{eff}}/2}$, Δ and Ω_{eff} are dependent on the angle θ between NV orientations and applied magnetic field. Defining Pauli operators $\sigma_{\tilde{x}}, \sigma_{\tilde{y}}, \sigma_{\tilde{z}}$ in the eigenbasis of H_Δ we

find

$$H_+ = 2\omega_{\rm eff}\sigma_{\tilde z} + \gamma_n B I_{z'} + 2(\sigma_{\tilde x}\sin\varphi + \sigma_{\tilde z}\cos\varphi)(a_{x'}I_{x'} + a_{z'}I_{z'}), \quad (19)$$

in which the angle φ is determined by

$$\sin\varphi = \frac{\Omega_{\rm eff}}{\sqrt{4\Delta^2 + \Omega_{\rm eff}^2}}.$$

The Hamiltonian H_+ can be simplified further under two main assumptions, namely (i) $a_{x'} \ll \gamma_n B$, that is, for weakly coupled nuclear spins, and (ii) $|\frac{\gamma_n B}{2} - \omega_{\rm eff}| \ll a_{x'}$ that is, we satisfy a Hartmann-Hahn condition. Then the polarization transfer dynamics is described by

$$H_{\rm trans} = 2\omega_{\rm eff}\sigma_{\tilde z} + \gamma_n B I_{z'} + 2a_{z'}\cos\varphi\sigma_{\tilde z}I_{z'} + \frac{a_{x'}\sin\varphi}{2}(|\chi_+,\downarrow\rangle\langle\chi_-,\uparrow| + \text{H.c.}), \quad (20)$$

where $2a_{z'}\cos\varphi\sigma_{\tilde z}I_{z'}$ does not affect the flip-flop interaction.

Let us briefly highlight the key difference of this off-resonant driving in comparison to previously introduced polarization schemes, namely its relatively high robustness with respect to the angle θ between the external magnetic field and the natural quantization axis of the NV center. If we were to follow the scheme of Ref. [24], even for $\theta = 1^\circ$, the detuning of the MW frequency from the NV electronic resonance exceeds $(2\pi)1$ MHz, which prevents efficient polarization transfer [for $\theta = 20^\circ$ we find $(2\pi)500$ MHz detuning]. In our scheme, for as long as $D(\theta) \gg \Omega$, the energy difference between the states $|-\rangle$ and $|+\rangle$ scales as $2\Omega^2/D(\theta)$ and so does the effective Rabi frequency $\Omega_{\rm eff}$. For deviation $\theta \in [0^\circ,20^\circ]$, if $\Omega = (2\pi)65$ MHz, the effective Rabi frequency is roughly within $[(2\pi)3$ MHz,$(2\pi)3.6$ MHz], which narrows the range of the detuning of the resonant frequency.

2. *Integrated solid effect*

In the discussion so far, we have assumed that the electron spin of the NV center is held continuously at a Hartmann-Hahn resonance with a specific target nuclear spin to achieve polarization transfer. In practice, however, this will only capture a small fraction of the NV centers and nuclear spins as the resonance condition will depend on $\Delta = \gamma_e B + \delta(\theta) - \omega_M$ which in turn is a function of the angle θ via $\delta(\theta)$ [Fig. 2(b)]. In the range $\theta \in [0^\circ,20^\circ]$, we have $\delta(\theta) \in [0,(2\pi)45$ MHz], as shown in Fig. 2(b) which can lead to a violation of the Hartmann-Hahn resonance for a large fraction of the NV centers. In order to achieve polarization transfer for a larger fraction of the NV centers, we will use our ability to control the strength of the externally applied magnetic field or the frequency of the applied microwave field to implement a sweep of Δ.

In order for us to understand qualitatively the conditions that such a sweep has to satisfy, we briefly examine the energy-level diagram of a system consisting of one electron and one nuclear spin as described by Eq. (20). This reveals that there are two resonance points A_1 and A_2 for $\Delta = \pm\Delta_{HH}$ owing to the symmetry of the Hamiltonian. In a fully adiabatic sweep, polarization would exchange twice and result in a vanishing net polarization transfer. Hence the sweep rate needs to be chosen such that around the A_i the system becomes nonadiabatic for the two branches including $|\chi_+,\downarrow\rangle$ and $|\chi_-,\uparrow\rangle$ as this will lead to an approximately 50% probability for polarization transfer. At the same time the sweep has to remain adiabatic with respect to the energy gap for transitions between the $\{|\chi_+,\downarrow\rangle,|\chi_-,\uparrow\rangle\}$ and the $\{|\chi_+,\uparrow\rangle,|\chi_-,\downarrow\rangle\}$ manifold as transitions between these two manifolds, induced by nonadiabaticity or in fact dephasing events, would lead to depolarization. These requirements set some limitations on the sweep rate that are, fortunately, not too stringent.

The quasiadiabatic sweep described above realizes an instance of the so-called integrated solid effect (ISE) [34] and can achieve polarization transfer between a large fraction of the NV spins and nuclear spins. Therefore, magnetic control of the nuclear spin and efficient polarization exchange become possible even for relatively large angles between the natural quantization axis of the NV center and the external magnetic field. In the following we will examine this idea in more detail.

Let us now examine two regimes of the quasiadiabatic transfer described above, namely (i) those parts of the sweep parameters that are far from the Hartmann-Hahn resonance points A_1 and A_2 which will lead to an upper bound on the sweep rate, and (ii) the behavior around the Hartmann-Hahn resonances which will provide lower bounds on the sweep rate.

For regime (i), as the coupling between electron and nuclear spin is negligible, it suffices to examine the electronic part of Eq. (16), that is

$$H'_\Delta = \begin{pmatrix} \frac{\Omega_{\rm eff}}{2} & \Delta(t) \\ \Delta(t) & -\frac{\Omega_{\rm eff}}{2} \end{pmatrix}, \quad (21)$$

in which $\Delta(t) = \gamma_e B - \delta(\theta) - \omega_M$. For simplicity we assume the detuning to vary at a constant rate $v > 0$, i.e., $\Delta(t) = \Delta(t_i) + vt$, where $\Delta(t_i)$ is the initial detuning at the start of sweep. According to the quantum adiabatic condition we require, at all times, that

$$\frac{\langle E_{1m}(t)|\dot E_{1n}(t)\rangle}{|E_{1m}(t) - E_{1n}(t)|} \gg 1, \quad m \neq n, \quad (22)$$

where $E_{1m}(t)$ and $E_{1n}(t)$ are the instantaneous eigenvalues, $|E_{1m}(t)\rangle$ and $|E_{1m}(t)\rangle$ are the eigenstates of effective Hamiltonian H_Δ, respectively. Then the condition for the sweep to be adiabatic is given by

$$\frac{\Omega_{\rm eff}^2}{|v|} \gg 1. \quad (23)$$

Adiabatic evolution implies that the initial eigenstate of this Hamiltonian H_Δ will remain close to the instantaneous eigenstate at any time during the sweep. In particular, during approach to the Hartmann-Hahn resonances and indeed during the entire sweep there will be no transitions of the type $|\chi_-,\downarrow\rangle$ to $|\chi_+,\downarrow\rangle$ which, as is easily seen by examination of Fig. 4, would have a depolarizing effect in the subsequent sweep.

To gain a feeling for the upper limit on the sweep rates that this implies for typical experimental parameters suppose as in the previous section that $\Omega = (2\pi)65$ MHz so that in the range $\theta \in [0^\circ,20^\circ]$ we find $\Omega_{\rm eff}$ in the range $[(2\pi)3$ MHz,$(2\pi)3.6$ MHz]. This in turn implies that $v < (2\pi)10$MHz/μs guarantees that the adiabatic condition is satisfied. As shown in Fig. 2(b) in this range we have

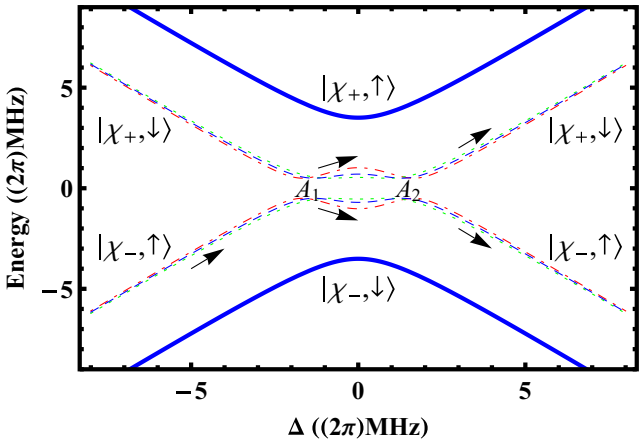


FIG. 4. (Color online) Eigenenergies of Eq. (20) for $B = 0.36$ T in which $|\frac{a_{x'}\sin\varphi_l}{2}| = (2\pi)0.5$ MHz, $\Omega_{\rm eff} = (2\pi)2.2$ MHz (dot-dashed red line), $\Omega_{\rm eff} = (2\pi)3$ MHz (dotted green line), $\Omega_{\rm eff} = (2\pi)3.6$ MHz (dashed blue line). The level diagram shows the progression of the eigenvalues of the Hamiltonian during the ISE sweep. Energies of the states $|\chi_+,\uparrow\rangle$ and $|\chi_-,\downarrow\rangle$ (solid blue line) for $\Omega_{\rm eff} = (2\pi)2.2$ MHz are included. Transitions from states represented by solid blue lines to state represented by dashed lines may lead to depolarization of the nuclear bath.

$\delta(\theta) \in [0,(2\pi)45\ \text{MHz}]$. Suppose a sweep rate $v = (2\pi)6\text{MHz}/\mu\text{s}$, then no more than 10 μs are required to cover all NV centers within $\theta \in [0°,20°]$. Experimentally such sweep rates are easily obtained using arbitrary wave form generators.

Let us now proceed to discuss case (ii), namely the sweep around the Hartmann-Hahn resonances which will provide lower bounds in the sweep rate. Near the resonant points, the effective Hamiltonian Eq. (20) in the subspace spanned by $\{|\chi_+,\downarrow\rangle,|\chi_-,\uparrow\rangle\}$ is well approximated by the matrix form

$$H^l_{\rm mat} = \begin{pmatrix} (-1)^l v(t-t_l)\cos\varphi_l & \frac{a_{x'}\sin\varphi_l}{2} \\ \frac{a_{x'}\sin\varphi_l}{2} & (-1)^{l+1} v(t-t_l)\cos\varphi_l \end{pmatrix}. \tag{24}$$

Here $l = 1,2$ corresponds to points A_1 and A_2, and near these two points we make use of the expansion

$$\omega_{\rm eff}(t) = \omega_{\rm eff}(t_l) + \frac{\partial\omega_{\rm eff}(t)}{\partial t}|_{t_l}(t-t_l) = (-1)^l v(t-t_l)\cos\varphi_l.$$

According to Landau-Zener (LZ) theory [35], transitions are possible between two approaching levels as a control parameter is swept across the point of minimum energy splitting. The asymptotic probability of a LZ-tunneling transition is given by

$$P_{LZ} = e^{-2\pi\mu} \tag{25}$$

where, by virtue of the Hartmann-Hahn condition $\gamma_n B = \sqrt{4\Delta^2 + \Omega^2_{\rm eff}}$ at resonant points A_1 and A_2, we find

$$\mu = \frac{\left(\frac{a_{x'}\sin\varphi_l}{2}\right)^2}{2|v|\cos\varphi_l} = \frac{\Omega^2_{\rm eff}a^2_{x'}}{8|v|(\gamma_n B)\sqrt{(\gamma_n B)^2 - \Omega^2_{\rm eff}}}.$$

This enters the unitary transformation

$$N^l = \begin{pmatrix} \sqrt{1-P_{LZ}}e^{i\tilde{\varphi}_s} & -\sqrt{P_{LZ}} \\ \sqrt{P_{LZ}} & \sqrt{1-P_{LZ}}e^{-i\tilde{\varphi}_s} \end{pmatrix} \tag{26}$$

that is taking place when traversing the avoided crossing. Here $\tilde{\varphi}_s = \varphi_s - \pi/2$ is due to the Stokes phase φ_s.

The full sweep takes the system from $\Delta \ll 0$ to $\Delta \gg 0$ across both A_1 and A_2. At each resonance point polarization transfer is possible between the electron and the nuclear spins [36]. Consider a sweep starting at $\Delta(0) \ll -\Omega_{\rm eff}$ for which the electron spin is initialized in state $|\chi_-\rangle$ and the adiabatic condition Eq. (23) is satisfied. If the nuclear spin is initially found in state $|\downarrow\rangle$, the electron-nuclear system will start and finish the sweep in state $|\chi_-,\downarrow\rangle$, i.e., the nuclear polarization is unchanged. If on the other hand the nuclear spin is initially found in state $|\uparrow\rangle$, the evolution of the system will start in $|\chi_-,\uparrow\rangle$. In this case the probability for experiencing a polarization transfer at the end of the full sweep, that is, finding the system in state $|\chi_+,\downarrow\rangle$, is given by

$$\begin{aligned} P &= P_{\rm max}\sin^2[\Phi_{St}] \\ &= 4P_{LZ}(1-P_{LZ})\sin^2[\Phi_{St}]. \end{aligned} \tag{27}$$

Here Φ_{St} is determined by the initial phase of the system and the phases acquired during the adiabatic evolution and the nonadiabatic transitions. We do not discuss these dynamical phase shifts in detail as they depend on details of the evolution and orientations that vary from NV center to NV center and it is therefore reasonable to assume that Φ_{St} is random [37,38]. Hence, when averaged over many sweeps, the average polarization transfer probability is given by

$$\overline{P} = 2P_{LZ}(1-P_{LZ}),$$

as shown in Fig. 5. The value of P_{LZ} and hence the maximum $\overline{P} = 2P_{LZ}(1-P_{LZ})$ is determined by the hyperfine coupling strength $a_{x'}$, the rate of the ISE sweep v, and to a lesser extent on the strength of the applied microwave field.

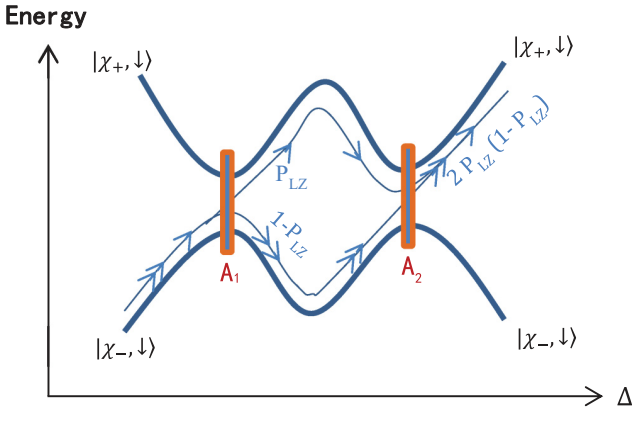


FIG. 5. (Color online) Double-passage transition. A schematics of a pair of the adiabatic energy levels as in Fig. 4. At each crossing there is a probability of P_{LZ} for a Landau-Zener transitions. The lines with one (two) arrows show the two paths where the transition to the upper level happens during passage of the first (second) resonance point. The average probability for a polarization transfer at the end of the completed passage is given by $2P_{LZ}(1-P_{LZ})$.

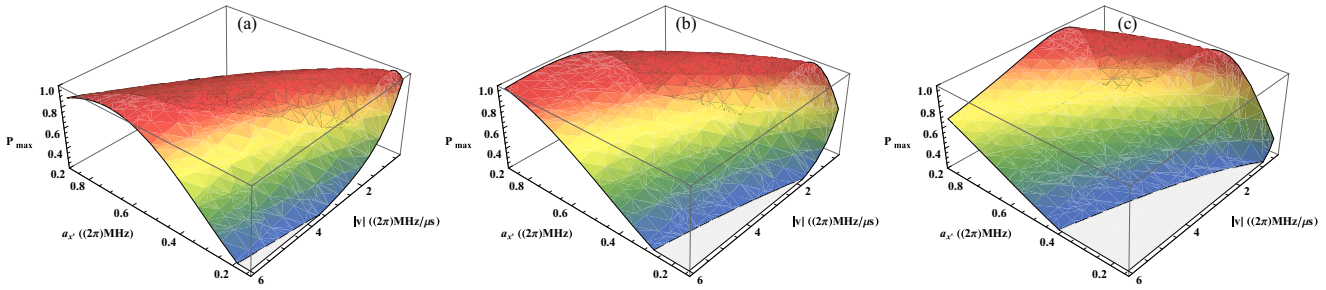


FIG. 6. (Color online) The maximal polarization transfer $P_{\max}$ as a function of the effective coupling Ω_{eff}. (a) $\Omega_{\text{eff}} = (2\pi)3.6$ MHz (b) $\Omega_{\text{eff}} = (2\pi)3$ MHz; (c) $\Omega_{\text{eff}} = (2\pi)2.3$ MHz.

It is straightforward to see that $P_{\max}$ and hence $\overline{P}$ vanish for both $v \gg 0$ and $v \to 0$, corresponding to the diabatic and adiabatic sweep. The maximum value is achieved for $P_{LZ} = 1/2$ and the parameters for achieving this maximum are quite flexible; see Fig. 6. $P_{\max}$ remains high across a wide range of sweep rates as shown in Figs. 6(a) and 6(b). Note furthermore, that for a given sweep rate we obtain efficient polarization transfer to the nuclear spins in a broad range of different microwave Rabi frequencies; see Fig. 6. For example, for $\Omega_{\text{eff}} = (2\pi)3.6$ MHz, a speed $v = (2\pi)6\text{MHz}/\mu\text{s}$ can obtain $P_{\max} > 0.2$ in the coupling range $a_{x'} \in [(2\pi)0.18, (2\pi)0.9]$ MHz. Furthermore, a slower sweep gives a better polarization transfer for a smaller effective Rabi frequency and a weaker coupling strength between the electron spin and the nuclear spin. In order to polarize the nuclear spins with larger distance from the NV spin, one can slow down the ISE sweep, or increase the Rabi frequency of the microwave field, as shown in Fig. 6(c).

C. Preparation of the initial state

So far we have assumed the preparation of a specific initial state in the polarization sequence to be achieved with perfect fidelity. However, due to the random orientations of the NV centers, optical pumping leads to the initialization of the electron spin of the NV center in a wide range of different states. Furthermore, due to the broad distribution of zero-field splittings of the NV center in randomly oriented nanodiamonds, any applied microwave field will experience an uncertain and potentially large detuning from the electronic resonance. This presents challenges to the preparation of the electron spin of the NV center in the initial state that is required for our polarization scheme. We address these challenges with an adiabatic sweep of the frequency of the microwave field which we will show to deliver robust and rapid state preparation.

Let us consider as an example the initialization of the NV center in the state $|-1\rangle$. For moderate θ optical pumping will lead to a state that possesses a significant overlap with $|0\rangle$. In order to map this state to the target $|-1\rangle$, we make use of the fact that in the relatively high magnetic fields that we are considering (e.g., $B \cong 0.36$ T) the energy gap on the $|-1\rangle \leftrightarrow |0\rangle$ transition is very different from the energy gap of the $|0\rangle \leftrightarrow |+1\rangle$ transition. Hence it is possible to use a circular polarized microwave driving field

$$H_{dr} = \Omega_{M-}(S_x \cos\omega_- t + S_y \sin\omega_- t), \tag{28}$$

in which $\Omega_{M-} = \sqrt{2}\Omega_-$ is the Rabi frequencies of the MW field, with frequency ω_- to drive dominantly the $|-1\rangle \leftrightarrow |0\rangle$ transition. The resulting effective two-level system consisting of the states $|0\rangle$ and $|-1\rangle$ can be described in the matrix representation by

$$H_{0,-1} = \begin{pmatrix} \Delta_{MW}(t)/2 & \Omega_- \\ \Omega_- & -\Delta_{MW}(t)/2 \end{pmatrix}, \tag{29}$$

in which $\Delta_{MW}(t) = \gamma_e B + \delta(\theta) + D(\theta) - \omega_-(t)$. Now we assume that $\omega_-(t)$ experiences a constant rate sweep such that $\Delta_{MW}(t) = \Delta_{MW}(t_i) + \dot{\Delta}_-(t - t_i)$. We set $t_i = 0$ for simplicity. The condition for the sweep to be adiabatic is then

$$\frac{8\Omega_-^2}{|\dot{\Delta}_-|} \gg 1. \tag{30}$$

Adiabatic evolution implies that the initial eigenstate of this Hamiltonian $H_{0,-1}$ will remain close to the instantaneous eigenstate at any time during the sweep. The eigenstates and eigenenergies are

$$|E^{\pm}(t)\rangle = \zeta_1^{\mp}(t)|-1\rangle \pm \zeta_1^{\pm}(t)|0\rangle,$$
$$E^{\pm}(t) = \pm\sqrt{[\Delta_{MW}(t)/2]^2 + \Omega_-^2}, \tag{31}$$

with $\zeta_1^{\pm} = \sqrt{\frac{E^+(t) \mp \Delta_{WM}(t)}{2E^+(t)}}$. If at the start of the sweep $\Delta_{WM}(0) < 0$ and $|\Delta_{WM}(0)| \gg 2\Omega_-$ and the electron spin is prepared in the state $|0\rangle$, the state will evolve along the path $|E^+(t)\rangle$ to end in the state $|-1\rangle$.

As an example, consider a Rabi frequency $\Omega_- = (2\pi)20$ MHz and $\theta \in [0^\circ, 20^\circ]$. Then a sweep from $\Delta_{WM}(t_i) > (2\pi)160$ MHz to $\Delta_{WM}(t_f) < -(2\pi)160$ MHz includes all NV centers in the sweep. For $|\omega_1(t_f) - \omega_1(t_i)| = \dot{\omega}_1 t_f \simeq (2\pi)870$ MHz we require $t_f \gg [\omega_1(t_f) - \omega_1(t_i)]/8\Omega_-^2 = 0.04$ μs to achieve adiabaticity. Hence very high fidelity preparation of the state $|-1\rangle$ can be achieved within 0.4 μs which is faster than the optical polarization cycle.

So far we have assumed that the optical initial state $|0\rangle$ is well prepared. However, for the relatively high magnetic fields that we are considering, the optical initial state is given by $|0\rangle_\theta = \cos\theta|0\rangle + \frac{\sin\theta}{\sqrt{2}}(e^{i\phi}|+1\rangle - e^{-i\phi}|-1\rangle)]$ [see Eq. (5)]. For a perfect adiabatic sweep we obtain the average polarization in the range $\theta \in [0^\circ, 20^\circ]$ as

$$\overline{P_{N_1}} = \frac{\int_S \left(\cos^2\theta - \frac{\sin^2\theta}{2}\right) dS}{S}. \tag{32}$$

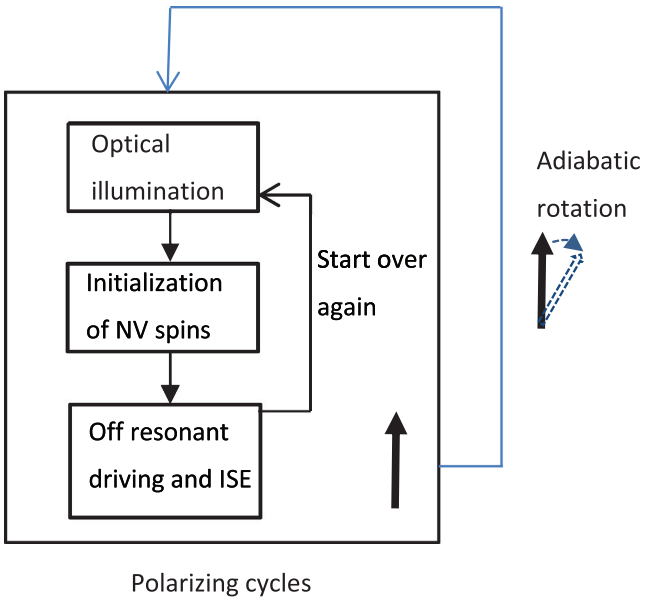


FIG. 7. (Color online) A simple flow diagram of the entire polarization scheme: For a given direction of magnetic field, the large box includes numerous polarization cycles (each polarization cycle includes optical initialization of the NV spin, adiabatic preparation of the state $|-1\rangle$, and then polarization transfer by matching a H-H resonance condition by using off-resonant microwave driving and the ISE technique). After the adiabatic rotation of the magnetic field (the thick black arrow represent the magnetic field orientation which is rotated to another direction denoted by the dashed blue arrow) we repeat our polarizing cycles to achieve the polarization of additional nuclear spins.

Here S is the surface area of the two sectors within θ deviation and dS is the corresponding area element. The reachable polarization for nearby nuclear spins and the average polarizations are $\overline{P_{N_1}} = 0.91$ for $\theta \in [0°,20°]$.

D. Polarizing cycles and effective ranges

We can now summarize the polarizing cycles as follows (see also the black box of the flow diagram Fig. 7): (i) Optical pumping initializes the NV spin and (ii) a subsequent adiabatic transfer brings the electron spin to the $|-1\rangle$ state. (iii) By using off-resonant driving and a quasiadiabatic sweep across two Hartmann-Hahn resonance points (ISE technique) polarization is transferred from the NV spin to the nuclear spin. Steps (i)–(iii) are repeated as required. This method has two primary advantages: (1) the impact of the random orientations is minimized, and NV spins in a wide range of orientations are still accessible for polarization. (2) Using this method, the coupling strength between the NV and nuclear spins is doubled because it involves the double quantum transitions between the states $|-1\rangle$ and $|+1\rangle$.

In Fig. 8 we simulate many cycles of this polarization protocol for a system of one NV center and a single nuclear spin under the assumption that the NV center is initialized to the state $|-1\rangle$ as an example. The initial density matrix of the unpolarized nuclear spin is $\rho_0 = \mathbf{I}/2$, with $\mathbf{I}$ being the unit matrix. For the state ρ_k of the nuclear spin after the kth iteration of the polarization protocol we have the following relation:

$$\rho_{k+1} = \mathrm{tr}_e[U_t(\rho_k \otimes |\chi_-\rangle\langle\chi_-|)U_t^\dagger], \tag{33}$$

where $U_t = e^{-\int iH_{\mathrm{trans}}dt}$ is time evolution operator and H_{trans} is the Hamiltonian Eq. (20); we denote by Δt the sweep time and by tr_e the trace over the electron spin. The polarizing P is defined as $P = \langle I_{z'}\rangle/\langle I_{z'}\rangle_0$ with $\langle I_{z'}\rangle$ denoting the expectation value of the nuclear spin and $\langle I_{z'}\rangle_0$ the expectation value of the completely polarized state.

Finally, as we have discussed in the previous sections, the ISE requires an adiabatic slow passage. For $\theta \in [0°,20°]$ we find $\delta(\theta) \in [0,(2\pi)45\ \mathrm{MHz}]$ and in order to include the entire range of detunings in the sweep we can estimate the required polarizing time. At a sweep rate of $v = (2\pi)6\mathrm{MHz}/\mu\mathrm{s}$ we find $\Delta t \sim 10\ \mu$s. In Fig. 8(a), assuming the perfect initialization of the NV spin in the state $|-1\rangle$, we take one nuclear spin with the typical coupling $a_{x'} = (2\pi)0.6$ MHz as an example to demonstrate the polarization transfer [the nuclear spin is about 0.5 nm from the NV spin and $a_{z'} = (2\pi)0.64$ MHz]. Here the polarization transfer after the first cycle, P_1, does not quite achieve the maximum possible value in Fig. 6 due to the existence of the phase shift Φ_{St}; more precisely $P_1 = 0.58 < P_{\max} = 0.7$ when $\Omega_{\mathrm{eff}} = (2\pi)3$ MHz [see both Figs. 6(b) and 8(a)]. Simulations for different hyperfine couplings are shown in Fig. 8(b). Again the sweep rate $v = (2\pi)6\mathrm{MHz}/\mu\mathrm{s}$ and polarization is transferred to the nuclear spins with different coupling to the NV spin, which agree with Fig. 6. Additionally, slowing

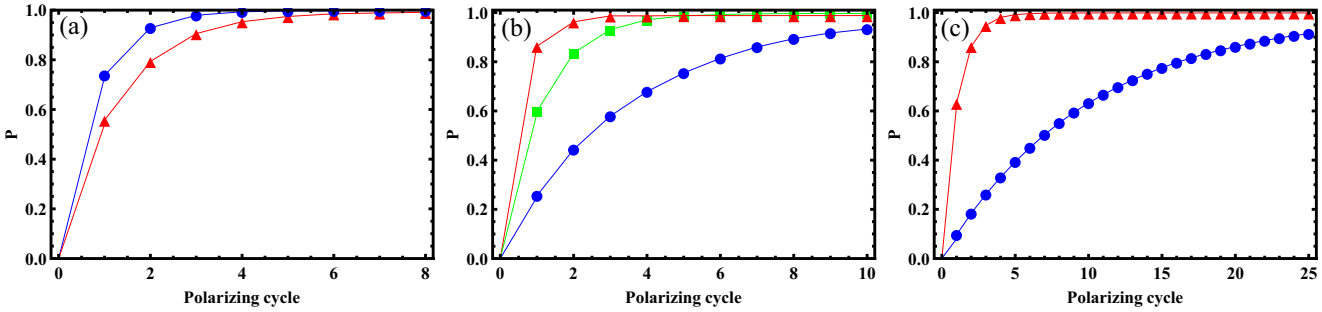


FIG. 8. (Color online) Exact polarization dynamics with $B = 0.36$ T, $v = (2\pi)6\mathrm{MHz}/\mu\mathrm{s}$ and $\Delta t = 10\ \mu$s: (a) The coupling strength is given as $a_{x'} = (2\pi)0.6$ MHz, $\Omega_{\mathrm{eff}} = (2\pi)3$ MHz (blue circles), and $\Omega_{\mathrm{eff}} = (2\pi)3.6$ MHz (red triangles). (b) We have $\Omega_{\mathrm{eff}} = (2\pi)3.5$ MHz, $a_{x'} = (2\pi)0.7$ MHz (red triangles), $a_{x'} = (2\pi)0.5$ MHz (green cubes), and $a_{x'} = (2\pi)0.3$ MHz (blue circles). (c) Exact polarization dynamics with $v = (2\pi)0.8\mathrm{MHz}/\mu\mathrm{s}$, $\Delta t = 50\ \mu$s, and $\Omega_{\mathrm{eff}} = (2\pi)2.3$ MHz, $a_{x'} = (2\pi)0.3$ MHz (red triangles), and $a_{x'} = (2\pi)0.1$ MHz (blue circles).

down the ISE sweep, as shown in Fig. 8(c) for a sweep rate $v = (2\pi)0.8\text{MHz}/\mu\text{s}$ we can polarize more distant nuclear spins with a coupling strength $a_{x'} = (2\pi)0.1$ MHz, which corresponds to a distance of about 1 nm from the NV center. This coupling is approaching the limitation of our polarization scheme, since the rotating-frame spin-lattice relaxation time of NV spin in nanodiamonds is estimated to be about 100 μs which places a lower limit of the duration of the full sweep [39].

III. BENEFIT OF ADIABATIC ROTATIONS

The NV polarization in our scheme is limited by the adiabatic sweep range and efficiency of the initialization of NV spins, enabling the polarization up to a maximum angle between NV center and external magnetic field. As discussed above, our scheme certainly performs well for NV centers whose orientation forms an angle of less than 20° from the externally applied magnetic field (and may potentially work for somewhat larger angles). It is however desirable to extend the polarization to a larger fraction of the nanodiamond ensemble, ideally covering the entire solid angle. One method for achieving this applies an adiabatic change of the orientation of the magnetic field relative to the NV center, either by rotation of the magnetic field or by rotation of the nanodiamond. For example, following the magnetic field rotation to the Z' direction, another set of NV centers with orientations in a solid angle (shown in red in Fig. 9) around the new magnetic field direction will participate in the polarization dynamics while the NV centers in the original orientations (the blue cone in Fig. 9) will be inactive. Hence previously polarized nuclear spins will not be affected by the polarization sequences, but these nuclear spins may use this "idle" time to spread their polarization by spin diffusion across larger volumes until further rotations subject them to another polarization cycle.

More specifically, let us consider the rotation of the magnetic field as an example. The Hamiltonian that is describing the rotation of the magnetic field from the Z direction to the Z' direction is given by

$$H_B = \gamma_N B_Z[\cos(\dot{\vartheta}t)I_Z + \sin(\dot{\vartheta}t)I_X] = \gamma_N B_Z I_{\vartheta(t)},$$

where $\vartheta(t) = \dot{\vartheta}t$ is the angle between the rotated magnetic field and its initial direction and $\gamma_N B_Z = (2\pi)4$ MHz.

Similar to the discussion in the initialization scheme, the well-known adiabatic condition requires $\dot{\vartheta} \ll 2\gamma_N B_Z$. For a rotation by $\vartheta = 180°$ this leads to the condition $t_r \gg 0.078\ \mu$s for the minimal rotation time t_r. This implies that $t_r \cong 0.78\ \mu$s will ensure adiabaticity and minimal perturbation of nuclear spin polarization for a rotation to an arbitrary orientation. This rotation time is much shorter than even a single polarization cycle. Hence, after running a few polarization cycles that achieve a high net polarization of nuclear spins for NV centers oriented along the Z direction, we can adiabatically rotate the magnetic field to another direction. The polarization of the nuclear spins will then be achieved for this new direction, as shown in Fig. 9. Note though that the rapid rotation of a strong magnetic field is challenging. Hence one needs to resort either to a mechanical rotation of the sample as a whole or, as explained in the next section, make use of the Brownian rotation of nanodiamonds in solution.

In addition to the rotation of the externally applied magnetic field for nanodiamond powder, another option consists of the use of random Brownian rotations of nanodiamonds in a solution. If the Brownian rotation is sufficiently slow to satisfy our adiabatic rotation condition, the polarized nuclear spins will maintain their polarization in the direction of the externally applied magnetic field. The time scale of Brownian rotations is determined by [40]

$$\tau_B = \frac{3V_H\eta}{kT}, \tag{34}$$

where k is the Boltzmann constant, T is the temperature, V_H is the hydrodynamic volume of the particle, and η the viscosity of the surrounding carrier liquid. Note that the hydrodynamic volume is an effective volume that includes both the true particle volume and the volume of a fluid that is displaced when the particle rotates due to particle-fluid interaction. A

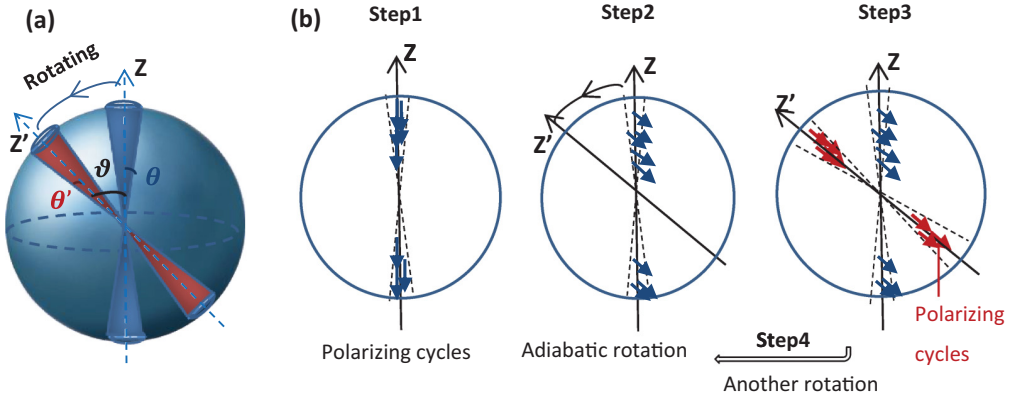


FIG. 9. (Color online) (a) Diagram of adiabatic rotating direction of the magnetic field. Blue spherical sectors present $\theta°$ deviation tolerance for Z direction of the magnetic field. Magnetic field is rotated by angle ϑ to get red spherical sectors with the half angle of the cone angle θ' to be involved. (b) Flow diagrams of polarizing steps of our scheme related to the adiabatic rotations of the magnetic field. The small blue and red arrows are the nuclear spins nearby the different NV spins in different spherical sectors. Four steps are given for our polarizing scheme. We use two-dimensional plotting for simplicity, the sphere is presented by a circle, and the areas formed by the dashed lines denote the corresponding spherical sectors. It is shown by the arrows that all the nuclear spins follows the rotated magnetic fields.

typical average hydrodynamic diameter for nanodiamonds of 30 nm in water gives a Brownian relaxation time of $\tau_B \simeq 9$ μs, which is comparable with our polarizing cycle time. One can increase the Brownian relaxation time by using nanodiamonds with a larger diameter, a more viscous fluid, or lower temperatures. Additionally, surface coating can increase the average hydrodynamic diameter, i.e., after adsorption of ferritin the diameter of nanodiamond was determined to be 85 nm [41].

Here we assume that the hydrodynamic diameter of nanodiamond is 85 nm, and the Brownian relaxation time is $\tau_B \simeq 205$ μs. On average after a time τ_B, the nanodiamonds will have rotated to another random direction, and different NV centers will now participate in the polarization dynamics of nearby nuclear spins while other NV centers will be inactive as they are effectively decoupled from their neighboring nuclear spin due to the absence of a Hartmann-Hahn condition. When an NV center "leaves" the coherent exchange range via a random rotation, the polarization of the polarized nuclear spins will still be transferred to the other nuclear spins by spin diffusion. Considering maximum of 20° deviation, 6% of the NV spins are involved at each given time, and each NV will be in this range after 16 random rotations on average.

IV. INTERNUCLEAR INTERACTION AND SPIN DIFFUSION

So far, we have considered polarization of an individual nuclear spin and have therefore ignored the effects of internuclear coupling on both the polarization cycle and on the nuclear-spin polarization diffusion towards more distant nuclear spins that are not directly interacting with the NV center. This section discusses these effects of nuclear dipolar interactions. Considering our off-resonant driving in the dressed state basis and the suitable rotating frame, the effective Hamiltonian of the whole system consisting of an NV spin and its nearby nuclear spins can be written as

$$H_{\rm tot} \approx H_{NV} + H_{hf} + H_{d-d} + H_{Nu}. \tag{35}$$

Here H_{NV} denotes the NV center effective energy Hamiltonian, H_{hf} is the effective electron-nuclear hyperfine interaction, H_{d-d} is the dipole-dipole coupling among nuclear spins, and H_{Nu} is the magnetic field splitting of nuclear spins,

$$H_{NV} = 2\Delta(t)\sigma_x + \Omega_{\rm eff}\sigma_z, \tag{36}$$

$$H_{hf} \simeq \sum_i \sigma_x\left(2a_{x_i'} I_i^{x'} + 2a_{z_i'} I_i^{z'}\right), \tag{37}$$

$$H_{d-d} \simeq \sum_{ij,j>i} d_{ij}[\vec{I}_i\vec{I}_j - 3(\vec{I}_i\cdot\vec{e}_{r_{ij}})(\vec{I}_j\cdot\vec{e}_{r_{ij}})], \tag{38}$$

$$H_{Nu} = \sum_i \gamma_n B I_i^{z'}, \tag{39}$$

with $a_{x_i'}$ and $a_{z_i'}$ denoting the hyperfine coupling strength between the ith nuclear spin and the electron spin. $d_{ij} = \frac{\mu_0}{4\pi}\frac{\gamma_n\gamma_n}{r_{ij}^3}$ is the coupling strength between the i and j nuclear spins. with $r_{ij} = |\vec{r}_{ij}|$ denoting the distance between the two nuclear spins and $\vec{e}_{r_{ij}} = \vec{r}_{ij}/r_{ij}$. The i and j indices are summed over all nuclei.

In order to estimate the effect of internuclear interactions on the polarization transfer from the NV center to the nuclei in the multiple nuclear-spins case we consider five nuclear spins and one electron spin, including hyperfine and nuclear dipolar couplings. After each polarization cycle, the electron spin is re-initialized in the state $|-1\rangle$. The concatenated evolution of the nuclear-spin density matrix is determined by an equation analogous to Eq. (33). The initial density matrix of the five unpolarized nuclear spins can be written as $\rho_0 = \mathbf{I}/2^5$, with $\mathbf{I}$ being a unit matrix of dimension 2^5, and the time evolution is given by the operator $U_t = e^{-i\int H_{\rm tot}dt}$, with $H_{\rm tot}$ denoting the total Hamiltonian Eq. (35). The polarization is defined as in Sec. II, $P_k = \langle I_{z'}^k\rangle/\langle I_{z'}^k\rangle_0$ in which the subscript k presents different nuclear spins and $P = \frac{1}{5}\sum_k^5 P_k$. We assume in these simulations only nearest neighbor internuclear-spin coupling with rates $d_{12} = d_{23} = d_{34} = d_{45} = 2$ kHz.

The simulation results are presented in Figs. 10(a) and 10(b). We consider the case that the NV is strongly coupled to all five ^{13}C spins, $a_{x_1'} = (2\pi)0.7$ MHz, $a_{x_2'} = (2\pi)0.5$ MHz, $a_{x_3'} = (2\pi)0.4$ MHz, $a_{x_4'} = (2\pi)0.32$ MHz, and $a_{x_5'} = (2\pi)0.2$ MHz. The polarization is built up for all the five nuclear spins with different coupling to the NV spin, which matches our theory. In this case, the coupling between the nuclear spins is too small to affect the evolution of the polarization dynamical built up [Fig. 10(a)]. Due to small interaction among the nuclear spins, there is almost no difference between polarization in the presence or absence of the interactions among the nuclear spins, which means our scheme works in the frozen core.

Now we would like to exemplify the benefits of internuclear interactions which leads to nuclear-spin diffusion and a considerable extension of the range of polarization. Suppose a typical configuration of nuclear spins distributed around the NV. To estimate the polarization efficiencies in a large system, we adopted the simple spin temperature approximation, namely neglecting the nuclear-spin coherence [42], which provides a good estimation of polarization transfer efficiency when the sweep time step is sufficiently small. This approximation yields independent rate equations for each individual nuclear spin and should give a conservative estimate for the achieved polarization. For the Δt sweep times described above, this approximation serves as a lower bound, as the achieved polarization in one cycle with our scheme is higher than the polarization achieved during the same time with small sweep steps.

For the diffusion step, the interaction between the nuclear spins is taken into account, where we use the Gaussian approximation for the nuclear spins. As is typical for paramagnetic centers, the NV center strongly affects the spin diffusion in nearby nuclear spins (the "frozen core") due to the energy mismatch caused by the S_zI_z hyperfine term. However, when the NV center is in the $|m_s = 0\rangle$ state, this energy mismatch is suppressed and diffusion to external nuclear spins is allowed. To give a conservative estimate, we assume that no diffusion in the frozen core takes place when the NV center is in the $|m_s = \pm 1\rangle$ states. For this purpose, we simulate the NV center as a classical spin with the probability of being in each eigenstate given by the optical initialization corresponding to the NV orientation.

As the nanodiamonds are in a solution, we assume that the differences in polarization transfer for the different

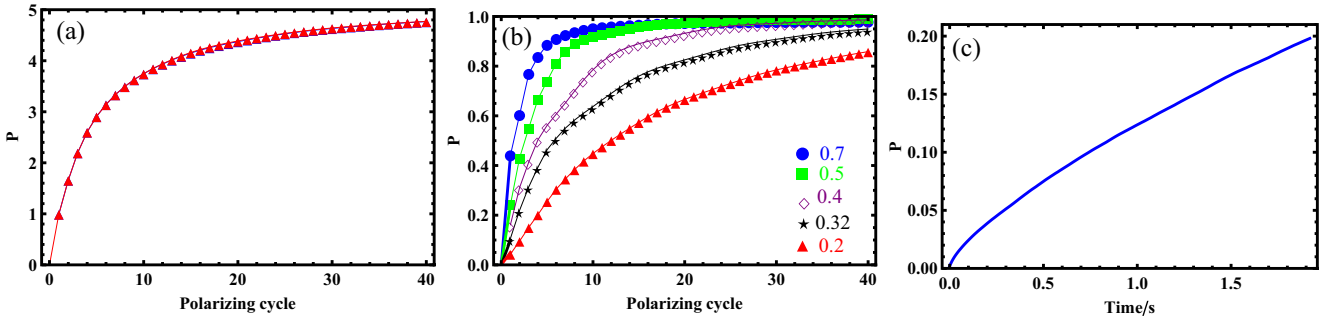


FIG. 10. (Color online) The polarization buildup for five nuclear spins for $\Omega_{\text{eff}} = 3.23$ MHz. The nuclear spins are strongly interacting with the NV center spin, $a_{x_1'} = (2\pi)0.7$ MHz, $a_{x_2'} = (2\pi)0.5$ MHz, $a_{x_3'} = (2\pi)0.4$ MHz, $a_{x_4'} = 0.32$ MHz, and $a_{x_5'} = (2\pi)0.2$ MHz. (a) The blue and red triangles denote the presence and absence of the interaction among the nuclear spins. Internuclear interactions do not lead to significant changes in the polarization dynamics because the dipole-dipole interaction of nuclear spins is much smaller than the electron-nuclear coupling. (b) The polarization dynamics of the individual nuclear spins in the set of five spins represented by different markers within different colors. (c) Numerical simulation of the polarization buildup in a large number of polarization cycles in a system consisting of an NV spin and around 548 ^{13}C nuclear spins in a volume of 50 000 lattice sites by using Brownian rotation. The internuclear dynamics is treated within the bosonic approximation and we simulate a polarization buildup time of 2 sec. The system benefits from polarization diffusion between nuclear spins resulting in a high level of polarization.

orientations of the NV spins within the 20° deviation range can be neglected. Consider a random configuration of nuclear spins, with 548 nuclear spins in the vicinity of an NV center (lattice of 50 000 nuclei per NV center) whose orientation is within the 20° deviation range. The net polarization is built up by using Brownian rotations as shown in Fig. 10(c). There are two steps in the simulation. First, we assume that the orientation of the NV center satisfies $\theta \in [0°,20°]$ and we consider $\Omega_{\text{eff}} = (2\pi)2.3$ MHz, sweep rate of $v = (2\pi)0.8\text{MHz}/\mu\text{s}$, and $\Delta t = 70\mu$s. The polarization transfer from the NV center to the neighboring nuclear spins is achieved by using our combination of off-resonantly driven double quantum transition and the ISE technique. The polarizing cycles are repeated during the Brownian relaxation time $\tau_B = 205\ \mu$s. Second, after the Brownian relaxation time, the nanodiamond is randomly rotated to another direction. As we discussed in Sec. III, it takes roughly 3.5 ms for the nanodiamond to rotate back to our maximal deviation range for polarization, and nuclear-spin diffusion dominates during this time period (taking into account the NV effect on diffusion in the frozen core). In this step more distant nuclear spins can become polarized by diffusion. These two steps occur sequentially over a 2-sec time range. In line with previous sections, the polarization is defined as $= \langle I_{z'}\rangle/\langle I_{z'}\rangle_0$, where $I_{z'} = \sum_i^M I_i^{z'}$, M is the number of the involved nuclear spins. Interestingly, the slope of polarization is close to linear. This demonstrates that in the long diffusion time, where the nanodiamond is not involved in the polarization cycles, we do not see a bottleneck caused by slow diffusion and significant polarization is transferred from the NV spin to the nuclear spins within each step 1. The final net polarization reaches 0.2, equivalent to about 110 ^{13}C fully polarized spins are polarized within 2 sec in our scheme.

V. A LARGE ANGLE POLARIZATION SCHEME

So far we have concentrated so far on a range of angles $\theta \in [0°,20°]$ between the NV center and the external magnetic field. Note however, that this is not the only range in which efficient polarization transfer can be achieved. Indeed, we have another interesting range of the NV orientations, concentrated around the direction perpendicular to the magnetic field, i.e., $\theta \in [70°,110°]$, which involves 34% of the NV spins. Here the condition $D(\theta) < 0$ leads to the Hamiltonian H_- in Eq. (16). Following steps that are analogous to those leading up to Hamiltonian Eq. (20) we find for the subspace $\{|\chi_-,\downarrow\rangle,|\chi_+,\uparrow\rangle\}$

$$H_{\text{matrix}} = \begin{pmatrix} \omega_{\text{eff}} - \frac{\gamma_n B}{2} & \frac{a_{x'}\sin\varphi}{2} \\ \frac{a_{x'}\sin\varphi}{2} & -\omega_{\text{eff}} + \frac{\gamma_n B}{2} \end{pmatrix}. \tag{40}$$

Suppose now that the NV center is initialized in state $|-1\rangle$ by using the off-resonant driving. Then we make use of the ISE technique to sweep adiabatically across the two possible Hartmann-Hahn resonance points of the dressed NV spin and nuclear-spin pair. As a result the population is transferred between $|\chi_-,\downarrow\rangle$ and $|\chi_+,\uparrow\rangle$, with the other states being unaffected. As before, this allows the nuclear spins to be polarized but now in a direction opposite to the case $\theta \in [0°,20°]$. In the following we discuss the details of this case.

A. Initial polarization of the NV spins

We begin with a discussion of the initialization of the NV center spins. As explained in previous sections, optical pumping of the NV spins results in the $|m_s = 0\rangle$ state in the NV frame, that is

$$|0\rangle_\theta = \cos\theta|0\rangle + \frac{\sin\theta}{\sqrt{2}}(e^{i\phi}|+1\rangle - e^{-i\phi}|-1\rangle),$$

where the states $|0\rangle,|\pm 1\rangle$ are defined in the laboratory frame. For $\theta \in [70°,110°]$ the population in state $|0\rangle$ is very small and the initial state is well approximated by $\frac{1}{\sqrt{2}}(e^{i\phi}|+1\rangle - e^{-i\phi}|-1\rangle)$ which, in the relevant subspace spanned by $\{|+1\rangle,|-1\rangle\}$, is unpolarized.

We address this problem by means of an adiabatic sweep. For concreteness, consider $\Omega = (2\pi)20$ MHz and an

adiabatic sweep from $\Delta_{WM}(t_i) = (2\pi)320$ MHz to $\Delta_{WM}(t_f) < -(2\pi)320$ MHz. For a sweep range $|\omega_1(t_f) - \omega_1(t_i)| \simeq (2\pi)640$ MHz, the time for an adiabatic sweep is of the order of 0.4 μs. Such a sweep induces an adiabatic population transfer from state $|-1\rangle$ to state $|0\rangle$ so that the state of the NV center evolves to

$$|0\rangle_\theta \longrightarrow \cos\theta|-1\rangle + \frac{\sin\theta}{\sqrt{2}}(e^{i\phi}|+1\rangle - e^{-i\phi}|0\rangle),$$

where we ignore any dynamical and geometric phase that has been accumulated in the sweep. It is now crucial to note that the state $|0\rangle$ does not contribute to the polarization dynamics as it does not take part in the far detuned dynamics that is induced by the applied microwave fields. Hence the relevant quantity is the polarization in the subspace spanned by the states $\{|+1\rangle,|-1\rangle\}$. Normalized by the population that is found in this subspace we find

$$\overline{P^r_{N_2}} = \frac{\int_S N_r\left(\frac{\sin^2\theta}{2} - \cos^2\theta\right)dS}{S}, \tag{41}$$

where $N_r = 1/(\frac{\sin^2\theta}{2} + \cos^2\theta)$ is the normalized coefficient and $\overline{P^r_{N_2}} \sim 0.85$.

B. The sweep range for ISE

Owing to the different behavior of the energy shifts $D(\theta)$ and $\delta(\theta)$ we need to change the sweep range in the ISE. In order to achieve optimum polarization transfer, we choose $\Omega = (2\pi)40.5$ MHz, which results in a range of effective Rabi frequency $\Omega_{\text{eff}} \in [(2\pi)2.3\,\text{MHz},(2\pi)3.6\,\text{MHz}]$. The adiabatic slow passage needs to cross the range $\Delta \in [-(2\pi)21\,\text{MHz},(2\pi)21\,\text{MHz}]$. For a sweep rate of $v = (2\pi)6\text{MHz}/\mu\text{s}$ we estimate the required polarizing time as $\Delta t > 7\,\mu$s. Apart from these parameter changes, the principles underlying our discussion of the polarization transfer in Sec. II are still valid.

If we assume that the NV spin is initial polarized perfectly, we have $P_{\max} > 0.2$ in a coupling range $a_{x'} \in [0.4,0.9]$ for $|\Omega_{\text{eff}}| = (2\pi)2.27$ MHz in Fig. 6(c), compared to $a_{x'} \in [0.18,0.9]$ for $|\Omega_{\text{eff}}| = (2\pi)3.6$ MHz in Fig. 6(a). We can say that our off-resonant driving and ISE technique allow polarization transfer for all the NV orientations within $\theta \in [70^\circ,110^\circ]$. Considering that the average polarization of the NV spins in this case is about 0.5 and twice the effective Rabi frequency range here, applying a single sweep speed becomes not very efficient for all the NV orientations, especially for the nuclear spins with weak couplings to the NV spin. As we discussed, we have another choice: slowing down the ISE sweep can involve the nuclear spins with weaker coupling to the NV spin, i.e., as shown in Fig. 8(c), we can use another a speed rate $v = (2\pi)0.8\text{MHz}/\mu\text{s}$ ($\Delta t \sim 50\ \mu$s) to make it possible to polarize the ^{13}C spins with coupling strength $a_{x'} = (2\pi)0.1$ MHz.

In conclusion, off-resonant driving and the ISE technique allow for polarization transfer between the NV spin and its surrounding nuclear spins, when the orientation of the NV spin matches $\theta \in [70^\circ,110^\circ]$, but we need to sacrifice half the population to provide a high initial polarization of the dressed NV spins. On the other hand the fact that around 34% of the NV centers participate in the polarization dynamics even without magnetic field rotation is an attractive feature.

VI. DEPOLARIZING EFFECT

Our approach to increase the fraction of NV center that participates in the polarization sequences by means of adiabatic rotations may potentially have an undesired side effect as nuclear spins that have been polarized for one magnetic field orientation may be depolarized again when transferred to a different magnetic field orientation. Consider for example the case shown in Fig. 9 where, after polarization transfer is achieved for the blue spherical sectors, the magnetic field is rotated from the Z direction to a different direction Z'. If the NV spins in the blue sectors have not been polarized in advance and our combination of off-resonant driving and ISE achieves a Hartmann-Hahn condition at some instant, then the depolarized state of the NV center will be transferred to nuclear spins, whose polarization reduces as a result. In the protocol for the case $\theta \in [0^\circ,20^\circ]$ this depolarization is negligible due to the rapid increase of the detuning $\delta(\theta)$ outside of this range. Only NV centers in the range $\theta \in [20^\circ,25^\circ]$ may still experience undesired resonances. As these NV centers are still well initialized by means of optical pumping, depolarization is negligible.

The situation is different and indeed more complex for the second protocol that covers the range $\theta \in [70^\circ,90^\circ]$. NV centers with orientations in the range $\theta \in [35^\circ,43^\circ]$ are difficult to be polarized to the required state. Unfortunately, they have almost the same energy distributions $|D(\theta)|$ and $\delta(\theta)$ as the NV centers in the range $\theta \in [70^\circ,110^\circ]$; see Fig. 2. Our off-resonant driving and ISE technique scheme can lead to Hartmann-Hahn resonances at some instant which then cause polarization exchanges between the unpolarized NV centers and the polarized nuclear spins. Thus, magnetic field rotations could lead to depolarization dynamics in the previously polarized nuclear spins for the protocol that is adapted to the case $\theta \in [70^\circ,110^\circ]$.

We consider a simple system consisting of one NV and one nuclear spin as an example for studying the depolarizing effect of this case. The depolarizing cycle time is the same as our polarizing cycle time, since every initialization process is implemented on all the NV spins. Consider a nuclear spin that is initially polarized and in contact with an unpolarized electron spin $\rho_{e0} = \mathbf{I}/2$. The evolution of the nuclear-spin density matrix is then given by

$$\rho \to \cdots U'_t \text{tr}_e[U'_t(|\downarrow\rangle\langle\downarrow| \otimes \rho_{e0})U'^\dagger_t] \otimes \rho_{e0} U'^\dagger_t \ldots, \tag{42}$$

where $U'_t = e^{-i\int H^{\delta'}_{\text{matrix}}dt}$ is time evolution operator. $H^{\delta'}_{\text{matrix}}$ is given by Eq. (20) with the choice $\Omega_{\text{eff}} = (2\pi)3.5$ MHz and δ' denoting that a magnetic field in the Z' direction is being considered. The polarization P of the nuclear spin is defined as in Sec. II. As shown in Fig. 11, the nuclear spin is depolarized very rapidly. The depolarization range $\theta' \in [35^\circ,43^\circ]$ includes 9% of the NV orientations while the range in which the polarization is active includes 34% of the NV centers. Hence, although adiabatic rotation of the magnetic field brings an unexpected depolarizing effect, it is nevertheless quite attractive as the fraction of NV spins that are contributing

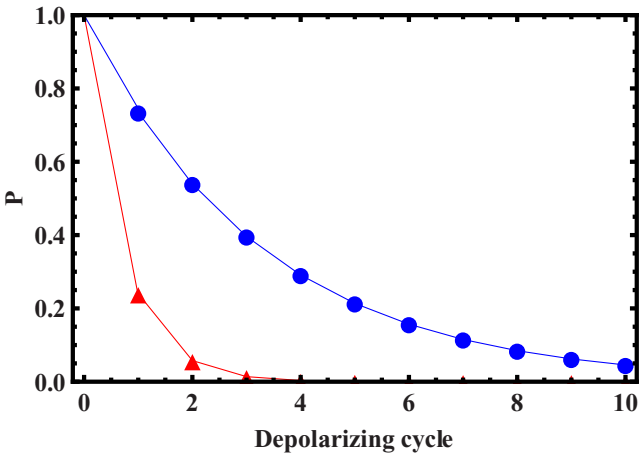


FIG. 11. (Color online) The depolarization of the previously polarized nuclear spin with $B = 0.36$ T, $\Omega_{\text{eff}} = (2\pi)3.5$ MHz, $v = (2\pi)6\text{MHz}/\mu\text{s}$, and $\Delta t = 10$ μs. The coupling strength is given as $a_{x'} = (2\pi)0.3$ MHz, (blue circles) and $a_{x'} = (2\pi)0.6$ MHz (red triangles).

to the polarization transfer even without magnetic field rotation strongly outweighs the small fraction of 9% of the NV centers that suffer depolarization.

VII. DISCUSSION

To summarize, our polarization scheme for ensembles of nanodiamonds (see Fig. 7 and Fig. 9) is as follows.

Step 1: A moderate to strong magnetic field is applied along the Z direction (of order $B = 0.36$ T). A polarization cycle consists of optically pumping and initialization of the NV center spins, and the subsequent application of off-resonant microwave driving and the integrated solid effect to realize a robust adiabatic sweep across Hartmann-Hahn resonance points. This achieves the coherent polarization transfer from the NV center spins to the nuclear spins with a range of orientations of the NV center relative to the magnetic field. This polarization cycle is repeated several times.

Step 2: Adiabatic rotations (of the magnetic field or of the nanodiamonds) change the magnetic field orientation relative to the NV centers to a new Z' direction, while the nuclear spins follow the direction of the magnetic field.

Step 3: Repeat steps 1 and 2.

Apart from control imperfections, the achievable ^{13}C-bath spin polarization will be limited by the spin-lattice relaxation time T_1 of the nuclear spins. In recent experiments, by using electron paramagnetic resonance (EPR), solid-state NMR, and DNP techniques, a variety of nanodiamond samples, of varying manufacturing processes and particle sizes, were examined [16,18,43]. Several types of nanodiamonds, especially those milled from diamonds produced from high-pressure, high-temperature (HPHT) methods exhibit very long nuclear-spin lifetimes, up to several minutes. As bulk diamonds with a comparable paramagnetic impurity concentration can exhibit nuclear-spin relaxation times of several hours, surface impurities are considered to form one of the main sources for relaxation in nanodiamonds. This is also supported by the correlation between nanodiamond size and nuclear relaxation times [16,43]. This suggest that the nanodiamond relaxation time may be improved by surface cleaning and treatment of the nanodiamonds [44,45].

Additionally, the polarization transfer rests on NV spins having a sufficiently long rotating-frame spin-lattice relaxation time $T_{1\rho}$ in nanodiamonds during the adiabatic passages that are required for the implementation of ISE. Using a strong MW field driving, $T_{1\rho}$ can be estimated as 100 μs [39,46], which is much longer than our sweep time in one polarization cycle. Assuming a polarization cycle duration of $\Delta t = 10$ μs, when rotating the magnetic field, 17 rotations of the magnetic field are required to involve all the NV spins. For a nuclear-spin lifetime of more than 2 min, this would allow the execution of around 10^5 polarization cycles for each NV spin involved before the nuclear spins start to relax. For nanodiamonds in a solution, each nanodiamond is involved in the polarization cycles roughly once every 17 random Brownian rotations. Assuming $\tau_B \simeq 205$ μs, with a pure nuclear diffusion period of roughly 3 ms after every Brownian relaxation time τ_B, 2 min lifetime of the nuclear spin would allow in excess of 10^5 polarization cycles for every NV center.

We can now obtain a rough estimate of the total amount of the net polarization that could be achieved under realistic experimental conditions. Consider a $1 - \text{mm}^3$ nanodiamond powder, dissolved in a solution. The nanodiamonds are assumed to have a diameter of 85 nm, with an NV center concentration of $C = 2 \times 10^{18}$ cm^{-3} (see [47] and references therein for achievable NV concentrations). In the limit of a uniform spatial distribution, this gives about 642 NV spins per nanodiamond, with the total amount of NV spins given by 8.35×10^{15} NV spins. Considering the natural abundance of the ^{13}C spins (1.1%), the total nuclear spins in this powder of nanodiamond is approximately 8.18×10^{18} [48]. Taking account of the high degree of nuclear polarization achieved, in excess of 0.2 as demonstrated in Sec. IV, we find that a total amount of polarization equivalent to 1.6×10^{18} nuclear spins should be achievable in such a sample within 2 sec.

The 20% nuclear-spin polarization that may be achieved with our method compares favorably with the thermal polarization of 0.1% of nonoptically excited electron spins at the moderate magnetic field of $B = 0.36$ T which sets an upper limit on the achievable nuclear-spin polarization in such protocols. Thus, even compared with the theoretical limit reachable via polarization transfer from regular electron spins to nuclear spins, the polarization reached by optical DNP and our protocols is more than 100 times larger. Cryogenic environments and higher magnetic fields dissolution-DNP methods could be used for obtaining comparable polarization, but these require much longer time for polarization (1 h) as well as expensive cryostats and hardware. Furthermore, not all diamond nanoparticles that have been functionalized with biomacromolecules may be hyperpolarized by these methods, as the fast reheating after polarization might disrupt the structure of these biomolecules.

In this work we have assumed diamonds with natural ^{13}C abundance (1.1%) which would already lead to a considerable signal enhancement in MRI applications. It is possible however to apply our scheme to diamonds with higher ^{13}C concentrations as the polarization transfer from electron to nuclear spin is not significantly affected by the presence of

^{13}C very close to the NV. A higher ^{13}C concentration will be beneficial however as the increase in the internuclear dipolar interaction leads to more effective polarization diffusion and hence a faster nuclear-spin polarization. The same effect will however lead to a reduction of the polarization lifetime as the faster diffusion allows polarization loss on the nanodiamond surface to diffuse more rapidly to the bulk. The latter shows that surface treatment of ^{13}C isotope enriched nanodiamonds can be expected to be particularly beneficial.

VIII. CONCLUSION

In conclusion, in the high magnetic field limit, we propose a scheme achieving macroscopic levels of ^{13}C nuclear-spin polarization in randomly oriented ensembles of nanodiamonds, realized as powder or solutions. To address the lack of a common natural quantization axis for the NV centers, an off-resonant microwave drive realizes a resonant double quantum transition and this, together with the integrated solid effect, enables microwave coupling and control of NV spins whose orientation deviates from the external magnetic field by less than 20°. Matching the effective Rabi frequency of the off-resonant double quantum transition of the NV centers to the nuclear-spin Larmor frequency enables near resonant coupling between NV electron spins and the nuclear spins, and the transfer of polarization from the initialized NV spins to the neighboring ^{13}C nuclear spins. Additionally, the effect of nuclear dipole-dipole interactions allows the weakly coupled nuclear spins to be polarized by spin diffusion. Adiabatic rotation (of the magnetic field or sample) can then extend the polarizing scheme to more NV spins, achieving a net polarization of all nuclear spins via our scheme. By using our polarization scheme, room-temperature, optical based polarization of the nuclear spins is made possible.

These results introduce several exciting opportunities for the application of hyperpolarized nanodiamonds, especially in the biomedical sciences. Diamond nanoparticles are biocompatible, exhibit no *in vivo* toxicity [49], and can be attached to a wide range of specific proteins, peptides, or antibodies [17] while maintaining long $T1$ times. Thus, hyperpolarized nanodiamonds present an exciting platform as MRI probes for molecular imaging. Finally, we would like to stress that the techniques that we have presented here for overcoming the random orientation and large zero-field splitting of NV centers in nanodiamonds apply more widely to color centers in any type of material that possesses an electron spin $S = 1$ in the ground state and admit optical pumping of this electron spin such as silicon divacancies in silicon-carbide and defect centers in quartz or silicon nanoparticles.

ACKNOWLEDGMENTS

We acknowledge helpful discussions with B. Luy, J. M. Cai, and Z. Y. Wang. This work was supported by the ERC Synergy grant BioQ, the EU projects DIADEMS, EQUAM, and SIQS, the Marie Curie Career Integration Grant (CIG) IonQuanSense (Grant No. 321798), the Niedersachsen-Israeli Research Cooperation Program, the Israel Science Foundation (Grant No. 1500/13), and an Alexander von Humboldt Professorship.

APPENDIX: EFFECTIVE HAMILTONIAN OF AN NV CENTER AT THE HIGH MAGNETIC FIELD LIMIT

In our work we assume that in the laboratory frame of reference a strong magnetic field is applied along the z direction, $\gamma_e B_z \gg D$. In the following we derive the representation of the NV center Hamiltonian Eq. (3) in the laboratory frame of coordinates. To this end we need to transform the zero-field splitting tensor, which is diagonal in the natural coordinate system defined by the NV center axes, to the laboratory frame of reference. We assume that the angle between the magnetic field, i.e., the z direction, and the NV axis, the z_θ direction, is given by θ and that the angle between the laboratory frame, y direction, and the NV center, y_θ directions, is given by ϕ in the x-y plane, as shown in Fig. 12. The spin operators in the NV system of coordinates, S_{x_θ}, S_{y_θ}, and S_{z_θ}, are then related to the spin operators S_x, S_y, and S_z in the laboratory coordinates by

$$\begin{aligned} S_{x_\theta} &= \sin\theta S_z + \cos\theta(\cos\phi S_x - \sin\phi S_y), \\ S_{y_\theta} &= \cos\phi S_y + \sin\phi S_x, \\ S_{z_\theta} &= \cos\theta S_z - \sin\theta(\cos\phi S_x - \sin\phi S_y). \end{aligned}$$

The Hamiltonian of the electron spin,

$$\begin{aligned} H_N^e = &\left(-\tfrac{1}{3}D + E\right)S_{x_\theta}S_{x_\theta} + \left(-\tfrac{1}{3}D - E\right)S_{y_\theta}S_{y_\theta} \\ &+ \left(\tfrac{2}{3}D\right)S_{z_\theta}S_{z_\theta} + \gamma_e B S_z, \end{aligned}$$

can then be rewritten in the basis defined by the eigenstates of the S_z operator of the electron spin, $\{|+1\rangle, |0\rangle, |-1\rangle\}$, as

$$H''_{NV} = \begin{pmatrix} D(\theta) + \gamma_e B_z & -G_1 & G_2 \\ -G_1^* & 0 & G_1 \\ G_2^* & G_1^* & D(\theta) - \gamma_e B_z \end{pmatrix}$$

with

$$\begin{aligned} D(\theta) &= \frac{D[1 + 3\cos(2\theta)] + 3E[1 - \cos(2\theta)]}{4}, \\ G_1 &= \frac{(D - E)\sin\theta\cos\theta e^{i\phi}}{\sqrt{2}}, \\ G_2 &= \frac{[D + 3E + (E - D)\cos 2\theta]e^{2i\phi}}{4}. \end{aligned}$$

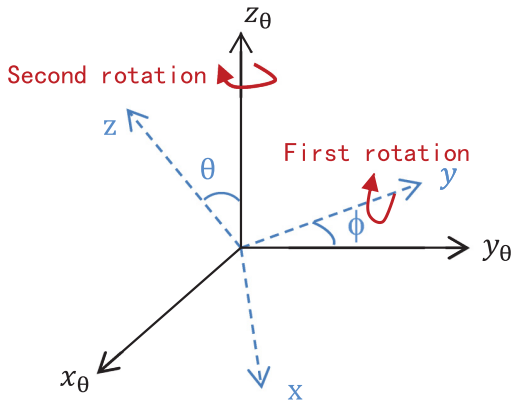


FIG. 12. (Color online) Two related rotations of the coordinate system are used to map from the natural orientation z_θ axis of the NV spin to z axis which is defined by the high magnetic field.

There exist two uncontrollable components, the angles θ and ϕ as well as the local strain E, which modifies the spin level structure.

As we know, a high magnetic field suppresses the effect of the off-diagonal terms in H''_{NV}. Assume that the Hamiltonian is of the form $H''_{NV} = H''_{NV0} + \epsilon V$, where H''_{NV0} is the diagonal part of the Hamiltonian and ϵV is the off-diagonal part. In our case the magnetic field is sufficiently large for us to assume that the off-diagonal part is a weak perturbation. By using the Schrieffer-Wolff transformation in condensed matter, the second-order corrections due to the off-diagonal terms ϵV can be obtained as

$$\langle\alpha|H''_M|\beta\rangle = \frac{\epsilon^2}{2}\left(\frac{\langle\alpha|V|i\rangle\langle i|V|\beta\rangle}{E_\alpha - E_i} - \frac{\langle\alpha|V|i\rangle\langle i|V|\beta\rangle}{E_i - E_\beta}\right),$$

in which H''_M is defined as the corrected Hamiltonian. By simple calculation, we find

$$\langle+1|H''_M|+1\rangle = \frac{|G_1|^2}{\gamma_e B + D(\theta)} + \frac{|G_2|^2}{2\gamma_e B},$$

$$\langle-1|H''_M|-1\rangle = \frac{|G_1|^2}{-\gamma_e B + D(\theta)} - \frac{|G_2|^2}{2\gamma_e B}.$$

After shifting the zero of energy, the effective Hamiltonian in the laboratory frame is given by

$$H''_{\text{eff}} = \gamma_e B S_z + D(\theta) S_z^2 + \delta(\theta) S_z,$$

in which

$$\delta(\theta) = \frac{\gamma_e B |G_1|^2}{(\gamma_e B)^2 - [D(\theta)]^2} + \frac{|G_2|^2}{2\gamma_e B}.$$

Therefore a strong magnetic field suppresses the first-order effect of the off-diagonal terms in H''_{NV} but results in a second-order modification of the diagonal elements $\delta(\theta)$. This is the Hamitonian as in Eq. (3).

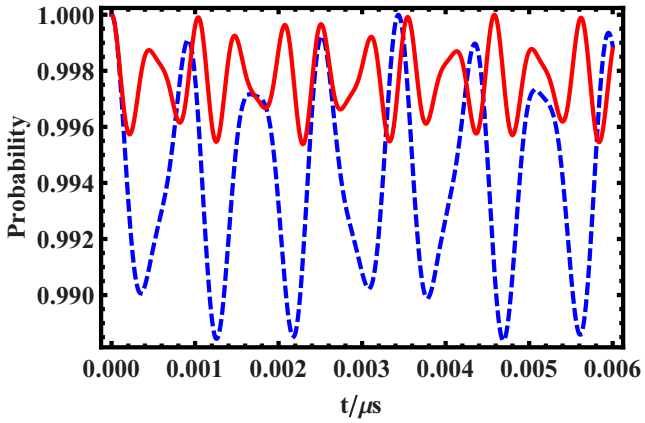


FIG. 13. (Color online) Validation of neglecting off-resonant coupling with $D = (2\pi)2870$ MHz, $\theta = 10^\circ$, $E = (2\pi)20$ MHz. The dashed blue line and solid red line present the time evolutions of the probability of the state $|0\rangle$ corresponding to $B = 0.36$ T and $B = 0.54$ T, respectively.

In order to estimate the validity of this approximation in the high magnetic field limit we have prepared the system in the state $|m_s = 0\rangle$ and observed the subsequent time evolution of its population under Hamiltonian H''_N in Fig. 13 (see caption for simulation parameters). It is evident that the population of the initial state $m_s = 0$ remains essentially constant which implies in turn that the effect of the off-diagonal elements in Hamiltonian H''_{NV} are indeed negligible for the moderate to high magnetic field case that is relevant to our work.

[1] F. Bloch, W. W. Hansen, and M. Packard, The nuclear induction experiment, Phys. Rev. **70**, 474 (1946).

[2] E. M. Purcell, H. C. Torrey, and R. V. Pound, Resonance absorption by nuclear magnetic moments in a solid, Phys. Rev. **69**, 37 (1946).

[3] S. Månsson, E. Johansson, P. Magnusson, C.-M. Chai, G. Hansson, J. S. Petersson, F. Ståhlberg, and K. Golman, ^{13}C imaging—a new diagnostic platform, Eur. J. Radiol. **16**, 57 (2006).

[4] P. C. Lauterbur, Image formation by induced local interactions: Examples employing nuclear magnetic resonance, Nature (London) **242**, 190 (1973).

[5] P. Dutta, A. Le, D. L. Vander Jagt, T. Tsukamoto, G. V. Martinez, C. V. Dang, and R. J. Gillies, Evaluation of LDH-A and glutaminase inhibition in vivo by hyperpolarised ^{13}C-pyruvate magnetic resonance spectroscopy of tumors, Cancer Res. **73**, 4190 (2013).

[6] F. A. Gallagher, M. I. Kettunen, D.-E. Hu, P. R. Jensen, M. Karlsson, A. Gisselsson, S. K. Nelson, T. H. Witney, S. E. Bohndiek, G. Hansson *et al.*, Production of hyperpolarised [1, 4-^{13}C$_2$] malate from [1, 4-^{13}C$_2$] fumarate is a marker of cell necrosis and treatment response in tumors, Proc. Natl. Acad. Sci. USA **106**, 19801 (2009).

[7] F. A. Gallagher, M. I. Kettunen, S. E. Day, D.-E. Hu, J. H. Ardenkjær-Larsen, P. R. Jensen, M. Karlsson, K. Golman, M. H. Lerche, K. M. Brindle *et al.*, Magnetic resonance imaging of pH in vivo using hyperpolarised ^{13}C-labelled bicarbonate, Nature (London) **453**, 940 (2008).

[8] J. H. Ardenkjær-Larsen, B. Fridlund, A. Gram, G. Hansson, L. Hansson, M. H. Lerche, R. Servin, M. Thaning, and K. Golman, Increase in signal-to-noise ratio of $>10,000$ times in liquid-state NMR, Proc. Natl. Acad. Sci. USA **100**, 10158 (2003).

[9] K. Golman, M. Thaning *et al.*, Real-time metabolic imaging, Proc. Natl. Acad. Sci. USA **103**, 11270 (2006).

[10] C.-G. Joo, K.-N. Hu, J. A. Bryant, and R. G. Griffin, In situ temperature jump high-frequency dynamic nuclear polarization experiments: Enhanced sensitivity in liquid-state NMR spectroscopy, J. Am. Chem. Soc. **128**, 9428 (2006).

[11] S. Bowen and C. Hilty, Time-resolved dynamic nuclear polarization enhanced NMR spectroscopy, Angew. Chem. **120**, 5313 (2008).

[12] J. Leggett, R. Hunter, J. Granwehr, R. Panek, A. J. Perez-Linde, A. J. Horsewill, J. McMaster, G. Smith, and W. Köckenberger, A dedicated spectrometer for dissolution DNP NMR spectroscopy, Phys. Chem. Chem. Phys. **12**, 5883 (2010).

[13] Q. A. Pankhurst, J. Connolly, S. Jones, and J. Dobson, Applications of magnetic nanoparticles in biomedicine, J. Phys. D **36**, R167 (2003).

[14] J. W. Aptekar, M. C. Cassidy, A. C. Johnson, R. A. Barton, M. Lee, A. C. Ogier, C. Vo, M. N. Anahtar, Y. Ren, S. N. Bhatia *et al.*, Silicon nanoparticles as hyperpolarised magnetic resonance imaging agents, ACS Nano **3**, 4003 (2009).

[15] P. Dutta, G. V. Martinez, and R. J. Gillies, Nanodiamond as a new hyperpolarizing agent and its ^{13}C MRS, J. Phys. Chem. Lett. **5**, 597 (2014).

[16] E. Rej, T. Gaebel, T. Boele, D. E. Waddington, and D. J. Reilly, Hyperpolarised nanodiamond with long spin relaxation times, Nat. Commun. **6**, 8459 (2015).

[17] V. N. Mochalin, O. Shenderova, D. Ho, and Y. Gogotsi, The properties and applications of nanodiamonds, Nat. Nanotechnol. **7**, 11 (2012).

[18] L. B. Casabianca, A. I. Shames, A. M. Panich, O. Shenderova, and L. Frydman, Factors affecting DNP NMR in polycrystalline diamond samples, J. Phys. Chem. C **115**, 19041 (2011).

[19] F. Jelezko, T. Gaebel, I. Popa, M. Domhan, A. Gruber, and J. Wrachtrup, Observation of Coherent Oscillation of a Single Nuclear Spin and Realisation of a Two-Qubit Conditional Quantum Gate, Phys. Rev. Lett. **93**, 130501 (2004).

[20] M. G. Dutt, L. Childress, L. Jiang, E. Togan, J. Maze, F. Jelezko, A. Zibrov, P. Hemmer, and M. Lukin, Quantum register based on individual electronic and nuclear spin qubits in diamond, Science **316**, 1312 (2007).

[21] V. Jacques, P. Neumann, J. Beck, M. Markham, D. Twitchen, J. Meijer, F. Kaiser, G. Balasubramanian, F. Jelezko, and J. Wrachtrup, Dynamic Polarization of Single Nuclear Spins by Optical Pumping of Nitrogen-Vacancy Color Centers in Diamond at Room Temperature, Phys. Rev. Lett. **102**, 057403 (2009).

[22] P. Neumann, J. Beck, M. Steiner, F. Rempp, H. Fedder, P. R. Hemmer, J. Wrachtrup, and F. Jelezko, Single-shot readout of a single nuclear spin, Science **329**, 542 (2010).

[23] J. P. King, P. J. Coles, and J. A. Reimer, Optical polarization of ^{13}C nuclei in diamond through nitrogen vacancy centers, Phys. Rev. B **81**, 073201 (2010).

[24] P. London, J. Scheuer, J.-M. Cai, I. Schwarz, A. Retzker, M. B. Plenio, M. Katagiri, T. Teraji, S. Koizumi, J. Isoya *et al.*, Detecting and Polarizing Nuclear Spins with Double Resonance on a Single Electron Spin, Phys. Rev. Lett. **111**, 067601 (2013).

[25] E. Togan, Y. Chu, A. Imamoglu, and M. Lukin, Laser cooling and real-time measurement of the nuclear spin environment of a solid-state qubit, Nature (London) **478**, 497 (2011).

[26] H.-J. Wang, C. S. Shin, C. E. Avalos, S. J. Seltzer, D. Budker, A. Pines, and V. S. Bajaj, Sensitive magnetic control of ensemble nuclear spin hyperpolarisation in diamond, Nat. Commun. **4**, 1940 (2013).

[27] G. A. Álvarez, C. O. Bretschneider, R. Fischer, P. London, H. Kanda, S. Onoda, J. Isoya, D. Gershoni, and L. Frydman, Local and bulk ^{13}C hyperpolarization in nitrogen-vacancy-centered diamonds at variable fields and orientations, Nat. Commun. **6**, 8456 (2015).

[28] R. Fischer, C. O. Bretschneider, P. London, D. Budker, D. Gershoni, and L. Frydman, Bulk Nuclear Polarization Enhanced at Room Temperature by Optical Pumping, Phys. Rev. Lett. **111**, 057601 (2013).

[29] S. Hartmann and E. Hahn, Nuclear double resonance in the rotating frame, Phys. Rev. **128**, 2042 (1962).

[30] J. Cai, F. Jelezko, M. B. Plenio, and A. Retzker, Diamond-based single-molecule magnetic resonance spectroscopy, New J. Phys. **15**, 013020 (2013).

[31] J. Cai, B. Naydenov, R. Pfeiffer, L. P. McGuinness, K. D. Jahnke, F. Jelezko, M. B. Plenio, and A. Retzker, Robust dynamical decoupling with concatenated continuous driving, New J. Phys. **14**, 113023 (2012).

[32] J. Cai, A. Retzker, F. Jelezko, and M. B. Plenio, A large-scale quantum simulator on a diamond surface at room temperature, Nat. Phys. **9**, 168 (2013).

[33] The components of $\vec{S} = S_x\vec{e}_x + S_y\vec{e}_y + S_z\vec{e}_z$ are given by $S_x = \frac{1}{\sqrt{2}}\begin{pmatrix} 0 & 1 & 0 \\ 1 & 0 & 1 \\ 0 & 1 & 0 \end{pmatrix}$, $S_y = \frac{1}{\sqrt{2}}\begin{pmatrix} 0 & -i & 0 \\ i & 0 & -i \\ 0 & i & 0 \end{pmatrix}$, $S_z = \begin{pmatrix} 1 & 0 & 0 \\ 0 & 0 & 0 \\ 0 & 0 & -1 \end{pmatrix}$.

[34] A. Henstra, P. Dirksen, and W. T. Wenckebach, Enhanced dynamic nuclear polarization by the integrated solid effect, Phys. Lett. A **134**, 134 (1988).

[35] C. Zener, Non-adiabatic crossing of energy levels, in *Proceedings of the Royal Society of London A: Mathematical, Physical and Engineering Sciences* No. 833 (The Royal Society, London, 1932), Vol. 137, pp. 696–702.

[36] A. Henstra, T.-S. Lin, J. Schmidt, and W. T. Wenckebach, High dynamic nuclear polarization at room temperature, Chem. Phys. Lett. **165**, 6 (1990).

[37] A. Henstra and W. T. Wenckebach, Dynamic nuclear polarization via the integrated solid effect I: theory, Mol. Phys. **112**, 1761 (2014).

[38] T. Eichhorn, B. v. d. Brandt, P. Hautle, A. Henstra, and W. T. Wenckebach, Dynamic nuclear polarization via the integrated solid effect II: experiments on naphthalene-h_8 doped with pentacene-d_{14}, Mol. Phys. **112**, 1773 (2014).

[39] A. Laraoui and C. A. Meriles, Approach to dark spin cooling in a diamond nanocrystal, ACS Nano **7**, 3403 (2013).

[40] J. Frenkel, *Kinetic Theory of Liquids* (Dover Publications, New York, 1955).

[41] A. Ermakova, G. Pramanik, J.-M. Cai, G. Algara-Siller, U. Kaiser, T. Weil, Y.-K. Tzeng, H. Chang, L. McGuinness, M. B. Plenio *et al.*, Detection of a few metallo-protein molecules using color centers in nanodiamonds, Nano Lett. **13**, 3305 (2013).

[42] H. Christ, J. I. Cirac, and G. Giedke, Quantum description of nuclear spin cooling in a quantum dot, Phys. Rev. B **75**, 155324 (2007).

[43] A. M. Panich, N. A. Sergeev, A. I. Shames, V. Yu. Osipov, J. P. Boudou, and S. D. Goren, Size dependence of ^{13}C nuclear spin-lattice relaxation in micro-and nanodiamonds, J. Phys.: Condens. Matter **27**, 072203 (2015).

[44] M. Kaviani, P. Deak, B. Aradi, T. Frauenheim, J. P. Chou, and A. Gali, Proper surface termination for luminescent near-surface NV centers in diamond, Nano Lett. **14**, 4772 (2014).

[45] A. Krueger, New carbon materials: Biological applications of functionalized nanodiamond materials, Chem. Eur. J. **14**, 1382 (2008).

[46] C. Belthangady, N. Bar-Gill, L. M. Pham, K. Arai, D. Le Sage, P. Cappellaro, and R. L. Walsworth, Dressed-State Resonant Coupling Between Bright and Dark Spins in Diamond, Phys. Rev. Lett. **110**, 157601 (2013).

[47] L.-J. Su, C.-Y. Fang, Y.-T. Chang, K.-M. Chen, Y.-C. Yu, J.-H. Hsu, and H.-C. Chang, Creation of high density ensembles of

nitrogen-vacancy centers in nitrogen-rich type Ib nanodiamonds, Nanotechnology **24**, 315702 (2013).

[48] A spherical shaped nanodiamond of diameter 30 nm has the volume $3.21 \times 10^{-17}\text{cm}^3$. Each unit cell of the diamond crystal has the volume $4.49 \times 10^{-23}\,\text{cm}^3$; the number of unit cells in the given particle is 7.14×10^6. Eight carbon atoms per unit cell of diamond crystal gives the total number of carbon atom 5.71×10^7. Natural abundance of the ^{13}C 1.1% leads to the total number of ^{13}C nuclear spin in a 30-nm nanodiamond of 2.29×10^5.

[49] Y. Zhu, J. Li, W. Li, Y. Zhang, X. Yang, N. Chen, Y. Sun, Y. Zhao, C. Fan, and Q. Huang, The biocompatibility of nanodiamonds and their application in drug delivery systems, Theranostics **2**, 302 (2012).

Part II

External polarization

3 External molecule Polarization

With the vision of developing a general hyperpolarization method using optically polarized NV centers, we set out on tackling the challenge of transferring polarization from ultra-shallow NV centers (less than 10 nm from the diamond surface) to nuclear spins in external molecules. One open question was how to model and effectively transfer the polarization to fast-diffusing molecules from a stationary diamond. Our first approach involved using NV centers in very small nanodiamonds (roughly 10 nm diameter) to induce polarization in liquid flowing around the nanodiamond [16]. The advantage of this approach is that a large volume of fluid can be polarized quickly, due to the large surface area of the small nanodiamonds. In this approach we utilized the diffusion of the molecules to our advantage. As the minimal distance between the molecule and NV is on the order of 10 nm, the correlation time can still be long enough (hundreds of nanoseconds) to enable a resonant transfer (i.e. distinguish between rotating and counter-rotating terms in the rotating frame). This leads to an efficient polarization transfer to the surrounding molecules. On the other hand, the correlation time due to the fast diffusion of the molecules is short enough to produce noticeable broadening of the resonance, thereby enabling nanodiamonds with a variety of angles between their NV axes and the magnetic field to be involved in the polarization transfer. We have combined calculations and simulations to demonstrate how by using a setup of nanodiamonds in a mesh, e.g. hydrogel, the parameters can be tuned to generate macroscopic hyperpolarization in molecules within seconds.

We realized however that the short correlation time of the interaction between the NV center and the molecules limits the efficiency of the polarization. We therefore started to explore the option of resonant polarization transfer to molecules in viscous liquids [17]. A key difference in polarization using NV centers from most liquid-state DNP methods, in that the distance of the electron spin to the nuclear spins is very large on the molecular scale (roughly 10 nanometers compared to Angstroms). As

$\tau_c \propto d^2/D$, with d defined as the NV center depth, D is the diffusion coefficient and τ_c the correlation time, by using relatively viscous fluids such as oil ($D \approx 1\,\mu m^2/s$), one can reach correlation times of 10s to 100s of microseconds for $d \approx 10$ nm. On this time scale $1/\tau_c$ is on the same time scale as g_{tot}, with g_{tot} defined as the total flip-flop coupling between the NV center and the proton spin bath in the oil. In this regime, the polarization transfer can be performed resonantly and becomes much more efficient. We combined the theory with an experiment transferring polarization from single NV centers, demonstrating for the first time that polarization can be transferred from an ultra-shallow NV center to diffusing oil molecules external to the diamond, see Fig. 3.1(a) for an illustration. Using the NOVEL sequence (Fig. 3.1(b)), we spin-locked the NV center spin evolution in a rotating basis such that the transition between two "dressed states" can achieve resonance with the Larmor frequency of the surrounding nuclear spins (Figure 3.1(c)). In the case of a resonance, this induces polarization transfer, which can be seen by reading out optically the NV spin state following the polarization transfer (Figure 3.1(d)). Critically, the polarization transfer is very fast, taking less than 20 μs (Figure 3.1(e), as fast as polarization of 13C nuclear spins inside the diamond).

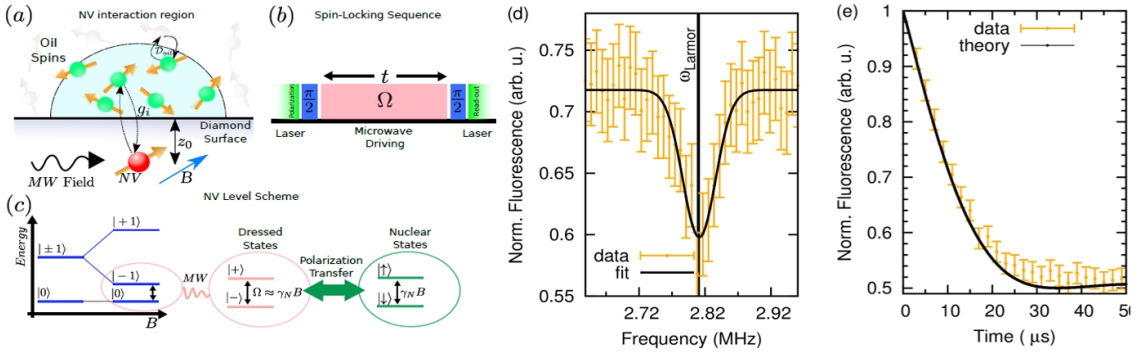


Figure 3.1: polarization of molecules using near-surface NV centers in diamond. (a) illustration of the setup, (b) optical and DNP sequence (NOVEL) used for polarization, (c) energy diagram of NV center and effect of MW spin-locking scheme, (d) experimental verification of polarization transfer on resonance, compared to no polarization transfer off resonance (e) polarization rate demonstrating polarization transfer in under 20 μs.

Finally, I realized that current DNP sequences are inadequate for fully utilizing NV center polarization to external molecules and a new type of DNP sequence has to be developed [18]. Existing methods for utilizing coherent transfer include spin locking sequences (e.g. NOVEL) or sequences utilizing frequency/magnetic field sweeps

(e.g. ISE). Spin-locking sequences are very efficient, and useful for transferring polarization from a single NV center. However, in the case of small electron-nuclear coupling (e.g. such as when transferring polarization to external nuclear spins), they are very ineffective even for small frequency detuning between the microwave irradiation frequency and the NV resonance. This detuning typically occurs from inhomogeneous broadening, either due to an inhomogeneous external magnetic field or variations between NV centers (for example due to strain, surrounding paramagnetic impurities). This makes spin-locking sequences unusable when scaling to an ensemble of NV centers. On the other hand ISE sequences, such as we used in the polarization of nanodiamonds, are very robust to frequency detuning. However, the efficiency of ISE sequences scales quadratically with the coupling strength. In NVs which are located 5nm or more from the diamond surface, the coupling to the external nuclear spins is typically 10 KHz or less, and the quadratic scaling makes ISE incredibly inefficient. Therefore, a new type of polarization sequence had to be devised, which is both robust to detuning and efficient even in the regime of small coupling.

I took inspiration from the dynamical decoupling protocols used for decoupling NV centers from the environment [19], used for example in sensing ac magnetic fields using NV centers. Due to the strong microwave drive, these sequences can be robust to large frequency detuning. The question was, can we engineer an average Hamiltonian which will produce flip-flops between the electron and nuclear spins (and therefore induce polarization transfer) using only strong π and $\pi/2$ pulses applied on the NV centers? This would lead to a new family of coherent polarization transfer protocols, based on strong pulses instead of continuous microwave irradiation. We have thus invented the PulsePol sequence, which, in addition to being efficient and robust, rapidly produces an average flip-flop dynamic and is therefore not adversely affected by the short correlation time with the nuclear spins in the diffusing molecules. PulsePol is now the best-in-class polarization sequence, and is being used in a variety of hyperpolarization experiments.

3.1 Resonance-inclined nuclear spin polarization of liquids in diamond structures

Title:	Resonance-inclined nuclear spin polarization of liquids in diamond structures
Authors:	Chen, Q. and Schwarz, I. and Jelezko, F. and Retzker, A. and Plenio, M. B.
Journal:	Physical Review B 93, 060408
Year:	2016
Copyright:	©2016 American Physical Society. Reprinted with permission from Chen et al. Physical Review B 93, 060408 (2016), ©2016 by the American Physical Society
DOI:	{https://doi.org/10.1103/PhysRevB.93.060408}

PHYSICAL REVIEW B **93**, 060408(R) (2016)

Resonance-inclined optical nuclear spin polarization of liquids in diamond structures

Q. Chen,[1,2,*] I. Schwarz,[1,2] F. Jelezko,[2,3] A. Retzker,[4] and M. B. Plenio[1,2]
[1]*Institut für Theoretische Physik, Universität Ulm, Albert-Einstein-Allee 11, 89069 Ulm, Germany*
[2]*IQST, Universität Ulm, Albert-Einstein-Allee 11, 89069 Ulm, Germany*
[3]*Institut für Quantenoptik, Universität Ulm, 89073 Ulm, Germany*
[4]*Racah Institute of Physics, The Hebrew University of Jerusalem, Jerusalem 91904, Israel*
(Received 13 October 2015; revised manuscript received 3 February 2016; published 24 February 2016)

Dynamic nuclear polarization (DNP) of molecules in a solution at room temperature has the potential to revolutionize nuclear magnetic resonance spectroscopy and imaging. The prevalent methods for achieving DNP in solutions are typically most effective in the regime of small interaction correlation times between the electron and nuclear spins, limiting the size of accessible molecules. To solve this limitation, we design a mechanism for DNP in the liquid phase that is applicable for large interaction correlation times. Importantly, while this mechanism makes use of a resonance condition similar to solid-state DNP, the polarization transfer is robust to a relatively large detuning from the resonance due to molecular motion. We combine this scheme with optically polarized nitrogen-vacancy (NV) center spins in nanodiamonds to design a setup that employs optical pumping and is therefore not limited by room temperature electron thermal polarization. We illustrate numerically the effectiveness of the model in a flow cell containing nanodiamonds immobilized in a hydrogel, polarizing flowing water molecules 4700-fold above thermal polarization in a magnetic field of 0.35 T, in volumes detectable by current NMR scanners.

DOI: 10.1103/PhysRevB.93.060408

Introduction. Nuclear spin hyperpolarization, i.e., a population difference between the nuclear spin states that exceeds significantly the thermal equilibrium value, is a key emerging method for increasing the sensitivity of nuclear magnetic resonance (NMR) [1,2] which is proportional to the sample polarization. By enhancing the magnetic resonance signals by several orders of magnitude, a wide range of novel applications in biomedical sciences are made possible, such as metabolic MR imaging [3] or the characterization of molecular chemical compositions [4,5]. Dynamic nuclear polarization (DNP), by which electron spin polarization is transferred to nuclear spins, is one of the promising methods to reach such a large enhancement of the signal.

Over the past decades, one of the outstanding challenges is the hyperpolarization of molecules in a solution [6–13]. In typical solutions, resonance-based polarization mechanisms commonly used in solid-state systems [14,15] are not effective due to the averaging of the electron-nuclear anisotropic interaction of the molecules by their rapid motion. Thus, cross-relaxation mechanisms such as the Overhauser effect [7,12,13] are typically applied to realize the polarization of fluids under ambient conditions. So far, the largest hyperpolarization is achieved for fast diffusing small molecules and is severely limited by the low thermal electron polarization in moderate magnetic fields. For example, for 2,2,6,6-tetramethyl-1-piperidine-1-oxyl (TEMPO), trityl, or biradical systems, the electron spin polarization amounts to only 0.08% for a magnetic field of $B = 0.36$ T [8,9]. In this Rapid Communication, we demonstrate that the use of optically hyperpolarized electron spins offers an exciting possibility for overcoming the limitation on the degree and rate of electron polarization. Specifically, nitrogen-vacancy (NV) centers in nanodiamonds (NDs) are excellent candidates for optically pumped hyperpolarization agents. The unique optical properties of the negatively charged nitrogen-vacancy center in nanodiamonds allow for over 90% electron spin polarization to be achieved in less than a microsecond by optical pumping [16] while exhibiting a relaxation time in the millisecond range even at room temperature [17]. Methods for the creation of high polarization in ^{13}C nuclear spins inside of bulk diamond have already been developed theoretically and demonstrated experimentally [18–24].

However, for NV centers the interaction correlation time τ_c [25] with nuclear spins in the surrounding molecules is atypically large, as τ_c scales with the square of the minimum distance with the nuclear spins, which is very large (a few nanometers) for NV centers in NDs. Thus, NV centers typically cannot be used with standard Overhauser cross-relaxation protocols. Here, we present a theoretical framework for polarizing molecules for systems with a large correlation time. Specifically, we apply resonance-based schemes, such as the solid effect, where under continuous microwave (MW) radiation the electron spin is driven to approach resonance with the nuclear spin of choice. Importantly, we will proceed to demonstrate that this scheme remains robust even in the presence of molecular motion and, unlike solid-state polarization methods, is tolerant to a relative large detuning from the resonance frequency.

We then consider a specific setup that realizes this protocol, where the NDs are immobilized in a hydrogel inside a flow channel, increasing τ_c, as well as limiting the nuclear spin relaxation due to electron spins to the polarization region. Detailed numerical simulations show that a very high nuclear spin polarization is achieved for volumes that are detectable in current NMR scanners.

Spin polarization via resonance-inclined transfer (SPRINT). We consider the polarization transfer induced by magnetic dipole-dipole coupling between an electron spin and all the surrounding solvent spins. Suppose, as shown

*qiong.chen@uni-ulm.de

 ©2016 American Physical Society

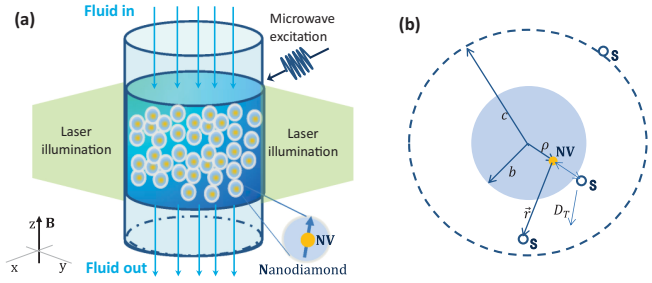


FIG. 1. (a) Schematic setup for polarization of nuclear spin in solution via NV centers in nanodiamonds. Fluid enters a channel containing a hydrogel cell with immobilized nanodiamonds for continuous DNP polarization. Optical polarization of the NV electron spins and microwave irradiation facilitates the polarization transfer to nuclear spins in the surrounding molecules. A permanent magnetic field B is applied along the z axis, which defines the coordinate system. (b) Illustration of the model parameters.

in Fig. 1(b), that the electron spin is located in the center of a ND, and we denote the distance of closest approach of the electron and nuclear spins by b. Denoting the molecular diffusion coefficient in solution with D_T, the interaction between the electron and solvent spins evolves in time with a characteristic correlation time $\tau_c = b^2/D_T$. c and ρ in Fig. 1(b) are related to an absorbing boundary and off-center effect, respectively, which are negligible in our case [see the Supplemental Material (SM) [26]].

In resonance-based DNP schemes, continuous MW radiation is applied to the electron spin [14,15], thus creating an "effective frequency" of the electron spin ω_E in the rotating frame. When the energy difference $\omega_0 = \omega_E - \omega_S$ between the effective frequency and the Larmor frequency ω_S of a specific nuclear spin species vanishes, a Hartmann-Hahn (H-H) resonance is achieved [27] and energy-conserving flip-flop transitions can occur between the electron and nuclear spins. Energy nonconserving flip-flip transitions are suppressed due to a large energy mismatch compared with the effective coupling between the electron and nuclear spin ($\omega_2 = \omega_E + \omega_S \gg g$). This difference between the flip-flop and flip-flip transitions leads to a net polarization transfer from electron spins to nuclear spins [26,28].

In the liquid phase, due to fast molecular diffusion, we can calculate perturbatively the transition probabilities W_i ($i = 0,2$) of the flip-flop transition rate $W_0 = \alpha_0 J(\omega_0)$ and flip-flip transition rate $W_2 = \alpha_0 J(\omega_2)$, in which the spectral density function is given by [26,29,30]

$$J(\omega) = \Gamma \,\mathrm{Re}\left[\frac{1+\frac{\sqrt{i\xi}}{4}}{1+\sqrt{i\xi}+\frac{4\left(\sqrt{i\xi}\right)^2}{9}+\frac{\left(\sqrt{i\xi}\right)^3}{9}}\right], \qquad (1)$$

where $\xi = \omega\tau_c$. α_0 is a constant involving the nuclear properties of the interacting system. Γ is the coefficient determined by system parameters, such as the minimum distance between the electron and solvent spins, the dipole-dipole coupling strength and translational diffusion coefficient, etc. (see the SM [26] for details). In simple solvents of low viscosity, such as protons in free water molecules, $D_T = D_w = 2 \times 10^{-9}$ m^2/s [31], and for a minimal distance of the electron and solvent spins of $b = 0.5$ nm, we find $\tau_c = b^2/D_T \sim 0.1$ ns. Then $\xi \ll 1$ is always satisfied for weak and moderate magnetic fields (i.e., $B < 1$ T), resulting in $\omega_S = (2\pi)16$ MHz for $B = 0.36$ T [see the blue dashed line in Fig. 2(a)]. Applying a MW driving fulfilling $\omega_E = \omega_S$ will lead to no appreciable difference between flip-flip and flip-flop effects, as $J(\omega_2) \cong J(\omega_0) \cong J(0)$ in general. This indifference of the transition rates to the energy mismatch is the main reason why resonance-based polarization schemes are not applicable to solutions with small τ_c. However, larger interaction correlation times achieved by increasing the distance $b = 5$ nm and decreasing the diffusion coefficient to induce $\tau_c = 100$ ns, as shown in the purple dotted line in Fig. 2(a), demonstrate a clear incline of net polarization towards a resonance condition. Using the same parameters discussed above, we now obtain $J(\omega_0) = J(0) \sim 1$ and $J(\omega_2) \sim 0$. Therefore, it is possible to achieve a polarization transfer in a solution with large τ_c by matching a H-H resonant condition. It is interesting to note that the relationship between our scheme and standard Overhauser cross polarization is similar to the sideband resolved regime and the Doppler (unresolved) regime in the laser cooling of cold trapped ions (see SM [26]). This results in a more efficient polarization transfer, which enables DNP via more distant electron spins, and with a weaker dipolar coupling to the nuclear spins.

The steady-state populations in the different nuclear spin states and the resulting polarization can then be determined from a detailed balance analysis. We find (here we ignore the relaxation times; see the SM [26] for a more detailed treatment)

$$P_s = -\frac{J(\omega_0) - J(\omega_2)}{J(\omega_0) + C_0 J(\omega_S) + J(\omega_2)}, \qquad (2)$$

in which $C_0 = 2\cot\varphi$ with $\cot\varphi = \epsilon/\Omega$ depending on the Rabi frequency of the MW radiation Ω and detuning of the MW field from the electron energy scale ϵ. Here, we assume that the electron spin is continuously pumped into a polarized state. Figure 2(b) shows the dependence of the achieved steady-state polarization on the detuning from the resonance condition and correlation time. As we are using the solid effect, we tune the MW field to achieve a resonant interaction as $\omega_S = \sqrt{\epsilon^2 + \Omega^2} = \omega_E = (2\pi)16$ MHz (see the SM [26]), where we have chosen $\epsilon = \Omega = (2\pi)8\sqrt{2}$ MHz. As shown in Fig. 2(a), for a large correlation time satisfying $\tau_c > 10$ ns, different rates between the flip-flop and flip-flip transitions induce a high steady-state polarization, quite similar to solid-state mechanisms. However, contrary to the solid-state phase, we can see that high steady-state polarization is achieved for a wide range of detuning from the resonance, as shown in Fig. 2(b). For example, for $\tau_c = 100$ ns, we observe a high steady-state polarization for a detuning as large as $\Delta' \sim (2\pi)10$ MHz. This is a unique characteristic of our theory in the liquid phase and different from the solid phase in which polarization transfer only occurs when the detuning is comparable to or smaller than the effective collective flip-flop coupling between the electron spin and nuclear spins [18,24]. Thus, this polarization by cross relaxation requires an inclination towards resonance, but the resonance condition does not have to be matched exactly.

Optical SPRINT with nanodiamonds. To model the dynamics of nuclear spin polarization transfer from NV centers in

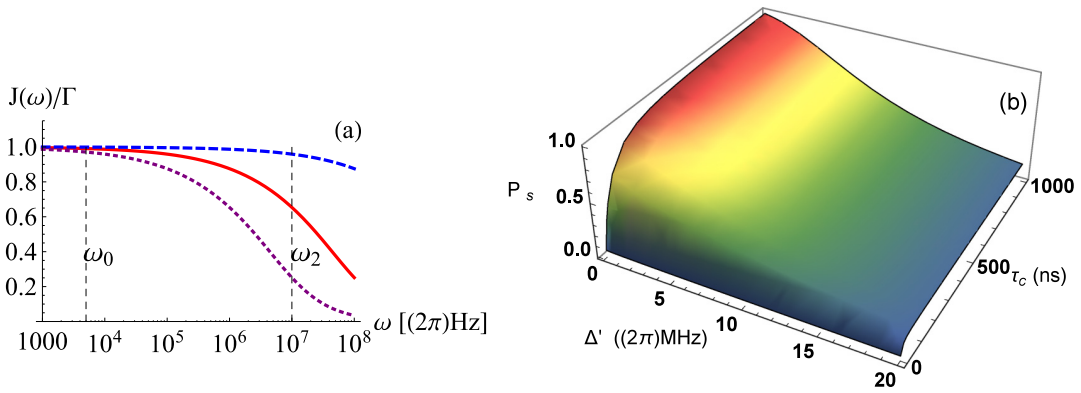


FIG. 2. (a) Spectra density function $J(\omega)/\Gamma$ as a function of frequency ω and interaction correlation time τ_c. The blue dashed, red solid, and purple dotted lines correspond to $\tau_c = 0.1$, 10, and 100 ns, respectively. (b) The steady-state polarization of the nuclear spins. $\omega_S = (2\pi)16$ MHz, $\epsilon_0 = \Omega = (2\pi)8\sqrt{2}$ MHz, and $\Delta' = \epsilon(\theta) - \epsilon_0$ is the detuning from the resonance point.

nanodiamonds to the protons in water, we consider a setup of Fig. 1(a). The solvent spins of the target molecules are pumped through a flow cell containing a hyperpolarization region in which nanodiamonds are immobilized in a hydrogel layer (see Fig. 1), causing a dipolar magnetic interaction between the NV spins and their surrounding solvent spins with a characteristic correlation time τ_c. Here, the electron spins of the NV centers will be strongly polarized by optical pumping, and the hydrogel provides a method for increasing the correlation time by reducing the diffusion rate of water molecules by a factor of 10^2–10^3 via controlling the mesh sizes and types of hydrogels [25].

A dc magnetic field $B \cong 0.36$ T whose direction defines the z axis of the laboratory frame is applied to the system. We assume $\gamma_e B \gg D$, where D is its zero-field splitting. As discussed in Ref. [18], in this regime the quantization axis of all NV centers is along $\vec{B}$, and the orientation of the symmetry axis of the NV center relative to $\vec{B}$ is uniformly distributed over the unit sphere. Here, θ denotes the angle between the NV center symmetry axis and the magnetic field axis. The random orientations of the NV centers cause two difficulties for the polarization transfer from the NV spin to the nuclear spins. First, a high optical polarization of the NV center spins is only achieved for the NV orientation near $\theta = 0^\circ$ and $\theta = 90^\circ$ by using 532 nm green laser illumination and, second, there is a variation of the energy splitting with θ (see SM [26]).

The rate of the polarization transfer is given by $W = W_0 - W_2 = \alpha_0(J(\omega_0) - J(\omega_2))$ [26]. Assuming the magnetic field is given by $B = 0.36$ T, $\omega_S = (2\pi)16$ MHz, for utilizing the effect of resonance in the current setup, we tune the MW frequency to achieve a resonant interaction for $\theta = 90^\circ$, and $\varepsilon_0 = \varepsilon(90^\circ) = \Omega = (2\pi)8\sqrt{2}$ MHz for matching a H-H resonance. Due to the strong dependence of the energy splitting between the spin levels on θ, for each NV spin with a specific $\epsilon(\theta)$, there is a detuning from resonance which leads to Δ' in Fig. 2(b). Here, we focus on the near resonant case around $\theta = 90^\circ$ because the same detuning leads to more NV spins to be involved in the $\theta = 90^\circ$ case as compared to the $\theta = 0^\circ$ case [e.g., $\Delta' < (2\pi)10$ MHz involves 5% NV spins in NDs in the former as compared to just 0.1% NV spins for the latter [18]]. We estimate the efficiency of our scheme by calculating the average polarization rate of the solvent spins $\overline{W}_{\text{eff}} = S^{-1}\int_S W P_C \cos\varphi dS$, with $P_C \cos\varphi$ the initial polarization of the corresponding NV spin according to the solid effect polarization mechanism [15] and S the solid angle covered.

For continuous optical pumping and $\theta = 90^\circ$ such that $P_C \simeq 0.5^2 = 0.25$ (corresponding to about 80% optical initialization), the dependence of the average polarization rate of the solvent spins for NDs of 5 nm radius on the ratio of the decreased translational diffusion k is shown in Fig. 3(a). Slow translational diffusion of the solvent molecules affects the polarization transfer in two competing ways: (i) increasing the correlation time to enhance the polarization transfer and (ii) decreasing the number of involved NV spins contributing to the polarization transfer (as slower diffusion leads to smaller accessible detuning from resonance for our scheme). Figure 3(a) predicts that the former will dominate (as expected, since the first effect is linear and the second sublinear). Thus, a fast polarization transfer can be achieved via a decrease of the

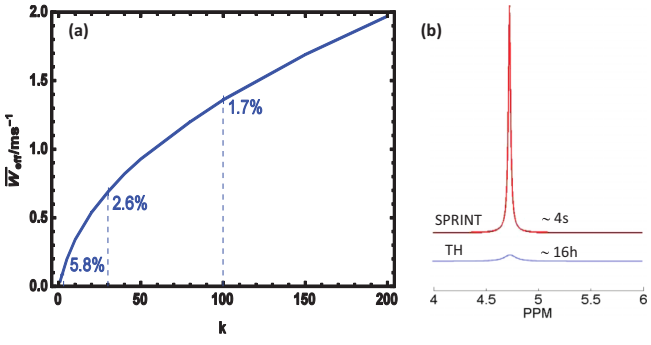


FIG. 3. (a) The averaged polarization rate of the solvent spins $\overline{W}_{\text{eff}}$. A $b = 5$ nm ND radius was assumed. $k = D_w/D_T$, with $D_w = 2 \times 10^{-9}$ m^2/s the diffusion coefficient in free water at room temperature, and D_T is the decreased translational diffusion coefficient. The percent of involved NV spins accounting for 90% of the polarization transfer is given for three different points. (b) The predicted water proton NMR spectrum by using the SPRINT technique (red) for a single shot NMR acquisition compared with 16 h accumulation of thermal polarization (blue) for $B = 0.36$ T.

diffusion rate. For example, when the size of the nanodiamond is $b = 5$ nm, $\overline{W}_{\text{eff}} \approx 0.04\,\text{ms}^{-1}$ for $k = 1$ and $\overline{W}_{\text{eff}} \approx 1.4\ \text{ms}^{-1}$ for $k = 100$.

The proposed setup is feasible with current experimental technology. Over the past decade, several experiments have realized polarization of flowing solvents by immobilized electron spins such as TEMPO and radicals in hydrogel layers [8,9,11] for $B \simeq 0.35$ T. Furthermore, it has been demonstrated that one can use functional groups on the diamond surface to replace these radicals with nanodiamonds in the hydrogel [32,33]. The nanodiamonds are immobilized in the hydrogel and it is not necessary to consider rotational diffusion. While the implementations employing either radicals or nanodiamonds are similar in spirit, it is crucial that the transparency of the hydrogel allows for the optical polarization of nanodiamonds, which has the potential to lead to a 300-fold increase of the achievable nuclear polarization over the implementations using radicals.

To estimate the total polarization of the solvent spins, we use an approximate formula for the steady-state bulk nuclear spin polarization of the solvent neglecting polarization diffusion, $P_{\text{lim}} \approx \frac{N_e}{N_p}\overline{W}_{\text{eff}} T_p$. Here, $\frac{N_e}{N_p}$ is the ratio of the number of the NV spins to proton spins in the polarization region (see SM), and T_p is the smaller of either the time the solvent is in contact with the hydrogel matrix or the solvent relaxation time. Suppose the flow channel is composed of a tube of a diameter of 0.3 mm, the size of the hydrogel layer is 10 mm, and the resulting volume is filled with NDs of 10 nm diameter such that they account for 12% of the total volume. Assuming, furthermore, that $k = 100$, we choose the flow rate of $v = 10^{-2}$ m/s (this flow rate is achieved with commercial pumps, where larger flow rates have been achieved in similar systems [11,34], and negligibly affects the molecular dynamics within τ_c) such that $T_p \sim T_1 \sim 1$ s. Given the density of protons in free water $66.6\ \text{nm}^{-3}$, we obtain $N_e/N_p \sim 4 \times 10^{-6}$, $\overline{W}_{\text{eff}} \approx 1.4\ \text{ms}^{-1}$, $T_p \approx 1$ s to arrive at a polarization of $P_{\text{lim}} \approx 0.6\%$ for the solution. This polarization, achieved in 1 s for a volume of 1 μl, is roughly 4700 times the thermal polarization and would already suffice for detection in a commercial NMR scanner [35]. This enhancement is illustrated in Fig. 3(b), where a simulated water proton NMR spectrum is compared for a single shot readout with DNP, and 16 h of thermal accumulation [37].

In the following, we briefly discuss various requirements and possible limitations in our setup. Optimal NV spin optical polarization in our setup requires around 10 μs mean repolarization time of the NVs in the 0.8 mm^3 volume. Fortunately, due to the small ND radius, Mie scattering does not limit the optical penetration depth in the 7 mm^3 volume for the ND concentration in the proposed setup (see SM). However, due to the efficient optical absorption by the NV centers which is partially converted to phonons, we expect heating of around 2 W for the 1 s a molecule spends in the polarization region for the chosen velocity. This heating power can be easily removed using active cooling. Even cooling only being performed from outside the sample tube (e.g., by fluid or gas cooling) will result in a maximal temperature difference of 25 °C [26] inside the sample, sufficiently low for experimental realization. Far from optical saturation, both the maximally achievable polarization and the heating depend linearly on $\frac{P_{\text{laser}}}{v}$, with P_{laser} denoting the incoming laser power. Thus, an increase in the maximal polarization would require a more efficient cooling scheme. A stringent limitation on the channel diameter is due to microwave absorption in water, which leads to a maximal capillary inner diameter of 1 mm [6], with no adverse effects for a diameter of 0.3 mm. Another important factor for the polarization transfer is the relaxation time T_1 of the protons in the hydrogel layer: As discussed in Ref. [25], this would depend on the material and mesh size in the gel, but can be assumed to be 0.3–2 s. As stated before, for optimal polarization and throughput, the flow speed should be chosen such that $T_p \sim T_1$. Molecules with a longer relaxation time could therefore achieve a higher maximal polarization in the same setup. As the polarization decays quickly back to thermal equilibrium, it is important to increase the flow speed outside the polarization zone, to reduce the time between polarization and detection. This can be achieved by, e.g., narrowing the channel diameter, intersecting with a fast-flowing channel, or by a mechanical shuttle.

We would like to stress that a wide variety of molecules can be polarized with the same methodology and setup, including ones with different nuclear spins (e.g., ^{13}C pyruvic acid for biomedical imaging) or of a larger size (e.g., biomacromolecules). More importantly, SPRINT can potentially be effective for nonoptical DNP systems, not involving nanodiamonds, for example, for DNP in high magnetic fields and/or with biomacromolecules (e.g., proteins). In these systems, if the interaction correlation time between the polarizing electron (e.g., in a radical) and the molecule can be increased, it would be relatively straightforward to apply our scheme. We anticipate that, with minor modifications, resonance-inclined transfer could be applied in combination with other solid-phase schemes, such as the cross effect.

Conclusion. We developed SPRINT, a resonance-inclined mechanism for the polarization of nuclear spins for large interaction correlation times in a solution. Importantly, this is a complementary method to the Overhauser effect, which is most efficient in the extreme narrowing regime. Due to molecular motion, our scheme is tolerant to a relatively large deviation from the resonant frequency. Furthermore, we propose a polarization setup using NV centers in nanodiamonds held in a hydrogel inside a flow cell which combines the advantages of this scheme with optical electron polarization. Under realistic experimental conditions, a polarization enhancement of 4700 times is observed. Our resonance-inclined scheme applies in a wide variety of DNP realizations, especially with biomacromolecules or large magnetic fields.

Acknowledgments. We thank Yuzhou Wu, Pelayo Fernandez Acebal, Oded Rosolio, Benedikt Tratzmiller, and Martin Bruderer for insightful discussions. This work was supported by an Alexander von Humboldt professorship, the ERC Synergy Grant BioQ, the ERC POC grant NDI, an IQST Ph.D. Fellowship, the EU projects SIQS, DIADEMS, and HYPERDIAMOND, as well as the DFG CRC TR 21 and Volkswagenstiftung.

Q.C. and I.S. contributed equally to this work.

[1] F. Bloch, W. W. Hansen, and M. Packard, Phys. Rev. **70**, 474 (1946).
[2] E. M. Purcell, H. C. Torrey, and R. V. Pound, Phys. Rev. **69**, 37 (1946).
[3] M. Law, S. Cha, E. A. Knopp, G. Johnson, J. Arnett, and A. W. Litt, Radiology **222**, 715 (2002).
[4] C. Luchinat and G. Parigi, Appl. Magn. Reson. **34**, 379 (2008).
[5] I. Bertini, Y. K. Gupta, C. Luchinat, G. Parigi, C. Schlörb, and H. Schwalbe, Angew. Chem. **117**, 2263 (2005).
[6] Y. E. Nesmelov, A. Gopinath, and D. D. Thomas, J. Magn. Reson. **167**, 138 (2004).
[7] A. Abragam, *The Principles of Nuclear Magnetism*, International Series of Monographs on Physics No. 32 (Oxford University Press, Oxford, UK, 1961).
[8] E. R. McCarney, B. D. Armstrong, M. D. Lingwood, and S. Han, Proc. Natl. Acad. Sci. USA **104**, 1754 (2007).
[9] E. R. McCarney and S. Han, J. Magn. Reson. **190**, 307 (2008).
[10] C.-G. Joo, K.-N. Hu, J. A. Bryant, and R. G. Griffin, J. Am. Chem. Soc. **128**, 9428 (2006).
[11] S. Ebert, A. Amar, C. Bauer, M. Kölzer, P. Blömler, H. W. Spiess, D. Hinderberger, and K. Münnemann, Appl. Magn. Reson. **43**, 195 (2012).
[12] W. Anderson and R. Freeman, J. Chem. Phys. **37**, 85 (1962).
[13] S. Gabl, O. Steinhauser, and H. Weingärtner, Angew. Chem. **125**, 9412 (2013).
[14] A. Abragam and M. Goldman, Rep. Prog. Phys. **41**, 395 (1978).
[15] W. T. Wenckebach, Appl. Magn. Reson. **34**, 227 (2008).
[16] N. B. Manson, J. P. Harrison, and M. J. Sellars, Phys. Rev. B **74**, 104303 (2006).
[17] F. Jelezko, T. Gaebel, I. Popa, M. Domhan, A. Gruber, and J. Wrachtrup, Phys. Rev. Lett. **93**, 130501 (2004).
[18] Q. Chen, I. Schwarz, F. Jelezko, A. Retzker, and M. B. Plenio, Phys. Rev. B **92**, 184420 (2015).
[19] J. M. Cai, F. Jelezko, M. B. Plenio, and A. Retzker, New J. Phys. **15**, 013020 (2013).
[20] J. P. King, K. Jeong, C. C. Vassiliou, C. S. Shin, R. H. Page, C. E. Avalos, Hai-Jing Wang, and A. Pines, Nat. Commun. **6**, 8965 (2015).
[21] G. A. Álvarez, C. O. Bretschneider, R. Fischer, P. London, H. Kanda, S. Onoda, J. Isoya, D. Gershoni, and L. Frydman, Nat. Commun. **6**, 8456 (2015).
[22] J. M. Cai, B. Naydenov, R. Pfeiffer, L. P. McGuinness, K. D. Jahnke, F. Jelezko, M. B. Plenio, and A. Retzker, New J. Phys. **14**, 113023 (2012).
[23] J. M. Cai, A. Retzker, F. Jelezko, and M. B. Plenio, Nat. Phys. **9**, 168 (2013).
[24] P. London, J. Scheuer, J. M. Cai, I. Schwarz, A. Retzker, M. B. Plenio, M. Katagiri, T. Teraji, S. Koizumi, J. Isoya, R. Fischer, L. P. McGuinness, B. Naydenov, and F. Jelezko, Phys. Rev. Lett. **111**, 067601 (2013).
[25] Y. E. Shapiro, Prog. Polym. Sci. **36**, 1184 (2011).
[26] See Supplemental Material at http://link.aps.org/supplemental/10.1103/PhysRevB.93.060408 for the detailed calculations.
[27] S. Hartmann and E. Hahn, Phys. Rev. **128**, 2042 (1962).
[28] I. Solomon, Phys. Rev. **99**, 559 (1955).
[29] L. P. Hwang and J. H. Freed, J. Chem. Phys. **63**, 4017 (1975).
[30] B. Halle, J. Chem. Phys. **119**, 12372 (2003).
[31] K. Krynicki, C. D. Green, and D. W. Sawyer, Faraday Discuss. Chem. Soc. **66**, 199 (1978).
[32] H. Huang, E. Pierstorff, E. Osawa, and D. Ho, Nano Lett. **7**, 3305 (2007).
[33] E. von Haartman, H. Jiang, A. A. Khomich, J. Zhang, S. A. Burikov, T. A. Dolenko, J. Ruokolainen, H. Gu, O. A. Shenderova, I. I. Vlasov, and J. M. Rosenholm, J. Mater. Chem. B **1**, 2358 (2013).
[34] The pressure difference required for sustaining this flow rate in the 1 mm^3 hydrogel layer is negligible, on the order of 1 Pa.
[35] It is interesting to note that a recently proposed setup for polarization of fluids in a microfluidic diamond channel achieves a similar degree of polarization, but due to the limitations on the microfluidic channel size in the proposed protocol, it requires over 1000 parallel channels for polarizing 1 μl of solvent within 1 s [36].
[36] D. Abrams, M. E. Trusheim, D. R. Englund, M. D. Shattuck, and C. A. Meriles, Nano Lett. **14**, 2471 (2014).
[37] A. M. Castillo, L. Patiny, and J. Wist, J. Magn. Reson. **209**, 123 (2011).

Supplementary material to the manuscript "Resonance-inclined optical nuclear spin polarization of liquids in diamond structures"

I. MECHANISM

A. Basic Hamiltonian

For illustration of the basic idea, let us first consider a general system that is composed of an immobilized electron spin 1/2 (notice that the NV spin $S = 1$ could be simplified to be a two-level system which we will discuss later) and all its nearby diffusing solvent spins $I = 1/2$. The Hamiltonian for such a system is then

$$H = \omega_{0s}\sigma_z + 2\Omega(\cos\omega_{dr}t)\sigma_x + \sum_{n=0}^{N_p}\gamma_n B I_z^n + \sum_{n=0}^{N_p} g_n\Big[\vec{\sigma}\vec{I}^n - 3(\vec{\sigma}\cdot\vec{e}_{nr})(\vec{I}^n\cdot\vec{e}_{nr})\Big], \tag{1}$$

in which ω_{0s} represents the Zeeman splitting of the electron spin and the last term is the magnetic dipole-dipole interaction between the electron and nuclear spin. The length dependant factor g_n and orientation of the inter-spin vector $\vec{e}_{nr}$ is modulated by the translational diffusion coefficient D_T, the rotational diffusion coefficient of the electron spin is not considered due to its immobilization in our setup. ω_{dr} is the driving microwave field of frequency, Ω is the Rabi frequency and γ_n are the nuclear gyromagnetic ratio. Assuming a point-dipole interaction, neglecting the contact term and moving to a frame rotating with the drive frequency, we obtain

$$H' = \epsilon\sigma_z + \Omega\sigma_x + \sum_{n=0}^{N_p}(\sigma_z\cdot\mathbf{A_n}\cdot\vec{I}^n + \gamma_n B I_z^n), \tag{2}$$

where $\epsilon = \omega_{0s} - \omega_{dr}$, $\mathbf{A_n} = g_n\sqrt{1+3(e_{nr}^z)^2}\vec{h}_n = A_n\vec{h}_n$ is the hyperfine interaction tensor for the nuclear spin, with $g_n = \frac{\mu_0}{4\pi}\frac{\hbar\gamma_e\gamma_n}{r_n^3}$ with $r_n = |\vec{r}_n|$ denoting the distance from electron spin to a nuclear spin. $\vec{h}_n$ determined by $\vec{e}_{nr}$: $h_n^x = 3e_{nr}^x e_{nr}^z/\sqrt{1+3(e_{nr}^z)^2}$, $h_n^y = 3e_{nr}^y e_{nr}^z/\sqrt{1+3(e_{nr}^z)^2}$, and $h_n^z = (3(e_{nr}^z)^2-1)/\sqrt{1+3(e_{nr}^z)^2}$. We also define $e_{nr}^z = \cos\theta_n'$, $e_{nr}^x = \sin\theta_n'\cos\phi_n'$ and $e_{nr}^y = \sin\theta_n'\sin\phi_n'$. For simplicity, we define the new nuclear coordinate system x', y', z' and get:

$$H_B = \omega_E\sigma_{\tilde{z}} + \sum_{n=0}^{N_p}[\omega_S I_{z'}^n + (\sigma_{\tilde{x}}\sin\varphi + \sigma_{\tilde{z}}\cos\varphi)\cdot(a_{x_n'}I_+^n + a_{z_n'}I_{z'}^n + h.c.)], \tag{3}$$

in which $\omega_S = \gamma_n B$, the angle φ and ω_E are determined by

$$\sin\varphi = \frac{\Omega}{\sqrt{\epsilon^2+\Omega^2}}, \quad \omega_E = \sqrt{\epsilon^2+\Omega^2}, \quad \omega_E\sigma_{\tilde{z}} = \Omega\sigma_z + \epsilon\sigma_x$$

with $a_{x_n'} = 3g\cos\theta_n'\sin\theta_n' e^{-i\phi_n'}/2r_n^3$ and $a_{z'} = g(3\cos^2\theta_n' - 1)/r_n^3$ in which $g = \frac{\mu_0\hbar\gamma_e\gamma_n}{4\pi}$. Note that we consider the regime where the electron frequency ω_{0s} is large enough to fulfill $\omega_{0s}\tau_c > 1$, i.e. outside the so-called "extreme-narrowing" limit. This condition allows us to disregard fast-oscillating terms when applying the MW driving.

We can rewrite the Hamiltonian as

$$H_B' = \omega_E\sigma_{\tilde{z}} + \sum_{n=0}^{N_p}\omega_S I_{z'}^n + (\sigma_{\tilde{x}}\sin\varphi + \sigma_{\tilde{z}}\cos\varphi)\cdot[\frac{3g}{r_n^3}\sqrt{\frac{8\pi}{15}}Y_2^1(\theta_n',\phi_n')I_+^n + \frac{g}{r_n^3}\sqrt{\frac{16\pi}{5}}Y_2^0(\theta_n',\phi_n')I_{z'}^n + h.c.], \tag{4}$$

with the spherical harmonics $Y_2^1(\theta_n',\phi_n') = -\frac{1}{2}\sqrt{\frac{15}{2\pi}}\cos\theta_n'\sin\theta_n' e^{i\phi_n'}$ and $Y_2^0(\theta_n',\phi_n') = \frac{1}{4}\sqrt{\frac{5}{\pi}}(3\cos^2\theta_n' - 1)$. The Hartmann-Hann resonant condition is given by $\omega_E = \omega_S$.

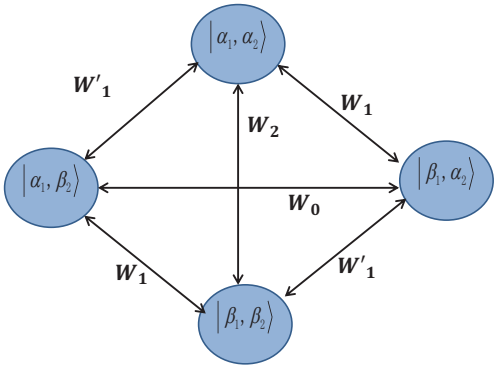


FIG. 1: Transition probabilities between the eigenstates of the spin operators.

B. Transition probability

In first order in perturbation theory the transition probability is given by $W_{ij} = \frac{1}{t}\left\langle |\int_0^t \langle i|H'_B(t')|j\rangle e^{i\omega_{ij}t'}dt'|^2 \right\rangle_{noise}$ we readily arrive [1]

$$\begin{aligned} W_{ij} &= \frac{1}{t}\left\langle \int_0^t\int_0^t \langle i|H'_B(t')|j\rangle\langle j|H'_B(t'')|i\rangle e^{i\omega_{ij}(t'-t'')}dt'dt'' \right\rangle_{noise} \\ &= \frac{1}{t}\int_0^t\int_0^t \left\langle \langle i|H'_B(t')|j\rangle\langle j|H'_B(t'')|i\rangle \right\rangle_{noise} e^{i\omega_{ij}(t'-t'')}dt'dt'', \end{aligned} \tag{5}$$

In principle this result is valid for short times as long as $W_i t \ll 1$, for longer times perturbation theory is invalid. However, this result is still valid for longer times in the limit $g\tau_c/r^3 \ll 1$ and $t \gg \tau_c$, which is correct in the regime of this work. In this regime and in the assumption of Gaussian noise we get two integrals which are connected by the fluctuation dissipation theorem for which the imaginary part is just the power spectrum of the noise, or alternatively,

$$W_i(\omega_i) = \alpha_i Re[\int_{-\infty}^{+\infty} G_i(t')e^{i\omega_i t'}dt'] = \alpha_i J(\omega_i), \tag{6}$$

in which $\alpha_0 = \alpha_2 = \frac{3\pi g^2 \sin^2\varphi}{10}$, $\alpha_1 = \frac{3\pi g^2\cos^2\varphi}{5}$, $\omega_0 = \omega_E - \omega_S$, $\omega_2 = \omega_E + \omega_S$ and $\omega_1 = \omega_S$. All the related transitions are presented in Fig. 1, in which $|\alpha_1\rangle$, $|\beta_1\rangle$, $|\alpha_2\rangle$ and $|\beta_2\rangle$ are the eigenstates of electron and nuclear spins. $G_i(t')$ is the space-dependent time-correlation function for dipolar interaction between spins NV and proton, which is expressed by

$$G_i(t') = \int\int N_p P(\vec{r_0})P(\vec{r_0}|\vec{r_1},t')\frac{Y_2^{i'}(\theta^0,\phi^0)Y_2^{i'}(\theta^1,\phi^1)}{r_0^3 r_1^3}d\vec{r_0}d\vec{r_1},$$

in which $i = 0,1,2$, $i' = [(-1)^i + 1]/2$ and $G_2(t') = G_0(t')$. Here $P(\vec{r_0}) = 1/V$ with the volume V. $P(\vec{r_0}|\vec{r_1},t')$ is the well-known solution of the diffusion equation. As shown in Eq. (6), the spectral density function is the real part of the Fourier-Laplace transform of the corresponding time autocorrelation function. Consider the diffusion coefficient D_T in the whole space, one has [2, 3]

$$J(\omega) = \Gamma Re\left[\frac{1+\frac{\sqrt{i\xi}}{4}}{1+\sqrt{i\xi}+\frac{4(\sqrt{i\xi})^2}{9}+\frac{(\sqrt{i\xi})^3}{9}}\right], \tag{7}$$

in which the coefficient $\Gamma = \frac{8n_p}{27D_T b}$. Here n_p is the proton number density, D_T is the translational diffusion coefficient in hydrogel, b is the closest distance between NV center and protons, and

$$\xi = \frac{\omega b^2}{D_T} = \omega\tau_c.$$

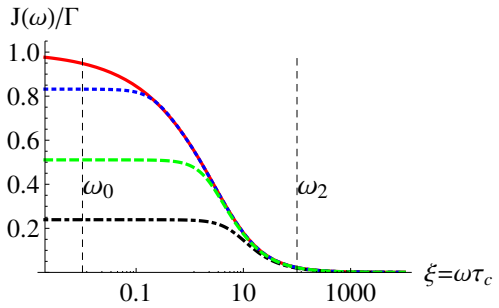


FIG. 2: Normalized spectra density function $J(\omega)/\Gamma$ with $\tau_c = 10$ ns as a function of ξ for selected absorbing boundary, from top to bottom referring to $b = 5$ nm, $c = \infty$ (red solid), 50 (blue dotted), 17 (green dashed) and 10 (black dot-dashed) nm. Here we define $\omega_E - \omega_S = \omega_0$ and $\omega_E + \omega_S = \omega_2$.

It is interesting to know, the principle part of this integral will induce a two body shift: $(\sigma_z+1)(\sigma_z-1)+(\sigma_z-1)(\sigma_z+1)$, which is proportional to the power spectrum of ω_{diff} and $(\sigma_z+1)(\sigma_z+1)+(\sigma_z-1)(\sigma_z-1)$, which is proportional to the power spectrum of ω_{sum}. This term will create an energy shift if the NV which depends on the polarisation which for high polarizations should be compensated by changing the drive.

A detailed balance between the populations in the different energy levels yields the steady-state polarization of solvent nuclear spins as [1]

$$P_s = -\frac{W_0 - W_2}{W_0 + 2W_1 + W_2 + \frac{1}{T_1}} = -\frac{\alpha_0 J(\omega_0) - \alpha_2 J(\omega_2)}{\alpha_0 J(\omega_0) + 2\alpha_1 J(\omega_1) + \alpha_2 J(\omega_2) + \frac{1}{T_1}}, \tag{8}$$

in which T_1 is relaxation time of the NV spins. By ignoring T_1, we can achieve Equation (2) in the main text and $C_0 = 2\alpha_1/\alpha_0$. The rate of the polarization transfer is found to be given by

$$W = W_0 - W_2 = \alpha_0 J(\omega_0) - \alpha_2 J(\omega_2). \tag{9}$$

Notice that W_0 and W_2 are the transition rates of the flip-flop and flip-flip transitions, which are defined in the main text, respectively. The polarization built up depends on the imbalance between spectra density functions $J(\omega_0)$ and $J(\omega_2)$.

The rate equation for the polarization transfer is in the form [4]

$$\frac{d\langle I\rangle}{dt} = -\frac{\langle I\rangle}{T_1} - \frac{N_e}{N_p} W\langle\sigma\rangle, \tag{10}$$

in which $\langle\sigma\rangle$ corresponding to the effective initial polarization of the electron spins. Therefore, when $\frac{d\langle I\rangle}{dt} = 0$, in the stationary state, the formula for bulk nuclear spin polarization takes the approximate form,

$$P_{lim} = \frac{N_e}{N_p} W T_p \langle\sigma\rangle, \tag{11}$$

in which $\frac{N_e}{N_p}$ is the ratio of the number of the NV spin and protons, and for solid effect the effective polarization which could be transferred to the nuclear spins is $P_C \cos\varphi$ with P_C the optical polarization of the electron spin [5] by continual optical pumping.

C. Connection to cooling

Polarization is strongly connected to cooling as in both cases the aim is to prepare the system in a defined state. Thus, as the field of laser cooling is very advanced it is interesting to compare the presented theory with the theory of laser cooling. Cooling is of atoms, ions [6–8] and mechanical oscillators [9, 10] is divided into two main regimes. The unresolved limit, or Doppler cooling [11] and the resolved regime or sideband cooling [12–14] and more advanced methods as dark state cooling [15–18]. In this work we point out for the first time the availability of the regime in which the sideband are resolved for dynamical nuclear polarization.

In both cases the final temperature and the rate are derived from the power spectrum of the noise [19]. For laser cooling the noise originates from the interaction of the atoms with the vacuum while in our case there are two sources of noise. The first one is the noise due to the random feature of the interaction between the NV and the nuclear spins. The second one is the vacuum which induces polarization via the lasers exactly as in the atomic version. In this work we assume that the second one is less significant which means that NV decay time (T_1) is longer than the decay time induced by the interaction noise.

In our case we have derived directly the rates from the first order term in perturbation theory while for laser cooling the noise and the auxiliary system are being adiabatically eliminated in order to derive a new Master equation for the system alone. The same could be done here. The adiabatic elimination could be done in two stages. In the first stage the noise should be eliminated to derive a Master equation of the nuclear spins and the NV. The adiabatic elimination could be done in the weak coupling limit and assuming Gaussian noise [20–22]. At the second stage the NV should be eliminated. In case of no nuclear driving only the the Lindbladian terms and an energy shift survive.

Thus, the final results are readily derived from the power spectrum of the noise (Eq. (7)), which could also be written as:

$$J(\xi)=\Gamma\frac{81\left(2\xi+5\sqrt{2}\sqrt{\xi}+8\right)}{8\left(4\sqrt{2}\xi^{5/2}+27\sqrt{2}\xi^{3/2}+\xi^3+16\xi^2+81\xi+81\sqrt{2}\sqrt{\xi}+81\right)}. \tag{12}$$

The two interesting limits are derived in $\xi\to 0$, which corresponds to the Doppler limit and the limit $\xi\gg 1$ which corresponds to the resolved sideband limit. In the resolved regime, the power spectrum is $\frac{J(\xi)}{\Gamma}=\frac{81}{4\xi^2}+O\left(\left(\frac{1}{\xi}\right)^{5/2}\right)$ and thus the final occupation is $1-\frac{81}{2\xi^2}+O\left(\left(\frac{1}{\xi}\right)^{5/2}\right)$, which deviates from full polarization with the scaling of $\left(\frac{1}{\omega_0\tau_c}\right)^2$. In comparison to atom or ion cooling in which the occupation behaves as $\left(\frac{\gamma}{\nu}\right)^2$, where ν is the trap frequency which is analogous to ω_0 and γ is the decay rate which is analogous to the correlation time. The analogy between the correlation time and γ is due to the fact that γ sets the correlation time in the atomic case. It can be seen that the same scaling is achieved up to the proportionality coefficient.

In the unresolved limit, i.e., the Doppler limit, the power spectrum behaves as $1-\frac{3\sqrt{\xi}}{8\sqrt{2}}+O\left(\xi^{3/2}\right)$ and thus the final occupation is $\frac{3}{4\sqrt{2}}\sqrt{\omega\tau_c}$. Due to the $\sqrt{\xi}$ scaling the effective temperature is not only a function of the decay rate as is in the laser cooling case, but a function of the energy gap as well, meaning, the final temperature is $\sqrt{\frac{\omega}{\tau_c}}$.

D. Restricted uniform diffusion with absorbing boundary

Here we isolate the contribution of the polarization transfer from the solvent spins located in the shell $b<R<c$, in which c is the variable radial distance from the center of the nanodiamond. Therefore, assuming absorption boundary condition at the radial distance c from the center of the nanodiamond, we can have

$$J_l(\xi)=Re\Big\{\frac{2n_s}{\xi^2D_Tb}\Big[\frac{1-l^3}{3}-\frac{3(1+l^5)}{\xi^2}+\frac{1}{C_2}(\frac{6l^3}{\xi^4}-\frac{9C_1}{\xi^3}-\frac{l^4C_3}{\xi})\Big]\Big\}, \tag{13}$$

in which

$$\begin{aligned} C_1 &= i_2(\xi)k_2(\xi/l)-k_2(\xi)i_2(\xi/l),\\ C_2 &= i_2'(\xi)k_2(\xi/l)-k_2'(\xi)i_2(\xi/l),\\ C_3 &= i_2'(\xi)k_2'(\xi/l)-k_2'(\xi)i_2'(\xi/l), \end{aligned} \tag{14}$$

with $l=b/c$. Here $i_2(\xi)$ and $k_2(\xi)$ are the related modified spherical Bessel functions [3]. To elucidate the resulting interplay of the molecular frequency and the spectrometer frequency, suppose $b=5$ nm, we also show the complete normalized frequency spectrum for selected absorbing boundary $c=\infty$, 50, 17 and 10 nm, see Fig. 2. It's also very important to notice that, in the low frequency limit, the normalized spectra density has substantial contribution from solvent spins far beyond the first hydration layer, which enhances the polarization transfer rate.

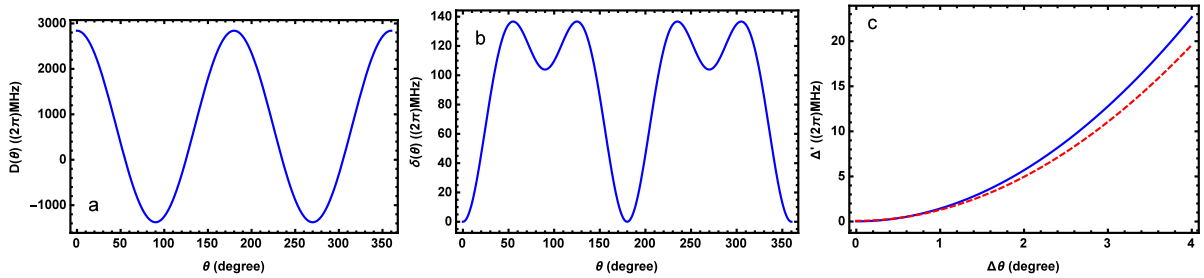


FIG. 3: a, Zero-field distribution $D(\theta)$ of the NV spins in nanodiamonds with $D = (2\pi)2.87$ GHz and $E = (2\pi)20$ MHz. b, The second order corrections which induce a energy distribution $\delta(\theta)$. c, The detuning distributions $\Delta' = \epsilon - \epsilon_0$ vs the angle deviations for $\varepsilon_0 = \epsilon(90^\circ)$ presented by the red dashed line and $\epsilon_0 = \epsilon(0^\circ)$ by the blue solid line, respectively.

II. OPTICAL NUCLEAR SPIN POLARIZATION WITH NANODIAMONDS

A. Random orientations of the NV spins in nanodiamonds

Zero-field and external magnetic field distribution: In the laboratory frame the applied magnetic field defines the z-axis, the NV is placed at the origin of the coordinate system. The Hamiltonian of the electron spin is then [23]

$$H_{NV} = (\gamma_e B + \delta(\theta))S_z + D(\theta)S_z^2 \tag{15}$$

in which

$$D(\theta) = \frac{D(1+3\cos(2\theta)) + 3E(1-\cos(2\theta))}{4}, \quad \delta(\theta) = \frac{\gamma_e B|G_1|^2}{(\gamma_e B)^2 - [D(\theta)]^2} + \frac{|G_2|^2}{2\gamma_e B}, \tag{16}$$

with $G_1 = \frac{(D-E)\sin\theta\cos\theta}{\sqrt{2}}$, $G_2 = \frac{D+3E+(E-D)\cos 2\theta}{4}$, zero-field splitting $D = (2\pi)2.87$ GHz and the local strain $E = (2\pi)20$ MHz. Clearly, the random orientations of the NV centers cause a variation of the zero-field splitting $D(\theta)$ across the entire interval $[-(2\pi)1.43\text{GHz}, (2\pi)2.87\text{GHz}]$ and $\delta(\theta)$ across the interval $[0\text{MHz}, (2\pi)140\text{MHz}]$ as shown in Fig. 3a and b, respectively.

Considering the ground state, the states $m_s = 0$ and $m_s = -1$ manifold form a two-level system, a microwave (MW) field of frequency ω_M is applied as a drive of the spin transitions $|-1\rangle \leftrightarrow |0\rangle$, $H_{dri} = \Omega_M S_x \cos\omega_M t$ (Ω_M is the Rabi frequency of the driving field and ω_M is its frequency). Working in a frame that rotates with the microwave frequency ω_M, we find

$$H = \frac{\Omega}{2}(|0\rangle\langle -1| + |-1\rangle\langle 0|) + \epsilon(\theta)|-1\rangle\langle -1| + (|-1\rangle\langle -1|)\cdot\mathbf{A}\cdot\vec{I} + \gamma_n B I_z, \tag{17}$$

The detuning is given by $\epsilon(\theta) = D(\theta) - \gamma_e B - \delta(\theta) + \omega_M$, and $\Omega = \Omega_M/\sqrt{2}$. Representing the system with the electronic dressed states $|\pm\rangle = \frac{1}{\sqrt{2}}(|-1\rangle \pm |0\rangle)$ and defining the Pauli operator as $\sigma_z = \frac{1}{2}(|+\rangle\langle +| - |-\rangle\langle -|)$, $\sigma_x = \frac{1}{2}(|+\rangle\langle -| + |-\rangle\langle +|)$, then the polarisation transfer dynamics is described by

$$H_{trans} = \Omega\sigma_z + \epsilon\sigma_x + \omega_S I_{z'} + a_{z'}\sigma_z I_{z'} + a_{x'}\sigma_x I_{x'}. \tag{18}$$

Here $\omega_S = \gamma_n\vec{B} - \vec{A}$, And we can rewrite this Hamiltonian as Equation (4).

Optical initialization: A randomly oriented nanodiamond ensemble concerns the optical polarisation of electron spins of the NV center. For bulk diamonds, the magnetic field can be aligned with the principal axis of the NV center and the electronic spin of the NV center can be optically polarised to the state $|m_s = 0\rangle$ by illumination with a 532 nm green laser. However, although in the laboratory frame of reference a strong magnetic field is applied along the z-direction, $\gamma_e B_z \gg D$, for an ensemble of randomly oriented nanodiamonds, the NV centers will be optically pumped to the state $|m_s = 0\rangle_\theta$ that is defined by the relative orientation of the NV center with respect to the externally applied magnetic field which defines the laboratory frame [23]. Here the misalignment angle between the NV-axis and the magnetic field is θ.

As discussed in Ref. [23], we have two coordinate systems which can be transformed into each other and, employing of $S_{z_\theta} = \cos\theta S_z - \sin\theta(\cos\phi S_x - \sin\phi S_y)$, we can express the eigenstate $|m_s = 0\rangle_\theta$, i.e. in the lab frame,

$$|m_s = 0\rangle_\theta = \cos\theta|0\rangle + \frac{\sin\theta}{\sqrt{2}}(e^{i\phi}|+1\rangle - e^{-i\phi}|-1\rangle). \tag{19}$$

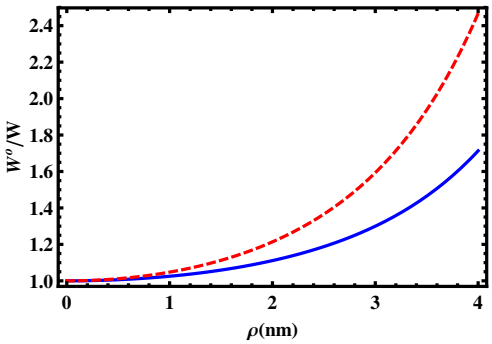


FIG. 4: The ratio of polarization transfer with and without eccentricity vs the distance from the center of the nanodiamond. The red dashed and blue solid line show the dependence of comparison of the polarization built up for $\omega_S = (2\pi)16$ MHz, $\Delta_0 = \Omega = (2\pi)8\sqrt{2}$ MHz, and $\Delta' = 0$ and $\Delta' = (2\pi)10$ MHz, respectively.

If θ is large, the eigenstate $|0\rangle$ of the NV center in the laboratory frame differs significantly from the zero-field eigenstate $|0\rangle_\theta$ of the NV center. Hence optical initialisation of randomly oriented NV centers lead to very different states depending on the orientation of the NV center.

Notice that for small misalignment between the NV center and external magnetic field, the initialisation of the NV center is well approximated to $|0\rangle$. Indeed, for $\theta < 10°$, we can arrive significant polarisation of the electron spins along the quantisation axis defined by the external magnetic field $P_{NV} \simeq 1$. For $\theta \in [80°, 100°]$, the population in state $|0\rangle$ is very small and the initial state is well approximated by $\frac{1}{\sqrt{2}}(e^{i\phi}|+1\rangle - e^{-i\phi}|-1\rangle)$. In the subspace spanned by the states $\{|0\rangle, |-1\rangle\}$, the NV spin is well-polarized in state $|-1\rangle$ with polarization $P_{NV} \simeq 0.5$. So consider a continual optical pumping, it's reasonable to have the initial polarization of the NV spin $P_C \simeq 0.25$.

Detuning from the resonance: MW field is applied to have $\epsilon_0 = \Omega = (2\pi)8\sqrt{2}$ MHz which matches the resonant condition $\omega_S = \omega_E = (2\pi)16$ MHz. Since high polarization is achieved for $\theta < 10°$ and $\theta \in [80°, 100°]$, assume two resonant points with $\epsilon_0 = \epsilon(0°)$ or $\epsilon_0 = \epsilon(90°)$, we calculate the detuning from the resonance which is defined as $\Delta' = \epsilon(\theta) - \epsilon_0$ and varies with the angle deviation from 0° and 90°, respectively. As shown in Fig. 3c, if the angle deviation $\Delta\theta \sim 4°$, this detuning reaches $(2\pi)20$ MHz both for $\theta < 10°$ and $\theta \in [80°, 100°]$.

B. Off-center effect

It's quite normal when the NV spin is not located in the center of the nanodiamond, so we intend to discuss the polarization transfer under the off-center effect. Suppose a NV center is located off-center and its distance from the center of the nanodiamond is ρ. Consider a series expansion in terms of the eccentricity parameters, we can include the off-center effect in the spectra density function which is given by [24]

$$J^O(\xi) = [J(\xi)] \times [(1 + \frac{1}{6}\sum_{L=1}^{\infty}(L+1)(L+2)(2L+3)\rho^{2L}\frac{Re[J^{L+2}(\xi)]}{J(\xi)}], \tag{20}$$

where

$$J^{L+2}(\xi) = Re[\frac{2n_s}{i\xi D_T b}\{\frac{1}{2L-1} - \frac{L+1}{i\xi}[1 + \frac{(L+1)K_{L+1/2}(\sqrt{i\xi})}{\sqrt{i\xi}K_{L-1/2}(\sqrt{i\xi})}]^{-1}\}], \tag{21}$$

with a modified Bessel function $K_\mu(\sqrt{i\xi})$. Thus the rate of polarization transfer including off-center effect is given by $W^O = W_0^O - W_2^O = \alpha_0(J^O(\omega_0) - J^O(\omega_2))$. Fig. 4 illustrates the dependence of the polarization built-up on the eccentricity of the NV center. One can find that polarization built up only is enhanced by factor 1.7 ($\Delta' = 0$ MHz) or 2.4 ($\Delta' = (2\pi)10$ MHz). It is manifested that the polarization transfer is benefited by the eccentricity due to the reduced distance between the NV and the neighboring nuclear spins, but this enhancement is not significant. The possible main reason is the long range nature of the spectral density function, which includes contributions from a large amount of the distant solvent spins.

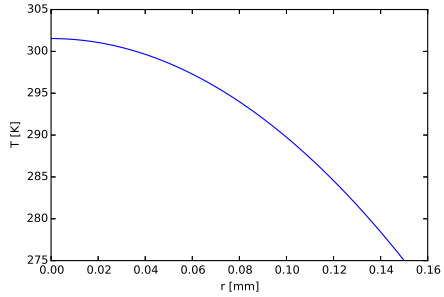


FIG. 5: Temperature dependence on the radius after 1 second of heating. This distribution is almost identical to the steady state, which is reached after about 1.5 seconds.

C. Optical heating

For calculating the heating due to the incoming optical illumination, we focus on the phonons generated by the NV centres due to optical absorptions (the NV centres are by far the most efficient absorbers in the applied laser wavelength). To optically polarize the NV spins in our setup within 12 μm, would require a photon rate of $J_{pht} = N_{NV}\eta/\tau_{ph}$, with N_{NV} denoting the number of NV spins (in case of one NV per nanodiamond $N_{NV} = V_p/(4/3\pi r_d)$, with V_p denoting the polarization volume and r_d the average distance betwen nanodiamond centers), η the number of photons required per NV polarization (typically around 1-5) and τ_{ph} the time between polarization cycles. After excitation, the NV electron relaxation will generate a phonon(s) with energy similar to the photon (in case of nonradiative decay) or based on the difference between excitation (532 nm) and the maximal phonon sideband (700 nm). Thus, on average the energy of the generated phonons E_{phn} will be around 20-40% of the photon energy. The heating is then given by

$$Q = E_{phn} J_{pht} t.$$

For our setup, given 50 μs optical repolarization time, this will result in around 2 W heating power. Given active cooling at the channel boundary, we find a temperature difference of 26 degrees between the centre and boundary of the channel at steady state. When including the heat diffusion, we get that the heat distribution approaches the steady state on a time scale of less than one second. Deciding on a cooling around 5° C of the boundary will give a temperature distribution in the channel between 5-31° C, as shown on Fig. 5. In this regime, the diffusion rate of water molecules stays at the same order and our scheme is feasible [25]. Also, we notice that as the laser absorption of the NVs depends on laser polarization angle, orienting the laser polarization to the magnetic field direction, will likely result in a decreased absorption by unwanted NV orientations (probably about half) [26].

D. Optical and MW penetration depth

Lasers typically used in NV experiments provide the intensity to enable optical polarisation of the NV centre electron spins within 10-100 μs in 1 mm^3 volume. There are two main limitations on the penetration depth when applying optical irradiation to the polarisation structure of the hydrogel containing imobilized diamond: scattering due to nanodiamonds and optical absorption (mainly by NV centre spins). Taking into account the optical cross section of the NV centres and the relatively low NV concentration in this setup we expect the optical penetration depth by the NVs to be a little larger than 1 mm. The optical scattering due to nanodiamonds could become an issue which limits the total penetration depth. As the nanodiamond size is small compared to the optical wavelength, but not negligibly so, we use Mie scattering to calculate the optical transmission through our setup (taking into account only the scattering from the nanodiamonds). It can be seen that the optical penetration decreases sharply with the nanodiamond radius, as shown in Fig. 6. However, for the ND size of interest $b = 5$ nm, the scattering from NDs in 1 mm is almost negligible. A more stringent limitation on the channel diameter is due to microwave absorption in water which leads to a typical capillary radius of 1mm [27].

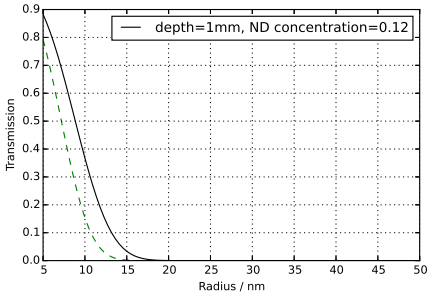


FIG. 6: The optical transmission through our setup dependence on the nanodiamond radius, taking into account Mie scattering from the nanodiamonds. We assume 1 mm thickness and 12% ND concentration. The black solid and green dashed lines correspond to a refractive index of the medium in between the nanodiamonds of water and air respectively.

[1] I. Solomon, Phys. Rev., 99(2): 559, 1955.
[2] L. P. Hwang, J H. Freed J. Chem. phys. 1975, 63(9): 4017-4025.
[3] B. Halle J. Chem. phys. 2003, 119(23): 12372-12385.
[4] D. Abrams, M. E. Trusheim, D. R. Englund, et al. Nano Lett. vol. 14(5): p. 2471, 2014.
[5] W. T. Wenckebach, *Applied Magnetic Resonance*, vol. 34, no. 3-4, pp. 227–235, 2008.
[6] S. Chu, Rev. Mod. Phys. **70**, 685 (1998).
[7] C. N. Cohen-Tannoudji, Rev. Mod. Phys. **70**, 707 (1998).
[8] W. D. Phillips, Rev. Mod. Phys. **70**, 721 (1998).
[9] I. Wilson-Rae, N. Nooshi, W. Zwerger, and T. J. Kippenberg Phys. Rev. Lett. **99**, 093901 (2007).
[10] F. Marquardt, Joe P. Chen, A. A. Clerk, and S. M. Girvin Phys. Rev. Lett. **99**, 093902 (2007).
[11] T. Hansch and A. Schawlow, Opt. Commun 13, **68** (1975).
[12] D. Wineland and H. Dehmelt, Bull. Am. Phys. Soc **20**, 637 (1975).
[13] D. J. Wineland, R. E. Drullinger, and F. L. Walls, Phys. Rev. Lett. **40**, 1639 (1978).
[14] S. Stenholm, Rev. Mod. Phys. **58**, 699 (1986).
[15] A. Aspect, E. Arimondo, R. Kaiser, N. Vansteenkiste, and C. Cohen-Tannoudji, Phys. Rev. Lett. **61**, 826 (1988).
[16] R. Dum, P. Marte, T. Pellizzari, and P. Zoller, Phys. Rev. Lett. **73**, 2829 (1994).
[17] G. Morigi, J. Eschner, and C. H. Keitel Phys. Rev. Lett. **85**, 4458 (2000).
[18] J. Cerrillo, A. Retzker, M. B. Plenio, Phys. Rev. Lett. **104**, 043003 (2010).
[19] J. I. Cirac, R. Blatt, P. Zoller and W. D. Phillips, Phys. Rev. A. **46**, 2668 (1992).
[20] J. E. Avron, O. Kenneth, A. Retzker and M. Shalyt, New Journal of Physics **17**, 1367 (2015).
[21] H. Spohn, J.L. Lebowitz. ,in: S.A. Rice (Ed.), Advances in Chemical Physics, Wiley, New York (1978).
[22] R. Alicki and M. Fannes, 2001 Quantum Dynamical Systems (Oxford: Oxford University Press)
[23] Q. Chen, I. Schwarz, F. Jelezko, A. Retzker, and M. B. Plenio,(2015) arxiv.org/1504.02368.
[24] J. P. Albrand, M. C. Taieb, P. Fries, and E. Belorizky, (1981). The Journal of Chemical Physics, 75(5), 2141-2146.
[25] M. Holz, S. R. Heil, A. Sacco, (2000) Phys. Chem. Chem. Phys., 2(20): 4740-4742.
[26] R. J. Epstein, F. M. Mendoza, Y. K. Kato, et al. (2005) Nat. Phys., 1(2): 94-98.
[27] Y.E. Nesmelov, A. Gopinath, and D.D. Thomas J. Magn. Reson. **167**, 138–146 (2004).

]

3.2 Toward Hyperpolarization of Oil Molecules via Single Nitrogen Vacancy Centers in Diamond

Title:	Toward Hyperpolarization of Oil Molecules via Single Nitrogen Vacancy Centers in Diamond
Authors:	P. Fernández-Acebal, O. Rosolio, J. Scheuer, C. Müller, S. Müller, S. Schmitt, L. B. McGuinness, I. Schwartz, Q. Chen, A. Retzker, Z. Wang, C. Müller, B. Naydenov, F. Jelezko and M. B. Plenio
Journal:	Nano Lett. 2018, 18, 3, 1882-1887
Year:	2018
Copyright:	Reprinted with permission from P. Fernández-Acebal et al. Nano Letters 18, 3, 1882-1887 (2018) ©2018 the American Chemical Society.
DOI:	https://doi.org/10.1021/acs.nanolett.7b05175

NANO LETTERS
Cite This: Nano Lett. 2018, 18, 1882−1887
Letter
pubs.acs.org/NanoLett

Toward Hyperpolarization of Oil Molecules via Single Nitrogen Vacancy Centers in Diamond

P. Fernández-Acebal,*[,†] O. Rosolio,[‡] J. Scheuer,[∥] C. Müller,[∥] S. Müller,[∥] S. Schmitt,[∥] L.P. McGuinness,[∥] I. Schwarz,[†] Q. Chen,[†] A. Retzker,[‡] B. Naydenov,[∥] F. Jelezko,[∥] and M.B. Plenio[†]

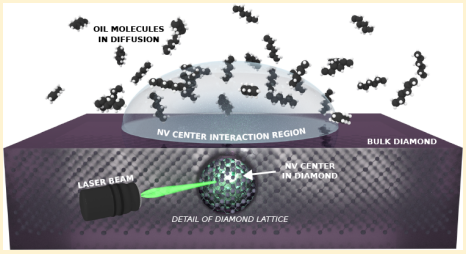
[†]Institut für Theoretische Physik and Center for Integrated Quantum Science and Technology (IQST), Universität Ulm, Albert-Einstein Allee 11, 89069 Ulm, Germany

[‡]Racah Institute of Physics, The Hebrew University of Jerusalem, Jerusalem, 91904 Givat Ram, Israel

[∥]Institute for Quantum Optics and Center for Integrated Quantum Science and Technology (IQST), Universität Ulm, Albert-Einstein-Allee 11, 89069 Ulm, Germany

Supporting Information

ABSTRACT: Efficient polarization of organic molecules is of extraordinary relevance when performing nuclear magnetic resonance (NMR) and imaging. Commercially available routes to dynamical nuclear polarization (DNP) work at extremely low temperatures, relying on the solidification of organic samples and thus bringing the molecules out of their ambient thermal conditions. In this work, we investigate polarization transfer from optically pumped nitrogen vacancy centers in diamond to external molecules at room temperature. This polarization transfer is described by both an extensive analytical analysis and numerical simulations based on spin bath bosonization and is supported by experimental data in excellent agreement. These results set the route to hyperpolarization of diffusive molecules in different scenarios and consequently, due to an increased signal, to high-resolution NMR.



KEYWORDS: *Nitrogen vacancy center, hyperpolarization, dynamic nuclear polarization, diamond, spin qubit*

Nuclear magnetic resonance (NMR) is a fundamental tool in the biomedical sciences.[1,2] As the sensitivity of NMR is proportional to the sample polarization, hyperpolarized samples, where the population difference between nuclear spins exceeds significantly its thermal value, are desirable for achieving a higher NMR signal. One of the promising methods achieving such a hyperpolarization is dynamic nuclear polarization (DNP) in which a polarized electron spin transfers its polarization to a nuclear bath via dipolar coupling. While currently commercially available techniques require cryogenic temperatures to polarize the electron spins, we take a different route based on optical polarization of nitrogen vacancy (NV) centers in diamonds at room temperature.

NV centers are negatively charged paramagnetic defects in diamond with an unpaired electronic spin triplet in their ground state.[3] These color centers can be significantly polarized (exceeding 92%) by optical pumping without the need for low temperatures nor high magnetic fields.[4] This polarization process can be achieved in less than a microsecond, while the NV center relaxation time can be in the order of milliseconds. Furthermore, the highly polarized NV center electron spins can be brought into resonance with adjacent nuclear spins, making them great candidates for DNP.

A special interest over the last years has been paid to hyperpolarization of molecules in solution.[5−9] Due to the molecular motion and short correlation times in fluids, the anisotropic interaction between the electron and the target spins averages out. Consequently, cross-relaxation mechanisms are commonly used in polarization of liquids at ambient conditions since common methods developed for DNP of stationary spins such as the solid effect[10,11] are less efficient.

In this work, we demonstrate that polarization loss from a single shallow implanted NV center can be understood as the result of polarization transfer to ^{1}H nuclei in surrounding oil molecules. As the NV center is several nanometers away from the diffusing molecules and oil exhibits a high viscosity at room temperature, the nuclei diffuse in and out of the NV center interaction region in a time scale comparable with the interaction strength. This results in an increase of the polarization rate enabling resonant transfer.[6] We use the Hartmann−Hahn double resonance (HHDR) scheme,[12] where the electron spin is driven with a Rabi frequency that matches the Larmor frequency of diffusive nuclei. Consequently, the interaction between the NV center and the ^{1}H nuclei is strengthened, while the effects of noise sources on the NV center are weakened. Thus, the HHDR scheme serves as a continuous dynamical decoupling (CDD) protocol,[13−21] allowing us to polarize the specified nuclear species efficiently.

Received: December 8, 2017
Revised: February 16, 2018
Published: February 22, 2018

ACS Publications © 2018 American Chemical Society

DOI: 10.1021/acs.nanolett.7b05175
Nano Lett. 2018, 18, 1882−1887

In fact, HHDR has been used to successfully hyperpolarize nuclear spins inside diamond.[22−24] Also, our method is limited by the relaxation time in the rotating frame, $T_{1\rho}$, (finding its origin in T_2 processes in the nonrotating frame), in contrast to recently proposed microwave-free protocols that are highly affected by the much shorter dephasing time T_2*.[25]

This Letter is organized as follows: First, the Hamiltonian describing the interaction between one electronic (NV) spin and a bath of N diffusive nuclear spins is presented. We then derive an analytical solution for the polarization loss of the NV center. In order to compare the theoretical prediction to a robust numerical simulation and due to the fact that large spin baths can not be fully simulated, we use the Holstein−Primakoff approximation (HPA),[26] which considers spins as bosons, allowing us to perform an efficient numerical implementation. Finally, we validate our theoretical findings, carried out with no free parameters, by performing experiments with two different shallow NV centers coupled to oil molecules. Theory and experiment show an excellent agreement and, therefore, support that polarization loss of the NV center in one single cycle is best explained by polarization transfer to oil at room temperature.

Our system consists of a shallow NV center in bulk diamond located at a distance, z_0, underneath the diamond surface. Immersion oil containing the ^1H nuclei is deposited onto the surface. The setup is depicted in Figure 1. At room temperature, the oil molecules diffuse with the diffusion coefficient $\mathcal{D}_{\text{oil}}$, which results in a finite correlation time, τ_c,

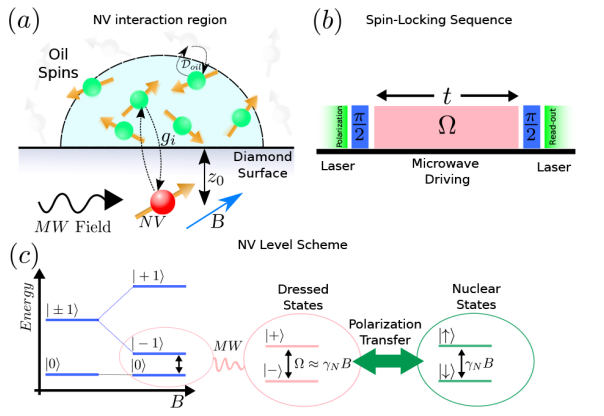


Figure 1. Schematic setup for hyperpolarization of oil molecules with shallow NV centers in bulk diamond and important parameters. (a) The NV center is located at a distance, z_0, beneath the diamond surface. The quantization axis of the NV center coincides with the [1,1,1] direction inside the diamond lattice. The oil is deposited on top of the diamond. The ^1H spins in the oil molecules move stochastically with a diffusion coefficient $\mathcal{D}_{\text{oil}}$, by means of this motion they diffuse in and out the detection volume (blue semisphere). Only the N spins inside the volume (in green) are considered, while the interaction with outer spins (in gray) is neglected. (b) Spin-locking sequence applied to measure the NV center polarization loss. The NV center is initially polarized and read-out using a green-laser pulse. During the microwave driving time, t, the NV center interacts with the nuclear spins. (c) Energy levels of the NV center. In the absence of the magnetic field, the NV center is a spin−1 system with projections m_s = 0, ±1. Degeneracy between m_s = ±1 levels is lifted by applying an external magnetic field, B, parallel to the NV center axis. The transition between m_s = 0 and m_s = −1 is driven with a microwave field inducing a Rabi frequency, Ω, which matches the nuclear Larmor frequency, ω_N = $\gamma_N B$, permitting polarization transfer.

for the electron−nuclear spin interaction. (See the Supporting Information and refs 27 and 28.)

In solid samples at HHDR, flip−flop transitions (polarization transfer) between electron and nuclear spins predominate over flip−flip processes (depolarization), which are energetically forbidden, thus generating a net polarization transfer at weak coupling. For liquid samples, however, the transfer efficiency is mainly determined by a parameter $\chi \equiv \omega_N \tau_c$ (Supporting Information and ref 6), with ω_N, the Larmor frequency of the nuclei in diffusion. For $\chi \ll 1$, as is typical for strongly diffusing molecules, such as water, the effective interaction time is shorter than ω_N^{-1}. In this regime, the imbalance between flip−flip and flip−flop transitions is suppressed, even on resonance, so no net polarization is achieved. However, as the NV center is several nm apart from the diffusing molecules and as the oil possesses a high viscosity at room temperature ($\mathcal{D}_{\text{oil}} \approx 0.5\ \text{nm}^2\ \mu\text{s}^{-1}$), the resulting correlation time is large, making $\chi \gg 1$, for shallow NV centers ($z_0 \approx 3$−5 nm). Therefore, once the HHDR condition is achieved, flip−flip transitions are suppressed by fast rotations so that, in the presence of flip−flop transitions, an efficient polarization transfer from the electronic spin to the ^1H nuclei is expected. The same argument applies to other nonsecular terms apart from flip−flip.

In order to model the described system, we consider a single NV center, electronic spin−1, interacting with N diffusive nuclear spins−1/2. In the secular approximation,[22] this interaction is described by $H_{int} = I_Z^{NV} \sum_i \mathbf{A}^i(t)\ \mathbf{I}_i$, where $\mathbf{I}^{NV}$ is the spin−1 operator of the NV center, with projections m_s = 0, ±1, $\mathbf{I}_i$ is the spin operator of the i^{th} nucleus and $\mathbf{A}^i(t)$ is the hyperfine vector between them (Supporting Information). The NV center is driven by a microwave field with Rabi frequency Ω resonant with the $m_s = 0 \rightarrow m_s = -1$ transition, creating an effective two-level system. In the presence of an external magnetic field $\mathbf{B}$, the nuclear Larmor frequency is $\omega_N = \gamma_N |\mathbf{B}|$, with γ_N, the nuclear gyromagnetic ratio. The magnetic field generated by the driven NV center perturbs the external field acting on the nuclear spins; hence, ω_N fluctuates due to this effect. Polarization transfer occurs at the HHDR condition, $\Omega = \omega_N$. In the dressed-state basis, $|\pm\rangle = \frac{1}{\sqrt{2}}(|0\rangle \pm |-1\rangle)$ for the NV center and assuming $\tau_c\ \omega_N \gg 1$ in our setup, we can assume the rotating wave approximation to find the effective Hamiltonian ($\hbar = 1$)

$$H = \Omega S_z + \sum_{i=1}^{N} \omega_N I_z^i + \sum_{i=1}^{N} g_i(t) S_+ I_-^i + g_i^*(t) S_- I_+^i \qquad (1)$$

with $S_z = \frac{1}{2}(|+\rangle\langle+| - |-\rangle\langle-|)$ and the coupling strength $g_i(\mathbf{x}_i(t)) \equiv g_i(t) = \frac{1}{4}(A_x^i(t) + iA_y^i(t))$, where $\mathbf{x}_i(t)$ is the relative position between the NV and the i^{th} nucleus and $A_\alpha^i(t)$ are the different components of the hyperfine vector $\mathbf{A}^i(t)$. Note that $g_i(t)$ is a stochastic variable with a certain correlation time, τ_c.

Indeed, over time intervals larger than τ_c, the system state may be expressed as $\langle\rho\rangle(t) = \langle\rho\rangle_{NV}(t) \otimes \rho_B$, with $\rho_B = \bigotimes_{i=1}^{N} \frac{1}{2}\mathbb{I}$ the I thermal state of the nuclei, $\langle\rho\rangle$ the system density matrix averaged over all stochastic trajectories of $g_i(t)$, and $\langle\rho\rangle_{NV}$ the NV center density matrix. Within this description, correlations among spins are neglected, which

DOI: 10.1021/acs.nanolett.7b05175
Nano Lett. 2018, 18, 1882−1887

allows us to obtain for the average NV center population, $\langle n\rangle = \frac{1}{2} + \mathrm{Tr}(S_z\langle\rho\rangle_{\mathrm{NV}})$, the dynamical equation

$$\dot{\langle n\rangle} + \frac{1}{4}N\gamma(t)\langle n\rangle = \frac{1}{4}N\gamma(t)\langle n\rangle_B \tag{2}$$

where we define $\gamma(t) = \int_0^t \langle \xi_\alpha^i(t')\xi_\alpha^i(0)\rangle dt'$, $\xi_\alpha^i(t) = A_\alpha^i(t) - \langle A_\alpha^i(t)\rangle$ and $\langle n\rangle_B$ is the average nuclear population, which is $\langle n\rangle_B = 1/2$ for the thermal bath. Eq 2 reflects a net incoherent polarization transfer toward the nuclear reservoir.

The description of $A_\alpha^i(t)$ as a stochastic variable is not trivial. Even if the nuclei undergo thermal random motion, which is Gaussian and thus easy to characterize, the intricate dependence of $A_\alpha^i(t)$ on the relative position between the NV center and nuclei makes $A_\alpha^i(t)$ itself not a Gaussian variable. Consequently, the derivation of a close analytic solution for $\langle A_\alpha^i\rangle$ or γ is not straightforward. Instead, a full analytical description of the polarization evolution may be derived when assuming $A_\alpha^i(t)$ is such that (i) its higher order cumulants are negligible compared to its mean and variance. (ii) The correlation decays exponentially, then $\gamma(t) = \sigma^2\tau_c\ (1 - \exp(-t/\tau_c))$, with σ^2 the variance of $A_\alpha^i(t)$. Note that we have dropped α and i since, for homogeneous diffusion, all nuclei have equal average properties. These two assumptions have been numerically tested (Supporting Information). With these considerations, the solution of eq 2 is

$$\langle n\rangle = \frac{1}{2} + \frac{1}{2}\exp\left(\frac{1}{4}N\tau_c^2\sigma^2(1 - t/\tau_c - \mathrm{e}^{-t/\tau_c})\right) \tag{3}$$

For $t \ll \tau_c$, $\langle n\rangle$ shows a Gaussian decay with a polarization rate $\sqrt{\frac{1}{8}N\sigma^2}$. On the other hand, for $t \gg \tau_c$, we find $\langle n\rangle$ exhibits an exponential behavior with a rate $\frac{1}{4}N\sigma^2\tau_c$. Eqs 2 and 3 are only valid for times such that $N\langle\xi_\alpha{}^{i3}\rangle\tau_c{}^2 \ll t^{-1}$ and $N\langle g\rangle^2\,\tau_c \ll t^{-1}$. (Note that, for non-Gaussian variables, the third moment does not vanish; see the Supporting Information.) The derived equations describe the polarization dynamics of the system and do not include $T_{1\rho}$ relaxation. For a discussion of the latter, see the Supporting Information.

Aiming to reinforce our theoretical findings and since exact computational simulations of large spin systems are not possible, we perform simulations based on Gaussian states to compute the dynamical evolution of a system ruled by eq 1. Specifically, we make use of the Holstein−Primakoff approximation (HPA)[26] representing a polarized spin as a boson in its ground state. In the lowest order of the approximation, the spin operators are substituted by bosonic operators, $S_- \to a$. This approximation holds for highly polarized spins, while for spins in its thermal state it offers a lower bound to the polarization dynamics.[29] The bosonic Hamiltonian is then obtained from eq 1 as

$$H = \Omega a^\dagger a + \sum_{i=1}^{N}\omega_N b_i^\dagger b_i + \sum_{i=1}^{N} g_i a^\dagger b_i + g_i^* a b_i^\dagger \tag{4}$$

which is quadratic in the operators $\{a,a^\dagger,b_i,b_i^\dagger\}$, allowing an efficient numerical simulation describing the dynamical evolution via the covariance matrix. (See the Supporting Information and refs 30 and 31.)

The full numerical simulation is performed considering N independently moving nuclei in a finite box with periodic boundary conditions. The box represents the detection volume of the NV center, and its length is proportional to the NV center depth.[27,32] When a nucleus crosses the box walls, it is substituted by a nucleus from the reservoir, thus losing its correlation with the NV center and the rest of spins. Each particle describes a 3-dimensional Brownian motion.[33] Due to the molecular motion, internuclear coupling among nuclei is averaged out. Therefore, a specific molecular structure is not relevant in the main dynamics. Rotations and vibrations of the molecule are not considered in the simulations. Results showing the agreement between the solution of eq 2 and a full numerical simulation are depicted in Figure 2. We remark

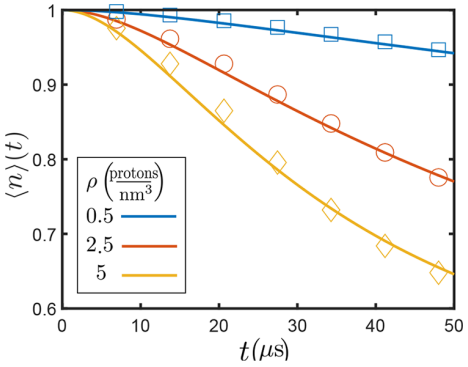


Figure 2. Comparison between theoretical predictions, eq 2 for a spin system (lines), and full numerical simulations using the bosonic approximation, eq 4 (markers) for different sample densities and fixed $\mathcal{D}_{\mathrm{oil}}$ and z_0. For the theory curve, the values σ^2 and τ_c are calculated via direct numerical integration.

that when using HPA, correlations among spins build up during the time the nuclei are diffusing inside the box. As a consequence, the presence of slowly moving nuclei in the diamond vicinity may cause coherent polarization transfer; see Figure 4. This feature is not captured in our theoretical description, eq 2.

The polarization rate depends solely on N, σ^2, and τ_c, which are extensive parameters, which in turn depend on intensive quantities, namely, ρ_{oil}, the proton density in oil, $\mathcal{D}_{\mathrm{oil}}$ and z_0. Once $\{\rho_{\mathrm{oil}}, \mathcal{D}_{\mathrm{oil}}, z_0\}$ are fixed, the polarization curve is obtained directly by a numerical simulation, while the extensive parameters may be calculated via a numerical integration (Supporting Information) and then used as input for eq 3. Therefore, our model is without free fitting parameters.

For an experimental verification of our model, the polarization loss from two different NV centers was measured. It is observed via the fluorescence of the NV center after a spin-locking sequence matching the HHDR with the hydrogen nuclear spins. First, a single NV is optically polarized using a green laser (532 nm), followed by a MW $\pi/2$ pulse, which rotates the NV's electron spin phase-dependent to the $|+\rangle$ or $|-\rangle$ state in an alternating manner. Then, a suitable microwave field is applied in order to fulfill the HHDR condition. This MW pulse is phase-shifted by 90° and hence performs a spin-locking. During this period, the NV transfers its high polarization to the environment. A final $\pi/2$ pulse projects the NV center's spin state back to the z-axis, where it can be read-out optically. Depending on the occurrence of a spin flip, a bright or dark fluorescence signal is observed. In order to confirm the HHDR condition, one may perform the described experiment varying the driving frequency of the spin-locking pulse. The result of such a procedure is shown in Figure 3; it is

DOI: 10.1021/acs.nanolett.7b05175
Nano Lett. 2018, 18, 1882−1887

seen as the precise match of the dip in fluorescence at the hydrogen Larmor frequency, ω_N.

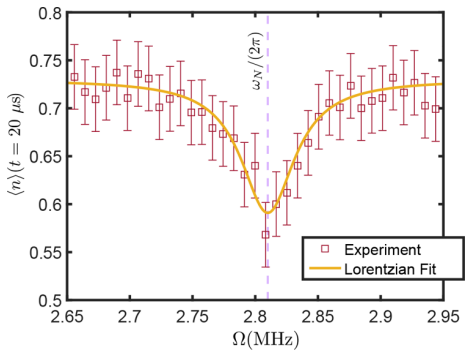


Figure 3. Population of a single NV center for different Rabi frequencies, Ω, and corresponding fitting curve. When the electronic spin is spin-locked with a driving field such that its Rabi frequency is similar to the Larmor frequency of the ^1H spins, ω_N, polarization transfer occurs giving origin to a pronounced dip in the spectrum. Conversely, when the NV center is driven out of resonance, the electronic spin solely suffers from $T_{1\rho}$ noise. {Shown data corresponds to $z_0^2 = 5.3$ nm, $\omega_N/2\pi = 2.81$ MHz, and spin-locking time $t = 20\ \mu$s. The error bars represent photon shot-noise (Supporting Information).}

The ^{12}C enriched diamond sample was grown by chemical vapor deposition with a low concentration of impurities ($^{12}C >$ 99.999%; nitrogen isotopes ≈ 5 ppb). A ^{12}C enriched diamond ensures a clear interpretation of the data, since the signal does not contain spurious noise from intrinsic ^{13}C in diamond.[34] These experiments would have been possible likewise with a natural abundance ^{13}C diamond. Nitrogen ions were implanted with a low energy and dose (2.5 keV and 10^8 ions/cm^2) such that experiments can be performed with shallow NV centers (here $z_0^1 = 3.2 \pm 0.2$ nm and $z_0^2 = 5.3 \pm 0.1$ nm[35]), ensuring strong coupling with near-surface nuclei. Immersion oil (Fluka Analytical 10976) is deposited on top of the diamond. A magnetic field of 660 G is applied parallel to the NV center quantization axis, resulting in a ^1H Larmor frequency $\omega_N/(2\pi)$ = 2.8 MHz, where the effective field generated by the NV center can be neglected. The Rabi frequency during the spin-locking pulse is adjusted to be resonant with ω_N, to allow electron spin−nuclear spin flip−flop processes. The experiments were performed on a home-built confocal microscope controlled with the Qudi software suite.[36]

Figure 4 shows the comparison between the measured polarization loss, which can be seen as change of the average population $\langle n\rangle$, the full numerical simulation based on Gaussian states, and the theoretical prediction from eq 3. In both cases, we observe polarization loss in a time scale of the order of μs. Off-resonant measurements reveal that environmental magnetic noise affecting the NV center manifests in similar time scales. These effects are included in our predictions by adding a relaxation term to the master equation proportional to $T_{1\rho}$[37] (Supporting Information).

The experimental data is well reproduced given the nominal $\mathcal{D}_{\text{oil}}$ for the used immersion oil, the measured NV depth, the proton density in oil at room temperature ρ_{oil} = 50 protons/nm^3, which is a typical value used for organic samples,[32,38] and the measured relaxation times, ($T_{1\rho}^1 = 11\ \mu$s, $T_{1\rho}^2 = 17\ \mu$s) (Supporting Information). For this density, the number of hydrogen spins in an interaction volume of 20^3 nm^3, which is taken as the volume of the simulation box, is $N \approx 4 \cdot 10^5$. (See the Supporting Information for details on the simulation technique.) Given the depths of the used NV centers ($z_0^1 = 3.2$ nm, $z_0^2 = 5.3$ nm) and the slow diffusion of the oil molecules ($\mathcal{D}_{\text{oil}} = 0.5$ nm$^2\ \mu$s^{-1}), the correlation time was numerically calculated (Supporting Information), obtaining $\tau_c^1 = 10\ \mu$s and $\tau_c^2 = 25\ \mu$s, respectively. As stated, for $\chi \gg 1$, the flip−flop dominates over flip−flip rate and other nonsecular terms

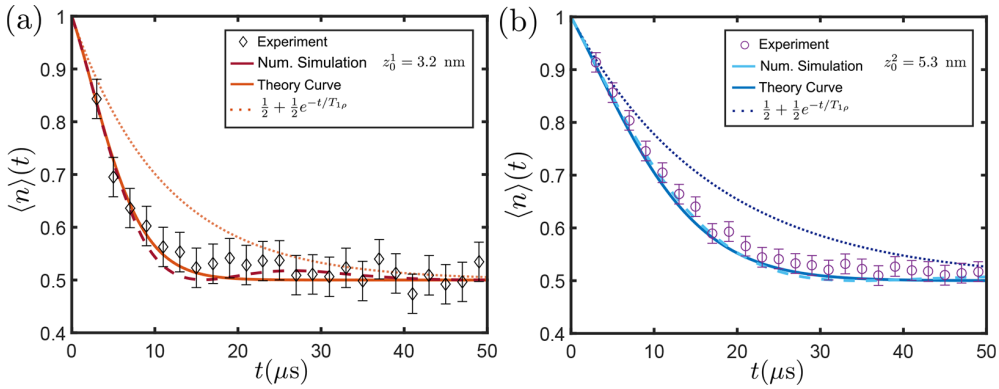


Figure 4. Measured polarization loss from two different NV centers compared with numerical and theoretical predictions. The qualitative behavior is well predicted by both theory and full numerical simulation. The polarization interchanged dictated by eq 3 happens in the same time scale as relaxation processes characterized by $T_{1\rho}$. The polarization loss attributable solely to relaxation is plotted as an exponential curve (dotted line) with rate $T_{1\rho}$. In all curves, an initial decay determined by $-t/T_{1\rho}$ is followed by a exponential tail, with rate $\left(\frac{1}{4}N\tau_c\sigma^2 + \frac{1}{T_{1\rho}}\right)$. (a) Results for the shallower NV center, $z_0^1 = 3.2$ nm. After an initial decay, at $t \approx 25\ \mu$s, numerical simulations reveal a coherent interchange of polarization between the NV center and slowly moving nuclei near the surface. This feature is not captured in our theoretical prediction. (b) Result for $z_0^2 = 5.3$ nm. For a deeper NV center, the polarization is better described by eq 3 with no traces of coherent transfer. {In the calculations, $\mathcal{D}_{\text{oil}} = 0.46$ nm$^2\ \mu$s^{-1}, $\rho_{\text{oil}} = 50$ spins/nm^3 have been used, which are directly estimated from the experimental conditions, together with the experimentally measured relaxation times $T_{1\rho}^1 = 11\ \mu$s and $T_{1\rho}^2 = 17\ \mu$s. The error bars represent photon shot-noise (Supporting Information).}

DOI: 10.1021/acs.nanolett.7b05175
Nano Lett. 2018, 18, 1882−1887

(Supporting Information); hence, the latter does not produce a significant effect.

Fast molecular motion effectively broadens the nuclear lines for the HHDR condition; hence, it confers to our scheme a certain robustness against frequency detunings when compared to DNP in solid samples. Typical sources of these detunings are fluctuations in the magnetic field or Rabi frequency errors. Also, we have exclusively considered particles in free-diffusion, which is an accurate description for molecules in bulk but may not describe molecular motion at the oil−diamond interface correctly. Nonetheless, as the majority of the nuclei inside the interaction volume move, the most relevant features for hyperpolarization protocols are well described solely by diffusive particles; traces from slowly moving particles will be seen only as secondary effects.

Indeed, as shown in Figure 4a, the electronic spin may undergo a coherent polarization transfer with the nuclei that diffuse in its immediate vicinity during the interrogation time, t. This coherent oscillation is depleted by nuclear diffusion; coherent effects would only dominate over net polarization transfer when the position of the nuclei is stationary and no diffusion takes place, that is, in rigid solids.

The good agreement between our model and the experimental data supports the hypothesis that the NV polarization loss in one single cycle mainly occurs due to polarization transfer to the ^1H nuclei and $T_{1\rho}$ relaxation. Therefore, the amount of transferred polarization is just a fraction of the total, $\alpha = \frac{1/\tau_p}{1/\tau_p + 1/T_{1\rho}}$, where $\tau_p^{-1} \equiv \frac{1}{4}N\tau_c\sigma^2$ is the polarization rate. In our setup, we obtain $\alpha \sim 80\%$ for both NV centers, indicating that transfer is efficient. Still, the average polarization gain per nuclei around the NV is $\frac{1}{2}\frac{1}{N}\alpha$, which is very small for a large N. Thus, significant nuclear polarization will only be achieved when the proposed protocol is repeated many times. That is, the NV center must be periodically reinitialized after a time τ_p.

Assuming a diamond sample with a moderate-high density of NV centers, such that the NV centers do not interact among them, a thin layer of oil of a few microns deposited onto its surface and typical nuclear relaxation time $T_{1n} \approx 1$ s,[39,40] the maximum achievable polarization per nuclei may be roughly estimated as $P_n \approx 10^{-3}$ (Supporting Information), which exceeds by several orders of magnitude the thermal nuclear polarization at this temperature and field $P_n^{Th} \approx 10^{-7}$. In addition, other DNP methods for hyperpolarization in solution and at room temperature, such as Overhauser DNP,[41,42] bear a theoretical limit for the maximum achievable polarization of $P_n \approx 10^{-4}$ (at B = 660 G), namely, 1 order of magnitude lower than the one reported here.

Besides, writing the dependence of the polarization rate explicitly as a function of the diffusion coefficient, proton density, and NV depth, one obtains that $\frac{1}{\tau_p} \propto \frac{\rho_{1H}}{z_0\mathcal{D}}$ (Supporting Information). Thus, making it easy to estimate the polarization rate for different solvents or NV samples.

In summary, we present a theoretical description of efficient polarization transfer from a shallow NV center to diffusive organic molecules above the diamond surface validated by experiments with an excellent agreement. The experimental results are explained qualitatively and quantitatively by both theoretical work and numerical simulations. We remark that our approach is easily extended to other scenarios such as polarization of macromolecules in low diffusive environments or polarization schemes using nanodiamonds. In fact, our model does not depend on any free parameters, and thus the polarization rate depends solely on the NV depth and the diffusion properties of the solvent. Also, the dynamical behavior at the liquid−solid interface may be examined with our description. Due to the fast diffusion of the nuclei, the direct detection of polarization remains a challenge that needs to be addressed in future work. In this direction, similar setups along with refine analysis techniques have been proved to make the NV center a high sensitive NMR detector.[43]

■ ASSOCIATED CONTENT

Supporting Information

The Supporting Information is available free of charge on the ACS Publications website at DOI: 10.1021/acs.nanolett.7b05175.

Full derivation of eq 3, simulation details on bosonization techniques, and experimental details (PDF)

■ AUTHOR INFORMATION

Corresponding Author

*E-mail: pelayo.fernandez@uni-ulm.de.

ORCID

P. Fernández-Acebal: 0000-0003-4520-3488

Notes

The authors declare no competing financial interest.

■ ACKNOWLEDGMENTS

This work was supported by an Alexander von Humboldt Professorship, the ERC Synergy grant BioQ, the EU projects HYPERDIAMOND and DIADEMS, the Volkswagenstifung and the Integrated Center for Quantum Science and Technology (IQST).

■ REFERENCES

(1) Bloch, F.; Hansen, W. W.; Packard, M. *Phys. Rev.* **1946**, *70*, 474−485.
(2) Purcell, E. M.; Torrey, H. C.; Pound, R. V. *Phys. Rev.* **1946**, *69*, 37−38.
(3) Wu, Y.; Jelezko, F.; Plenio, M. B.; Weil, T. *Angew. Chem., Int. Ed.* **2016**, *55*, 6586−6598.
(4) Waldherr, G.; Beck, J.; Steiner, M.; Neumann, P.; Gali, A.; Frauenheim, T.; Jelezko, F.; Wrachtrup, J. *Phys. Rev. Lett.* **2011**, *106*, 157601.
(5) Chen, Q.; Schwarz, I.; Jelezko, F.; Retzker, A.; Plenio, M. B. *Phys. Rev. B: Condens. Matter Mater. Phys.* **2015**, *92*, 184420.
(6) Chen, Q.; Schwarz, I.; Jelezko, F.; Retzker, A.; Plenio, M. B. *Phys. Rev. B: Condens. Matter Mater. Phys.* **2016**, *93*, 060408.
(7) Abrams, D.; Trusheim, M. E.; Englund, D. R.; Shattuck, M. D.; Meriles, C. A. *Nano Lett.* **2014**, *14*, 2471−2478.
(8) Ardenkjær-Larsen, J. H.; Fridlund, B.; Gram, A.; Hansson, G.; Hansson, L.; Lerche, M. H.; Servin, R.; Thaning, M.; Golman, K. *Proc. Natl. Acad. Sci. U. S. A.* **2003**, *100*, 10158−10163.
(9) Joo, C.; Hu, K.; Bryant, J. A.; Griffin, R. G. *J. Am. Chem. Soc.* **2006**, *128*, 9428−9432.
(10) van Bentum, P.; Sharma, M.; van Meerten, S.; Kentgens, A. *J. Magn. Reson.* **2016**, *263*, 126−135.
(11) Wiśniewski, D.; Karabanov, A.; Lesanovsky, I.; Köckenberger, W. *J. Magn. Reson.* **2016**, *264*, 30−38.
(12) Hartmann, S. R.; Hahn, E. L. *Phys. Rev.* **1962**, *128*, 2042.
(13) Cai, J.; Jelezko, F.; Plenio, M.; Retzker, A. *New J. Phys.* **2013**, *15*, 013020.

DOI: 10.1021/acs.nanolett.7b05175
Nano Lett. 2018, 18, 1882−1887

(14) Viola, L.; Lloyd, S. *Phys. Rev. A: At., Mol., Opt. Phys.* **1998**, *58*, 2733−2744.
(15) Xu, X.; Wang, Z.; Duan, C.; Huang, P.; Wang, P.; Wang, Y.; Xu, N.; Kong, X.; Shi, F.; Rong, X.; Du, J. *Phys. Rev. Lett.* **2012**, *109*, 070502.
(16) Facchi, P.; Lidar, D.; Pascazio, S. *Phys. Rev. A: At., Mol., Opt. Phys.* **2004**, *69*, 032314.
(17) Fanchini, F.; Hornos, J.; Napolitano, R. *Phys. Rev. A: At., Mol., Opt. Phys.* **2007**, *75*, 022329.
(18) Gordon, G.; Kurizki, G.; Lidar, D. A. *Phys. Rev. Lett.* **2008**, *101*, 010403.
(19) Timoney, N.; Baumgart, I.; Johanning, M.; Varon, A. F.; Plenio, M. B.; Retzker, A.; Wunderlich, C. *Nature* **2011**, *476*, 185−188.
(20) Webster, S.; Weidt, S.; Lake, K.; McLoughlin, J.; Hensinger, W. *Phys. Rev. Lett.* **2013**, *111*, 140501.
(21) Aharon, N.; Drewsen, M.; Retzker, A. *Phys. Rev. Lett.* **2013**, *111*, 230507.
(22) London, P.; Scheuer, J.; Cai, J.-M.; Schwarz, I.; Retzker, A.; Plenio, M. B.; Katagiri, M.; Teraji, T.; Koizumi, S.; Isoya, J.; Fischer, R.; McGuinness, L. P.; Naydenov, B.; Jelezko, F. *Phys. Rev. Lett.* **2013**, *111*, 067601.
(23) Scheuer, J.; Schwartz, I.; Chen, Q.; Schulze-Sünninghausen, D.; Carl, P.; Höfer, P.; Retzker, A.; Sumiya, H.; Isoya, J.; Luy, B.; Plenio, M.; Naydenov, B.; Jelezko, F. *New J. Phys.* **2016**, *18*, 013040.
(24) Scheuer, J.; Schwartz, I.; Müller, S.; Chen, Q.; Dhand, I.; Plenio, M.; Naydenov, B.; Jelezko, F. *Phys. Rev. B: Condens. Matter Mater. Phys.* **2017**, *96*, 174436.
(25) Wood, J.; Tetienne, J.; Broadway, D.; Hall, L.; Simpson, D.; Stacey, A.; Hollenberg, L. *Nat. Commun.* **2017**, *8*, 15950.
(26) Holstein, T.; Primakoff, H. *Phys. Rev.* **1940**, *58*, 1098−1113.
(27) Staudacher, T.; Raatz, N.; Pezzagna, S.; Meijer, J.; Reinhard, F.; Meriles, C.; Wrachtrup, J. *Nat. Commun.* **2015**, *6*, 8527.
(28) Kong, X.; Stark, A.; Du, J.; McGuinness, L.; Jelezko, F. *Phys. Rev. Appl.* **2015**, *4*, 024004.
(29) Christ, H.; Cirac, J. I.; Giedke, G. *Phys. Rev. B: Condens. Matter Mater. Phys.* **2007**, *75*, 155324.
(30) Plenio, M.; Hartley, J.; Eisert, J. *New J. Phys.* **2004**, *6*, 36.
(31) Eisert, J.; Plenio, M. *Int. J. Quantum Inf.* **2003**, *1*, 479−506.
(32) Staudacher, T.; Shi, F.; Pezzagna, S.; Meijer, J.; Du, J.; Meriles, C. A.; Reinhard, F.; Wrachtrup, J. *Science* **2013**, *339*, 561−563.
(33) Gardiner, C. W. *Handbook of stochastic methods*; Springer: Berlin, 1985; Vol. 3.
(34) Loretz, M.; Boss, J.; Rosskopf, T.; Mamin, H.; Rugar, D.; Degen, C. *Phys. Rev. X* **2015**, *5*, 021009.
(35) Pham, L. M.; DeVience, S. J.; Casola, F.; Lovchinsky, I.; Sushkov, A. O.; Bersin, E.; Lee, J.; Urbach, E.; Cappellaro, P.; Park, H.; Yacoby, A.; Lukin, M.; Walsworth, R. L. *Phys. Rev. B: Condens. Matter Mater. Phys.* **2016**, *93*, 045425.
(36) Binder, J. M.; Stark, A.; Tomek, N.; Scheuer, J.; Frank, F.; Jahnke, K. D.; Müller, C.; Schmitt, S.; Metsch, M. H.; Unden, T.; Gehring, T.; Huck, A.; Andersen, U.; Rogers, L. J.; Jelezko, F. *SoftwareX* **2017**, *6*, 85−90.
(37) Slichter, C. P. *Principles of Magnetic Resonance*; Springer Science & Business Media, 1990; Vol. 1.
(38) Meriles, C. A.; Jiang, L.; Goldstein, G.; Hodges, J. S.; Maze, J.; Lukin, M. D.; Cappellaro, P. *J. Chem. Phys.* **2010**, *133*, 124105.
(39) Fullerton, G.; Potter, J.; Dornbluth, N. *Magn. Reson. Imaging* **1982**, *1*, 209−226.
(40) Shapiro, Y. E. *Prog. Polym. Sci.* **2011**, *36*, 1184−1253.
(41) Overhauser, A. *Phys. Rev.* **1953**, *92*, 411.
(42) Armstrong, B. D.; Lingwood, M.; McCarney, E.; Brown, E.; Blümler, P.; Han, S. *J. Magn. Reson.* **2008**, *191*, 273−281.
(43) Schwartz, I.; Rosskopf, J.; Schmitt, S.; Tratzmiller, B.; Chen, Q.; McGuinness, L.; Jelezko, F.; Plenio, M. *arXiv preprint arXiv:1706.07134*, **2017**.

DOI: 10.1021/acs.nanolett.7b05175
Nano Lett. 2018, 18, 1882−1887

Supporting Information: Toward Hyperpolarization of Oil Molecules via Single Nitrogen Vacancy Centers in Diamond

P. Fernández-Acebal,[*,†] O. Rosolio,[‡] J. Scheuer,[¶] C. Müller,[¶] S. Müller,[¶] S. Schmitt,[¶] L.P. McGuinness,[¶] I. Schwarz,[†] Q. Chen,[†] A. Retzker,[‡] B. Naydenov,[¶] F. Jelezko,[¶] and M.B. Plenio[†]

†*Institut für Theoretische Physik and Center for Integrated Quantum Science and Technology (IQST), Universität Ulm, Albert-Einstein Allee 11, 89069 Ulm, Germany*

‡*Racah Institute of Physics, The Hebrew University of Jerusalem, Jerusalem, 91904 Givat Ram, Israel*

¶*Institute for Quantum Optics and Center for Integrated Quantum Science and Technology (IQST), Universität Ulm, Albert-Einstein Allee 11, 89069 Ulm, Germany*

E-mail: pelayo.fernandez@uni-ulm.de

Hamiltonian Derivation

Our system consists of one electronic spin, the NV center, coupled to a set of N nuclear $\frac{1}{2}-$spins via dipole-dipole magnetic interaction. The general Hamiltonian for such a system has the form ($\hbar = 1$)

$$H = \omega_s \sigma_z + \sum_{i=1}^{N} \gamma_N \mathbf{B}\mathbf{I}^i + \sum_i f_i(\mathbf{r}_i(t)) \left[\sigma \mathbf{I}^i - 3\left(\sigma \hat{\mathbf{r}}_i(t)\right)\left(\mathbf{I}^i \hat{\mathbf{r}}_i(t)\right)\right], \tag{1}$$

where ω_s is the Zeeman splitting of the electronic spin, σ are the spin operators of the NV spin, which is spin-1, γ_N is the gyromagnetic ratio of the nuclei, $\mathbf{B}$ is an external magnetic field, $\mathbf{I}_i$ represent the spin operators of the nuclear spins, $f_i(\mathbf{r}_i(t)) \equiv \frac{\mu_0 \gamma_e \gamma_N}{4\pi \mathbf{r}_i^3}$, is the dipole-dipole force strength which depends on the relative position between the NV center and the $i-th$ nucleus, $\mathbf{r}_i$, the gyromagnetic ratios of the electron and nuclear spins γ_e,γ_N and the vacuum permeability μ_0 , and $\hat{\mathbf{r}}^i$ is the unitary vector joining the NV center with the $i-th$ nuclear spin. Interactions between the nuclear spins have been neglected since their effects are averaged out by the fast stochastic motion.

The nuclear spins move following a Brownian motion, which in turns make the dipole-dipole interaction to be a stochastic variable with certain correlation time τ_c. In our set-up, we consider that the particles move slowly enough such that $\omega_s \tau_c \gg 1$ and $\gamma_N |\mathbf{B}| \tau_c \gg 1$. In this regime, we can perform a secular approximation owning to the fact that $\omega_s \gg \gamma_N |\mathbf{B}|$, obtaining

$$H = \omega_s \sigma_z + \sum_{i=1}^{N} \gamma_N \mathbf{B} \mathbf{I}^i + \sigma_z \sum_i \mathbf{A}^i \left(\mathbf{r}_i(t)\right) \mathbf{I}_i. \tag{2}$$

With $\mathbf{A}^i(\mathbf{r}_i(t)) = f_i(\mathbf{r}_i(t)) \left(3\hat{x}_i\hat{z}_i, 3\hat{y}_i\hat{z}_i, 1 - 3\hat{z}_i^2\right)$ the so-called hyperfine vector. If now a resonant microwave field resonant with the NV $m_s = 0 \rightarrow m_s = -1$ transition is applied, $H_{\mathrm{MW}} = \Omega \sigma_x \cos(\omega_s t)$, the Hamiltonian in the frame rotating with ω_s reads

$$H = \Omega S_z + \sum_i^N \left(\gamma_N \mathbf{B} - \frac{1}{2} A_z^i(t)\right) \mathbf{I}^i + S_x \sum_i \mathbf{A}_i \left(\mathbf{r}_i(t)\right) \mathbf{I}_i. \tag{3}$$

We have introduced $\mathbf{S}$ as the NV spin operator in the dressed state basis, $S_z = \frac{1}{2}\left(|+\rangle\langle+| - |-\rangle\langle-|\right)$, $S_+ = |+\rangle\langle-|$ and $S_- = S_+^\dagger$.

In the Hartmann-Hahn double resonance (HHDR) scheme, the Rabi frequency Ω is set resonant with the nuclear Larmor frequency $\omega_N \equiv \gamma_N |\mathbf{B}|$. Working with a high magnetic field such that $\Omega, \omega_N \gg |\mathbf{A}_i| \, \forall i$, and given that $\omega_N \tau_c \gg 1$ is also fulfilled in our set-up, we neglect fast oscillating terms together with magnetic field misalignment caused by $A_z^i(t)$,

obtaining

$$H = \Omega S_z + \sum_i^N \omega_N I_z^i + \sum_i^N g_i(t) S_+ I_-^i + g_i(t)^* S_- I_+^i. \tag{4}$$

with $g_i(t) = \frac{1}{4}\left(A_x^i(t) + \mathrm{i}A_y^i(t)\right)$. This Hamiltonian corresponds to Eq.(1) in the main text.

Master Equation derivation

In this section we derive the master equation that describes the whole system and, in particular, the dynamical evolution of the NV polarization $\langle n \rangle (t) = \frac{1}{2} + \mathrm{Tr}\left(\rho S_z\right)$. In these derivations we treat both classical and quantum noises for a multiparticle system, which extends previous results in this field.[1,2]

In order to have a more complete description we start with a Hamiltonian that consists of both flip-flop and flop-flop terms. For doing so, we rewrite the interaction Hamiltonian, $H_{int} = \sum_i^N g_i(t) S_+ I_-^i + g_i^*(t) S_- I_+^i$, in the interaction picture with respect to the energy part $H_\omega \equiv \Omega S_z + \sum_i \omega_N I_z^i$, obtaining

$$\tilde{H} \equiv e^{-\mathrm{i}H_\omega t} H_{int} e^{\mathrm{i}H_\omega t} = \sum_{i=1}^N g_i(t) L^i e^{-\mathrm{i}\Delta t} + g_i^*(t) L^{i\dagger} e^{\mathrm{i}\Delta t} + g_i(t) O^i e^{-\mathrm{i}\omega' t} + g_i^*(t) O^{i\dagger} e^{\mathrm{i}\omega' t}. \tag{5}$$

Where $L^i \equiv S_+ I_-^i$, $O^i \equiv S_+ I_+^i$ and $\Delta = \Omega - \omega_N$, $\omega' = \Omega + \omega_N$. For the sake of simplicity, we set $\Delta = 0$, that is, we assume the HHDR condition is always fulfilled and thus, $\omega' = 2\Omega$. Next, this Hamiltonian may be split into a time-independent and a time-dependent stochastic part as

$$\tilde{H}_0(t) = \sum_{i=1}^{N} \langle g \rangle \, L^i + \langle g^* \rangle \, L^{i\dagger} + \langle g \rangle \, O^i e^{-\mathrm{i}2\Omega t} + \langle g^* \rangle \, O^{i\dagger} e^{\mathrm{i}2\Omega t}. \tag{6}$$

$$\tilde{H}_1(t) = \sum_{i=1}^{N} \xi_i(t) L^i + \xi_i^*(t) L^{i\dagger} + \xi_i(t) O^i e^{-\mathrm{i}2\Omega t} + \xi_i^*(t) O^{i\dagger} e^{\mathrm{i}2\Omega t}. \tag{7}$$

Where $\langle g \rangle$ is the average of $g_i(t)$ over all possible stochastic trajectories and $\xi_i(t) = g_i(t) - \langle g \rangle = \frac{1}{4}\xi_x^i(t) + \mathrm{i}\frac{1}{4}\xi_y^i(t)$ are the stochastic fluctuations around the average, with $\xi_\alpha^i(t) = A_\alpha^i(t) - \langle A_\alpha^i \rangle$. Note that for $\tilde{H}_0$ we can neglect fast rotating terms obtaining

$$\tilde{H}_0 \approx \sum_{i=1}^{N} \langle g \rangle \, L^i + \langle g^* \rangle \, L^{i\dagger}, \tag{8}$$

which is a time independent Hamiltonian. The master equation, also in the interaction picture with respect to H_ω reads

$$\frac{\partial}{\partial t}\tilde{\rho} = \mathcal{L}\tilde{\rho} = \left(\mathcal{L}_0 + \mathcal{L}_1(t)\right)\tilde{\rho}, \tag{9}$$

where we have introduced the Liouvillian operators $\mathcal{L}_i \equiv -\mathrm{i}\left[\tilde{H}_i, \cdot\right]$. We look to the average density matrix over all possible stochastic trajectories, $\langle \tilde{\rho} \rangle$, which obeys

$$\frac{\partial}{\partial t}\langle \tilde{\rho} \rangle = \langle \left(\mathcal{L}_0 + \mathcal{L}_1(t)\right)\tilde{\rho} \rangle \, . \tag{10}$$

In order to obtain a proper master equation for $\langle \tilde{\rho} \rangle (t)$ we follow.[3–5] We start taking an interaction picture with respect to $\mathcal{L}_0$ in Eq.(9) obtaining

$$\frac{\partial}{\partial t}\tilde{\rho}^{(0)} = \mathcal{L}_1^{(0)}(t)\tilde{\rho}^{(0)} \tag{11}$$

Note that by $\cdot^{(0)}$ it is indicated that the operators are in the interaction picture with respect to $\mathcal{L}_0$. The formal solution to the last equation is simply

$$\tilde{\rho}^{(0)}(t) = \mathcal{T} \exp\left(\int_0^t \mathcal{L}_1^{(0)}(\tau) d\tau\right) \tilde{\rho}^{(0)}(0), \tag{12}$$

where $\mathcal{T}$ represents the time ordering. Taking now the average over all possible stochastic trajectories we arrive to

$$\left\langle \tilde{\rho}^{(0)} \right\rangle (t) = \left\langle \mathcal{T} \exp\left(\int_0^t \mathcal{L}_1^{(0)}(\tau) d\tau\right) \right\rangle \tilde{\rho}^{(0)}(0). \tag{13}$$

We note that in our case the system is found always in the same initial state $\tilde{\rho}^{(0)}(0)$. Writing it explicitly, that is, making explicit the action of $\mathcal{T}$, the latter equation reads

$$\left\langle \tilde{\rho}^{(0)} \right\rangle (t) = \left[1 + \int_0^t dt_1 \left\langle \mathcal{L}_1^{(0)}(t_1) \right\rangle + \int_0^t dt_1 \int_0^{t_1} dt_2 \left\langle \mathcal{L}_1^{(0)}(t_1) \mathcal{L}_1^{(0)}(t_2) \right\rangle + \cdots \right] \tilde{\rho}^{(0)}(0). \tag{14}$$

Taking the time derivate in both sides leads us to

$$\frac{\partial}{\partial t} \left\langle \tilde{\rho}^{(0)} \right\rangle (t) = \left[\left\langle \mathcal{L}_1^{(0)}(t) \right\rangle + \int_0^t dt_1 \left\langle \mathcal{L}_1^{(0)}(t) \mathcal{L}_1^{(0)}(t_1) \right\rangle + \cdots \right] \tilde{\rho}^{(0)}(0). \tag{15}$$

In order to arrive to a master equation for the average density matrix the only thing needed is to invert Eq.(14), so we can express $\tilde{\rho}^{(0)}(0)$ in terms of $\left\langle \tilde{\rho}^{(0)} \right\rangle (t)$. Introducing the expression for the initial density matrix into the last equation we finally obtain

$$\frac{\partial}{\partial t} \left\langle \tilde{\rho}^{(0)} \right\rangle = \sum_n k_n \left\langle \tilde{\rho}^{(0)} \right\rangle \tag{16}$$

where the operators k_n are defined as

$$k_n = \int_0^t dt_1 \int_0^{t_1} dt_2 \cdots \int_0^{t_{n-2}} dt_{n-1} \left\langle \left\langle \mathcal{L}_1^{(0)}(t) \mathcal{L}_1^{(0)}(t_1) \mathcal{L}_1^{(0)}(t_2) \cdots \mathcal{L}_1^{(0)}(t_{n-1}) \right\rangle \right\rangle_c . \tag{17}$$

In the last expression we have used the brackets with subscript $\langle\langle \cdots \rangle\rangle\, c$ to denote ordered cumulants.[4]

We note that $\mathcal{L}_1$ is composed of a sum of N independent random variables, $\xi_i(t)$, with identical average properties, $\langle \xi_i \rangle = \langle \xi_j \rangle \equiv \langle \xi \rangle \ \forall i$. Due to the fact that for independent random variables all cross-cumulants vanish, each cumulant $\langle\langle \mathcal{L}_1(t) \cdots \mathcal{L}_1(t_{m-1}) \rangle\rangle_c$ is linear with N. A rough analysis of the $4-th$ cumulant allow us to make a prediction on the magnitude of the $n-th$ cumulant. For instance

$$\Big\langle\Big\langle \mathcal{L}_1^{(0)}(0)\mathcal{L}_1^{(0)}(0)\mathcal{L}_1^{(0)}(0)\mathcal{L}_1^{(0)}(0) \Big\rangle\Big\rangle_c \sim N \left\langle\left\langle \xi^4 \right\rangle\right\rangle_c = N\Big[\left\langle \xi^4 \right\rangle - 3 \left\langle \xi^2 \right\rangle^2 \Big]. \tag{18}$$

Note that in our notation the single bracket, $\langle \cdots \rangle$ represents the moment and not the cumulant. These terms can be found by explicit integration over the interaction volume

$$N \left\langle\left\langle \xi^4 \right\rangle\right\rangle_c = \left\langle \xi^4 \right\rangle - 3 \left\langle \xi^2 \right\rangle^2 = N\Big[\frac{1}{V}\int_V \xi^4 d\mathbf{r} - 3\frac{1}{V^2}\Big(\int_V \xi^2 d\mathbf{r}\Big)^2\Big] = \rho \int_V \xi^4 d\mathbf{r} - 3\frac{\rho}{V}\Big(\int_V \xi^2 d\mathbf{r}\Big)^2. \tag{19}$$

Since the interaction fluctuations $\langle \xi_i \rangle$ decay with the distance, taking $V \to \infty$, we can see that the $4-th$ cumulant is proportional to the $4-th$ order moment. This analysis holds for every order, as will be explained in the next section. Therefore, we take the second order of the expansion as leading order. The general solution for the master equation in the non-interaction picture with respect to $\mathcal{L}_0$, becomes

$$\frac{\partial}{\partial t} \langle \tilde{\rho} \rangle = \left[\mathcal{L}_0 + \int_0^t \left\langle\left\langle \mathcal{L}_1(t) e^{t\mathcal{L}_0} \mathcal{L}_1(t-\tau) \right\rangle\right\rangle_c e^{-t\mathcal{L}_0} d\tau \right] \langle \tilde{\rho} \rangle \,. \tag{20}$$

Now, under the assumption that $|\mathcal{L}_0|\tau_c \ll 1$, with τ_c the correlation time (see following section for an accurate definition), we approximate $e^{\pm\mathcal{L}_0} \approx 1$. This assumption is equivalent to $\sqrt{N}\,\langle g \rangle\, \tau_c \ll 1$, which is fulfilled in our set-up (see bellow). In our regime, the fluctuations are larger than the average value $\langle g \rangle$. In the following, we use that by definition $\langle \mathcal{L}_1(t) \rangle = 0$, obtaining

$$\frac{\partial}{\partial t}\left\langle \tilde{\rho}\right\rangle =\left[\mathcal{L}_{0}+\int_{0}^{t}\left\langle \mathcal{L}_{1}(t)\mathcal{L}_{1}(t-\tau)\right\rangle d\tau\right]\left\langle \tilde{\rho}\right\rangle . \tag{21}$$

We recall that this is a second order approximation in terms of $\left\langle {\xi_{\alpha}^{i}}^{n}\right\rangle \tau_{c}^{n-1}$, and thus, as we keep the cumulants till second order this approximation is valid for times $t\ll\tau_{c}/\left(N\left\langle {\xi_{\alpha}^{i}}^{3}\right\rangle \tau_{c}^{3}\right)$. The action of the correlator on the density matrix gives

$$\begin{aligned}\int_{0}^{t}\left\langle \mathcal{L}_{1}(t)\mathcal{L}_{1}(t-\tau)\right\rangle d\tau\left\langle \tilde{\rho}\right\rangle =\frac{1}{4}\gamma(0,t)\sum_{i=1}^{N}\left[D\left(L^{i}\right)+D\left(L^{i\dagger}\right)\right]\left\langle \tilde{\rho}\right\rangle +\\ \frac{1}{4}\gamma(2\Omega,t)\sum_{i=1}^{N}\left[D\left(O^{i}\right)+D\left(O^{i\dagger}\right)\right]\left\langle \tilde{\rho}\right\rangle .\end{aligned} \tag{22}$$

Where $D(\cdot)$ denotes the Lindblad superoperator, whose action on the density matrix is simply

$$D(A)\left\langle \tilde{\rho}\right\rangle =A\left\langle \tilde{\rho}\right\rangle A^{\dagger}-\frac{1}{2}\left\{A^{\dagger}A,\left\langle \tilde{\rho}\right\rangle \right\}, \tag{23}$$

where A is a given operator. In Eq.(22) all the fast oscillating terms have been neglected. We remark that since the particles move independently then $\xi_{i}(t)$ are independent random variables and thus, we have used that $\left\langle \xi_{\alpha}^{i}(\tau)\xi_{\beta}^{j}(0)\right\rangle =\left\langle \xi_{\alpha}^{i}(\tau)\xi_{\alpha}^{i}(0)\right\rangle \delta_{\alpha,\beta}\delta_{i,j}$. Also, as the diffusion is homogeneous, the correlation function does not depend on the direction of the hyperfine vector, α, or on the particle, i, $\left\langle \xi_{\alpha}^{i}(\tau)\xi_{\alpha}^{i}(0)\right\rangle \equiv\left\langle \xi(\tau)\xi(0)\right\rangle$. Moreover, we have introduced

$$\gamma(\omega,t)=\int_{0}^{t}\left\langle \xi_{\alpha}^{i}(\tau)\xi_{\alpha}^{i}(0)\right\rangle \cos\left(\omega\tau\right)d\tau. \tag{24}$$

Note that for $t\gg\tau_{c}$, with τ_{c} the correlation time, the upper limit of the integral may be extended to infinity, obtaining $\lim_{t\to\infty}\gamma_{\alpha}(\omega,t)=\frac{1}{2}S_{\alpha}(\omega)$, with $S(\omega)$ the spectral density function of $\xi_{\alpha}^{i}(t)$. A net polarization transfer is only possible if flip-flop induced relaxation

predominates over all the other effects. That is, $S(2\Omega)/S(0) \ll 1$. For a Lorentzian spectral density this condition translates into $\chi \equiv \Omega\tau_c \gg 1$. In our set-up $\tau_c \approx 10\,\mu$s, $\omega_N = 2.8\,$MHz, so $S(2\Omega)/S(0) \approx 10^{-4}$, that means that flip-flip terms may be neglected. In fact, following similar calculations other relaxations mechanisms related to Hamiltonian terms such as $S_\pm I_z^i$ or $\mathbb{I} \otimes \mathbf{I}^i$, may be neglected when $\Omega\tau_c \gg 1$.

Taking all mentioned conditions into account, the effective master equation back in the Schrödinger picture reads

$$\frac{\partial}{\partial t}\langle\rho\rangle = \langle\dot{\rho}\rangle = -\mathrm{i}\left[H_0, \langle\rho\rangle\right] + \frac{1}{4}\gamma(t)\sum_{i=1}^{N} D\left(S_+ I_-^i\right)\langle\rho\rangle + D\left(S_- I_+^i\right)\langle\rho\rangle\,, \tag{25}$$

which is a master equation in Lindblad form with time dependent coefficient $\gamma(t) \equiv \gamma(0,t)$. The action of Eq. (25) is well understood. There are two main contributions. On the one hand, a Hamiltonian part, H_0, whose principal effect is a coherent transfer of polarization between the NV center and the nuclear spins. On the other hand, the Lindbladian term that generates an irreversible polarization transfer towards the nuclei caused by the stochastic motion.

In order to obtain a close equation for the population transfer, we first analyze the coherent part of the dynamics ruled by H_0, this will allow us to perform a Born approximation that will be fundamental for our following approach. First, we take a look into the form of H_0

$$H_0 = \Omega S_z + \sum_{i=1}^{N}\langle\omega\rangle I_z^i + \sum_{i=1}^{N}\langle g\rangle S_+ I_-^i + \langle g\rangle^* S_- I_+^i. \tag{26}$$

It corresponds to the Hamiltonian of a single NV center interacting with a solid bath of N nuclear spins, all of them with the same energy splitting $\langle\omega\rangle$ and with the same coupling strength $\langle g\rangle$. We recall, $\langle\cdots\rangle$ is the average over the stochastic trajectories of the nuclei. More specifically, this solid bath is composed by the N spins that are enclosed in certain NV interaction volume V. As the nuclei diffuse rapidly in the whole space, we assume that they

only spend certain time τ_B inside the NV interaction volume V. This τ_B may be seen as the time that a particle needs to leave the interaction volume and thus, being replaced by some other particle. Therefore, the coherent evolution caused by H_0 takes place in a scale marked by $\sqrt{N}|\langle g\rangle|\tau_B$. Assuming that $\tau_B \approx \frac{1}{6}\frac{V^{2/3}}{\mathcal{D}_{oil}} \approx \tau_c$, where $\mathcal{D}_{oil}$ is the diffusion coefficient, and $V = L^3$ with $L \approx 2\,z_0$, we obtain for our set-up $\sqrt{N}|\langle g\rangle|\tau_B \approx 0.1 - 0.01 < 1$, depending on whether we use a shallow NV center, $z_0^1 = 3.2\,\text{nm}$ or a deeper NV, $z_0^2 = 5.3\,\text{nm}$. This condition is equivalent as being in the weak-coupling regime with the bath as described by.[5] Consequently, considering a time axis with time intervals larger than $\tau_c \approx \tau_B$, we can rewrite the average density matrix as

$$\langle\rho\rangle = \langle\rho\rangle_{NV} \otimes \rho_B, \tag{27}$$

where ρ_{NV} is the average density matrix for the NV center while ρ_B is the density matrix of the bath, which corresponds to a thermal state. We remark the latter equation is usually referred to as the Born approximation. This factorization of the density matrix allows us to trace out the nuclear spin space, obtaining a master equation solely for ρ_{NV}

$$\dot{\langle\rho\rangle}_{NV} = -\mathrm{i}[\Omega S_z, \langle\rho\rangle_{NV}] + \frac{1}{4}N\gamma(t)\left[\langle n\rangle_B D(S_+) + (1-\langle n\rangle_B)D(S_-)\right]\langle\rho\rangle_{NV}\,. \tag{28}$$

with $\langle n\rangle_B$ is the average population of the spins in the bath. Moreover, we can derive the evolution equation for the NV population $\langle n\rangle = \frac{1}{2} + \mathrm{Tr}\left(S_z\langle\rho\rangle_{NV}\right)$, obtaining

$$\dot{\langle n\rangle} + N\frac{1}{4}\gamma(t)\langle n\rangle = N\frac{1}{4}\gamma(t)\langle n\rangle_B\,. \tag{29}$$

This equation corresponds to Eq.(4) in the main text. We recall that this approximation is only valid for times $t \ll \tau_c/(N\langle\xi^3\rangle\tau_c^3) \approx 100\,\mu\text{s}$ and $t \ll \tau_B\frac{1}{(\sqrt{N}\langle g\rangle\tau_B)^2} \approx 100\,\mu s$.

Relaxation of spin system

The measured data reveals that the NV center is affected by some environmental noise. Namely, this noise will make the NV center lose its polarization at a given rate. Normally, when the spin is driven and we are in the dressed state bases this rate is called $T_{1\rho}$.[6] Including these effects in our approach is straightforwardly done by adding a dissipation term to the master equation Eq.(28). Obtaining

$$\dot{\langle\rho\rangle}_{NV} = -\mathrm{i}[\Omega S_z, \langle\rho\rangle_{NV}] + \frac{1}{4}N\gamma(t)\left[\langle n\rangle_B D(S_+) + (1-\langle n\rangle_B)D(S_-)\right]\langle\rho\rangle_{NV} + \frac{1}{2}\frac{1}{T_{1\rho}}\left[D(S_+)+D(S_-)\right]\langle\rho\rangle_{NV}. \tag{30}$$

This equation allow us to include the effects of $T_{1\rho}$ in our analysis and thus, have a complete perspective of the NV dynamics.

Hyperfine vector analysis

In the previous section we have seen the polarization dynamics is mainly determined by $\gamma(t) = \int \langle\xi(\tau)\xi(0)\rangle\, d\tau$. Despite the simple description of the nuclear trajectories, since they move in free-diffusion, a detailed analytical description of $\xi^i_\alpha(t)$ turns to be complicated. Aiming to derive an analytical solution for Eq. (29) we make two assumptions: i) Higher moments are negligible when compared to the average and variance, which is a necessary condition for Eq.(21). ii) The correlations are well approximated by an exponential curve.

The former assumption justifies the validity of using cumulants up to order two in the cumulant expansion performed in the previous section. We recall, that even in the absence of a correlation time, the $n-th$ order cumulant contribution is of order $\langle\xi^n\rangle\, t^{n-1}$.[4] In this case, we evaluate this time, t as the time in which most of the NV polarization is transferred to the nuclear spins. This can be estimated by: i) simulation of the system, and ii) evaluating this time assuming the second order is correct and then check for self-consistency. Both

methods yield the same time. Using the second method, the time for polarization should be - $\frac{1}{\langle \xi^2 \rangle \tau_c N} \sim 10\mu s$. Numerical calculations suggest that indeed, the second term may be taken as the leading term and higher order terms decay exponentially with n. Numerical calculations are shown in Fig.(S1).

With regard to the correlation profile, we numerically calculate the normalized correlation function. The result is depicted in Fig.(S1). We see the correlation decay fast for short times and presents a heavy tail for larger times. In our set-up, nuclei interact with the NV center for a short-time before diffusing away and being reinitialize. Within this short-time interval an exponential decay accurately fits the numerical calculated correlation function. This approximation results in being accurate when tested against full numerical simulation with HPA, see Fig.(S3).

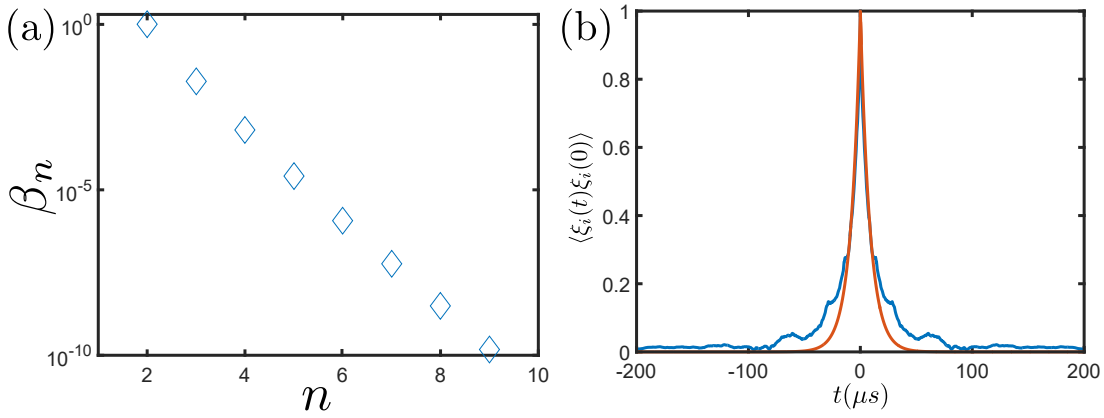


Figure S1: (a) Normalized contribution of the $n-th$ moment with respect to $\langle \xi^2 \rangle$, $\beta_n \equiv \frac{\langle \xi^n \rangle t^{n-1}}{\langle \xi^2 \rangle t}$. It decays rapidly with n, permitting us to accurately describe $\xi^i_\alpha(t)$ making use solely of its first and second moment. (b) Correlation profile of $\xi^i_\alpha(t)$ with an exponential fit.

Correlation function calculation

The correlation function of the coupling coefficient between the NV and each individual spin is important for determining the polarization rate. When the process is stationary, the correlation function is given by -

$$\langle \xi^i_\alpha(t)\xi^i_\alpha(0)\rangle = \int \xi^i_\alpha(\vec{r}_2;t)\xi^i_\alpha(\vec{r}_1;0)\rho(\vec{r}_2;t|\vec{r}_1;0)\rho(\vec{r}_1;0)d^3\vec{r}_1 d^3\vec{r}_2. \tag{31}$$

with $\xi^i_\alpha(t) = A^i_\alpha(t) - \langle A^i_\alpha\rangle$, $\rho(r_1;0)$ the distribution of the particle at the initial time (considered to be uniform) and $\rho(\vec{r}_2;t|\vec{r}_1;0)$ is the conditional probability of the particle being at $\vec{r}_2$ at time t given that it was in $\vec{r}_1$ at time $t=0$. This conditional probability is nothing but the solution of the diffusion equation with the initial condition at $\vec{r}_1$ with a reflective boundary condition at $z=z_0$, satisfying $\frac{d\rho}{dz}|_{z_2=z_0} = 0$

$$\rho(\vec{r_2};t|\vec{r_1};0) = \frac{1}{(4\pi\mathcal{D}t)^{\frac{3}{2}}} e^{-\frac{(x_1-x_2)^2}{4\mathcal{D}t}} e^{-\frac{(y_1-y_2)^2}{4\mathcal{D}t}} \left(e^{-\frac{(z_1-z_2)^2}{4\mathcal{D}t}} + e^{-\frac{(z_1+z_2-2z_0)^2}{4\mathcal{D}t}}\right) \tag{32}$$

with $\mathcal{D}$ the diffusion coefficient. The correlation function can not be calculated analytically and therefore one must calculate it using a numerical approach, either by numerical integration or by using data obtained by a stochastic molecular dynamics simulation. While the former approach is rather straight forward, the latter requires to obtain a number of possible trajectories and then averaging the correlation function over all trajectories. This was done using the *MATLAB* function *xcorr*.

In this context, we define the correlation time such that when $t = \tau_c$

$$\left\langle \xi^i_\alpha(\tau_c)\xi^i_\alpha(0)\right\rangle \equiv \frac{1}{e}\left\langle \xi^i_\alpha(0)\xi_\alpha\alpha^i(0)\right\rangle = 1/e, \tag{33}$$

in other words, the correlation time is a characteristic time such that when $t > \tau_c$, $\xi^i_\alpha(t)$ and $\xi^i_\alpha(0)$ can be treated as statistically independent.

Since the correlation time is inversely proportional to the diffusion coefficient, τ_c should also depend on a parameter with a dimension of length. This parameter was considered to be z_0. Intuitively, as the depth of the NV increases, an interacting nuclear spin has to be displaced more in order to change the interaction by a significant amount, increasing the correlation time. We can see in Fig.(S2) that the dependency of τ_c on the depth of the NV is indeed quadratic for shallow NVs ($z_0 \sim 6\,\text{nm}$). For deeper NVs, due to the long range

interaction ($\sim \frac{1}{r^3}$) this dependency deviates because the interaction length is comparable to the NV's depth and takes part in the correlation time.

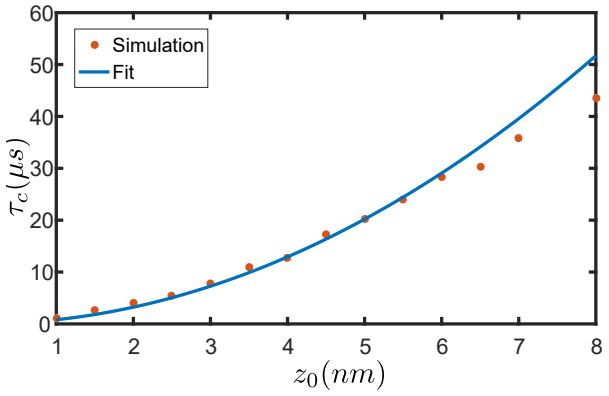


Figure S2: Correlation time vs NV depth. Results obtained from simulation. For Shallow NVs the data is fitted to a quadratic function.

Bosonic approximation and Gaussian states

In order to numerically simulate a large spin system we make use of the Holstein-Primakoff approximation (HPA),[7] which expresses the spin operators in terms of bosonic operators

$$S_+ = \sqrt{2S}a^\dagger\sqrt{1-\frac{a^\dagger a}{2S}} \approx \sqrt{2S}a^\dagger, \tag{34}$$

$$S_- = \sqrt{2S}\sqrt{1-\frac{a^\dagger a}{2S}}a \approx \sqrt{2S}a, \tag{35}$$

$$S_z = \left(-S + a^\dagger a\right), \tag{36}$$

Where, $S = \frac{1}{2}$ for spins-$\frac{1}{2}$. This approximation has been successfully used in other works for describing interacting spin baths in similar scenarios.[8] In fact, within the HPA a polarized spin is represented as a boson in its ground state. As far as only the ground and first excited states play a major role in the dynamical evolution of the system, the HPA yields satisfactory results. Since our system consists on numerous spins in thermal state with mainly flip-flop

interactions and moreover strong correlations between nuclei are not built up owning to the stochastic motion, the HPA is expected to accurately describe the desired polarization dynamics in the regime we are interested in. Performing the same approximation for the nuclear spin operator $\mathbf{I}$ on Eq. (4), we directly obtain the bosonic Hamiltonian

$$H = \Omega a^\dagger a + \sum_i^N \omega_N b_i^\dagger b_i + \sum_i g_i\, a^\dagger b_i + g^*\, a b_i^\dagger, \tag{37}$$

This Hamiltonian corresponds to a system of two coupled harmonic oscillators under the rotating wave approximation (RWA). Introducing the bosonic operator vector, $\mathbf{R} = (a, b_i, \cdots, b_N)^T$, we express the total Hamiltonian as

$$H = \frac{1}{2}\mathbf{R}^\dagger V \mathbf{R}, \tag{38}$$

with $V = V_0 + V_1$, containing all the interactions between the operators

$$V_0 = \begin{array}{c} \\ a \\ b \end{array} \begin{array}{c} \begin{array}{cc} a^\dagger & b^\dagger \end{array} \\ \begin{pmatrix} \Omega & 0 \\ 0 & \omega_N \end{pmatrix} \end{array}$$

$$V_1 = \begin{array}{c} \\ a \\ b \end{array} \begin{array}{c} \begin{array}{cc} a^\dagger & b^\dagger \end{array} \\ \begin{pmatrix} 0 & g_i \\ g_i^* & 0 \end{pmatrix} \end{array}$$

In the last expressions, for the sake of simplicity, only the matrices for 2 interacting bosons are written down.

A quadratic bosonic Hamiltonian as Eq. (37) induces a Gaussian unitary evolution. This means, given a certain Gaussian state, its evolution under the action of a quadratic bosonic Hamiltonian will preserve its Gaussian character.[9,10]

All the quantum information of a Gaussian state is contained in the first and second moments of the quadratures operator $\mathbf{R}$: the mean, $\langle \mathbf{R} \rangle$, and the covariance matrix, γ.

Moreover, if the Hamiltonian has not linear terms, and for initial states with $\langle \mathbf{R} \rangle = 0$, the whole system is described by the covariance matrix, defined as

$$\gamma_{j,k} = \left\langle b_j^\dagger b_k \right\rangle, \tag{39}$$

with $j, k \in \{0, N\}$, being $b_0 = a$. Making use of the von Nuemann equation for the evolution of $\left\langle b_i^\dagger b_j \right\rangle$ in time,

$$\left\langle \dot{b_i^\dagger} b_j \right\rangle = +\mathrm{i} \left\langle \left[b_i^\dagger b_j, H \right] \right\rangle, \tag{40}$$

derive a evolution equation for γ results straightforward,

$$\dot{\gamma} = -\mathrm{i} \left[V, \gamma \right]. \tag{41}$$

We remark, γ has dimensions $N + 1 \times N + 1$, where N is the total number of nuclei. This is the main advantages of the Gaussian state formalism, while for a spin system we will need to compute the 2^N elements of the density matrix to describe the system, for a bosonic system it is sufficient to evolve γ. Therefore, while simulating a spin system of $N \approx 15$ spins already becomes computationally hard, the use of HPA allows us to simulate systems with thousands of bosons easily.

Relaxation of the bosonic system

In order to implement a relaxation process that will take the place of $T_{1\rho}$ effects in a spin system, we include a dissipation part on the evolution equation of the bosonic system

$$\dot{\rho} = -\mathrm{i} \left[H, \rho \right] + \frac{1}{T_{1\rho}} \left(\frac{3}{2} D(a) + \frac{1}{2} D\left(a^\dagger \right) \right) \rho, \tag{42}$$

where ρ is the density matrix of the whole bosonic system, and $D(a), D\left(a^\dagger\right)$ are the Lindblad dissipator on the creation and annihalition operators. The evolution of the covariance matrix,

γ, under the action of such a master equation is given by

$$\dot{\gamma} = -\mathrm{i}\,[V,\gamma] + \frac{1}{2}\frac{1}{T_{1\rho}}\left[\Delta - \{\Delta,\gamma\}\right]. \tag{43}$$

where $\Delta_{i,j} = \delta_{0,i}\delta_{0,j}$ is a matrix that indicates the action of $T_{1\rho}$ affects only the NV center (labeled as 0). In addition to quadratic Hamiltonians, Lindblad equation of the form of Eq.(42) also maintains the Gaussian character of an initial Gaussian state.[11]

Numerical Simulation parameters

As stated in the main text, the numerical simulation based on HPA is performed considering N independently moving nuclei in a finite box with periodic boundary conditions and length l. This box represents the detection volume of the NV center. The simulation box sets a cut-off to other parameters such as the particle number, for a fixed particle density, ρ, then $N = \rho\, l^3$, or the interaction variance inside the box σ_l^2, with $\lim_{l\to\infty}\sigma_l^2 = \sigma^2$. That means, the selection of l is a compromise between the computational efficiency, set by N, and the ratio $\chi = \sigma_l^2/\sigma^2$, which should be $\chi \approx 1$ for a satisfactory description. Simulation results for different densities and lengths are depicted in Fig.(S3).

In our experiment, the oil density equals, $\rho_{oil} = 50\,\frac{\text{spins}}{\text{nm}^3}$. Therefore, it requires to consider a significantly large number of nuclei inside the simulation box. For a box length of $l = 20\,\text{nm}$, then $N = 4\cdot 10^5$ and $\chi \sim 92\%$. Even for this length, N is still too large, so we consider effectively $N_{\text{eff}} = 5\cdot 10^3$ spins with a effective interaction $g_{\text{eff}} = \sqrt{80}g$. This effective model has been proven to reproduce exactly the NV spin dynamics.

Determining the depth of shallow NV centers

In order to estimate the NV center depth z_0, the magnetic field noise produced by the Larmor precession of the hydrogen spins within the immersion oil (Fluka Analytical 10976)

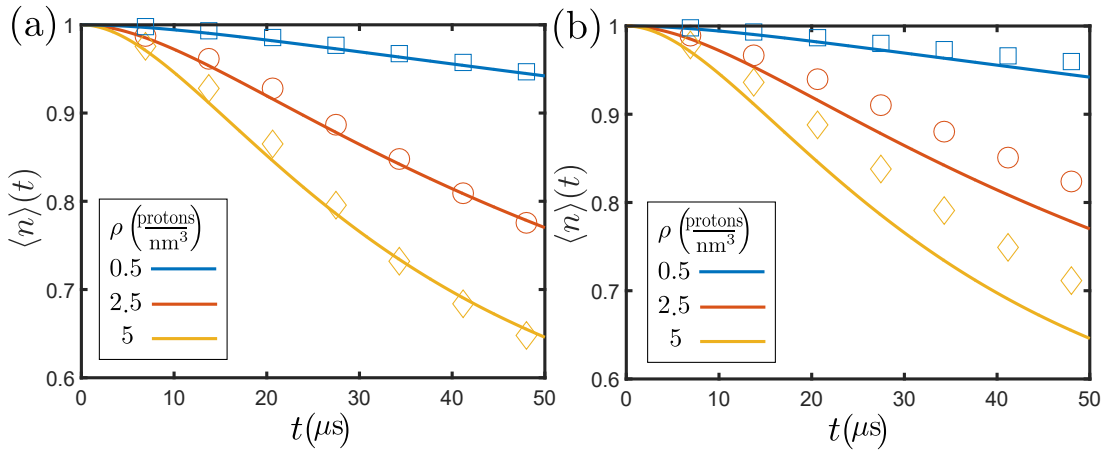


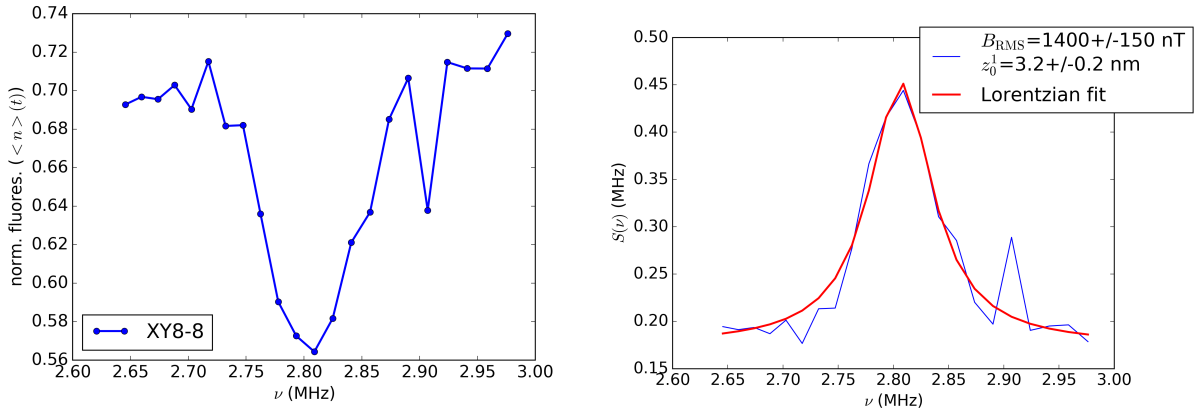
Figure S3: Confrontation between full numerical simulation with HPA (markers) and theoretical prediction for spins (solid lines) for different densities and $z_0 = 3.2\,\text{nm}$. (a) Simulations for bosons diffusing in a box with $l = 25\,\text{nm}$, $\chi = 95\%$. (b) Simulation for $l = 12.5\,\text{nm}$ and $\chi = 78\%$. For this box size the numerical simulation gives satisfactory results with fast computational time.

was measured via the XY8-N sequence. These measurements were performed at 660 G, which corresponds to a hydrogen Larmor frequency of $\nu \equiv \omega_N/(2\,\pi) = 2.81\,\text{MHz}$. We get the magnitude of the RMS magnetic field B_{RMS} from the measured XY8 signal by reconstructing the power spectral density $S(\nu)$ via a deconvolution process using the known filter function and then integrating the peak signal. From B_{RMS} the depth of the NV center can be calculated analytically (see e.g.[12]):

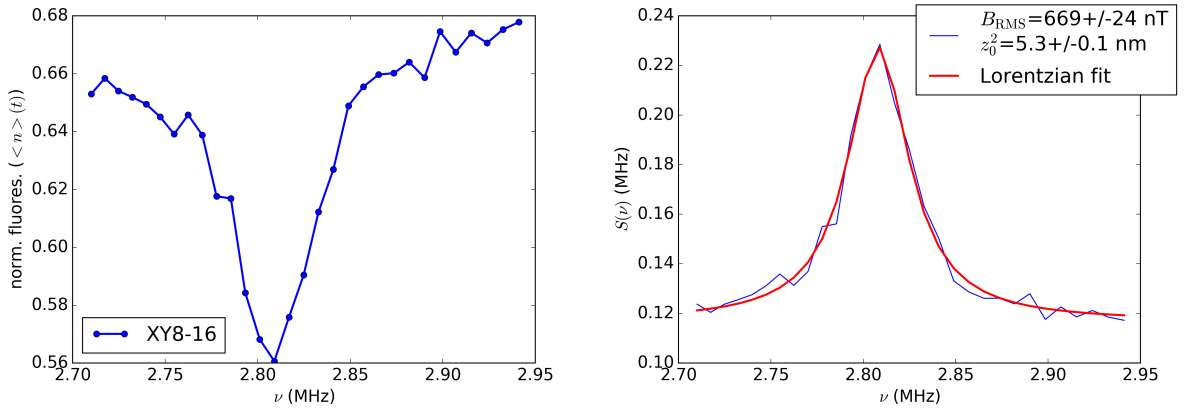
$$z_0 = \left[\frac{1}{B_{\text{RMS}}^2}\frac{5}{1536\pi}\mu_0^2 h^2 \gamma_{\text{N}}^2 \rho_{\text{oil}}\right]^{\frac{1}{3}}, \tag{44}$$

where $\gamma_{\text{N}} = 42.58\frac{\text{MHz}}{\text{T}}$ is the nuclear gyromagnetic ratio and $\rho_{\text{oil}} = 50\,\text{protons/nm}^3$ the proton density of the immersion oil.

Fig.(S4) shows the data of the XY8 measurements and the corresponding spectral density for the two NVs. From these measurements we can estimate the depths to be $z_0^1 = 3.2 \pm 0.2\,\text{nm}$ and $z_0^2 = 5.3 \pm 0.1\,\text{nm}$.



(a) Depth estimation for NV1



(b) Depth estimation for NV2

Figure S4: The left plots show the raw XY8 data, normalized to the Rabi contrast. Right side: The power spectral density is calculated from the XY8 data and by the area of the function around the ^{1}H Larmor frequency the depth can be calculated (see Eq.(44)) (a) Measurement corresponding to shallower NV center $z_0^1 = 3.2\,\mathrm{nm}$. (b) Depth measurement outcomes for an slightly deeper NV center $z_0^2 = 5.3\,\mathrm{nm}$.

Relaxation in the dressed state basis $T_{1\rho}$

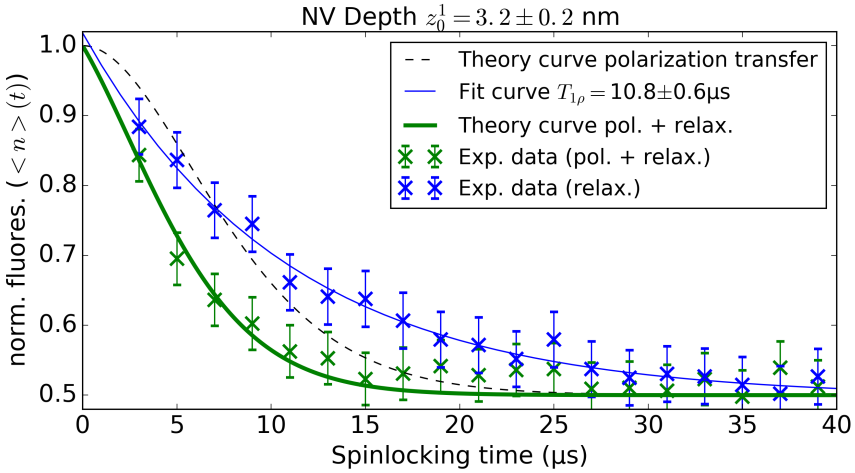
Besides the polarization transfer dynamics during the spin locking pulse there is also relaxation due to resonant magnetic noise. Since this decay happens in the same time scale as the polarization transfer process, the characteristic relaxation time in the dressed state basis $T_{1\rho}$ is detemined experimentally and taken into account in the theoretical predictions. This is done by measuring the decay of the NV spin state while the MW drive during the spin locking pulse is set off-resonant from the HHDR condition (by 500 kHz). In Fig.(S5) the NV decay during spin locking fulfilling HHDR condition (polarization transfer and relaxation) is compared to an off-resonant measurement (only relaxation). From a single exponential fit, $f(\tau) = a + b\exp[-\tau/T_{1\rho}]$, we obtain $T_{1\rho} = 10.8 \pm 0.6\,\mu$s for NV1 and $T_{1\rho} = 17.0 \pm 1.4\,\mu$s for NV2.

In all experimental data sets the fluorescence measured from a single NV center is normalized with the steady-state fluorescence at the end of the laser pulse and it scaled by the contrast of a by an additional Rabi experiment. The error bars are determined with photon shot-noise, error propagated with the fluorescence normalization and divided by the Rabi amplitude.

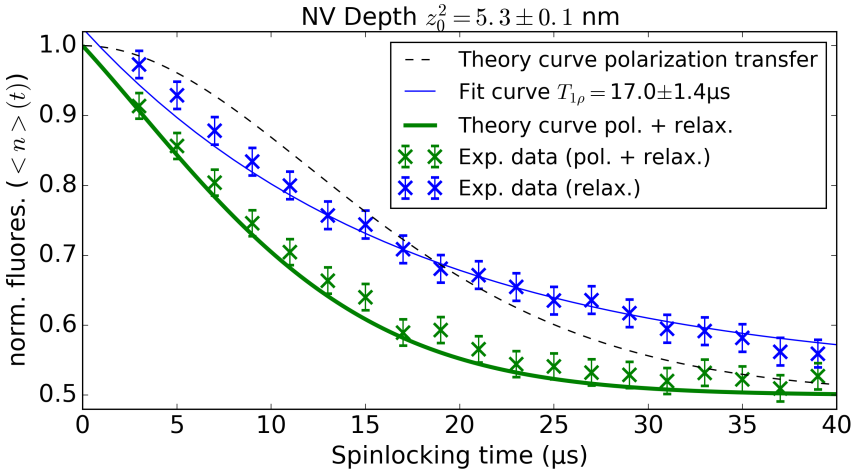
Steady-State polarization

Throughout this work we have focused on the polarization dynamics of one single NV center in one single cycle. In order to achieve significant polarization in the oil sample the protocol must be repeated numerous times, and the general set-up may be modified. The steady-state polarization, that is, the maximum achievable polarization using our protocol may be estimated as follows.

For hyperpolarization a diamond sample with high density of NV centers is needed. Given a bulk diamond with different NV centers distributed homogeneously through the whole volume, such that the interaction among different electronic spins is negligible, with a



(a) Resonant and off-resonant decay for NV1



(b) Resonant and off-resonant decay for NV2

Figure S5: Decay of NV fluorescence under fulfilled HHDR conditions (green points) and under off-resonant conditions (blue points). The off-resonant decay is fitted by a single exponential decay (blue curve). The fitting curve is not forced to pass through $\langle n \rangle (0) = 1$ since the normalization in the plot for the off-resonant curve is solely illustrative; only the decay rate $T_{1\rho}$ is important. The corresponding time constant $T_{1\rho}$ is included in the theoretical predictions (green curve). Not taking $T_{1\rho}$ processes and thus only taking polarization transfer into account would lead to the black dotted theory curve. (a) Polarization loss, $T_{1\rho}$ relaxation and theoretical predicted polarization curve for an NV center at $z_0^1 = 3.2\,\mathrm{nm}$. (b) Same for NV center at $z_0^2 = 5.3\,\mathrm{nm}$.

superficial density σ_{NV}. If a thin layer of oil of thickness L_{oil} is deposited onto the diamond surface, then particle reservoir for a single NV centers consists of a volume $V_T = L_{oil}/\sigma_{NV}$.

On the other hand, during one cycle a single NV exclusively interacts with N nuclei, which are inside its own interaction volume V. Therefore, after a polarization cycle, whose duration is τ_p, the average polarization per nucleus is $\frac{1}{2}\frac{1}{N}\alpha$, as defined in the main text. Nonetheless, in a single cycle the NV center has only interacted with a fraction V/V_T of the total number of ^1H in the oil. For all the nuclei to interact at least once with the NV, the cycle must be repeated n times with $n = V_T/V$. Hence, the total required time is $T = n\tau_p$.

In summary, at time $T = n\tau_p$ the average polarization per nucleus is $P = \frac{1}{2}\frac{1}{N}\alpha$. The same procedure can be repeated m times, and since the polarization acquisition is only limited by the nuclear relaxation time, T_{1n}, then for an optimal performance $m = T_{1n}/T$. Assuming that for small amounts the polarization is additive, we obtain that the maximal average polarization per nuclei is

$$P_{max} = \frac{T_{1n}}{T}\frac{1}{2}\frac{1}{N}\alpha = \frac{1}{2}\alpha\frac{T_{1n}}{\tau_p}\frac{\sigma_{NV}}{L_{oil}\rho_{oil}}, \tag{45}$$

For realistic values, $\alpha = 0.8$, $\tau_p \approx 5\,\mu s$, $T_{1n} \approx 1\,\mathrm{s}$, $\rho_{oil} \approx 50\,\frac{\mathrm{protons}}{\mathrm{nm}^3}$, $L_{oil} \approx 1\,\mu\mathrm{m}$, $\sigma_{NV} \approx 2\cdot 10^{-3}\,\frac{\mathrm{NV}}{\mathrm{nm}^2}$, the calculations yield $P_{max} = 10^{-3}$, which severally exceeds the thermal average polarization $P^{Th} = 10^{-7}$.

Measurement outcomes for rigid and semi-rigid samples

The dynamical behavior of oil molecules in the vicinity of the diamond sample is unknown. Chemical reactions such as adsorption may occur, hence blocking the stochastic motion of the molecules resulting in an effective rigid bath for the NV center. Nonetheless, in our model we consider the protons as randomly moving particles in free diffusion with certain diffusion coefficient $\mathcal{D}_{oil}$. This description is expected to be accurate when the detection volume is big enough and thus, the big majority of the molecules diffuse freely while only an

small fraction may participate in adsorption.

Still, using HPA and Eq.(43) we can estimate the measurable polarization loss from a NV center when interacting with a rigid or semi-rigid oil. The outcome of these simulations helps us to discriminate whether the measured polarization loss may be also attributable to a solid sample or if it is exclusively inherent to liquid oil.

Since molecular simulations with the used oil (Fluka Analytical 10976) are not available, we explore different proton configurations with different orderings. For the sake of simplicity, we start from an initial configuration in which all protons form a cubic lattice with lattice parameter a. From this starting point, different configurations are achievable by displacing each of the protons by a random quantity δ_i. In this context, the magnitude of δ_i sets the amount of disorder with respect to the initial cubic lattice, hence we quantify the disorder by $\chi \equiv \frac{2|\delta_i|}{a}$.

Consequently, we can study the different signals on the NV center coming from different types of bath: from a complete ordered crystal, $\chi = 0$, to homogeneously distributed non-overlapping protons, $\chi = 80\,\%$. We remark that our aim is not to predict the exact NV center dynamics but rather the general behavior for a given kind of bath.

For the numerical simulations we have used Eq.(43) with a time-independent Hamiltonian. The electronic spin relaxation, $T_{1\rho}$, is described by a local Lindblad equation. This description is accurate and valid for non correlated systems such as liquid oil. Nonetheless, here it is used for highly-correlated baths such as rigid oil since it is expected to give satisfactory results.[13] Further details on the simulation techniques may be found in the Secs. *Bosonic approximation and Gaussian states* and *Numerical Simulation parameters*.

The outcomes of the simulation are depicted in Fig.(S6). For a rigid bath, the amount of possible configurations of the protons is infinite and therefore we have chosen to present the average signal (obtained by averaging over all the plausible polarization loss curves), together with the standard deviation. Moreover, the average signal (blue curve Fig.(S6)), coincides with the signal that a semi-rigid solid produces on the NV center. In this context, a

semi-rigid solid consists of and ensemble of protons that are fixed during the duration of the spin-locking time, t, but move by a random quantity δ_i between two different measurements.

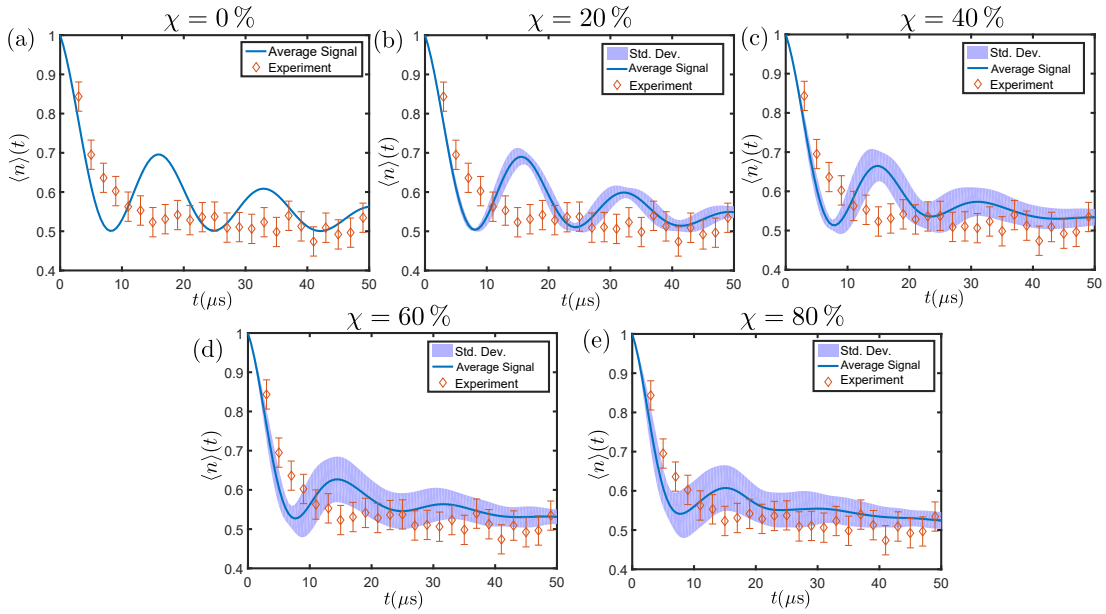


Figure S6: Comparison between rigid and semi-rigid baths and experimentally measured polarization loss for a shallow NV center at $z_0^1 = 3.2\,\text{nm}$ and $T_{1\rho} = 11\,\mu\text{s}$. For each order parameter, χ, infinite configurations are possible; in the figure there are shown the average value (blue line) and the standard deviation (blue shadow). (a) The protons are found at fixed positions conforming a cubic lattice with lattice parameter a. The NV center coherently interchanges polarization with the bath. Nuclear-nuclear interaction effectively detunes the nuclei from the HHDR and therefore full-oscillations are not seen.(b-e) Disorder models with different disorder parameter χ. The protons are assumed to be at random positions inside the detection volume, that is, disordered. Still, the coherent oscillations are appreciable. For larger disorder factors, the number of plausible nuclear configurations increase hence leading to a bigger standard deviation. {In the calculations, have been used, $N = 800$, $L = 20$, $\rho_{oil} = 50\,\text{spins/nm}^3$, $T_{1\rho} = 11\,\mu\text{s}$.}

The simulations suggest that for both rigid and semi-rigid baths the NV experiences coherent oscillations. Nonetheless, this behavior is attenuated when disorder dominates. When compared to the experimental measured data, none of the examined scenarios, neither rigid nor semi-rigid, can reproduce the observed behavior. Hence, we conclude that the description of the oil molecules as a liquid is adequate.

References

(1) Avron, J.; Kenneth, O.; Retzker, A.; Shalyt, M. *New J. Phys.* **2015**, *17*, 043009.

(2) Tanimura, Y. *J. Phys. Soc. Jpn.* **2006**, *75*, 082001.

(3) Van Kampen, N. G. *Stochastic processes in physics and chemistry*; Elsevier, 1992; Vol. 1.

(4) Kampen, N. V. *Physica* **1974**, *74*, 239 – 247.

(5) Breuer, H.; Petruccione, F. *The theory of open quantum systems*; Oxford University Press on Demand, 2002.

(6) Slichter, C. P. *Principles of Magnetic Resonance*; Springer Science & Business Media, 1990; Vol. 1.

(7) Holstein, T.; Primakoff, H. *Phys. Rev.* **1940**, *58*, 1098–1113.

(8) Christ, H.; Cirac, J. I.; Giedke, G. *Phys. Rev. B* **2007**, *75*, 155324.

(9) Plenio, M.; Hartley, J.; Eisert, J. *New J. Phys.* **2004**, *6*, 36.

(10) Eisert, J.; Plenio, M. *Int. J. Quantum Inf.* **2003**, *1*, 479–506.

(11) Ferraro, A.; Olivares, S.; Paris, M. *arXiv preprint quant-ph/0503237* **2005**,

(12) Pham, L. M.; DeVience, S. J.; Casola, F.; Lovchinsky, I.; Sushkov, A. O.; Bersin, E.; Lee, J.; Urbach, E.; Cappellaro, P.; Park, H.; Yacoby, A.; Lukin, M.; Walsworth, R. L. *Phys. Rev. B* **2016**, *93*, 045425.

(13) Rivas, A.; Plato, A. D. K.; Huelga, F. S.; Plenio, M. B. *New J. Phys.* **2010**, *12(11)*, 113032.

3.3 Robust optical polarization of nuclear spin baths using Hamiltonian engineering of nitrogen-vacancy center quantum dynamics

Title:	Robust optical polarization of nuclear spin baths using Hamiltonian engineering of nitrogen-vacancy center quantum dynamics
Authors:	I. Schwartz, J. Scheuer, B. Tratzmiller, S. Müller, Q. Chen, I. Dhand, Z. Wang, C. Müller, B. Naydenov, F. Jelezko and M. B. Plenio
Journal:	Science Advances 4 8 eaat8978
Year:	2018
Copyright:	The Authors, some rights reserved; exclusive licensee American Association for the Advancement of Science under the Creative Commons Attribution NonCommercial License 4.0 (CC BY-NC), https://creativecommons.org/licenses/by-nc/4.0/. In accordance to this license, the author has the right to reuse the full-text article in his dissertation.
DOI:	http://www.doi.org/10.1126/sciadv.aat8978

PHYSICS

Robust optical polarization of nuclear spin baths using Hamiltonian engineering of nitrogen-vacancy center quantum dynamics

Ilai Schwartz[1,2*†], Jochen Scheuer[3*], Benedikt Tratzmiller[1*], Samuel Müller[3], Qiong Chen[1†], Ish Dhand[1], Zhen-Yu Wang[1], Christoph Müller[2], Boris Naydenov[3], Fedor Jelezko[3], Martin B. Plenio[1†]

Copyright © 2018 The Authors, some rights reserved; exclusive licensee American Association for the Advancement of Science. No claim to original U.S. Government Works. Distributed under a Creative Commons Attribution NonCommercial License 4.0 (CC BY-NC).

Dynamic nuclear polarization (DNP) is an important technique that uses polarization transfer from electron to nuclear spins to achieve nuclear hyperpolarization. Combining efficient DNP with optically polarized nitrogen-vacancy (NV) centers offers promising opportunities for novel technological applications, including nanoscale nuclear magnetic resonance spectroscopy of liquids, hyperpolarized nanodiamonds as magnetic resonance imaging contrast agents, and the initialization of nuclear spin–based diamond quantum simulators. However, none of the current realizations of polarization transfer are simultaneously robust and sufficiently efficient, making the realization of the applications extremely challenging. We introduce the concept of systematically designing polarization sequences by Hamiltonian engineering, resulting in polarization sequences that are robust and fast. We theoretically derive sequences and experimentally demonstrate that they are capable of efficient polarization transfer from optically polarized NV centers in diamond to the surrounding ^{13}C nuclear spin bath even in the presence of control errors, making the above-mentioned novel applications possible.

INTRODUCTION

A key challenge in the quantum manipulation and detection of small nuclear spin ensembles is their minute level of polarization at thermal equilibrium, which is on the order of 10^{-5} for a magnetic field of 2 T at room temperature. Overcoming this challenge holds the key for the realization of quantum applications ranging from quantum simulators to nanoscale nuclear magnetic resonance (NMR) devices. These will be turned from laboratory demonstrations into realistic applications by polarization schemes that enable their efficient initialization and readout. An important breakthrough in this respect has been the realization that the electron spin of the nitrogen-vacancy (NV) centers in diamond (as well as color centers in silicon carbide and photoexcited triplet-state molecules) can be optically initialized nearly perfectly even at room temperature and under ambient conditions, allowing for rapid electron spin polarization to be generated optically or chemically far above thermal equilibrium and subsequently transferred to surrounding nuclei (*1*–*6*). These systems present a unique opportunity for polarizing and initializing spin baths and unlocking the potential of nanoscale applications including the initialization of quantum simulators based on nuclear spin arrays in diamonds (*7*, *8*), magnetic resonance imaging (MRI) tracers via diamond nanoparticles and powdered diamond (*9*–*13*), and the enhancement of NMR using NV spin ensembles (*14*).

However, when trying to achieve nuclear hyperpolarization via NV centers or similar systems (for example, silicon carbide and photoexcited triplet-state molecules), we are faced with two key challenges. First, optically polarizable electron spins are typically higher spin systems, with $S \geq 1$. The lattice-oriented zero-field splitting in the presence of external magnetic fields and disorder results in a large spectral range of the electron spin resonance, hindering effective polarization transfer to the surrounding nuclear spins. Second, many of these systems exhibit fast electron spin relaxation (for example, photoexcited triplet states) (*15*), requiring fast polarization transfer, or weak hyperfine coupling to the nuclear spins (for example, NV centers in diamonds, especially to external nuclear spins), limiting polarization transfer rates. Overcoming this combination of challenges presents a daunting task, as it requires a polarization transfer scheme that (i) works for a large spectral range of the electronic system and (ii) produces a fast and efficient polarization transfer from electron to nuclear spins.

Many dynamic nuclear polarization (DNP) protocols have been developed and applied over the past several decades, starting from continuous microwave (MW) irradiation (*16*) to more efficient pulsed schemes (*17*, *18*). A common theme in all protocols that are effective for low electron spin concentration is the use of a long MW pulse to match the Larmor frequency of the nuclear spins to the electronic Rabi rotation in the frame of reference of the MW drive, which is well known as a Hartmann-Hahn (H-H) resonance (*19*). Unfortunately, owing to the weak electron-nuclear interaction, even a small detuning from this resonance inhibits the polarization transfer, which renders these schemes strongly dependent on the intensity and frequency of the MW drive as well as the orientation and transition frequency of the NV center. While modified protocols such as the integrated solid effect (ISE) (*10*, *18*, *20*) improve the robustness across larger spectral ranges, this comes at the expense of a significantly slower polarization transfer. Thus, devising a DNP protocol that is both robust and fast has remained an unmet challenge.

Here, we present a new approach for performing DNP, termed PulsePol, which combines fast polarization transfer with remarkable robustness against a broad range of experimental imperfections including power and detuning fluctuations. In sharp contrast to the schemes described above, which allow for polarization transfer only during the pulses, this is achieved by the design of sequences of short pulses (*21*, *22*) (much shorter than the nuclear Larmor period), with extended waiting periods between the pulses, that refocus the electron-nuclear interaction such that polarization transfer is achieved through the accumulated dynamics between pulses. As we will demonstrate both theoretically and experimentally,

[1]Institut für Theoretische Physik und IQST, Albert-Einstein-Allee 11, Universität Ulm, 89081 Ulm, Germany. [2]NVision Imaging Technologies GmbH, Albert-Einstein-Allee 11, 89081 Ulm, Germany. [3]Institut für Quantenoptik und IQST (Center for Integrated Quantum Science and Technology), Universität Ulm, 89081 Ulm, Germany.
*These authors contributed equally to this work.
†Corresponding author. Email: qiong.chen@uni-ulm.de (Q.C.); ilai.schwartz@uni-ulm.de (I.S.); martin.plenio@uni-ulm.de (M.B.P.)

Downloaded from http://advances.sciencemag.org/ on November 18, 2019

this approach provides inherent robustness to MW errors and electron spectral width and a high degree of flexibility, which allows to take full advantage of pulse optimization methods developed in NMR (*23*, *24*) to tailor the polarization to the specific challenges of the experimental setup.

We start by describing the theoretical framework of Hamiltonian engineering and derive the PulsePol sequence whose robustness against detuning and pulse length/strength errors we establish theoretically. We then proceed to experimentally confirm the efficiency of the protocol for a single NV center in a diamond surrounded by ^{13}C nuclei and compare the performance of the PulsePol protocol to state-of-the-art DNP schemes. Finally, we discuss several applications of our protocol.

THEORETICAL FRAMEWORK

For simplicity, we consider a system of a single electron **spin** $\vec{\mathbf{S}}$ ($S = \frac{1}{2}$ for simplicity, later realized by the $|m = 0\rangle$ and $|m = -1\rangle$ levels of the NV center) coupled to a single nuclear **spin** $\vec{\mathbf{I}}$, subject to intermediately applied MW pulses, which are used for control of the electron spin

$$H = \omega_S S_z + \omega_I I_z + \vec{\mathbf{S}}\mathcal{A}\vec{\mathbf{I}} + H_d \tag{1}$$

where $\omega_S(\omega_I)$ denotes the electron (nuclear) Larmor frequency, and $\mathcal{A}$ is the hyperfine tensor. $H_d = 2\Omega(t)S_x \cos(\omega_{MW}t + \varphi)$, in which ω_{MW} is the MW frequency, φ is its phase, and the Rabi frequency $\Omega(t)$ takes the value Ω_0 when the MW is on, and 0 otherwise.

For the realization of a robust and efficient interaction between the NV center and the surrounding nuclear spins, one needs to simultaneously achieve the decoupling of the NV electron spin from environmental noise while refocusing the desired interaction with the nuclear spin bath. This can be achieved by dynamical decoupling (DD) protocols (*25*, *26*) such as Carr-Purcell-Meiboom-Gill (*27*) or the *XY* pulse family (*28*), where equally spaced pulses separated by a time τ such that only interactions with nuclear spins precessing at a frequency $\omega_I = n\pi/\tau$ are preserved.

When these DD sequences achieve resonance with a nuclear spin, the resulting effective Hamiltonian that describes the time evolution is, in a suitable electronic basis, of the form $H_{\text{eff}} = \alpha A_x S_x I_x$, where A_x denotes the x component of the hyperfine vector, and $\alpha < 1$ is a constant determined by the filter function generated by the pulse sequence (*29*). H_{eff} does not transfer polarization, and the concept of pulsed polarization is to engineer this Hamiltonian to produce the desired flip-flop dynamics. To this end, for a short time interval $\Delta t \ll \omega_I^{-1}$, we apply a time evolution according to $H_{\text{eff}} = \alpha A_x S_x I_x$, and in a subsequent interval of length Δt, we let the system follow a time evolution according to $H_{\text{eff}} = \alpha A_x S_y I_y$. This is achieved by mapping both the electronic basis by an MW pulse and the nuclear spin basis by a suitable time delay from x to y (see Fig. 1). Repeating this sequence yields a time evolution that is governed, for times exceeding ω_I^{-1} and whenever the coupling strength satisfies $A_x \ll \omega_I$, by the effective flip-flop Hamiltonian

$$H_{\text{avg}} = -\frac{\alpha A_x}{4}(S_+ I_- + S_- I_+) \tag{2}$$

which is the sum of $H_{\text{eff}} = \alpha A_x S_x I_x$ and $H_{\text{eff}} = \alpha A_x S_y I_y$.

We would like to emphasize that the rapid switching in intervals Δt represents a crucial deviation from schemes that aim to achieve engineered electron-nuclear SWAP gates after a time πA_x^{-1} by first applying an evolution according to $\exp(-iA_x S_x I_x t/2)$ for half the total interaction time, followed by $\exp(-iA_x S_y I_y t/2)$ for the second half (*30*), as this achieves a SWAP gate only at $t = \pi A_x^{-1}$, while in between the evolution may include both flip-flip and flip-flop terms. Achieving flip-flop dynamics on the time scale of the Larmor frequency ω_I is crucial for DNP applications, especially those in which the nuclei are in rapid motion as standard SWAP pulse sequences are slow and are not suitable for ensembles of electron spins coupled to nuclear spin baths due to coupling strength variations. Furthermore, any loss of coherence faster than the interaction time, due to noisy environment or dynamics on fast time scales (for example, molecular motion), would completely destroy any polarization transfer. These effects are mitigated when the average dynamics are achieved on the nuclear Larmor time scale, which are very fast. However, one challenge (see the Supplementary Materials) remains, as the basic scheme using the rapid alternation between $A_x S_x I_x$ and $A_x S_y I_y$ on the time scale of the Larmor frequency, and other simple variants, come at the expense of an enhanced sensitivity to pulse errors and detunings

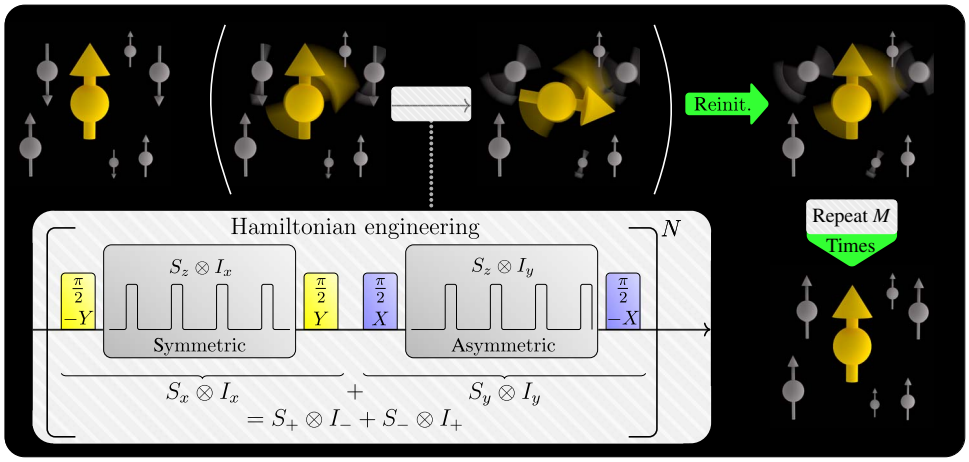


Fig. 1. Theoretical framework overview. Polarization of a bath of nuclear spins (gray) by an electron spin (yellow): The initially unpolarized bath and the polarized electron spin (upper left) evolve according to an engineered Hamiltonian that describes a flip-flop interaction, and the electron spin is periodically reinitialized. After several repetitions, the nuclear spin bath is polarized (lower right). Illustration of effective Hamiltonian engineering (gray box): A combination of standard symmetric and asymmetric DD sequences with the effective Hamiltonians $H \propto S_z \otimes I_{x/y}$ can be modified to a flip-flop Hamiltonian $H \propto S_x \otimes I_x + S_y \otimes I_y$ by introducing basis changes with $\pi/2$ pulses.

Downloaded from http://advances.sciencemag.org/ on November 18, 2019

because the change between S_x and S_y dynamics typically introduce unbalanced π/2 pulses, not part of standard DD sequences.

Thus, no robust pulse sequence or tailoring of DD sequence is known to produce the fast flip-flop dynamics on very short time scales, regardless of the coupling strength while satisfying (i) that detuning errors accumulated during the free evolution are canceled (for example, by π refocusing; see the Supplementary Materials) and preferably also decoupled from unwanted noise and fluctuations and (ii) that variable pulse lengths and detuning and Rabi frequency errors are canceled at least to the first order.

We have constructed such a sequence, termed PulsePol and depicted in Fig. 2A, analytically from components chosen to satisfy the above requirements (see the Supplementary Materials for a detailed discussion). PulsePol achieves polarization transfer for a choice of pulse spacing

$$\tau = \frac{n\pi}{\omega_I} \tag{3}$$

for odd n with the strongest coupling occurring for $n = 3$, where $\alpha = \frac{2}{3\pi}(2+\sqrt{2})$, and yields an effective flip-flop Hamiltonian for times longer than ω_I^{-1}. Full polarization transfer between NV and nuclei is found after a time $t = 2N\tau = 4\pi/(\alpha A_x)$, where N is the number of basic pulse cycles (Fig. 2A). As a consequence, PulsePol achieves polarization transfer in a time scale that is only 28% slower than that achieved with H-H coherent transfer under optimal conditions (Fig. 2B) and significantly faster than other polarization transfer schemes (for example, ISE and solid effect). Furthermore, PulsePol is robust to errors as it has several inherent advantages that enhance its robustness:

(i) Strong pulses with amplitude Ω_0, without the requirement of matching the H-H condition, are robust to detuning that satisfies $\Delta \ll \Omega_0$.

(ii) The PulsePol sequence cancels second-order errors in the pulse strength and first-order errors in the detuning (see the Supplementary Materials), making it robust to noise and small pulse imperfections, similar to DD sequences.

(iii) The individual pulses can be optimized by numerous methods developed in NMR, including composite pulses (*23*) and shaped pulses (*31*, *32*).

(iv) Phase errors in the applied pulses can be corrected to first order by a corresponding shift in the resonance condition with no loss of robustness to detuning and Rabi frequency errors (see the Supplementary Materials for further details).

For demonstrating the robustness of the PulsePol sequence, we introduce errors into the pulses and free evolutions, with the PulsePol evolution during the pulses described as

$$U_{\theta,\pm X/\pm Y} = \exp\left[-i\frac{\theta}{\Omega_0}\left(\Delta S_z \pm \tilde{\Omega}_0 S_{X/Y} + \sum_j \omega_I I_z^j + S_z\left(A_x^j I_x^j + A_z^j I_z^j\right)\right)\right] \tag{4}$$

including the detuning (frequency mismatch) Δ that is also present during every free evolution and accounting for deviations in pulse strength/length of the pulses by a Rabi frequency error $\delta\Omega = \Omega_0 - \tilde{\Omega}_0$. As the pulse duration is finite, it is subtracted from the waiting time between the pulses. Since the PulsePol sequence corrects the errors after two cycles lasting for a total of 2τ, fluctuations in Ω_0 or ω_S (and hence Δ), which occur on a slower time scale (for example, for X-band frequencies and ^{13}C or ^{1}H, this implies that $2\tau < 1$ μs) will have a similar effect to a constant error; thus, the following described robustness holds also for magnetic field or MW inhomogeneities.

Figure 2B demonstrates the effect of pulse errors by showing the evolution of the polarization of a single nuclear spins as quantified by $2\langle I_z\rangle$ near an initially fully polarized electron spin, when applying the PulsePol sequence and nuclear orientation via electron spin locking (NOVEL) sequence (*17*). The chosen parameters are typical for an NV center spin in a diamond surrounded by ^{13}C nuclear spins. Compared to NOVEL, where small errors can almost completely eliminate the polarization transfer, PulsePol is only slightly affected by these errors.

For a detailed characterization of the robustness, we consider a system of nuclear spins coupled to an electron spin in a diamond. Because

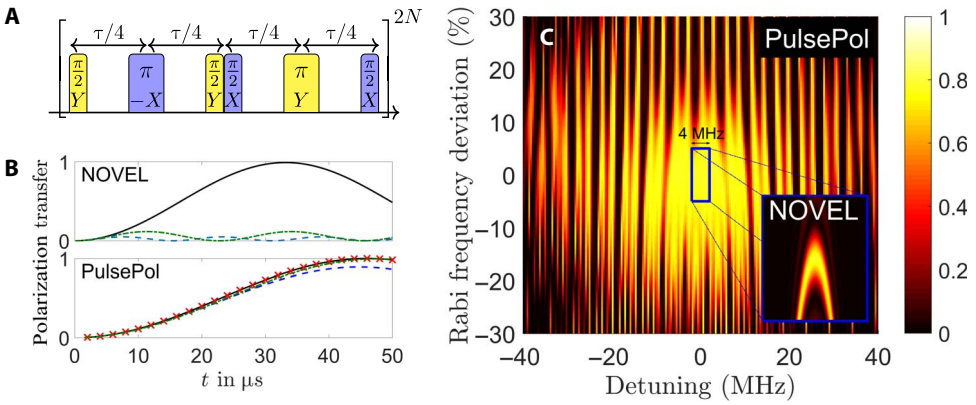


Fig. 2. PulsePol sequence and simulations of robustness. PulsePol sequence (**A**) and robustness compared to nuclear orientation via electron spin locking (NOVEL). (**B**) The polarization transfer to a single nuclear spin for NOVEL (upper graph) under perfect conditions (black line). A $\Delta = (2\pi)0.5$-MHz detuning error (dashed blue line) and 2% Rabi frequency error (dashed-dotted green line) drastically reduce polarization transfer. For PulsePol (lower graph) under perfect conditions (black line), the transfer is 28% slower, as predicted by the effective Hamiltonian of Eq. 2 (red crosses). Detuning errors $\Delta = 0.1\Omega_0 = (2\pi)5$ MHz (dashed blue line) and Rabi frequency errors $\delta\Omega = 0.1\Omega_0 = (2\pi)5$ MHz (dashed-dotted green line) have a very small effect. (**C**) Considering a system of one electron spin and five nuclear spins, for the same parameters $\omega_I = (2\pi)2$ MHz and $\Omega_0 = (2\pi)50$ MHz, polarization transfer versus Δ and $\delta\Omega/\Omega_0$ for the PulsePol sequence, with a comparison to a NOVEL sequence for its relevant detuning values $|\Delta| < (2\pi)2$MHz in the inset. The graphs result from averaging more than 100 realizations of the locations of the five closest nuclear spins to the NV center electron spin on a carbon lattice, and for PulsePol, a resonance shift of 2.5% and corresponding phase errors were used (see the Supplementary Materials).

Downloaded from http://advances.sciencemag.org/ on November 18, 2019

of the 1.1% natural abundance of ^{13}C isotopes, the interaction is dominated by the closest nuclear spins, and we restrict attention of the dynamics of the five closest nuclear spins to the NV center electron spin on the lattice. The resulting polarization transfer efficiency from the fully polarized NV center is quantified by $2\Sigma_i[\langle I_z^i(t)\rangle - \langle I_z^i(0)\rangle]$ for different values of Δ, $\delta\Omega$, and averaged over 100 nuclear spin configurations, as shown in Fig. 2C. As can be seen, efficient polarization transfer can be achieved in a $(2\pi)60$-MHz spectral range for the MW driving strength of $\Omega_0 = (2\pi)50$ MHz. Note that the periodic vertical polarization resonance lines in Fig. 2C are due to the detuning that matches a resonance condition $\Delta\tau/4 = k\pi$ for an integer k during the free evolution.

We find that the PulsePol polarization protocol is robust for a wide range of detuning and Rabi frequency errors, sufficient for overcoming inhomogeneities and enhancing the polarization transfer efficiency in many applications (for example, most radicals or electron defects in a solid/glass). However, for overcoming the wide spectral range inherent in some systems, including NV centers in nanodiamonds and photo-excited triplet states, a wider range of detuning robustness is beneficial. PulsePol can be optimized further by making use of broadband universal rotations that have been developed in NMR spectroscopy.

Composite pulses or numerically optimized pulses, especially those derived with optimal control algorithms, have been used in NMR (*24*) and, more recently in electron paramagnetic resonance (EPR) (*31*), can be used to engineer the pulses for a required amount of robustness to detuning and pulse strength. Symmetric phase pulses (see the Supplementary Materials) (*23*) or the BURBOP (broadband universal rotations by optimal control) pulses defined in (*24*) can extend the spectral range robustness of PulsePol by a factor of 2 to around $(2\pi)120$ MHz for the same pulse duration as those used in Fig. 2. Experimental effects, such as the resonator bandwidth, can be included in the numerical optimization and accommodated for in the engineered pulses (*31*).

It is worth noting that, unlike traditional methods in EPR/NMR using short pulses for transferring polarization between spins [for example, pulsed ENDOR (electron nuclear double resonance) (*33*) and INEPT (insensitive nuclei enhanced by polarization transfer) (*34*)], no radio frequency pulse or nuclear spin manipulation is required in PulsePol, making it much easier to implement experimentally and mitigate issues due to nuclear rotations taking three orders of magnitude longer time.

RESULTS

The NV center with its electron spin has recently gained considerable interest as a resource spin for optical DNP for polarizing nuclear spins inside the diamond (*1*–*5*, *10*) and in external molecules (*6*, *35*–*37*). The NV center realizes in its ground state an electronic spin triplet ($S = 1$), which exhibits a zero-field splitting of $D = (2\pi)2.87$ GHz that separates the $m_s = 0$ state energetically from the $m_s = \pm 1$ states, which are split by an applied magnetic field. One of them forms with $m_s = 0$ the desired effective two-level system shown in Fig. 3A. The NV spin can be optically polarized within 200 ns by a laser pulse that induces spin-selective relaxation into the $m_s = 0$ sublevel of the ground state, resulting in spin polarization exceeding 92% (*38*).

Using this setup, the NV center can be used to polarize the surrounding nuclear spins and to use the same center to read out the polarization using polarization readout by polarization inversion (PROPI) (*20*) with the sequence in Fig. 3B. This allows to probe the effectiveness of polarization schemes on the level of a single NV center, providing an experimental testbed for polarization schemes. Figure 3C demonstrates the polarization efficiency of PulsePol and its robustness to detuning compared to NOVEL. The resonance shift in the free evolution time due to hardware phase errors was checked and found to be near the optimal value (see the Supplemental Materials). The robust polarization of PulsePol for about $(2\pi)60$-MHz spectral width can be seen and is in very good agreement with the theoretical simulations with five nuclear spins. One should mention that this spectral width is only limited by the power of the MW (the larger the power, the larger the width).

Previously developed methods to compensate for the lack of robustness of NOVEL and the solid effect were based on sweep-based schemes, such as ISE. However, performing this sweep induces a trade-off between its robustness to detuning and the polarization efficiency (the polarization efficiency is inversely proportional to the sweep speed; thus, larger sweep range either decreases efficiency or increases sequence time), which is not present in PulsePol. Figure 3D shows the comparison for the polarization

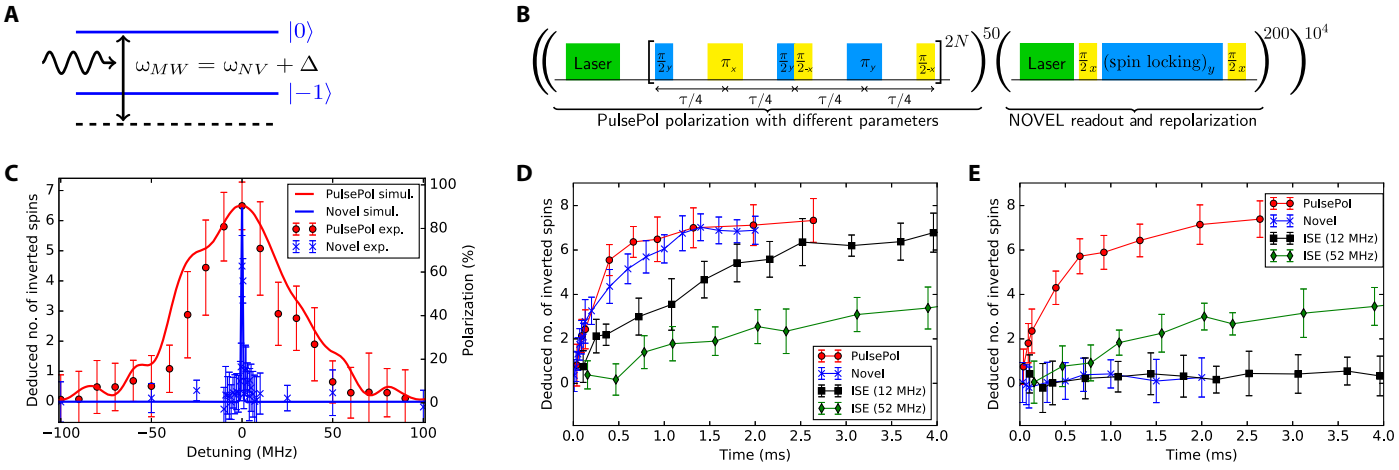


Fig. 3. Experimental implementation via optically polarized NV centers in diamond. (**A**) Probing robustness to detuning on a single NV by detuning the MW frequency from the NV $|m_s = 0\rangle \leftrightarrow |m_s = -1\rangle$ transition. (**B**) PROPI sequence used for detecting polarization efficiency of PulsePol. (**C**) PROPI readout for different detunings Δ for PulsePol (red) and NOVEL (blue). The lines are the smoothed simulation result of a comparable nuclear spin bath with no free parameters. For more details, see text. Polarization buildup by consecutive polarization transfers for NOVEL, PulsePol, and ISE (**D**) for $\Delta = 0$ MHz, where all sequences, (**E**) $\Delta = (2\pi)20$ MHz, where only PulsePol and very slow ISE are able to transfer polarization.

Downloaded from http://advances.sciencemag.org/ on November 18, 2019

buildup rate of PulsePol, NOVEL, and ISE [experimental parameters: Rabi frequency $\Omega = (2\pi)1.79$ MHz and inverse sweep rate of 3 μs/(2π) MHz, near optimal for this NV's coupling to the nuclear spin bath], under exact resonance conditions. For ISE, across a (2π)12-MHz bandwidth (the minimal range that is required to achieve polarization transfer for typical parameters) (*20*) and across a (2π)52-MHz bandwidth [which achieves polarization transfer across a (2π)40-MHz spectral range] were chosen. For the case of perfect resonance, the buildup rates for PulsePol and NOVEL are comparable because PulsePol has a factor α in its effective Hamiltonian Eq. 2 and encompasses the three resonances because of the hyperfine interaction with the nitrogen nuclear spin. However, for ISE [(2π)12 MHz] and ISE[(2π)52 MHz], the rate is significantly slower because of the quadratic dependence on the interaction with the nuclear spins in the efficiency of the MW sweep. Figure 3E shows a similar comparison with $\Delta = (2\pi)$20-MHz detuning. While the performance of PulsePol and ISE[(2π)52 MHz] remains essentially unchanged, for both NOVEL and ISE[(2π)12 MHz], the NV spin no longer transfers polarization to the surrounding nuclear spin bath.

DISCUSSION

Important hyperpolarization applications with NV centers in diamonds where PulsePol is directly applicable are as follows: (i) the polarization of nuclear spins in molecules external to the diamond with an ensemble of shallow NV centers (see Fig. 4A) (*6*, *35*, *36*), where polarization transfer efficiency is the bottleneck of the achieved polarization, and (ii) the hyperpolarization of nanodiamonds as MRI biomarkers. Nanodiamonds have been previously polarized at cryogenic temperatures (1 to 3 K) and high magnetic fields (*9*, *11*, *12*). Optical polarization via NV centers at room temperature offers several key advantages such as less complex and costly experimental setups and faster polarization buildup time (*10*). For NV center nanodiamond polarization, an outstanding challenge is that the NV resonance can be significantly shifted because of the random lattice orientation of the nanodiamond relatively to magnetic field orientation (Fig. 4B) and (iii) the initialization of quantum simulators based on two- and three-dimensional arrays of nuclear spins (*7*, *8*).

Common to all these applications are the requirement of near shallow NV centers, which can exhibit between (2π)2- and (2π)20-MHz variance in the NV resonance due to surface electric charges as well as interactions with P1 centers and other surface defects (potentially more in dense ensembles). As the coupling between the shallow NV spin and nuclear spin bath is very weak, even coherent polarization transfer approaches the NV relaxation time, and ISE will not markedly increase the polarization efficiency compared with NOVEL. It is important to note that, while the speed of polarization transfer of current DNP schemes such as NOVEL in a bulk diamond is not a limiting bottleneck, the speed of polarization buildup is vital in applications such as polarization of molecules in liquid, where building up a high polarization during the relaxation time of the nuclear spins in the molecules is expected to be the main challenge. We simulate the polarization transfer from the NV center to diffusing molecules via tensor-network methods for two diffusion coefficients in Fig. 4C, exploiting the time-evolving block decimation (TEBD). Critically, PulsePol shows more than 80% polarization efficiency, whereas NOVEL (as well as ISE) is expected to perform an order of magnitude worse for this parameter regime. The inset elucidates the reason for this high efficiency, as the frequency detunings of most shallow NV centers are corrected by PulsePol.

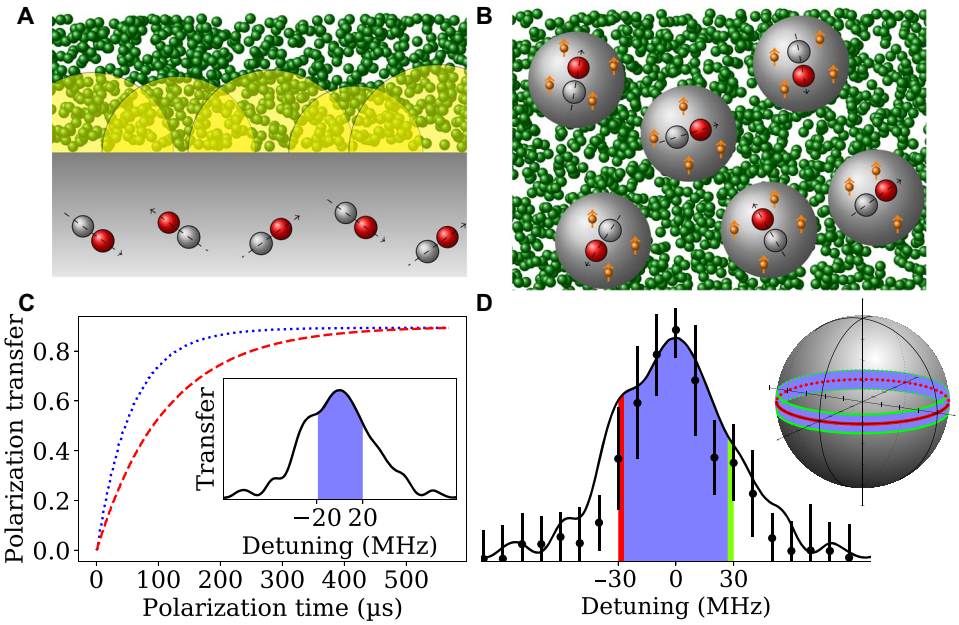


Fig. 4. Hyperpolarization applications with NV centers in diamonds. (**A**) Illustration of shallow NV polarization setup, where NV centers implanted ~3-nm-deep polarize-diffusing molecules in a solution outside of the diamond and (**B**) nanodiamonds with randomly oriented NV centers, where the polarization of ^{13}C spins (orange) allows for the usage as MRI contrast agents. (**C**) Polarization transfer from near-surface NV centers to a bath of 1200 nuclear spin bath, using the same Rabi and Larmor frequency and sequence as in Fig. 2C averaged over NV centers with transition frequencies drawn from a Gaussian distribution with a (2π)20-MHz width. The simulation uses matrix product states (*39*) and a diffusion coefficient of $D = 1.4/2.8 \times 10^{-12} m^2/s$ (blue dotted/red dashed curve), resulting in different correlation times and efficiencies. The inset shows that the NV linewidth is well within the working range of the PulsePol protocol [$\Omega = (2\pi)$50MHz]. More details of the simulation are included in the Supplementary Materials. (**D**) On the basis of the resilience to detunings $|\Delta| < (2\pi)$30MHz for a Rabi frequency of $\Omega = (2\pi)$50MHz, more than 11% of the NV orientations in nanodiamonds (azimuthal angle between 90° ± 6.5°, as shown on the sphere) contribute to polarization transfer.

Downloaded from http://advances.sciencemag.org/ on November 18, 2019

For being applicable to nanodiamond polarization, we have strong magnetic field along the z direction of laboratory frame of reference ($\gamma_e B \gg D$ with γ_e the gyromagnetic ratio) and uniformed laboratory frame of reference for different orientations of the NV center. However, due to the large zero-field splitting, the NV detuning can reach the order of a gigahertz. In addition, the optical polarization and readout of the NV decrease for high misalignment between the magnetic field and NV axis ($\theta > 20°$), although when approaching $\theta = 90°$, the NV center optical polarization and readout again become efficient (*10*). By choosing the MW frequency near the NV resonance corresponding to 90° angle between the diamond axis and external field (Fig. 4D), more than 11% of the NV orientations can be addressed within just $(2\pi)60$ MHz (*10*), which, in turn, can be achieved by applying PulsePol with $(2\pi)49$-MHz Rabi frequency (for comparison, note that even in bulk diamond, only 25% NV centers participate in polarization dynamics due to four possible orientations in the lattice). The involved orientations are shown in Fig. 4D. Because of the Brownian rotation of the nanodiamonds in a solution, this wide NV addressability leads to all nanodiamonds becoming hyperpolarized under reasonable conditions (*10*).

CONCLUSION

In conclusion, we have introduced a framework that allows for the design of highly robust and efficient pulsed DNP schemes that transfer polarization from electron to nuclear spins via pulse sequences that create an effective evolution that is described by a flip-flop Hamiltonian. We have presented a specific example sequence, PulsePol, which not only achieves polarization transfer rates that are similar to those for existing schemes when operated under ideal conditions but also affords a flexibility that confers a remarkable robustness to detuning, spectral width, and pulse errors because PulsePol does not need to satisfy an H-H resonance for the MW amplitude. We underline the practical potential of PulsePol, with the experimental demonstration of its efficiency in transferring polarization from an optically polarized NV center in diamond to the surrounding ^{13}C nuclear spin bath over a range of more than $(2\pi)60$-MHz detuning, where this range is only limited by the MW drive. This efficient and robust polarization transfer by PulsePol significantly enhances the potential of hyperpolarization of external molecules for nanoscale NMR or quantum simulators using near-surface NV centers and of nanodiamonds as hyperpolarized MRI markers and polarization agents.

The PulsePol sequence and the framework within which it was derived have considerable flexibility, which allows it to be used in a wide variety of DNP experiments, potentially including those conducted via radicals or at low temperatures. In addition to the advantages of robustness to MW and magnetic field inhomogeneity, the reduced sensitivity to the electron resonance frequency will enhance polarization transfer in cases where hyperfine splitting or the anisotropic g-tensor broadens the electron spectral width.

MATERIALS AND METHODS

Experiments in diamond: The PROPI sequence used consisted of two parts (Fig. 3B), which were repeated 5×10^4 times. The experiment started with a thermally polarized nuclear spin bath. With the first part of PROPI, nuclear spins were polarized into the $|\uparrow\rangle$ state with 50 sequence cycles of PulsePol. Then, with the second part of PROPI, the nuclear spin bath was fully polarized into the $|\downarrow\downarrow\downarrow\ldots\rangle$ direction with 200 cycles of a well-known polarization sequence; in this case, NOVEL with a 10-μs spin-locking time and matched H-H conditions was used. With this number of cycles, a saturation of the polarization transfer could be achieved. Hence, from the second repetition on, the first part of PROPI started with a fully polarized nuclear spin bath ($|\downarrow\downarrow\downarrow\ldots\rangle$), which reversed nuclear spins into the opposite ($|\uparrow\rangle$) direction up to a certain degree. The amount of transferred polarization depends on the efficiency of the sequence to be tested, for example, PulsePol, ISE, or NOVEL. The nuclear polarization signal was observed during the repolarization part (second part) by monitoring the NV's fluorescence. A bright signal, originated from flip-flop processes between the NV electron spin and nuclear spins, saturated to a darker signal when the spin bath reached a completely polarized state. Hereby, the area below the saturation curve (first 100 of 200 cycles) gave a measure of nuclear polarization.

To determine the behavior of PulsePol with regard to detuning errors, we added a detuning $\Delta = \omega_{1\leftrightarrow 0} - \omega_{MW}$ between the $|m_s = 0\rangle \leftrightarrow |m_s = -1\rangle$ transition frequency and the external MW field frequency (Fig. 3A), using a drive of approximately $\Omega_0 = (2\pi)49$-MHz Rabi frequency for the pulses. Additional experimental parameters: Rabi frequency $\Omega = (2\pi)1.86$ MHz matching H-H conditions and a spin-locking pulse of 10 μs.

All experiments were performed at a magnetic field of approximately 1740 G and an alignment of the external field in respect to the NV axis to better than 1°. The MW was applied to the NV through an electroplated stripline on diamond. The attenuation of this stripline was frequency-dependent, such that the amplitude of the MW during PulsePol was corrected up to a deviation of the Rabi frequency of < ±5%. Potential depolarization effects in the case of severely detuned pulses were checked and found to be negligible (see the Supplementary Materials).

Polarization of molecules via shallow NV centers: To simulate the surface NV ensemble interacting with diffusing spins, we performed the following. The quantum system to be simulated comprised the electron spin of an NV center and multiple nuclear spins. The parallel and perpendicular coupling constants describing the NV spin interaction were obtained numerically by simulating the diffusion of the 1200 most strongly coupled spins, which accounts for two-thirds of the total coupling strength. We simulated 100 different NV spin systems with (2π) 20-MHz SD in the NV resonance frequency to account for the broad linewidth. During evolution under PulsePol, the entanglement between the different constituents was limited and can therefore be simulated efficiently via tensor-network methods. We exploited the TEBD algorithm (*39*) to perform the final simulations (Fig. 4C).

SUPPLEMENTARY MATERIALS

Supplementary material for this article is available at http://advances.sciencemag.org/cgi/content/full/4/8/eaat8978/DC1

Supplementary Text
Section S1. Hamiltonian of the system
Section S2. Effective Hamiltonian of PulsePol
Section S3. Error robustness
Section S4. Finite pulses
Section S5. Composite pulses
Section S6. Effect of phase errors
Section S7. Hamiltonian with NV centers in nanodiamonds
Section S8. Depolarization behavior
Section S9. Simulation parameters for shallow NV centers
Fig. S1. MW pulse sequence for pulsed polarization transfer.
Fig. S2. Error resistance of PulsePol by using composite pulses.
Fig. S3. Effect of phase errors.
Fig. S4. Error resistance of PulsePol versus the resonance shift.
Fig. S5. Comparison between simulation results and experimental data of polarization buildup and depolarization.

Downloaded from http://advances.sciencemag.org/ on November 18, 2019

REFERENCES AND NOTES

1. P. London, J. Scheuer, J.-M. Cai, I. Schwarz, A. Retzker, M. B. Plenio, M. Katagiri, T. Teraji, S. Koizumi, J. Isoya, R. Fischer, L. P. McGuinness, B. Naydenov, F. Jelezko, Detecting and polarizing nuclear spins with nuclear double resonance on a single electron spin. *Phys. Rev. Lett.* **111**, 067601 (2013).
2. J. Scheuer, I. Schwartz, Q. Chen, D. Schulze-Sünninghausen, P. Carl, P. Höfer, A. Retzker, H. Sumiya, J. Isoya, B. Luy, M. B. Plenio, B. Naydenov, F. Jelezko, Optically induced dynamic nuclear spin polarisation in diamond. *New J. Phys.* **18**, 013040 (2016).
3. G. A. Álvarez, C. O. Bretschneider, R. Fischer, P. London, H. Kanda, S. Onoda, J. Isoya, D. Gershoni, L. Frydman, Local and bulk ^{13}C hyperpolarization in nitrogen-vacancy-centred diamonds at variable fields and orientations. *Nat. Commun.* **6**, 8456 (2015).
4. J. P. King, K. Jeong, C. C. Vassiliou, C. S. Shin, R. H. Page, C. E. Avalos, H.-J. Wang, A. Pines, Room-temperature in situ nuclear spin hyperpolarization from optically pumped nitrogen vacancy centres in diamond. *Nat. Commun.* **6**, 8965 (2015).
5. M. Drake, E. Scott, J. A. Reimer, Influence of magnetic field alignment and defect concentration on nitrogen-vacancy polarization in diamond. *New J. Phys.* **18**, 013011 (2015).
6. P. Fernández-Acebal, O. Rosolio, J. Scheuer, C. Müller, S. Müller, S. Schmitt, L. P. McGuinness, I. Schwartz, Q. Chen, A. Retzker, B. Naydenov, F. Jelezko, M. B. Plenio, Toward hyperpolarization of oil molecules via single nitrogen vacancy centers in diamond. *Nano Lett.* **18**, 1882–1887 (2018).
7. J. Cai, A. Retzker, F. Jelezko, M. B. Plenio, A large-scale quantum simulator on a diamond surface at room temperature. *Nat. Phys.* **9**, 168–173 (2013).
8. T. Unden, N. Tomek, T. Weggler, F. Frank, P. London, J. Zopes, C. Degen, N. Raatz, J. Meijer, H. Watanabe, K. M. Itoh, M. B. Plenio, B. Naydenov, F. Jelezko, Coherent control of solid state nuclear spin nano-ensembles; arXiv:1802.02921 (2018).
9. E. Rej, T. Gaebel, T. Boele, D. E. J. Waddington, D. J. Reilly, Hyperpolarized nanodiamond with long spin-relaxation times. *Nat. Commun.* **6**, 8459 (2015).
10. Q. Chen, I. Schwarz, F. Jelezko, A. Retzker, M. B. Plenio, Optical hyperpolarization of ^{13}C nuclear spins in nanodiamond ensembles. *Phys. Rev. B* **92**, 184420 (2015).
11. G. Kwiatkowski, F. Jähnig, J. Steinhauser, P. Wespi, M. Ernst, S. Kozerke, Direct hyperpolarization of micro- and nanodiamonds for bioimaging applications—Considerations on particle size, functionalization and polarization loss. *J. Magn. Reson.* **286**, 42–51 (2018).
12. C. O. Bretschneider, Ü. Akbey, F. Aussenac, G. L. Olsen, A. Feintuch, H. Oschkinat, L. Frydman, On the potential of dynamic nuclear polarization enhanced diamonds in solid-state and dissolution ^{13}C NMR spectroscopy. *ChemPhysChem* **17**, 2691–2701 (2016).
13. A. Ajoy, K. Liu, R. Nazaryan, X. Lv, P. R. Zangara, B. Safvati, G. Wang, D. Arnold, G. Li, A. Lin, P. Raghavan, E. Druga, S. Dhomkar, D. Pagliero, J. A. Reimer, D. Suter, C. A. Meriles, A. Pines, Orientation-independent room temperature optical ^{13}C hyperpolarization in powdered diamond. *Sci. Adv.* **4**, eaar5492 (2018).
14. I. Schwartz, J. Rosskopf, S. Schmitt, B. Tratzmiller, Q. Chen, L. P. McGuinness, F. Jelezko, M. B. Plenio, Blueprint for nanoscale NMR; arXiv:1706.07134 (2017).
15. K. Tateishi, M. Negoro, S. Nishida, A. Kagawa, Y. Morita, M. Kitagawa, Room temperature hyperpolarization of nuclear spins in bulk. *Proc. Natl. Acad. Sci. U.S.A.* **111**, 7527–7530 (2014).
16. A. Abragam, W. Proctor, A new method of dynamic polarization of atomic nuclei in solids. *Compt. Rend.* **246**, 2253 (1958).
17. A. Henstra, P. Dirksen, J. Schmidt, W. T. Wenckebach, Nuclear spin orientation via electron spin locking (NOVEL). *J. Magn. Reson.* **77**, 389–393 (1988).
18. A. Henstra, P. Dirksen, W. T. Wenckebach, Enhanced dynamic nuclear polarization by the integrated solid effect. *Phys. Lett. A* **134**, 134–136 (1988).
19. S. R. Hartmann, E. L. Hahn, Nuclear double resonance in the rotating frame. *Phys. Rev.* **128**, 2042 (1962).
20. J. Scheuer, I. Schwartz, S. Müller, Q. Chen, I. Dhand, M. B. Plenio, B. Naydenov, F. Jelezko, Robust techniques for polarization and detection of nuclear spin ensembles. *Phys. Rev. B* **96**, 174436 (2017).
21. S. Machnes, M. B. Plenio, B. Reznik, A. M. Steane, A. Retzker, Superfast laser cooling. *Phys. Rev. Lett.* **104**, 183001 (2010).
22. S. Machnes, J. Cerrillo, M. Aspelmeyer, W. Wieczorek, M. B. Plenio, A. Retzker, Pulsed laser cooling for cavity optomechanical resonators. *Phys. Rev. Lett.* **108**, 153601 (2012).
23. A. J. Shaka, A. Pines, Symmetric phase-alternating composite pulses. *J. Magn. Reson.* **71**, 495–503 (1987).
24. K. Kobzar, S. Ehni, T. E. Skinner, S. J. Glaser, B. Luy, Exploring the limits of broadband 90° and 180° universal rotation pulses. *J. Magn. Reson.* **225**, 142–160 (2012).
25. W. Yang, Z.-Y. Wang, R.-B. Liu, Preserving qubit coherence by dynamical decoupling. *Front. Phys.* **6**, 2–14 (2011).
26. A. M. Souza, G. A. Álvarez, D. Suter, Robust dynamical decoupling. *Philos. Trans. Ser. A Math. Phys. Eng. Sci.* **370**, 4748–4769 (2012).
27. H. Y. Carr, E. M. Purcell, Effects of diffusion on free precession in nuclear magnetic resonance experiments. *Phys. Rev.* **94**, 630 (1954).
28. A. A. Maudsley, Modified Carr-Purcell-Meiboom-Gill sequence for NMR fourier imaging applications. *J. Magn. Reson.* **69**, 488–491 (1986).
29. T. H. Taminiau, J. Cramer, T. van der Sar, V. V. Dobrovitski, R. Hanson, Universal control and error correction in multi-qubit spin registers in diamond. *Nat. Nanotechnol.* **9**, 171–176 (2014).
30. Z.-Y. Wang, J. Casanova, M. B. Plenio, Delayed entanglement echo for individual control of a large number of nuclear spins. *Nat. Commun.* **8**, 14660 (2017).
31. P. E. Spindler, Y. Zhang, B. Endeward, N. Gershernzon, T. E. Skinner, S. J. Glaser, T. F. Prisner, Shaped optimal control pulses for increased excitation bandwidth in EPR. *J. Magn. Reson.* **218**, 49–58 (2012).
32. J. Casanova, Z.-Y. Wang, I. Schwartz, M. B. Plenio, Shaped pulses for energy efficient high-field NMR at the nanoscale; arXiv:1805.01741 (2018).
33. E. R. Davies, A new pulse endor technique. *Phys. Lett. A* **47**, 1–2 (1974).
34. G. A. Morris, R. Freeman, Enhancement of nuclear magnetic resonance signals by polarization transfer. *J. Am. Chem. Soc.* **101**, 760–762 (1979).
35. Q. Chen, I. Schwarz, F. Jelezko, A. Retzker, M. B. Plenio, Resonance-inclined optical nuclear spin polarization of liquids in diamond structures. *Phys. Rev. B* **93**, 060408(R) (2016).
36. D. A. Broadway, J.-P. Tetienne, A. Stacey, J. D. A. Wood, D. A. Simpson, L. T. Hall, L. C. L. Hollenberg, Quantum probe hyperpolarisation of molecular nuclear spins. *Nat. Commun.* **9**, 1246 (2018).
37. D. Abrams, M. E. Trusheim, D. R. Englund, M. D. Shattuck, C. A. Meriles, Dynamic nuclear spin polarization of liquids and gases in contact with nanostructured diamond. *Nano Lett.* **14**, 2471–2478 (2014).
38. G. Waldherr, J. Beck, M. Steiner, P. Neumann, A. Gali, T. Frauenheim, F. Jelezko, J. Wrachtrup, Dark states of single nitrogen-vacancy centers in diamond unraveled by single shot NMR. *Phys. Rev. Lett.* **106**, 157601 (2011).
39. U. Schollwoeck, The density-matrix renormalization group in the age of matrix product states. *Ann. Phys. Rehabil. Med.* **326**, 96–192 (2011).

Acknowledgments: We thank J. F. Haase for useful discussions. **Funding:** This work was supported by the European Union project, the European Research Council Synergy grant, a PhD fellowship of the Integrated Center for Quantum Science and Technology, the Humboldt Research Fellowship for Postdoctoral Researchers, the Deutsche Forschungsgemeinschaft Collaborative Research Centre 1279, and the state of Baden-Württemberg through bwHPC (Baden-Wuerttemberg high performance computing). **Author contributions:** I.S., M.B.P., Q.C., and Z.-Y.W. conceived the idea. B.T. carried out the simulations and analytical work with input from I.S., Q.C., and M.B.P. J.S. and S.M. performed the experiments. I.D. performed the theoretical simulations for shallow NV centers. B.N., C.M., and F.J. advised on the several aspects of experiments. I.S., B.T., and Q.C. wrote the manuscript with input from all authors. All authors reviewed the manuscript and suggested improvements. M.B.P. supervised the overall research effort. **Competing interests:** I.S., M.B.P., Q.C., and Z.-Y.W. are inventors on patent application PCT/EP2017/084229 related to this work. M.B.P. holds a contractual agreement as adviser to NVision Imaging Technologies and holds an observer seat on the board of NVision Imaging Technologies. F.J. holds a contractual agreement as adviser to NVision Imaging Technologies. The other authors declare that they have no competing interests. **Data and materials availability:** All data needed to evaluate the conclusions in the paper are present in the paper and/or the Supplementary Materials. Additional data related to this paper may be requested from the authors.

Submitted 18 April 2018
Accepted 24 July 2018
Published 31 August 2018
10.1126/sciadv.aat8978

Citation: I. Schwartz, J. Scheuer, B. Tratzmiller, S. Müller, Q. Chen, I. Dhand, Z.-Y. Wang, C. Müller, B. Naydenov, F. Jelezko, M. B. Plenio, Robust optical polarization of nuclear spin baths using Hamiltonian engineering of nitrogen-vacancy center quantum dynamics. *Sci. Adv.* **4**, eaat8978 (2018).

Downloaded from http://advances.sciencemag.org/ on November 18, 2019

Science Advances
AAAS

advances.sciencemag.org/cgi/content/full/4/8/eaat8978/DC1

Supplementary Materials for

Robust optical polarization of nuclear spin baths using Hamiltonian engineering of nitrogen-vacancy center quantum dynamics

Ilai Schwartz*, Jochen Scheuer, Benedikt Tratzmiller, Samuel Müller, Qiong Chen*, Ish Dhand, Zhen-Yu Wang, Christoph Müller, Boris Naydenov, Fedor Jelezko, Martin B. Plenio*

*Corresponding author. Email: qiong.chen@uni-ulm.de (Q.C.); ilai.schwartz@uni-ulm.de (I.S.); martin.plenio@uni-ulm.de (M.B.P.)

Published 31 August 2018, *Sci. Adv.* **4**, eaat8978 (2018)
DOI: 10.1126/sciadv.aat8978

This PDF file includes:

Supplementary Text
Section S1. Hamiltonian of the system
Section S2. Effective Hamiltonian of PulsePol
Section S3. Error robustness
Section S4. Finite pulses
Section S5. Composite pulses
Section S6. Effect of phase errors
Section S7. Hamiltonian with NV centers in nanodiamonds
Section S8. Depolarization behavior
Section S9. Simulation parameters for shallow NV centers
Fig. S1. MW pulse sequence for pulsed polarization transfer.
Fig. S2. Error resistance of PulsePol by using composite pulses.
Fig. S3. Effect of phase errors.
Fig. S4. Error resistance of PulsePol versus the resonance shift.
Fig. S5. Comparison between simulation results and experimental data of polarization buildup and depolarization.

Supplementary Information

Section S1. Hamiltonian of the system

We consider a system of a single electron spin $\vec{S}$ ($S = \frac{1}{2}$) coupled to N nuclear spins $\vec{I}^{(n)}$ (spin-1/2). The System is described by the Hamiltonian

$$H = \omega_S S_z + \sum_{n=1}^{N} \omega_I I_z^{(n)} + \sum_{n=1}^{N} \vec{S}\mathcal{A}\vec{I}^{(n)} + 2\Omega(t) S_x \cos(\omega_{MW} t + \varphi) \tag{1}$$

where $\omega_S(\omega_I)$ denotes the electron (nuclear) Larmor frequency, $\mathcal{A}$ the hyperfine coupling tensor describing the interaction between electron and nuclear spins resulting from the magnetic dipole-dipole coupling, ω_{MW} the microwave frequency, φ the microwave phase, and the Rabi frequency $\Omega(t)$ has the value Ω_0 when the microwave is on, and 0 otherwise.
In a rotating frame with respect to $\omega_S S_z$ and after applying the secular approximation, the Hamiltonian is

$$H_{\text{int}} = \Delta S_z + \sum_{n=1}^{N} \omega_I I_z^{(n)} + \sum_{n=1}^{N} S_z \vec{\mathcal{A}}\vec{I}^{(n)} + \Omega(t)(S_x \cos\varphi + S_y \sin\varphi) \tag{2}$$

with $\Delta = \omega_S - \omega_{MW}$ denoting the detuning between the MW and electron Larmor frequency. In a nuclear spin basis such that $A_y = 0$ we obtain the basic Hamiltonian:

$$H_{\text{int}} = \Delta S_z + \sum_{n=1}^{N} \omega_I I_z^{(n)} + \sum_{n=1}^{N} S_z\left(A_x I_x^{(n)} + A_z I_z^{(n)}\right) + \Omega(t)(S_x \cos\varphi + S_y \sin\varphi) \tag{3}$$

According to this Hamiltonian, the free evolution operator for a time τ is

$$\begin{aligned} U_{\text{free}}(\tau) &= \exp\left(-i\tau\left(\Delta S_z + \sum_{n=1}^{N} \omega_I I_z^{(n)} + \sum_{n=1}^{N} S_z\left(A_x I_x^{(n)} + A_z I_z^{(n)}\right)\right)\right) \\ &= \exp\left(-i\tau\left(\sum_{n=1}^{N} \omega_I I_z^{(n)} + \sum_{n=1}^{N} S_z\left(A_x I_x^{(n)} + A_z I_z^{(n)}\right)\right)\right)\exp\left(-i\tau\Delta S_z\right) \end{aligned} \tag{4}$$

where the last equality holds as the ΔS_z term commutes with the other terms in the exponent.
The pulses have an additional Rabi term and are described by

$$U_{\phi,\pm\text{X}/\pm\text{Y}} = \exp\left(-i\frac{\phi}{\Omega_0}\left(\Delta S_z + \sum_{n=1}^{N} \omega_I I_z^{(n)} + \sum_{n=1}^{N} S_z\left(A_x I_x^{(n)} + A_z I_z^{(n)} \pm \Omega_0 S_{\text{X/Y}}\right)\right)\right) \tag{5}$$

As it is difficult to understand the dynamics from this description, the next section uses a model with only one nuclear spin to derive an effective Hamiltonian.

Section S2. Effective Hamiltonian of PulsePol

The PulsePol sequence as shown in the text is given by

$$\left[\left(\frac{\pi}{2}\right)_Y \overset{\tau/4}{\text{——}} (\pi)_X \overset{\tau/4}{\text{——}} \left(\frac{\pi}{2}\right)_Y \left(\frac{\pi}{2}\right)_{-X} \overset{\tau/4}{\text{——}} (\pi)_Y \overset{\tau/4}{\text{——}} \left(\frac{\pi}{2}\right)_{-X}\right]^{2N} \tag{6}$$

where $(\phi)_{X,\pm Y}$ denote pulses around the X-/Y-axis with duration $t' = \phi/\Omega$ and phase $\varphi = 0, \pm\pi/2$ and $\overset{\tau/4}{\text{——}}$ denotes a free evolution for a time $\tau/4$, which depends on the nuclear Larmor frequency. The basic sequence block is repeated $2N$ times, where N is a positive integer.

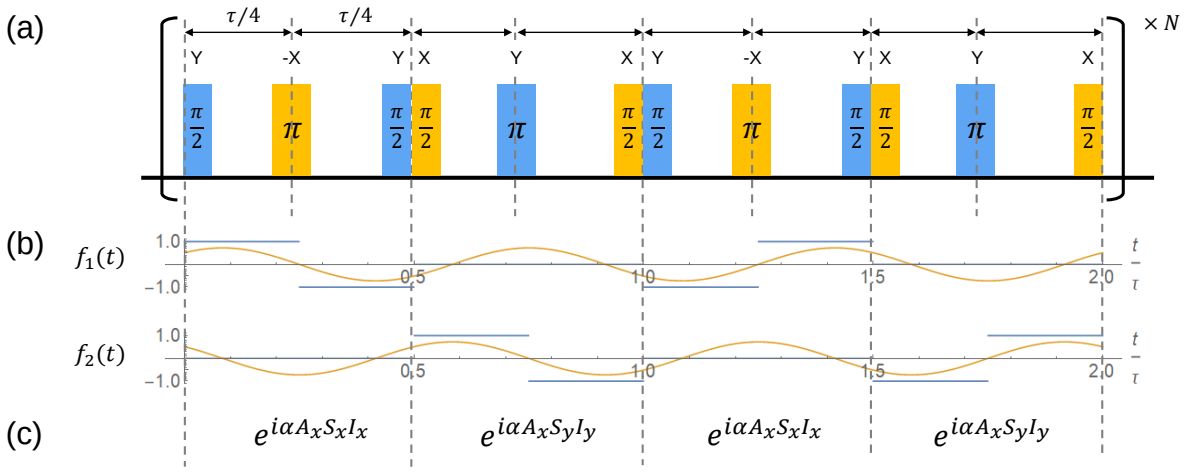


Fig. S1. MW pulse sequence for pulsed polarization transfer. (a) Schematics of the MW pulse sequence on the electron spin for pulsed polarisation transfer to nuclear spins. Blue bars denote Y pulses and orange ones X or -X pulses. The sequence alternates between four sections. (b) The values of the modulation functions for the sections are $f_1(t) \sim \cos(3\pi t/\tau - \pi/4)$ and $f_2(t) \sim -\sin(3\pi t/\tau - \pi/4)$ for S_x and S_y (blue), and their dominant Fourier component (orange) (c) The pulse sequence produces 4 distinct sections, each with an effective Hamiltonian in the rotating frame. The combination of a basis change for the electron spin in each section with the $\pi/2$ phase shift in the modulation function leads to the effective average Hamiltonian $S_x I_x + S_y I_y = 1/2(S_+ I_- + S_- I_+)$ which produces the polarisation transfer between electron spin and nuclei.

Here we express the spin operators in terms of the Pauli matrices σ_i ($i \in \{x, y, z\}$): $S_i = \frac{1}{2}\sigma_i$. According the PulsePol sequence in Eq. (6), by using $U_{\frac{\pi}{2},\mathrm{X}} \begin{pmatrix}\sigma_x\\ \sigma_y\\ \sigma_z\end{pmatrix} U_{\frac{\pi}{2},\text{-X}} = \begin{pmatrix}\sigma_x\\ \sigma_z\\ -\sigma_y\end{pmatrix}$ and $U_{\frac{\pi}{2},\mathrm{Y}} \begin{pmatrix}\sigma_x\\ \sigma_y\\ \sigma_z\end{pmatrix} U_{\frac{\pi}{2},\text{-Y}} = \begin{pmatrix}-\sigma_z\\ \sigma_y\\ \sigma_x\end{pmatrix}$, one can rewrite the evolution as

$$U_{\text{cycle}} = U_{\frac{\tau}{4},\text{-Y}} U_{\frac{\tau}{4},\mathrm{Y}} U_{\frac{\tau}{4},\text{-X}} U_{\frac{\tau}{4},\mathrm{X}} U_{\frac{\tau}{4},\mathrm{Y}} U_{\frac{\tau}{4},\text{-Y}} U_{\frac{\tau}{4},\mathrm{X}} U_{\frac{\tau}{4},\text{-X}} \tag{7}$$

where

$$U_{\tau,\pm\mathrm{X}/\pm\mathrm{Y}} = \exp\left(-i \sum_{n=1}^{N} \tau \left(\omega_I I_z^{(n)} \pm S_{x/y}(A_x I_x^{(n)} + A_z I_z^{(n)})\right)\right) \tag{8}$$

This means the evolution can be expressed with an effective Hamiltonian

$$H_{\text{eff}}^{(1)} = \sum_{n=1}^{N} \omega_I I_z^{(n)} + (-f_1(t) S_x - f_2(t) S_y)(A_x I_x^{(n)} + A_z I_z^{(n)}) \tag{9}$$

The functions $f_{1/2}$ and how they emerge from the sequence are shown in figure S1. They can be expressed as Fourier series

$$\begin{aligned} f_1(t + k \cdot 2\tau) &= \begin{cases} 1, & \text{for } 0\tau \leqslant t \leqslant \tau/4,\ 5\tau/4 \leqslant t \leqslant 3\tau/2 \\ -1, & \text{for } \tau/4 \leqslant t \leqslant \tau/2,\ \tau \leqslant t \leqslant 5\tau/4 \\ 0, & \text{otherwise} \end{cases} \\ &= \sum_{n=0}^{\infty} a_n^{(1)} \cos\frac{\pi n t}{\tau} + b_n^{(1)} \sin\frac{\pi n t}{\tau} \end{aligned} \tag{10}$$

and

$$f_2(t + k \cdot 2\tau) = f_1\left(t - \frac{\tau}{2}\right) = \sum_{n=0}^{\infty} a_n^{(2)} \cos\frac{\pi n t}{\tau} + b_n^{(2)} \sin\frac{\pi n t}{\tau} \tag{11}$$

The Fourier coefficients can be calculated as

$$a_n^{(1)} = \frac{2}{2\tau}\int_0^{8\tau} f_1(t)\cos\frac{\pi n t}{\tau} = \frac{1}{\pi n}\frac{1-(-1)^n}{2}\left[4\sin\frac{\pi n}{4} - 2\sin\frac{\pi n}{2}\right] \tag{12}$$

This expression equals 0 for every even value of n, the same holds for

$$b_n^{(1)} = \frac{2}{2\tau}\int_0^{8\tau} f_1(t)\sin\frac{\pi n t}{\tau} = \frac{1}{\pi n}\frac{1-(-1)^n}{2}\left[-4\sin\frac{\pi n}{4} + 2\right] \tag{13}$$

Due to the shift in the modulation functions 11 we get similar coefficients for f_2, $|a_n^{(2)}| = |b_n^{(1)}|$ and $|b_n^{(2)}| = |a_n^{(1)}|$. Notice that $a_1^{(1)} = -b_1^{(1)} = \frac{2}{\pi}\left(\sqrt{2}-1\right)$ and $a_3^{(1)} = b_3^{(1)} = \frac{2}{3\pi}\left(\sqrt{2}+1\right)$ result in $|a_3^{(1)}| \approx 1.94\,|a_1^{(1)}|$, which is the reason we choose the third order, namely $a_3^{(1)}$ and $b_3^{(1)}$. The related Fourier terms corresponding to $a_3^{(1)}$ and $b_3^{(1)}$ are plotted in the upper figure S1. This is achieved by choosing

$$\tau = 3\frac{\pi}{\omega_I} \tag{14}$$

In a rotating frame with respect to $\omega_I I_z$, discarding all fast-rotating terms, we get

$$\begin{aligned} H_{avg} &= -\sum_{n=1}^{N}\frac{A_x}{2}a_3^{(1)}\left(S_x I_x^{(n)} + S_y I_x^{(n)} - S_x I_y^{(n)} + S_y I_y^{(n)}\right) \\ &= -\sum_{n=1}^{N}\frac{A_x}{4}\alpha\left(\tilde{S}_- I_+^{(n)} + \tilde{S}_+ I_-^{(n)}\right) \end{aligned} \tag{15}$$

with $\alpha = \sqrt{a_3^{(1)} + b_3^{(1)}} = \frac{2}{3\pi}(2+\sqrt{2})$. The basis change resulting from $\tilde{S}_x = (S_x + S_y)\sqrt{2}$ and $\tilde{S}_y = (-S_x + S_y)\sqrt{2}$ does not affect the polarisation dynamics as only the x-y-plane is rotated and the z-axis remains.

Section S3. Error robustness

As a robust polarisation sequence PulsePol should meet the following criteria (i)-(iii) from the main text:
(i) It produces both S_x and S_y terms in the effective Hamiltonian with the modulation functions $f_1(t)$, $f_2(t)$, preferably by producing the phase change $f_2(t) = f_1(t + \pi/2)$.
(ii) The detuning errors accumulated during the free evolution need to be cancelled and preferably also decoupled from unwanted noise and fluctuations.
(iii) as pulses are not perfect, i.e. of a finite length and with detuning and Rabi frequency errors, the polarisation sequence should cancel such errors at least to the first order.
As criterion (i) is fulfilled as already shown in the previous section, we present the detailed proofs of the other criteria (ii) and (iii) as follows.
Criterion (ii), the cancellation of detuning errors accumulated during the free evolution, follows from the anti-commutation relation of Pauli matrices $[\sigma_{x/y}, \sigma_z]_+ = 0$. This relation can be used to derive the property $\exp(-i\tau\Delta S_z)\, S_{x/y} = S_{x/y}\exp(+i\tau\Delta S_z)$. As the ΔS_z term commutes with the rest of the free evolution, one can see the cancellation of the detuning errors accumulated during the free evolution around every perfect π pulse in the evolution operator with the help of (4)

$$U_{\text{free}}(\tau)U_{\pi,\text{X/Y}}U_{\text{free}}(\tau) = U_{\text{free}}(\tau)2S_{x/y}U_{\text{free}}(\tau) \tag{16}$$

$$= e^{-i\tau(\omega_I + S_z A_x I_x)}e^{-i\tau\Delta S_z}2S_{x/y}e^{-i\tau\Delta S_z}e^{-i\tau(\omega_I + S_z A_x I_x)} \tag{17}$$

$$= U_{\text{free},\Delta=0}(\tau)U_{\pi,\text{X/Y}}U_{\text{free},\Delta=0}(\tau). \tag{18}$$

The cancellation happens in every part of the sequence, leading to complete cancellation of detuning errors for perfect pulses. This means that improving the pulses also corrects errors accumulated during the free evolution.

For criterion (iii), the cancellation of pulse errors to 1st order, is fulfilled. Including a Rabi frequency error $\delta\Omega = \Omega_0 - \tilde{\Omega}_0$, the pulses with errors take the form

$$U_{\theta,\pm X/Y} = \exp\left(-i\frac{\theta}{\Omega}\left(\pm\tilde{\Omega}S_{x/y} + \Delta S_z\right)\right) \tag{19}$$

Introducing the definitions $\frac{\Delta}{\Omega} \equiv \epsilon k_1$ and $\frac{\tilde{\Omega}}{\Omega} = 1 - \frac{\delta\Omega}{\Omega} \equiv 1 + \epsilon k_2$, it is straightforward to show that in the evolution operator of one sequence block, neglecting the nuclear spins, the detuning and Rabi errors have an overall effect of

$$U_{\pi/2,-X}U_{\pi,Y}U_{\pi/2,-X}U_{\pi/2,Y}U_{\pi,X}U_{\pi/2,Y}U_{\pi/2,-X}U_{\pi,Y}U_{\pi/2,-X}U_{\pi/2,Y}U_{\pi,X}U_{\pi/2,Y} \tag{20}$$

$$= -(\mathbb{1} + \epsilon^2 k_1^2(-2i\sigma_z) + \epsilon^3 k_1^2 k_2 2\pi i\sigma_z) + O(\epsilon^4) \tag{21}$$

This means in the pulses Rabi errors are cancelled up to second order, detuning errors in first order. Note that the second order in detuning errors is a z-rotation and can therefore be compensated with a tau-shift for a specific detuning value, as shown for phase errors later. This completes the proof that the PulsePol sequence fulfills all of the desired properties. Notice that the PulsePol sequence is not the only option but the best sequence found. It can be derived as the simplest sequence fulfilling the above criteria (i)-(iii).
There are other possible sequences fulfilling the above properties, for example the PolXY sequence

$$\left(\frac{\pi}{2}\right)_Y \left[\overset{\tau/2}{\text{---}}(\pi)_X \overset{\tau}{\text{---}}(\pi)_Y \overset{\tau}{\text{---}}(\pi)_X \overset{\tau}{\text{---}}(\pi)_Y \overset{\tau/2}{\text{---}} \left(\frac{\pi}{2}\right)_X \overset{\tau}{\text{---}}(\pi)_Y \overset{\tau}{\text{---}}(\pi)_X \overset{\tau}{\text{---}}(\pi)_Y \overset{\tau}{\text{---}} \left(\frac{\pi}{2}\right)_X\right]^N \left(\frac{\pi}{2}\right)_{-Y} \tag{22}$$

with a resonance for $\tau = n\pi/\omega_L$, but PulsePol has the best properties concerning error stability. Furthermore PolXY and other sequences showed an undesired depolarisation behaviour for detuning values close to the Rabi frequency, which is significantly reduced for PolsePol as shown in section S8.
A sequence which has almost identical behaviour to PulsePol is

$$\left[\left(\frac{\pi}{2}\right)_Y \overset{\tau/4}{\text{---}}(\pi)_Y \overset{\tau/4}{\text{---}} \left(\frac{\pi}{2}\right)_{-Y} \left(\frac{\pi}{2}\right)_X \overset{\tau/4}{\text{---}}(\pi)_X \overset{\tau/4}{\text{---}} \left(\frac{\pi}{2}\right)_{-X}\right]^{2N} \tag{23}$$

Combining this with the actual PulsePol sequence leads to

$$\left[\left[\left(\frac{\pi}{2}\right)_Y \overset{\tau/4}{\text{---}}(\pi)_X \overset{\tau/4}{\text{---}} \left(\frac{\pi}{2}\right)_Y \left(\frac{\pi}{2}\right)_{-X} \overset{\tau/4}{\text{---}}(\pi)_Y \overset{\tau/4}{\text{---}} \left(\frac{\pi}{2}\right)_{-X}\right]^2 \left[\left(\frac{\pi}{2}\right)_Y \overset{\tau/4}{\text{---}}(\pi)_Y \overset{\tau/4}{\text{---}} \left(\frac{\pi}{2}\right)_{-Y} \left(\frac{\pi}{2}\right)_X \overset{\tau/4}{\text{---}}(\pi)_X \overset{\tau/4}{\text{---}} \left(\frac{\pi}{2}\right)_{-X}\right]^2\right]^N \tag{24}$$

which behaves as PulsePol, but here no oscillations for changing detuning values are present.
The latter two sequences and PulsePol itself can be derived with the following steps:

1. Criterion (i) suggests that the modulation functions of such a sequence of length 2τ consists of four different parts, $f_1(t) = 0$ in the second and fourth part represents a specific basis choice and $f_2(t) = f_1(t - \tau/2)$ represents the correct phase difference.

2. As detuning errors need to be cancelled according to criterion (ii), a relation similar to (16) needs to be fulfilled, i.e. the sequence must consist of blocks like $\overset{t}{\text{---}}(\pi)_\Phi \overset{t}{\text{---}}$. This, combined with 1., immediately leads to the modulation functions in figure S1(b).

3. The basis changes, criterion (i), require $\pi/2$-pulses before and after these blocks, the error cancellation (iii) determines the form to be $\left(\frac{\pi}{2}\right)_{\pm Y} \overset{t}{\text{---}}(\pi)_Y \overset{t}{\text{---}} \left(\frac{\pi}{2}\right)_{\mp Y}$ or $\left(\frac{\pi}{2}\right)_{\pm X} \overset{t}{\text{---}}(\pi)_Y \overset{t}{\text{---}} \left(\frac{\pi}{2}\right)_{\pm X}$ up to rotations and basis changes.

This leads to the PulsePol sequence (6) and other options like (23), (24).

Section S4. Finite pulses

In section S2 pulses were assumed to be perfect. With a finite Rabi frequency they also take a finite time, during which all parts of the system evolve, increasing the total time needed for every sequence block. In order to compensate that, the evolution times need to be reduced. As a block contains free evolutions lasting 2τ, eight $\pi/2$-pulses and four π-pulses, the free evolution time is

$$\tau = \frac{\pi}{\omega_I} \times n - \frac{4}{2} t_\pi - \frac{8}{2} t_{\pi/2} \tag{25}$$

where t_π and $t_{\pi/2}$ denote the time needed for π- and $\pi/2$-pulses. In case of simple pulses, the expression reduces to

$$\tau = \frac{\pi}{\omega_I} \times n - \frac{4}{2}\frac{\pi}{\Omega_0} - \frac{8}{2}\frac{\pi}{2\Omega_0} = \frac{\pi}{\omega_I} \times n - 4\frac{\pi}{\Omega_0} \tag{26}$$

In case of different pulses like in section S5, the correction term changes with the pulse times. In all cases it is important that the pulses do not reduce the free evolution time by a significant amount, simulations show that the pulse time should be less than 20% of the free evolution time. To reach this regime even for long pulses, the parameter n can be increased as described in the previous section.

Section S5. Composite pulses

The stability with respect to both detuning and Rabi frequency errors can be increased with composite pulses, which are designed to correct those errors within the pulses. As our main goal is to get reliable polarisation transfer for a wide range of detunings, we focus on the correction of detuning errors over Rabi frequency errors here.
In the numerical simulations we used different sequences described in (*18*). Best results were achieved with the pulses

$$90 = \overline{16}\ \ 300\ \ \overline{266}\ \ 54\ \ \overline{266}\ \ 300\ \ \overline{16} \tag{27}$$

for $\pi/2$ pulses and

$$180 = 325\ \ \overline{263}\ \ 56\ \ \overline{263}\ \ 325 \tag{28}$$

for π pulses.
The composite pulses mentioned above rotate around angles of $1218/180 \times \pi$ and $1232/180 \times \pi$, respectively, which means according to equation (25) that for PulsePol

$$\tau = \frac{\pi}{\omega_I} \times l - \left(2\frac{1232}{180} + 4\frac{1218}{180}\right)\frac{\pi}{\Omega_0} \tag{29}$$

The resulting error robustness is shown in figure S2 The composite pulses allow for significantly larger detuning (For $\Omega = 50$ MHz more than ± 40 MHz) than in case of shorter pulses considered. The results aren't improved by choosing even longer composite pulses, because the pulse duration should not take a large fraction of the free evolution time.

Section S6. Effect of phase errors

In figure S3 one can see the analytically calculated (first order) and the simulated dependence of the shift in resonance depending on a phase error α: In the PulsePol sequence, we assume every $\pi/2$ pulse that follows another pulse without a free evolution in between has a shifted phase

$$\left[\left(\frac{\pi}{2}\right)_{\overline{Y}} \overset{\tau/4}{\text{——}} (\pi)_X \overset{\tau/4}{\text{——}} \left(\frac{\pi}{2}\right)_Y \left(\frac{\pi}{2}\right)_{\overline{-X}} \overset{\tau/4}{\text{——}} (\pi)_Y \overset{\tau/4}{\text{——}} \left(\frac{\pi}{2}\right)_{-X}\right]^{2N} \tag{30}$$

where $\overline{Y} = Y\cos\alpha - X\sin\alpha$ and $\overline{-X} = -X\cos\alpha + Y\sin\alpha$.

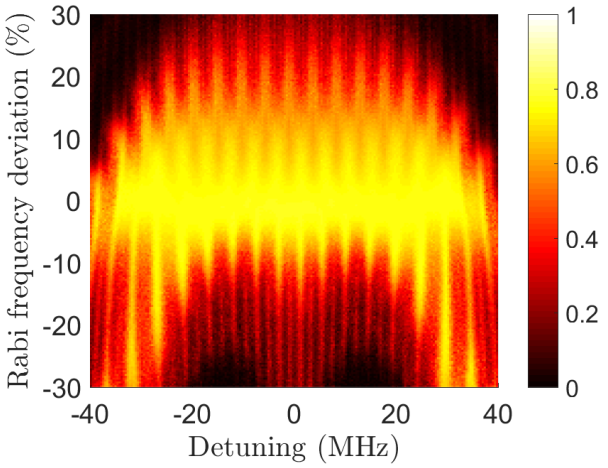


Fig. S2. Error resistance of PulsePol by using composite pulses. Error-resistance (polarisation transfer vs. Δ and $\delta\Omega/\Omega_0$) for PulsePol with composite pulses, parameters as in Fig. 2c in the main text: $\omega_I = 2$ MHz, $A_x = 0.03$ MHz and $\Omega_0 = 50$ MHz. Here the $l = 5$ resonance was used.

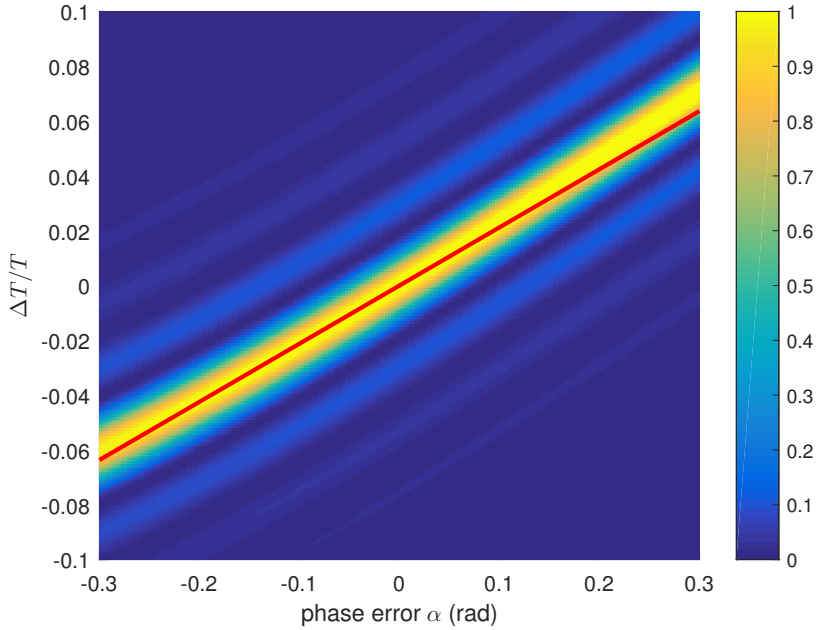


Fig. S3. Effect of phase errors. Simulated and calculated (red line, first order) dependence of the resonance shift on the error α. A high function value (yellow) indicated that the protocol works well for the corresponding parameters.

This description has the same effect as standard phase errors, we choose it as in the experiment the shift in resonance condition originates from this effect. For $\tau = 0$ in first order of α, the overall effect of this on the NV is described by

$$(U_{\pi/2,-X}U_{\pi,Y}U_{\pi/2,\overline{-X}}U_{\pi/2,Y}U_{\pi,X}U_{\pi/2,\overline{Y}})^2 \tag{31}$$

$$= \left(U_{\pi/2,-X}U_{\pi,Y}\left(U_{\pi/2,-X} + \frac{\alpha}{\sqrt{2}}U_{\pi,Y}\right)U_{\pi/2,Y}U_{\pi,X}\left(U_{\pi/2,Y} + \frac{\alpha}{\sqrt{2}}U_{\pi,-X}\right)\right)^2 + O(\alpha)^2 \tag{32}$$

$$= \exp\left(-4i\alpha S_z\right) + O(\alpha)^2 \tag{33}$$

This means the NV basis is rotated by -2α in the x-y-plane during the time 2τ. After a rotation of $-\pi$, the

modulation functions are inverted. This corresponds to a shift of half a period in the modulation functions, which corresponds to a time

$$\Delta T = \frac{1}{2n} 2\tau \tag{34}$$

where n is the (odd) resonance condition chosen.
Assuming the sequence needs M cycles for a π shift, we can determine the relation between the resonance shift and the phase error

$$\frac{\Delta T/T}{\alpha} = \frac{\tau/n \times 1/(2\tau M)}{\pi/(4M)} = \frac{2}{\pi n} \tag{35}$$

The corresponding line is plotted in figure S3 for $n = 3$. Especially around $\alpha = 0$, where higher orders are negligible, it fits the simulation very well.
Note that this is a continuous process of shifting the modulation functions and therefore has a direction as the modulation functions are shifted by $\pi/2$. For $n = 5$ the shift is in the opposite direction compared to $n = 3$. For normal XY-sequences such a shift cannot induce a resonance shift, as only one modulation function does not allow for a direction.
The major advantage of inducing such a resonance shift is that it allows to delete noise terms in the effective evolution. Assuming an effective Hamiltonian

$$H_{\text{eff}} = \omega_I I_z + A_x S_{\text{eff}} I_x \tag{36}$$

where

$$S_{\text{eff}} = f_1(t)\,(S_x + \epsilon_1 S_y + \epsilon_2 S_z) + f_2(t)\,(S_y + \epsilon_3 S_x + \epsilon_4 S_z) \tag{37}$$

the errors $\epsilon_{1/3}$ would only slightly inhibit polarisation transfer, but the errors $\epsilon_{2/4}$ have a considerable impact. The shift in τ shifts the frequency of $f_{1/2}$ from the resonance and therefore decouples S_z terms from the effective evolution. Only $S_{x/y}$ terms remain at the original resonance due to the rotation induced by α. Figure S4 shows that for $\Delta T/T \approx 2.5\%$ a considerably better resistance to Rabi and Detuning errors is achieved. The values result from an integration over heatmaps like in figure 2c in the main text (with a larger parameter space). Note that everything described in this section is independent of the nuclear spin bath and therefore the resonance shift is equal for all NV centres in an ensemble.

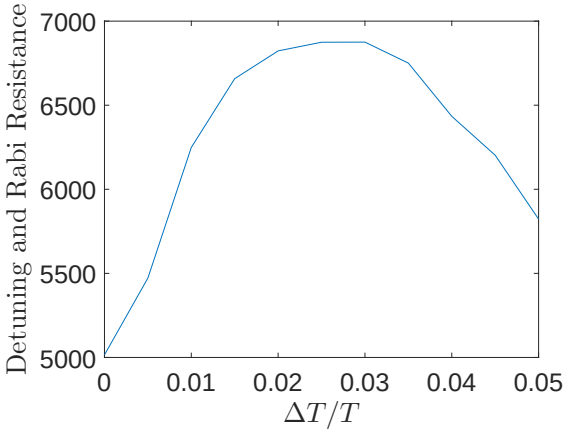


Fig. S4. Error resistance of PulsePol versus the resonance shift. Error resistance (arb. u.) of PulsePol depending on the resonance shift.

Section S7. Hamiltonian with NV centers in nanodiamonds

We apply a strong magnetic field $\gamma_e B \gg D$ along the z direction of laboratory frame of reference for the following technical reasons. (i) The time of the polarization built-up cycle is limited by the NV T_2, and the T_2 of the NV center is prolonged due to better dynamical decoupling at higher magnetic fields. (ii) Large magnetic fields result in longer ^{13}C T_1 relaxation times for polarization built-up. (iii) When $\gamma_e B \gg D$ with γ_e the gyromagnetic ratio, one has a uniform laboratory frame of reference (along the direction of the strong magnetic field) for different orientations of the NV center.
There is however a technical limit on going to very high fields (> 2T) as higher MW power is required, which is more difficult to realize experimentally. PulsePol can still be used at higher magnetic fields even if the MW power is limited by matching the time between the pulses to a higher harmonic of the nuclear Larmor as shown in Eq. (3) in main text, albeit at a tradeoff to the polarization efficiency.
In the strong magnetic field limit, the Hamiltonian can be written as

$$H = DS_{\tilde{z}}^2 + \omega_S S_z + \omega_I I_z + \vec{S}\mathcal{A}\vec{I} + 2\Omega_3(t) S_x \cos(\omega_{MW} t + \varphi) \tag{38}$$

in which the zero-field splitting term is based on the NV orientation $\tilde{z}$, which transforms as

$$S_{\tilde{z}} = S_z \cos\theta + S_x \sin\theta \cos\phi + S_y \sin\theta \sin\phi \tag{39}$$

Here θ is the polar angle between the magnetic field and NV orientation, and ϕ is the azimuthal angle. Going to the rotating frame with respect to $\omega_{MW} S_z$, we have

$$H = D\left(\cos^2\theta S_z^2 + \sin^2\theta S_x^2\right) + (\omega_S - \omega_{MW}) S_z + \omega_I I_z + S_z \vec{\mathcal{A}}\vec{I} + \Omega_3(t)(S_x \cos\varphi + S_y \sin\varphi) \tag{40}$$

The MW pulses are applied to drive the transition of two levels near resonantly (i.e., $m_s = 0$ and $ms = -1$), and the third level is not affected due to large frequency difference. Therefore, the NV centers in nanodiamonds can be simplified to two-level systems, and the Hamiltonian of NV centers interacting with nuclear spins can be simplified to be Eq. (3) with $\Delta = \omega_S - \omega_{MW} + D(\theta)$ in which

$$D(\theta) = D\left(\cos^2\theta + \frac{1}{2}\sin^2\theta - \sin^2\theta\right) = D\left(1 - \frac{3}{2}\sin^2\theta\right) = \frac{D}{4}\left(1 + 3\cos(2\theta)\right) \tag{41}$$

and the MW Rabi frequency is $\Omega(t) = 1/\sqrt{2}\Omega_3(t)$.

Section S8. Depolarization behavior

The numerical results that are compared with experimental data in figure 3 in the main text were obtained by smoothing the actual data that were oscillating fast due to resonances of the free evolution detuning term. Figure S5 also shows the unsmoothed data. For macroscopic polarisation buildup in all applications of interest not only the transfer efficiency is relevant, but also that the transfer is not reversed for other detuning values. Thanks to the implementation of phase errors (see section S6) PulsePol does not destroy a significant amount of polarisation for any detuning when applied in the other direction, i.e. to further polarise an already polarised bath. This is confirmed by the blue data in figure S5 with theoretical simulations and experimentally with PROPI by reversing the polarisation direction.

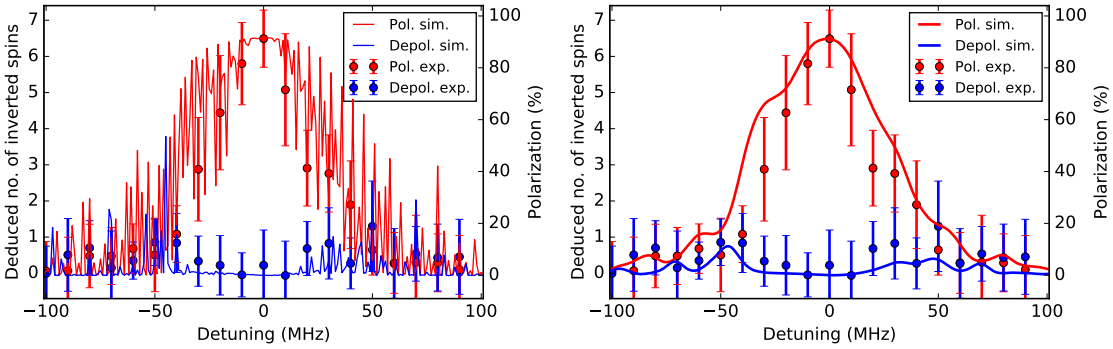


Fig. S5. Comparison between simulation results and experimental data of polarization buildup and depolarization. Simulation results (left: raw data, right: smoothed) compared to the experimental data for polarisation buildup (red) and depolarization (blue).

Section S9. Simulation parameters for shallow NV centers

Here we provide details about the numerical simulations performed to obtain the results of (Fig. 4c) of the main text. 1200 most strongly coupled spins are included in the simulations as these spins account for two thirds of the total coupling strength between the NVs and the whole spin bath. We simulate 100 independent baths of nuclear spins interacting with shallow NV centers that are placed 3 nm below the surface of a bulk diamond. The nuclear spins are assumed to be uniformly and randomly oriented in space. The position of the spins is assumed to be random initially and then a diffusion process is simulated to calculate their positions evolving over time with diffusion coefficients $D = 1.4/2.8 \times 10^{-12}\mathrm{m}^2/\mathrm{s}$ (blue dotted/red dashed curve in Fig. 4c). A magnetic field of strength 0.047 Tesla aligned with the NV crystal axis is applied. The couplings between the NV and the nuclear spins are calculated for different values of time based on their distance from and orientation with respect to the NV center. The NV-center transition frequencies are drawn from a Gaussian distribution with $(2\pi)20$ MHz width. The Rabi frequency is taken as $(2\pi)50$ MHz and the nuclear Larmor frequency is $(2\pi)2$ MHz.

During evolution under PulsePol, the entanglement between the different constituents is limited so the state of the NV and the spins can be efficiently represented by a matrix product state (MPS). The time evolution is simulated using the time-evolution via block decimation (TEBD) algorithm on the MPS representation. Owing to the robustness to protocol to the frequency fluctuation, the NV centers effect a high degree of nuclear polarization in the spin bath as depicted in (Fig. 4c).

Part III

Nanoscale sensing

4 Nanoscale Sensing

During the development of NV-based hyperpolarization, I encountered a lot of synergies with ideas and concepts from NV-based nanoscale sensing. Nanoscale sensing using NV centers is a burgeoning field of research, where the control in placing the NV centers spatially, the long NV coherence time and sensitivity to perturbations is utilized for sensing of various phenomena on the nanometric length-scale. A key measurement of interest is the sensing of ac magnetic field perturbations caused by nuclear spins in proximity to the diamond surface. By detecting the frequency of these magnetic fields, it is possible to identify the resonance of the nuclear spins on the nanoscale, and thus characterize the molecules similar to nuclear magnetic resonance (NMR) spectroscopy experiments. We investigated two points of synergy between nanoscale hyperpolarization and sensing:

Improved spectral filtering on the nanoscale using sequences inspired by hyperpolarization techniques - While working on external polarization transfer, we explored the idea of using a mediating surface electron spin to transfer polarization from deeper NV centers to nuclear spins. We arrived at a sequence which enabled polarization transfer even when the mediating spin has a short coherence time, at a cost of the sequence working efficiently only for a selective frequency range. We realized this can be turned to an advantage - By tuning the microwave drive of the mediating spin, one can selectively address, or sense, specific nuclear spins in a very narrow frequency window [20].

The method includes using an NV center as a mediator spin between a sensor nuclear spin and a target nuclear spin, while eliminating the NV center and the effect of its decoherence from the dynamics. By driving the NV center such that it is strongly detuned from the nuclear spins, the NV center induces a relatively large second-order coupling between the sensor and target nuclear spins. The NV center is periodically reinitialized by a dissipative process, making it possible to extend the coherent evolution of the nuclear spins well beyond the NV center relaxation time.

We show that by tuning the relative detuning of the NV center from the nuclear spin Larmor frequency, we can sense spins with different frequencies with very high spectral resolution, thus being able to sense and distinguish between carbon spins in external molecules. We demonstrated this in a simulation using a Valine molecule as an example.

Combining hyperpolarization and nanoscale sensing for creating the blueprint for nanoscale NMR - One of the most exciting applications made possible by NV centers in diamond, is the detection and characterization of molecules external to the diamond on the nanoscale. However, all current nanoscale NV sensing experiments suffer from poor spectral resolution. This is a key limitation, as it masks the nuclear chemical shift (a frequency detuning produced by the electronic environment of the nuclear spin in the molecule), the main information used in NMR spectroscopy for characterizing molecules. The reason for the poor spectral resolution is twofold:

- The sensing time is limited by the NV center T_2 or T_1 times. As for shallow NV centers the T_1 time is typically lower than 1 ms, this limits the spectral resolution to worse than 1 KHz.

- Spectral information is typically obtained for liquids. However, the molecular diffusion of the liquid molecules occurs very quickly on the nanoscale. Diffusion of molecules in and out of the NV sensing region scrambles the statistical polarization typically used for nanoscale sensing, therefore again limiting the achievable spectral resolution to the inverse of τ_c, the correlation time of the interaction between the NV center and the nuclear spins. For most liquids, this limits the spectral resolution to tens of KHz.

In order to overcome these limitations, I first showed that M_x polarization, defined as the average polarization along the x axis in the rotating frame defined by the nuclear Larmor frequency, is not affected by molecular diffusion. This is due to the fact that given that all molecules have the same average polarization, exchanging nuclear spins in the vicinity of the NV center due to diffusion does not change the average M_x polarization. This means that the standard NMR sequence of building up M_z polarization and applying a $\pi/2$ pulse for generating M_x polarization will not be limited spectrally by diffusion. Averaging several iterations of this process also reduces

the statistical polarization noise, and enables extracting the M_x polarization signal, even in the presence of very strong statistical polarization, as is the case in nanoscale sensing. Combining this realization with the Qdyne measurement scheme [11] and NV-based hyperpolarization of the external spins for enhanced signal [17] led to the first blueprint for nanoscale NMR using NV centers with spectral resolution sufficient for visualizing and distinguishing chemical shifts [21]. To demonstrate the viability of our strategy, termed Hypdyne, I ran an atomistic simulation of the diffusing nuclear spins, and generated a simulation of the fluctuating ac magnetic field experienced by the NV center from hyperpolarized nuclear spins (hyperpolarization level determined by simulation of NV-based hyperpolarization). In collaboration with the Institute of Quantum Optics, we inputed the simulated magnetic field into an arbitrary waveform generator, and showed that the NV center can detect via Qdyne an exceedingly sharp resonance, sufficient for determination of chemical shifts.

Moreover, we were interested in methods for lowering the detection limit, so as to be able to acquire signals from lower concentrations of the analytes and reduce averaging times. We employed signal processing methods based on Bayesian inference algorithms, enabling efficient utilization of the underlying signal. This allowed for orders of magnitude reduction of the number of measurements required for the successful identification of the nuclear signal. We showed that one can use this method for identifying and distinguishing between nuclear spins with different chemical shifts.

4.1 Dissipatively stabilized quantum sensor based on indirect nuclear-nuclear interactions

Title:	Dissipatively stabilized quantum sensor based on indirect nuclear-nuclear interactions
Authors:	Chen, Q and Schwarz, I and Plenio, Martin B
Journal:	Physical Review Letters 119.1, 010801
Year:	2017
Copyright:	©2017 American Physical Society. Reprinted with permission from Chen et al. Physical Review Letters 119.1, 010801 (2017) ©2017 by the American Physical Society
DOI:	https://doi.org/10.1103/PhysRevLett.119.010801

Dissipatively Stabilized Quantum Sensor Based on Indirect Nuclear-Nuclear Interactions

Q. Chen, I. Schwarz, and M. B. Plenio
Institut für Theoretische Physik & IQST, Albert-Einstein-Allee 11, Universität Ulm, 89069 Ulm, Germany
(Received 16 February 2017; published 6 July 2017)

We propose to use a dissipatively stabilized nitrogen vacancy (NV) center as a mediator of interaction between two nuclear spins that are protected from decoherence and relaxation of the NV due to the periodical resets of the NV center. Under ambient conditions this scheme achieves highly selective high-fidelity quantum gates between nuclear spins in a quantum register even at large NV-nuclear distances. Importantly, this method allows for the use of nuclear spins as a sensor rather than a memory, while the NV spin acts as an ancillary system for the initialization and readout of the sensor. The immunity to the decoherence and relaxation of the NV center leads to a tunable sharp frequency filter while allowing at the same time the continuous collection of the signal to achieve simultaneously high spectral selectivity and high signal-to-noise ratio.

DOI: 10.1103/PhysRevLett.119.010801

Introduction.—The nitrogen vacancy (NV) center is attracting increasing attention due to the possibility for creating hybrid quantum registers of nuclear spins controlled by the electron spin of the NV center [1–4] and due to its applications in nanoscale sensing [5–27]. However, for both quantum register and sensing applications at room temperature, the relatively short lifetime [28] of the NV center induces several outstanding challenges caused by the relaxation and decoherence processes of the electron spin as these limit quantum gate fidelities on nuclear registers as well as spectral resolution, selectivity, and signal to noise ratio in sensing applications. While the addition of the nuclear ancilla as the long-lived memory of the NV sensor can improve spectral resolution [19–27], by extending the time interval between interrogations, e.g., in correlation spectroscopy, this comes at a price of signal to noise ratio and remains limited by the relaxation time of the NV center.

Here we address directly the challenge of the NV center decoherence and relaxation by using the NV center as a mediator to couple two nuclear spins, eliminating the NV center and the effect of its decoherence and relaxation from the dynamics [Fig. 1(a)]. The key idea is the use of the substantial second-order coupling between the nuclear spins obtained through a strongly detuned NV center which is periodically reinitialized by a dissipative process [29]. The periodical resets of the NV center make it possible to extend the coherent evolution of the nuclear spins well beyond the NV center lifetime. Thus, coherent evolution between nuclear spins is achieved, which is no longer limited by the NV decoherence or even relaxation. The detuning and periodical reinitialization of the NV center decouple it from the dynamics and its effect on the system can be modeled by an effective but weak dissipation process. Thus, high fidelity of selective quantum gates between the nuclear spins, as well as an improved sensing setup, are made possible even at ambient condition.

We demonstrate that the NV-mediated interaction between nuclear spins yields a dissipation-enhanced quantum sensor by considering a basic setup including a single ^{13}C nuclear spin sensor nearby the shallow NV center to sense a target ^{13}C spins on the diamond surface, as shown in Fig. 1(b). Contrary to previous applications of nuclear spins acting as ancillary memory [19–27,30], the nuclear spin in our setup serves as a sensor, which is polarized in advance such that the polarization leakage of the nuclear sensor shows the presence of the target spin by using the effective interaction between the sensor and target. The NV spin is an ancillary mediator of the effective interaction, and at the beginning and end serves as a means for initialization and readout of the sensor spin. The effective coupling

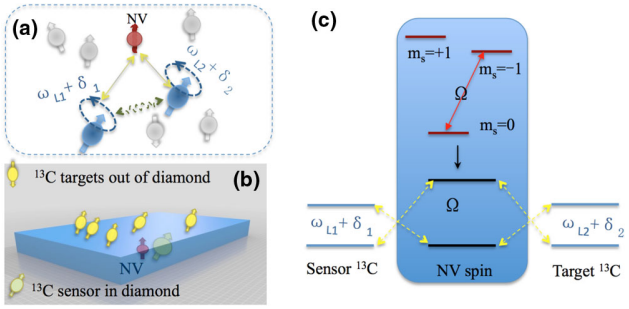


FIG. 1. (a) Illustration of the basic principle. An NV center mediates the coupling between two nuclear spins, while itself becoming decoupled from the dynamics, enabling long coherent interactions, e.g., for high fidelity selective quantum gates. (b) Dissipation-assisted sensing setup composed of a nuclear quantum sensor [a single ^{13}C spin (green) ~1 nm removed from the associated NV center (red)] and an NV implanted 3–4 nm below the diamond surface, where the target spins reside (yellow). (c) Energy level diagram. The Rabi frequency Ω of the MW drive is far off resonance from the Larmor frequency of the target nucleus which is on resonance with the sensor.

 © 2017 American Physical Society

between the two nuclear spins is controllable, which provides a tunable sharp frequency filter for achieving very high spectral resolution that is not limited by the NV decoherence and relaxation. Additionally, the signal is continuously accumulated by the nuclear sensor, with no dead-time, hence maintaining sensitivity by increasing the SNR. Furthermore, our scheme does not merely measure Larmor frequency [5] but retains the option of individually addressing the nuclear spins, useful for 2D spectroscopy [20,31,32] and quantum registers.

Effective master equation.—The basic setting we consider here includes a single NV center spin and two ^{13}C nuclear spins. Applying a weak magnetic field $\vec{B}_0$ lifts the degeneracy of $|m_s=-1\rangle$ and $|m_s=+1\rangle$ to allow for a selective continuous microwave (MW) driving field of one specific electronic transition. Working in a frame that is rotating with the MW frequency, resonant with the $|m_s=0\rangle \leftrightarrow |m_s=-1\rangle$ transition, the effective Hamiltonian of the NV spin is $H_{\rm NV}=\Omega\sigma_z$. Here, Ω is the Rabi frequency of the MW drive and $\{|+\rangle=(1/\sqrt{2})(|0\rangle+|-1\rangle), |-\rangle=(1/\sqrt{2})(|0\rangle-|-1\rangle)\}$ are the MW dressed eigenstates. Our goal is to use such MW dressed NV center spin as a mediator for indirect coherent interactions between two nuclear spins. The interaction between the NV and a nuclear spin is given by

$$H_{{\rm int}f}=\sigma_x\vec{A}_i\cdot\vec{I}_i=\sigma_x(a_{\parallel i}I_i^z+a_{\perp i}I_i^{\hat{x}}), \tag{1}$$

where $\sigma_x=(|+\rangle\langle-|+|-\rangle\langle+|)/2$, and I_i^q is the nuclear spin operator with $I_i^z=(|\uparrow_i\rangle\langle\uparrow_i|-|\downarrow_i\rangle\langle\downarrow_i|)/2$ and $I_i^{\hat{x}}=(|\uparrow_i\rangle\langle\downarrow_i|+|\downarrow_i\rangle\langle\uparrow_i|)/2$ with basis $\{|\uparrow_i\rangle,|\downarrow_i\rangle\}$ of nuclei. $\vec{A}_i$ is the hyperfine coupling vector and the direction of $\vec{I}_i$ is determined by the magnetic field unit vector $\vec{b}(\theta,\phi)$. $\vec{A}_i=(a_{\parallel_i},a_{\perp_i})$ with $a_{\parallel_i}$ and $a_{\perp_i}$ denoting the parallel and perpendicular coupling components to the nuclear spin quantization axes $a_{\parallel i}=\vec{A}_i\cdot\vec{b}$ and $a_{\perp i}=\sqrt{|\vec{A}_i|^2-a_{\parallel i}^2}$.

We derive a Lindblad master equation to describe the dynamics of the whole system ρ, which is described as $(d/dt)\rho=-i[H'_{\rm tot},\rho]+\mathcal{D}[\rho]$ in which $\mathcal{D}[\rho]=\mathcal{D}_e[\rho]+\mathcal{D}_n[\rho]$, corresponding to the relaxation and dephasing of the electron and nuclear spins, respectively. The effective total Hamiltonian of the three spins are thus rewritten as (for details see the Supplemental Material [33])

$$H'_{\rm tot}=\Omega\sigma_z+\sum_{i=1}^{2}\left(\gamma_{ni}B_0+\frac{a_{\parallel i}}{2}\right)I_i^z+\sigma_x\vec{A}_i\cdot\vec{I}_i, \tag{2}$$

with γ_{ni} the gyromagnetic ratio of the nuclear spin. The NV center is reinitialized periodically (every $t_{\rm re}$) to the state $|-\rangle$ of the dressed state basis, namely, $\rho(Nt_{\rm re})\to[{\rm Tr}_e\rho(Nt_{\rm re})]\otimes|-\rangle\langle-|$, where ${\rm Tr}_e$ denotes the partial trace over the electron spin and N is an integer.

The reinitialization of the NV results in nuclear subsystem evolution in the vicinity of the NV quasisteady state, $\rho_{ss}^{\rm NV}=p_+|-\rangle\langle+|+p_-|-\rangle\langle+|$, in which $p_+=1-[(e^{-t_{\rm re}/T_{1\rho}})/(2t_{\rm re}/T_{1\rho})]$, when $t_{\rm re}\le T_{1\rho}$ and $p_+=\frac{1}{2}-[(1-e^{-1})/(2t_{\rm re}/T_{1\rho})]$ when $t_{\rm re}>T_{1\rho}$, $p_-=1-p_+$. Notice that the effective relaxation rate of the NV spin is determined by the lifetime $T_{1\rho}$ and the reinitialization time $t_{\rm re}$, $\Gamma_N=1/T_{1\rho}+1/t_{\rm re}$. We can now use the electron spin as a bus to mediate the nuclear coupling [4,29], if the relevant energy scales satisfy $\Omega,\gamma_{n1}B_0,|\Omega-\gamma_{n1}B_0|\gg|\vec{A}_i|$. The Schrieffer-Wolff transformation for open systems [38,39] then allows for the derivation of an effective Liouvillian (see the Supplemental Material for details [33], and also the related theory [34,40–43]) for the nuclear subsystem ρ_n,

$$\frac{d}{dt}\rho_n=-i[H_{\rm eff},\rho_n]+\mathcal{D}_n[\rho_n]+\mathcal{D}_{\rm eff}[\rho_n]. \tag{3}$$

Here the coherent Hamiltonian is

$$H_{\rm eff}\approx\sum_{i=1,2}(\omega_{\rm Li}+\delta_i)I_i^z+pA_{wo}(I_1^+I_2^-+I_1^-I_2^+), \tag{4}$$

in which we have $I_i^+=|\uparrow_i\rangle\langle\downarrow_i|$, $I_i^-=|\uparrow_i\rangle\langle\downarrow_i|$, $p=p_+-p_-$, $\omega_{\rm Li}=\gamma_{ni}B_0$, $\delta_i\approx(a_{\parallel_i}/2)-(a_{\perp_i}^2/16)\{\Delta_{-i}/[\Delta_{-i}^2+(\Gamma_N/2)^2]\}+\{\Delta_{+i}/[\Delta_{+i}^2+(\Gamma_N/2)^2]\}$, and $A_{wo}\approx\sum_{i=1,2}[(a_{\perp_1}a_{\perp_2})/32]\times\{\Delta_{-i}/[\Delta_{-i}^2+(\Gamma_N/2)^2]\}+\{\Delta_{+i}/[\Delta_{+i}^2+(\Gamma_N/2)^2]\}$ with $\Delta_{\pm i}=\Omega\pm(\gamma_{ni}B_0+a_{\parallel i}/2)$. The virtual NV spin excitation results in an indirect dissipation contribution to Eq. (3),

$$\mathcal{D}_{\rm eff}[\rho_n]\approx\sum_{i,j=1,2}\Gamma_{ij}^{\rm eff}\left(I_i^-\rho_nI_j^+-\frac{1}{2}\{I_i^+I_j^-,\rho_n\}_+\right),$$

with $\Gamma_{ij}^{\rm eff}=[(a_{\perp_i}a_{\perp_j})/32]\{\Gamma_N/[\Delta_{+j}^2+(\Gamma_N/2)^2]\}+\{\Gamma_N/[\Delta_{-i}^2+(\Gamma_N/2)^2]\}$. Notice that the periodic reset of the NV maintains a net NV polarization ($p>0$), which is critical to our scheme. The NV center provides two channels for virtual electron spin flips, via $|-\rangle$ and $|+\rangle$ [33], which mediates interaction between the nuclei. As the two channels produce effective nuclear couplings with opposing sign, in the absence of periodic reinitialization, the mixing of the two channels would induce no net coherent evolution ($p=0$) for an evolution time that is longer than the NV lifetime $T_{1\rho}$, while a net interaction is achieved in the presence of periodic reinitialization ($p>0$).

Quantum gate implementation.—The effective coupling term in Eq. (4) gives rise to coherent flip-flop processes between the two nuclear spins, which achieves very high fidelity under the condition $pA_{wo}\gg\Gamma^{\rm eff}$. As the effective relaxation rate $\Gamma^{\rm eff}$ is inversely proportional to the square of the detuning $\Delta_{\pm i}$, we can adjust $\Delta_{\pm i}$ and the NV reset time, i.e., a large detuning $|\Delta_{\pm i}|\gg\Gamma_N$ and $t_{\rm re}\sim T_{1\rho}$ to minimize this induced dissipation. Thus, it is possible to have coherent internuclear evolution well beyond the lifetime of NV spin. Note that the experimental parameters, most

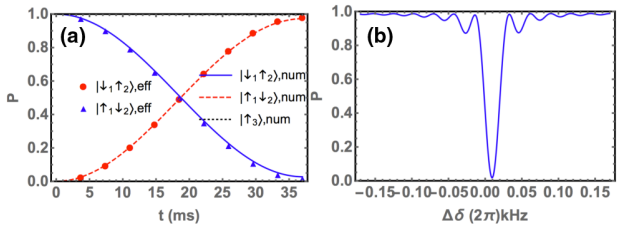


FIG. 2. (a) Comparison of the effective (eff) dynamics under master equation (3) and the exact numerical simulation (num) by using full Hamiltonian Eq. (2) and NV resets applied every $T_{1\rho} = t_{\mathrm{re}} = 1$ ms. The solid blue (dashed red) curve denotes the probability of measuring $|\downarrow,\uparrow\rangle$ ($|\uparrow,\downarrow\rangle$) as a function of time t. Choosing $[\Omega, \omega_{Li}] = (2\pi)[300, 200]$ kHz, we achieve a near perfect coherent flip-flop between nuclear spins 1 and 2 with $(a_{\parallel_1}, a_{\perp_1}) = (2\pi)(1.99, 2.01)$, $(a_{\parallel_2}, a_{\perp_2}) = (2\pi)(2.00, 5.01)$ kHz that are coupled via the NV spin, while the nuclear spin 3 with $(a_{\parallel_3}, a_{\perp_3}) = (2\pi)(2.30, 2.01)$ kHz is not affected. (b) The parameters are the same as in (a), with the blue line denoting the occupation probability of the state $|\downarrow,\uparrow\rangle$ for the evolution time $T = 37$ ms. The high selectivity is demonstrated by assuming a shift of the detuning of the second spin from the resonance condition, with $\Delta\delta = \delta_i - \delta_2$.

importantly the detuning $\Delta_{\pm i}$ and the reset time t_{re}, are constrained due to various trade-offs. The optimal reset time t_{re} has already been discussed between Eqs. (2) and (3) and in the following we identify the usefully accessible range of $\Delta_{\pm i}$. The lower bound for $\Delta_{\pm i}$ is due to the condition $|\Delta_{\pm i}| \gg a_{\perp_1}/4, a_{\perp_2}/4$, which is required to ensure validity of the perturbation theory, and due to $|\Delta_{\pm i}| \gg 2/T_{1\rho}$, which ensures high fidelity of the quantum gate (choosing $t_{\mathrm{re}} = T_{1\rho}$ and $\Gamma_N = 2/T_{1\rho}$) by suppressing the impact of the $T_{1\rho}$ process of the NV. On the other hand, an upper bound on $\Delta_{\pm i}$ is implied by the necessity that the effective nuclear interaction needs to prevail over the intrinsic decoherence and dissipation of the nuclei, which implies that, $pA_{wo} \gg 1/T_2^T$ is required for high gate fidelity.

In Fig. 2(a), we initialize three nuclear spins in state $|\downarrow_1\uparrow_2\uparrow_3\rangle$. The coherent flip-flop interaction between $|\downarrow_1\uparrow_2\rangle \leftrightarrow |\uparrow_1\downarrow_2\rangle$ induces an nuclear XX gate between the two nuclear spins, while 0.3 kHz deviation of the parallel component coupling from the resonance leaves the third nuclear spin unaffected. We compute the average gate fidelity to find 0.994 [44], significantly higher than the fidelity (<0.66) of nuclear-nuclear gates achieved so far with NV centers by using 4 electron-nuclear spin quantum gates (if each fidelity <0.90 [1]). Therefore, our method can address two nuclear spins that are weakly coupled with the NV center with high selectivity to implement a near perfect quantum gate at room temperature. This high selectivity is essential in a ^{13}C nuclear spin bath surrounding an NV spin, as it is important that quantum gates between two spins do not affect the other qubits in the register, see Fig. 2(b) for the high specificity of the interaction. The resulting spatial resolution that this high selectivity results in will be further discussed later.

Detection of a single nucleus.—The coupling between the nuclear spins mediated by a dissipative NV can also be used for sensing an isolated single nucleus outside of the diamond. Our scheme includes three steps: (i) Polarize the ^{13}C nuclear sensor by using the NV center. (ii) Achieve polarization transfer via a frequency selective flip-flop process between the two nuclear spins that is mediated by a dissipative NV center. (iii) Use the NV center to read out the polarization leakage of the nuclear sensor, which indicates the existence of a distant nuclear spin at the selected frequency. The electron spin of the NV center can be optically initialized and read out by using laser illumination. The nearby nuclear ^{13}C sensor spin can also be well controlled by a SWAP gate between NV and nuclear spin [22,45,46]; i.e., it can be polarized and its position can be detected.

Therefore, if the nuclear sensor is polarized to state $|\downarrow_1\rangle$, polarization leakage shows the target which is in a maximally mixed state by measuring the probability that the sensor ^{13}C spin remains in the state $|\downarrow_1\rangle$ as follows:

$$S = 1 - \frac{(pA_{wo})^2 \sin^2[(t/2)\sqrt{(pA_{wo})^2 + (\delta_1 - \delta_2)^2}]}{2[(pA_{wo})^2 + (\delta_1 - \delta_2)^2]}. \quad (5)$$

It is easy to find the resonance condition $\delta_1 = \delta_2$. In our setup, the coupling of the nuclear sensor (which is labeled spin 1 and whose position can be determined precisely) to the NV is far larger than that of the nuclear target to the NV. In order to match the resonance condition to the target nuclear spin, two main degrees of freedom are available—we can adjust the direction of the magnetic field, which gives a coarse tuning, and the Rabi frequency of the microwave drive on the NV spin, which allows a fine-tuning to match the resonance condition [33]. Note that the Rabi frequency has only second order contributions to the resonance condition, i.e., $a_{\perp_i}^2/16\Delta_{\pm i}$; thus, our scheme is not sensitive to small deviations or fluctuations of the Rabi frequency. Once the resonance condition is achieved, the signal dips around the time $t = \pi/4pA_{wo}$, marking the presence of nuclear spin.

Enhanced frequency resolution.—When using the NV as a sensor by observing the polarization leakage from the NV center to the nuclear spins [35], there exist two major limitations for the frequency resolution: that the NV T_1^ρ relaxation has to be longer than the NV-nuclear flip-flop time and the requirement that the hyperfine transverse component is small ($|a_{\parallel_i} - a_{\parallel_j}|/2 > a_{\perp_{i/j}}$). Our scheme solves both of these limitations. First, in our scheme the influence of NV decoherence (T_2) and relaxation (T_1) on the dynamics can be reduced at will below any desired level by increasing detuning $\delta_{\pm i}$ and the NV reset rate. Therefore, the resolution is limited only by the target spin decoherence T_2^T; see Fig. 3(a). Second, the broadening depends quadratically on $a_{\perp_i}$ and is essentially proportional to the effective coupling pA_{wo}, which is at least 1 order of magnitude smaller than $a_{\perp_{i/j}}$. Thus, the frequency resolution is improved accordingly as we now need to require

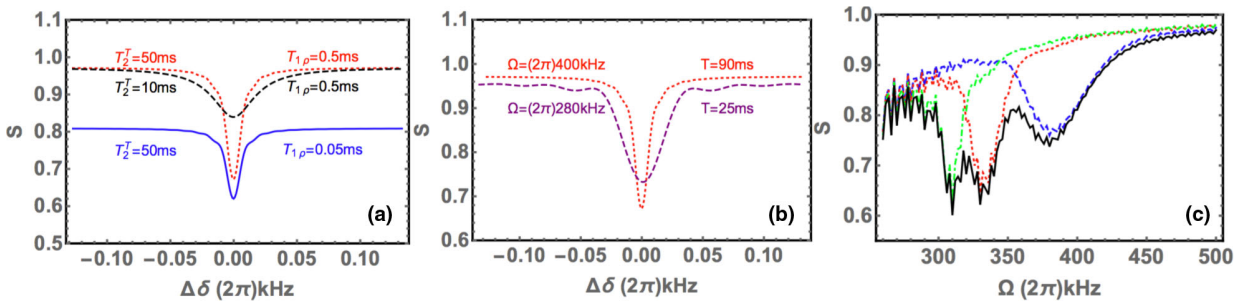


FIG. 3. (a) The effect of the NV $T_{1\rho}$ and the target spin decoherence time T_2^T on the detection bandwidth. The sensor signal S Eq. (5) is calculated by exact simulation for a total run time of $T = 90$ ms and three combinations of $T_{1\rho}$, T_2^T. The NV spin is reinitialized every $t_{\mathrm{re}} = T_{1\rho}$ and we chose frequencies and couplings for the sensor and targets as $[\omega_{L1}, \Omega, a_{\perp_1}, a_{\perp_2}] = (2\pi)[200, 400, 10, 1]$ kHz. (b) The tunable NV detuning $\Delta_{\pm i}$ as a frequency filter—the red dotted line has identical parameters to that in (a), the purple dashed line with different MW Rabi frequency results in smaller detuning which leads to increased linewidth due to increased A_{wo} and $\Gamma_{ij}^{\mathrm{eff}}$. (c) Assuming three ^{13}C nuclear spins in a Valine molecule. The NV spin is at the origin, the sensor at $[-0.601, 0.676, -0.692]$ nm, and targets at $[-1.260, -1.451, 2.904]$, $[-1.260, -1.317, 3.135]$, and $[-1.260, -1.317, 2.673]$ nm, with the magnetic field direction $[44.7°, 52.0°]$ and $T = 60$ ms. The black solid line represents the total signal of the three spins, when the dashed lines show individual contributions. The internuclear coupling has been suppressed by means of WAHUHA [33,36] decoupling, at the cost of a reduction factor in the dipolar coupling strength $1/\sqrt{3}$. The small amplitude oscillations on the observed signal are due to off-resonant contributions, which can be suppressed by choosing larger detunings $\Delta_{\pm i}$, i.e., larger Rabi frequency Ω.

$|\delta_i - \delta_j| \simeq |a_{\parallel_i} - a_{\parallel_j}|/2 > pA_{wo}$. Moreover, increasing the detuning $\Delta_{\pm i}$ of the NV induces a smaller effective coupling pA_{wo}, enhancing the frequency resolution [see Fig. 3(b)], which also gives a tunable frequency filter. For optimal resolution, one would fix the NV detuning $\Delta_{\pm i}$ to balance the two limitations, i.e., $1/pA_{wo} \lesssim T_2^T$. For example, for $[T_{1\rho}, T_2^T] = [0.05, 50]$ ms, the resolution could be improved 1000-fold compared to direct sensing via the NV center spin.

Recently, the use of a nuclear spin as ancillary memory to enhance the resolution of NV detection has been proposed for correlation spectroscopy [19,23,24]. Correlation spectroscopy exploits the evolution of the bath to establish a correlation between the phases picked up by the sensor in contact with target nuclei at two different times. A Fourier transform of the resulting signal allows us to spectroscopically separate target nuclei with differing hyperfine coupling constants, that is, for example, due to different positions. A particular advantage of this strategy is that the resolution of the resulting spectrum is inversely proportional to the T1 time characterizing the memory of the sensor. The interaction time with the target nuclei is limited by T_2^{NV} of the NV, while the longest time interval between interrogations, and, hence, the spectral resolution, is limited by the T_2^{ancilla} time of the nuclear ancilla. Therefore, the SNR for a given unit time is reduced by a factor of $T_2^{\mathrm{NV}}/T_2^{\mathrm{ancilla}} < 0.01$ due to the relatively long "dead time" in between measurements, which are especially limiting for the regime of interest in NV sensing, i.e., an NV $\sim$ 3–5 nm from the surface, attempting to sense targets ($a_\perp \approx 1$ kHz). However, this limitation is not presented in our setup, because we use the nuclear spin directly as a sensor. One can estimate the sensitivity of our scheme as follows: suppose $t_{\mathrm{re}} = T_{1\rho}$, as both $\sqrt{1/\Gamma_{\mathrm{eff}}}$ and pA_{wo} are linearly dependent on the detunings $\Delta_{\pm i}$, the sensitivity per unit time of our scheme is proportional to $pA_{wo}/(\sqrt{1/\Gamma_{\mathrm{eff}}}) \sim (a_{\perp_2}/4)/\sqrt{T_{1\rho}}$, which is independent of $\Delta_{\pm i}$. This is of the same order as the sensitivity achieved by direct detection of a nucleus by polarisation leakage of the NV [35] while obtaining enhanced spectral resolution. Therefore, our scheme achieves the enhanced resolution without a penalty to the sensitivity, and the scheme validity does not suffer from nearby nuclear spins or relatively low coupling to the nuclear spins.

Sensing application.—To evaluate the effectiveness of our scheme, we use it to determine the molecular structure of a target molecule malic acid (Valine), which plays an important role in biochemistry. In Fig. 3(c), we simulate the case of three ^{13}C spins in this molecule, attached to the diamond about 3.9 nm from the NV spin. The 1D NMR spectra show the information on the dipolar coupling to the nuclear spins. The dip height depends on the transverse coupling, as we have $S^d = 1 - \frac{1}{2}\sin^2(pA_{wo}T/2)$ with T the evolution time, and the longitudinal dipolar coupling can be derived from the energy matching condition, which gives parameters $(a_{\parallel_2}, a_{\perp_2})$. Although 1D NMR spectra is not sufficient for determination of the position of the target without extra chemical information, one can adjust the magnetic field orientation to determine precisely the 3D position of nuclear spins in the molecule. Because of the continuous collection of the signal, only a small number of measurement repetitions are required to reach the SNR threshold. Assuming $C \approx 0.2$ is the combined contrast and photon collection efficiency, with $pA_{wo} \sim (2\pi)2.5$ Hz and $T = 60$ ms, we estimate that the experimental time for registering one dip in Fig. 3(c) is about 1.8 s, assuming that we take measurements for 15 frequency steps.

Conclusion.—We have designed a method that achieves the coupling between distant nuclear spins mediated by a dissipatively decoupled electron spin of a NV center that suppresses the impact of NV decoherence and relaxation processes on these nuclei. This enables high fidelity selective quantum gates between two weakly coupled nuclear spins in a quantum register at ambient condition. Importantly for sensing applications, our method enables the direct use of a nuclear spin as a quantum sensor rather than merely as a memory. The controllable second-order coupling provides a tunable and sharp frequency filter for collecting the signal continuously, hence increasing the SNR, while remaining insensitive to decoherence and relaxation of the mediating NV. Therefore, making use of dissipation as a tool, the proposed NV-mediated scheme increases the ability of detection and coherence control of nuclear spins as well as analysis of complex spin structures.

The authors thank L. McGuinness and Zhenyu Wang for helpful discussions and advices. This work was supported by the ERC Synergy grant BioQ; the EU projects DIADEMS, HYPERDIAMOND, and EQUAM; the DFG CRC/TRR 21; and an Alexander von Humboldt Professorship.

Q. C. and I. S. contributed equally to this work.

[1] T. H. Taminiau, J. Cramer, T. van der Sar, V. V. Dobrovitski, and R. Hanson, Universal control and error correction in multi-qubit spin registers in diamond, Nat. Nanotechnol. **9**, 171 (2014).

[2] G. Waldherr, Y. Wang, S. Zaiser, M. Jamali, T. Schulte-Herbrüggen, H. Abe, T. Ohshima, J. Isoya, J. Du, P. Neumann *et al.*, Quantum error correction in a solid-state hybrid spin register, Nature (London) **506**, 204 (2014).

[3] J. Casanova, Z.-Y. Wang, and M. B. Plenio, Noise-Resilient Quantum Computing with a Nitrogen-Vacancy Center and Nuclear Spins, Phys. Rev. Lett. **117**, 130502 (2016).

[4] A. Bermudez, F. Jelezko, M. B. Plenio, and A. Retzker, Electron-Mediated Nuclear-Spin Interactions between Distant Nitrogen-Vacancy Centers, Phys. Rev. Lett. **107**, 150503 (2011).

[5] G. Waldherr, J. Beck, P. Neumann, R. Said, M. Nitsche, M. Markham, D. Twitchen, J. Twamley, F. Jelezko, and J. Wrachtrup, High-dynamic-range magnetometry with a single nuclear spin in diamond, Nat. Nanotechnol. **7**, 105 (2012).

[6] T. H. Taminiau, J. J. T. Wagenaar, T. van der Sar, F. Jelezko, V. V. Dobrovitski, and R. Hanson, Detection and Control of Individual Nuclear Spins Using a Weakly Coupled Electron Spin, Phys. Rev. Lett. **109**, 137602 (2012).

[7] S. Kolkowitz, Q. P. Unterreithmeier, S. D. Bennett, and M. D. Lukin, Sensing Distant Nuclear Spins with a Single Electron Spin, Phys. Rev. Lett. **109**, 137601 (2012).

[8] N. Zhao, J. Honert, B. Schmid, M. Klas, J. Isoya, M. Markham, D. Twitchen, F. Jelezko, R.-B. Liu, H. Fedder *et al.*, Sensing single remote nuclear spins, Nat. Nanotechnol. **7**, 657 (2012).

[9] S. Kaufmann, D. A. Simpson, L. T. Hall, V. Perunicic, P. Senn, S. Steinert, L. P. McGuinness, B. C. Johnson, T. Ohshima, F. Caruso *et al.*, Detection of atomic spin labels in a lipid bilayer using a single-spin nanodiamond probe, Proc. Natl. Acad. Sci. U.S.A. **110**, 10894 (2013).

[10] A. Ermakova, G. Pramanik, J.-M. Cai, G. Algara-Siller, U. Kaiser, T. Weil, Y.-K. Tzeng, H. C. Chang, L. P. McGuinness, M. B. Plenio *et al.*, Detection of a few metallo-protein molecules using color centers in nanodiamonds, Nano Lett. **13**, 3305 (2013).

[11] H. J. Mamin, M. Kim, M. H. Sherwood, C. T. Rettner, K. Ohno, D. D. Awschalom, and D. Rugar, Nanoscale nuclear magnetic resonance with a nitrogen-vacancy spin sensor, Science **339**, 557 (2013).

[12] T. Staudacher, F. Shi, S. Pezzagna, J. Meijer, J. Du, C. A. Meriles, F. Reinhard, and J. Wrachtrup, Nuclear magnetic resonance spectroscopy on a (5-nanometer) 3 sample volume, Science **339**, 561 (2013).

[13] M. Grinolds, M. Warner, K. De Greve, Y. Dovzhenko, L. Thiel, R. L. Walsworth, S. Hong, P. Maletinsky, and A. Yacoby, Subnanometre resolution in three-dimensional magnetic resonance imaging of individual dark spins, Nat. Nanotechnol. **9**, 279 (2014).

[14] C. Müller, X. Kong, J.-M. Cai, K. Melentijević, A. Stacey, M. Markham, D. Twitchen, J. Isoya, S. Pezzagna, J. Meijer *et al.*, Nuclear magnetic resonance spectroscopy with single spin sensitivity, Nat. Commun. **5**, 4703 (2014).

[15] A. O. Sushkov, I. Lovchinsky, N. Chisholm, R. L. Walsworth, H. Park, and M. D. Lukin, Magnetic resonance detection of individual proton spins using quantum reporters, Phys. Rev. Lett. **113**, 197601 (2014).

[16] F. Shi, Q. Zhang, P. Wang, H. Sun, J. Wang, X. Rong, M. Chen, C. Ju, F. Reinhard, H. Chen *et al.*, Single-protein spin resonance spectroscopy under ambient conditions, Science **347**, 1135 (2015).

[17] L. Trifunovic, F. L. Pedrocchi, S. Hoffman, P. Maletinsky, A. Yacoby, and D. Loss, High-efficiency resonant amplification of weak magnetic fields for single spin magnetometry at room temperature, Nat. Nanotechnol. **10**, 541 (2015).

[18] I. Lovchinsky, A. O. Sushkov, E. Urbach, N. de Leon, S. Choi, K. De Greve, R. Evans, R. Gertner, E. Bersin, C. Müller *et al.*, Nuclear magnetic resonance detection and spectroscopy of single proteins using quantum logic, Science **351**, 836 (2016).

[19] A. Laraoui, F. Dolde, C. Burk, F. Reinhard, J. Wrachtrup, and C. A. Meriles, High-resolution correlation spectroscopy of 13c spins near a nitrogen-vacancy centre in diamond, Nat. Commun. **4**, 1651 (2013).

[20] A. Ajoy, U. Bissbort, M. D. Lukin, R. L. Walsworth, and P. Cappellaro, Atomic-scale nuclear spin imaging using quantum-assisted sensors in diamond, Phys. Rev. X **5**, 011001 (2015).

[21] J. N. Greiner, D. D. B. Rao, P. Neumann, and J. Wrachtrup, Indirect quantum sensors: improving the sensitivity in characterizing very weakly coupled spins, Faraday Discuss. **184**, 163 (2015).

[22] Z.-Y. Wang, J. Casanova, and M. B. Plenio, Delayed entanglement echo for individual control of a large number of nuclear spins, Nat. Commun. **8**, 14660 (2017).

[23] S. Zaiser, T. Rendler, I. Jakobi, T. Wolf, S.-Y. Lee, S. Wagner, V. Bergholm, T. Schulte-Herbrüggen, P. Neumann, and J. Wrachtrup, Enhancing quantum sensing sensitivity by a quantum memory, Nat. Commun. **7**, 12279 (2016).

[24] M. Pfender, N. Aslam, H. Sumiya, S. Onoda, P. Neumann, J. Isoya, C. Meriles, and J. Wrachtrup, Nonvolatile quantum memory enables sensor unlimited nanoscale spectroscopy of finite quantum systems, arXiv:1610.05675.

[25] T. Rosskopf, J. Zopes, J. Boss, and C. Degen, A quantum spectrum analyzer enhanced by a nuclear spin memory, arXiv:1610.03253.

[26] S. Schmitt, T. Gefen, F. M. Stürmer, T. Unden, G. Wolff, C. Müller, J. Scheuer, B. Naydenov, M. Markham, S. Pezzagna, J. Meijer, I. Schwarz, M. B. Plenio, A. Retzker, L. P. Mc Guinness, and F. Jelezko, Sub-millihertz magnetic spectroscopy with a nanoscale quantum sensor (to be published).

[27] A. Ajoy, Y. Liu, and P. Cappellaro, dc magnetometry at the t_2 limit, arXiv:1611.04691.

[28] A. Jarmola, V. M. Acosta, K. Jensen, S. Chemerisov, and D. Budker, Temperature-and Magnetic-Field-Dependent Longitudinal Spin Relaxation in Nitrogen-Vacancy Ensembles in Diamond, Phys. Rev. Lett. **108**, 197601 (2012).

[29] A. Bermudez, T. Schätz, and M. B. Plenio, Dissipation-Assisted Quantum Information Processing with Trapped Ions, Phys. Rev. Lett. **110**, 110502 (2013).

[30] Y. Matsuzaki, T. Shimo-Oka, H. Tanaka, , Y. Tokura, K. Semba, and N. Mizuochi, Hybrid quantum magnetic-field sensor with an electron spin and a nuclear spin in diamond, Phys. Rev. A **94**, 052330 (2016).

[31] M. Kost, J. M. Cai, and M. B. Plenio, Resolving single molecule structures with nitrogen-vacancy centers in diamond, Sci. Rep. **5**, 11007 (2015).

[32] J. Scheuer, A. Stark, M. Kost, M. B. Plenio, B. Naydenov, and F. Jelezko, Accelerated 2d spectroscopy of single spins using matrix completion, Sci. Rep. **5**, 17728 (2016).

[33] See Supplemental Material at http://link.aps.org/supplemental/10.1103/PhysRevLett.119.010801 for details of how to derive the effective master equation of the whole system, as well as trade-offs and limitations of the scheme, which includes [4,34–37].

[34] E. M. Kessler, Generalized Schrieffer-Wolff formalism for dissipative systems, Phys. Rev. A **86**, 012126 (2012).

[35] J. Cai, F. Jelezko, M. B. Plenio, and A. Retzker, Diamond-based single-molecule magnetic resonance spectroscopy, New J. Phys. **15**, 013020 (2013).

[36] J. S. Waugh, L. M. Huber, and U. Haeberlen, Approach to High-Resolution NMR in Solids, Phys. Rev. Lett. **20**, 180 (1968).

[37] P. C. Maurer, G. Kucsko, C. Latta, L. Jiang, N. Y. Yao, S. D. Bennett, F. Pastawski, D. Hunger, N. Chisholm, M. Markham *et al.*, Room-temperature quantum bit memory exceeding one second, Science **336**, 1283 (2012).

[38] C. Cohen-Tannoudji, J. Dupont-Roc, G. Grynberg, and P. Thickstun, *Atom-Photon Interactions: Basic Processes and Applications* (Wiley Online Library, 1992).

[39] J. R. Schrieffer and P. A. Wolff, Relation between the anderson and kondo Hamiltonians, Phys. Rev. **149**, 491 (1966).

[40] H. M. Wiseman and G. J. Milburn, *Quantum Measurement and Control* (Cambridge University Press, Cambridge, England, 2009).

[41] K. Jacobs, *Quantum Measurement Theory and its Applications* (Cambridge University Press, Cambridge, England, 2014).

[42] N. Altamirano, P. Corona-Ugalde, R. B. Mann, and M. Zych, Unitarity, Feedback, Interactions–Dynamics Emergent from Repeated Measurements, New J. Phys. **19**, 013035 (2017).

[43] J. Zhang, Y. X. Liu, R. B. Wu, K. Jacobs, and F. Nori, Quantum feedback: theory, experiments, and applications, Phys. Rep. **679**, 1 (2017).

[44] M. A. Nielsen, A simple formula for the average gate fidelity of a quantum dynamical operation, Phys. Lett. A **303**, 249 (2002).

[45] L. Jiang, J. S. Hodges, J. R. Maze, P. Maurer, J. M. Taylor, D. G. Cory, P. R. Hemmer, R. L. Walsworth, A. Yacoby, A. S. Zibrov *et al.*, Repetitive readout of a single electronic spin via quantum logic with nuclear spin ancillae, Science **326**, 267 (2009).

[46] P. Cappellaro, L. Jiang, J. S. Hodges, and M. D. Lukin, Coherence and Control of Quantum Registers Based on Electronic Spin in a Nuclear Spin Bath, Phys. Rev. Lett. **102**, 210502 (2009).

4.2 Blueprint for nanoscale NMR

Title:	Blueprint for nanoscale NMR
Authors:	Schwartz, Ilai and Rosskopf, Joachim and Schmitt, Simon and Tratzmiller, Benedikt and Chen, Qiong and McGuinness, Liam P. and Jelezko, Fedor and Plenio, Martin B.
Journal:	Scientific Reports 9.1
Year:	2019
Copyright:	The Authors, some rights reserved; exclusive licensee American Association for the Advancement of Science under the Creative Commons Attribution License 4.0 (CC BY), https://creativecommons.org/licenses/by/4.0/. In accordance to this license, the author has the right to reuse the full-text article in his dissertation.
DOI:	https://doi.org/10.1038/s41598-019-43404-2

SCIENTIFIC REPORTS

OPEN

Blueprint for nanoscale NMR

Ilai Schwartz[1,2], Joachim Rosskopf[1], Simon Schmitt[3], Benedikt Tratzmiller[1], Qiong Chen[1], Liam P. McGuinness[3], Fedor Jelezko[3] & Martin B. Plenio[1]

Received: 28 January 2019
Accepted: 11 April 2019
Published online: 06 May 2019

Nitrogen vacancy (NV) centers in diamond have been used as ultrasensitive magnetometers to perform nuclear magnetic resonance (NMR) spectroscopy of statistically polarized samples at 1–100 nm length scales. However, the spectral linewidth is typically limited to the kHz level, both by the NV sensor coherence time and by rapid molecular diffusion of the nuclei through the detection volume which in turn is critical for achieving long nuclear coherence times. Here we provide a blueprint supported by detailed theoretical analysis for a set-up that combines a sensitivity sufficient for detecting NMR signals from nano- to micron-scale samples with a spectral resolution that is limited only by the nuclear spin coherence, i.e. comparable to conventional NMR. Our protocol detects the nuclear polarization induced along the direction of an external magnetic field with near surface NV centers using lock-in detection techniques to enable phase coherent signal averaging. Using the NV centers in a dual role of NMR detector and optical hyperpolarization source to increase signal to noise, and in combination with Bayesian inference models for signal processing, nano/microscale NMR spectroscopy can be performed on sample concentrations in the micromolar range, several orders of magnitude better than the current state of the art.

Nuclear magnetic resonance (NMR) and magnetic resonance imaging (MRI) are technologies whose applications in organic chemistry, biology, medicine and material science have enabled fundamental scientific breakthroughs and continue to be drivers of scientific and technological progress[1]. Despite these successes, it is recognized that nuclear magnetic resonance applications have limitations due to the minute nuclear magnetization of analytes which leads to limited sensitivity in comparison to other analytic techniques such as mass spectrometry.

Strategies that are being pursued to overcome this challenge include an evolution towards larger applied magnetic fields which improves sensitivity due to the resulting increase of thermal equilibrium polarization and signal frequency[2] but comes at the cost of growing size, purchase and operating costs of these devices, which in turn limits portability and challenge their integration with desired applications. More compact magnets lead to smaller usable detection volumes and thus limit sensitivity. A promising alternative strategy is the reduction in size of the radio frequency coils used to excite and detect the NMR signals[3] as this results in a sensitivity enhancement with decreasing coil-diameter and promises the development of portable on-chip NMR spectrometers[4]. Limitations and challenges in this approach include the homogeneity of the system which limit resolution and the thermal noise in the readout coil, i.e. thermal Johnson noise, which, together with the low sample volume, limits sensitivity. A further avenue towards improved NMR sensitivity is to increase the nuclear spin polarization beyond its thermal equilibrium value by means of techniques such as dynamical nuclear polarization[5]. Despite promising results, the integration of these approaches with NMR involve significant challenges, as they typically require low temperatures and dissolution of the sample - significantly reducing its concentration.

Addressing these challenges in a single device to achieve simultaneously improved sensitivity, ideally in the micromolar regime, portability and the ability to vary sample volumes from the nano- to the millimeter scale would decisively enhance a broad range of applications thus offering the potential for new ground breaking insights. These include NMR studies of single cells and neurons[6], surfaces, surface chemistry and catalysis at smallest volumes[7], and on-chip NMR based metabolic fingerprinting with applications in personalized medicine[8,9]. Moreover, if such NMR detection can be performed in ultra-low magnetic fields, information-rich spectra can be obtained due to the J coupling in this regime, as shown in the field of zero and ultra-low field (ZULF) NMR[10–13].

Here we present a novel physical platform for NMR detection that we show is capable of overcoming these challenges for samples ranging from the nano- to the millimeter-scale using nitrogen vacancy (NV) centers in diamond as a well-established quantum sensor[14–20]. We introduce an NMR protocol that permits spectroscopy

[1]Institute of Theoretical Physics and IQST, Universität Ulm, Albert-Einstein-Allee 11, 89081, Ulm, Germany. [2]NVision Imaging Technologies GmbH, Universität Ulm, Albert-Einstein-Allee 11, 89081, Ulm, Germany. [3]Institute of Quantum Optics and IQST, Universität Ulm, Albert-Einstein-Allee 11, 89081, Ulm, Germany. Correspondence and requests for materials should be addressed to I.S. (email: ilai.schwartz@uni-ulm.de) or M.B.P. (email: martin.plenio@uni-ulm.de)

of such volumes with chemical resolution and micromolar range sensitivity and demonstrate signal processing algorithms that allow for a significant reduction in signal acquisition time, thereby yielding sample analysis with dramatic speed-up. The feasibility of this approach is experimentally demonstrated by detecting magnetic signals applied to a single NV center in diamond. The signal dynamics are obtained from atomistic simulations of a diffusive nanoscale nuclear sample, with a signal intensity scaled to correspond to an NV depth of 6.2 nm.

Results

Background and key design elements. High-resolution NMR spectroscopy makes use of several properties of bulk matter in resolving chemical shifts and J-couplings for molecular structure determination. The rapid molecular diffusion and rotation leads to the suppression of internuclear interaction down to the Hz-level while not limiting the signal coherence due to the large volume from which the signal is collected. Furthermore, for bulk samples, the thermal polarization (scaling with the sample volume V) greatly exceeds the statistical polarization fluctuations (scaling with $V^{1/2}$). This allows on the one hand for the controlled initialization of the signal and therefore phase coherent signal accumulation resulting in a rapid growth of the signal to noise ratio (SNR) and on the other hand for long signal coherence times and therefore high spectral resolution.

However, for $(1\ \mu m)^3$ of water in a 1 Tesla field, the statistical polarization of the hydrogen nuclei is comparable to the thermal polarization and becomes dominant at the nanoscale. This observation has motivated successful experimental efforts towards NMR detection of statistical polarization of nanoscale samples[21]. On the other hand, the stochastic nature and random phase of the observed statistical polarization prevent phase coherent signal averaging and the impact of diffusion limits signal coherence time and thus spectral resolution[22]. Overcoming these limitations calls for new modes of observation. Here we will consider, perhaps counter-intuitively, the detection of the signal originating from the thermal polarization, even for nanoscale samples for which the statistical component is expected to dominate. We use three key features to compensate for this apparent shortcoming, namely, (i) the signal phase can be controlled by an initializing $\pi/2$-pulse to allow for phase coherent accumulation across subsequent measurements, (ii) because the thermal polarization component is uniform across the entire sample beyond the immediate detection region, the signal coherence time becomes essentially independent of diffusion allowing for high spectral resolution, (iii) and for the same reasons the signal is uniform across the sample which allows for the use of multiple NV-centers for simultaneous signal acquisition thus further improving SNR.

The platform and protocols described in the following leverage the unique characteristics of color centers in diamond[23] to make use of these three key features. First, we use optically detected magnetic resonance in either individual or ensembles of color centers[15,24] to detect small magnetic fields emanating from the sample which, by making use of a recently developed lock-in technique, Qdyne, allows for spectral resolution in the μHz range[25–27]. This substitutes the electrical detection via rf-microcoils which is accompanied by thermal Johnson noise by optical detection which is only limited by the non-thermal photon shot noise. Secondly, the ability to bring color centers to within nanoscale distance of the sample allows for their use as a source of nuclear hyerpolarization even under ambient conditions using laser induced polarization of the electron spin native to the color center and the subsequent microwave assisted transfer to the sample nuclei[28–30]. This obviates the need for a strong magnetic field and holds the potential for an orders of magnitude increase in signal strength, thus bringing sub-millimolar sensitivities into reach while at the same time reducing nuclear spin polarization fluctuations induced by diffusion. Thirdly, in order to reduce averaging times required for achieving sub- millimolar sensitivities, we employ signal processing methods based on Bayesian inference algorithms that allow for orders of magnitude reduction of measurements required for the identification of signal components due to chemical shifts. The remainder of this work will describe these key elements and present theoretical and experimental results that demonstrate the feasibility of the approach.

Qdyne for nuclear magnetic resonance. The recently developed Qdyne method introduces a quantum lock-in spectroscopy technique[25–27] whose spectral resolution is independent of the sensor coherence time. Using Qdyne, a coherent external oscillating radiofrequency (RF) field, could be measured with a spectral linewidth of 607 μHz[25], thereby making the technique promising for realizing true nanoscale NMR via shallow NV centers.

In Qdyne, the sensor qubit is tailored to collect a signal that depends not only on the amplitude and frequency of the detected field, but also on the phase with respect to the start of each measurement. Performing N measurements each of length T_L, a different phase is accumulated in each measurement due to the difference between T_L and period of the oscillatory field. As shown in ref.[25], for an XY8 measurement sequence when the excitation and detection $\pi/2$ pulses are perpendicular to each other, the detected signal is given by

$$P = \frac{1}{2}\sin\left(\frac{4k\tau_m}{\pi}\cos(\delta t + \phi)\right) + \frac{1}{2}, \tag{1}$$

where k is the total interaction strength, τ_m the interaction time, ϕ is an arbitrary initial phase of the RF field, and δ denotes the frequency of the accumulated phase.

As with most NV sensing schemes, when using a shallow NV for detection, due to the small number N_I of spins in the vicinity of the NV, the signal detected by Qdyne is dominated by the statistical polarization of the nuclear spins in the sensing volume - $B_{rms}(t) = \sum_i A_x^i(t) I_x$, with $A_x^i(t)$ denoting the coupling of the NV center to the i-th nuclear spin.

Diffusion of molecules into and out of this volume leads to random fluctuations of the detected signal, which is governed by a correlation function $\langle B_{rms}(t) B_{rms}(t+\tau)\rangle = B_{rms}^2 \exp(-\tau/\tau_c)$, where τ_c is the correlation time. Thus, the phase ϕ in Eq. (1) becomes a stochastic variable, $\hat{\phi}(t)$, which denotes the instantaneous phase of the statistical nuclear spin polarization within the NV detection region. Some fluctuations in ϕ are still expected due

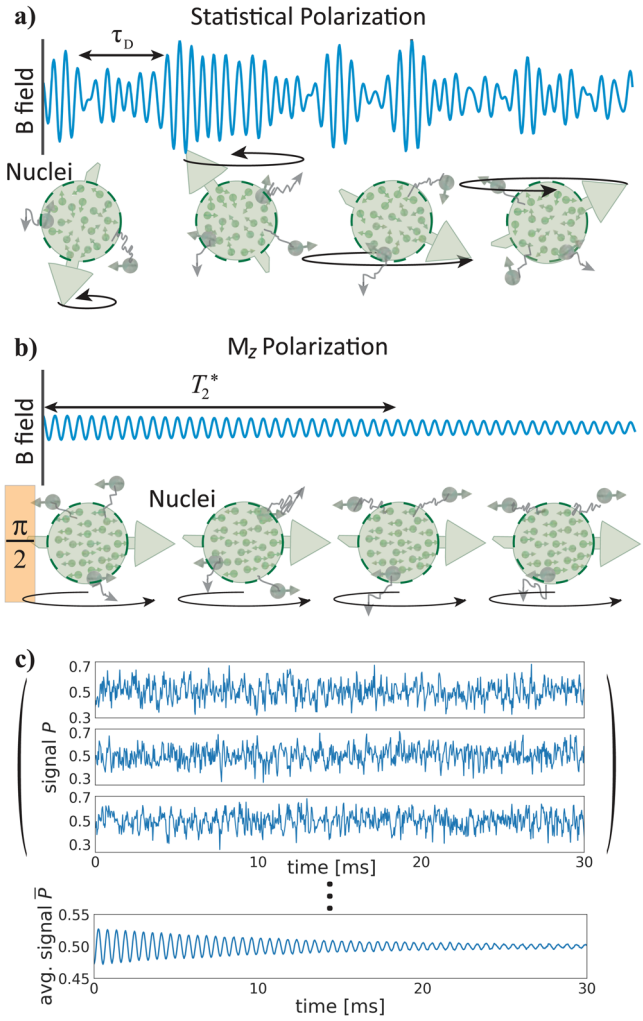


Figure 1. (**a**) Illustration of the Qdyne signal and the detected statistical magnetization by the NV center. The diffusion of nuclear spins in or out of the NV detection range leads to rapid fluctuations of the detected phase, introducing a short signal coherence time-scale, τ_D, on the order of the interaction correlation time. (**b**) The adoption of M_z Qdyne enables the detection of the FID signal from the nuclear z magnetization (thermal or hyperpolarized), regardless of the molecular diffusion. (**c**) An atomistic simulation of the time-dependent magnetic field induced by the diffusing nuclear spins on a 6.2 nm deep NV, where the statistical polarization is still clearly stronger than the hyperpolarized $M_z = 0.1\%$ polarization. However, M_z Qdyne can be averaged over many runs N_m, significantly reducing the statistical polarization signal by $1/\sqrt{N_m}$ while the M_z signal remains unchanged (due to the same initial phase at every run). The bottom figure shows the averaged signal for nuclear $T_2 = 5\ ms$ with $N_m = 1500$, where only the smaller M_z polarization (oscillates between ± 0.05) remains visible.

to spatial deviations of the molecule locations, however, this is expected to be negligible even for shallow NVs. k in equation (1) would also fluctuate due to the density and spin fluctuations, but to a much lesser extent than $\hat{\phi}(t)$.

This stochastic variable ties the observed Qdyne signal to the molecular diffusion of the moving molecules, leading to a stringent limitation on the minimal observable line-width, thereby obscuring small but important details such as chemical shift and quadrupole information. See Fig. 1(a) for an illustration of a statistical magnetization detected by a Qdyne measurement, and the diffusion effect on the phase of the detected signal.

To solve this issue, and decouple the Qdyne signal from molecular diffusion, we modify the sequence to detect thermal nuclear magnetization along the z-axis of the applied magnetic field. This modified M_z Qdyne sequence consists of N_m measurements, and, at the beginning of the sequence, a $\pi/2$ pulse which rotates the nuclear z magnetization to the x-y plane, where it can be detected by the XY dynamical decoupling measurement with the correct filter function, similar to a free induction decay (FID) in traditional NMR. Importantly, at the beginning of each of the N_m sequences, the initial phase of the z magnetization on the x-y plane is known and *identical*. Moreover, as the phase is identical for all nuclear spins across the sample, the diffusion of molecules in or out of the NV center detection region has no effect on the signal phase, and the detected linewidth becomes limited only by the nuclear coherence times, see Fig. 1(b).

In a realistic NMR scenario using a 5–100 nm deep NV center, both the statistical and M_z sample magnetizations contribute to the detected signal, with the statistical polarization generally dominating the z-magnetization.

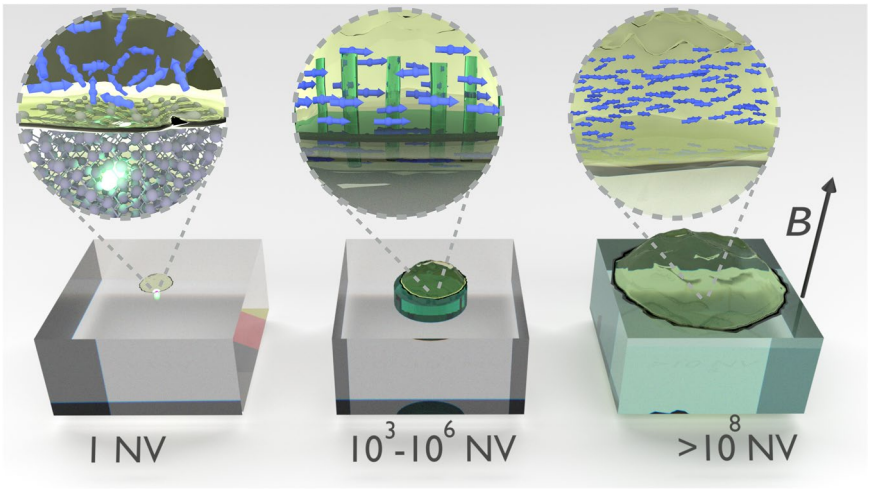


Figure 2. Illustration of the three different regimes made possible by M_z Qdyne. On the r.h.s. is the "classical" regime, where a macroscopic diamond with densely packed NV centers senses the thermalpolarization, providing a substitute to traditional NMR micro-coils. In the middle figure, using the NV center ensemble in a dual role- polarizing the nuclear spin bath to increase the nuclear signal and detection of the NMR signal, thus termed Hyperdyne, enables superb sensitivities in the nano- and micro-scale regimes (the illustration includes a nanostructured diamond for enhanced polarization efficiency). Hyperdyne can be pushed to the extreme nano-scale limit, using a single NV center (l.h.s.) albeit at a significantly reduced polarization/sensitivity efficiency.

However, the summation of N_m repeated measurements can be used to reduce the statistical signal by a factor of $1/\sqrt{N_m}$ due to its random phase and magnitude, while locking-in to the phase of M_z-magnetization so as to prevent its cancellation. Thus, especially when combined with hyperpolarization, the detection of M_z magnetization is feasible even with relatively shallow NV centers, and therefore even sub-micron detection volumes. Figure 1(c) shows the Qdyne phase accumulated by the NV in an atomistic simulation of diffusing hyperpolarized ($\langle M_z \rangle = 0.1\%$) nuclear spins near a 6.2 nm deep NV center. The diffusion coefficient was chosen to be $D = 10^{-12}\, m^2/s$, similar to oil molecules. Clearly the statistical polarization is larger than the hyperpolarized signal in this regime as the FID is not visible. However, when averaging the signal over 300 runs, the smaller M_z polarization can be clearly seen due to the reduction of the contribution from the statistical polarization.

An additional advantage of M_z Qdyne due to the averaging of N_m measurements is better statistical information on each measured point. This improves the low photon collection efficiency inherent in NV-based detection, with the statistical detection process becoming a Poissonian distribution rather than a Bernoulli process. Moreover, as the M_z-polarization is uniform across the entire sample, different NV centers now detect the same phase ϕ, which allows the measurement to be performed with ensembles of NV centers. The accumulated fluorescence from the different NV centers acts identically to repeated measurements N_m of the single NV center, i.e. improving statistical information and averaging out the statistical polarization. Thus, the number of statistical averages is given by $N = N_{NV} \times N_m$, where N_{NV} is the number of NV centers used as sensors.

M_z Qdyne unlocks the potential of NV-based NMR, allowing for volumes ranging from nanometric to macroscopic scales. However, as the nuclear thermal polarization is very weak, especially at lower magnetic fields, achieving a good SNR in this regime requires macroscopic diamonds with densely packed NV centers and roughly 1 μl samples (1 mm^3) for practical NMR applications (r.h.s. of Fig. 2). Pushing the limits of this regime to even large micro-scale would require averaging of several hours of measurement time for acquiring a sufficient SNR, due to the small signal produced by thermal polarization. Thus, in this regime the NV ensemble in the diamond serves as a "classical" macroscopic NMR sensor, similar to currently used micro-coils, albeit with the advantage of different noise processes which could lead to improved sensitivity. To push the application into the micro- and nano-scale regimes, the M_z polarization needs to be enhanced, in a manner which still allows fast repetitive measurements. Fortuitously, optically polarized NV centers have been demonstrated to be superb polarization sources for nuclear spin hyperpolarization either inside the diamond[31–35] or in external molecules[28–30]. Thus by using the NV centers in a dual role of hyperpolarization sources and NMR detectors, with shallow NVs used for polarization and deeper ones for detection, the NMR SNR of each measurement can be increased over 10,000-fold, without the need for shuttling between polarization and detection zones and without suffering other detrimental side-effects of dissolution DNP (e.g. cooling the sample to $T = 1\ K$, reduction of analyte concentration upon dissolution). Thus, using interleaved hyperpolarization/detection sequences on the NV centers (the Hyperdyne protocol) one can achieve true NMR applicability on the (sub)micronscale, see middle of Fig. 2. Note that the combination of hyperpolarization and spin-based readout has been shown to be instrumental in ZULF NMR applications[10–13]. The Hyperdyne protocol builds on these developments and enables performing for the first time both the hyperpolarization and mesoscopic NMR detection using the same electron spins. This is in contrast to the recent use of traditional DNP techniques based on admixed electron spin radicals in combination with NV center based detection[36] which is limited in achievable degree of nuclear polarisation by the electron radical thermal polarization.

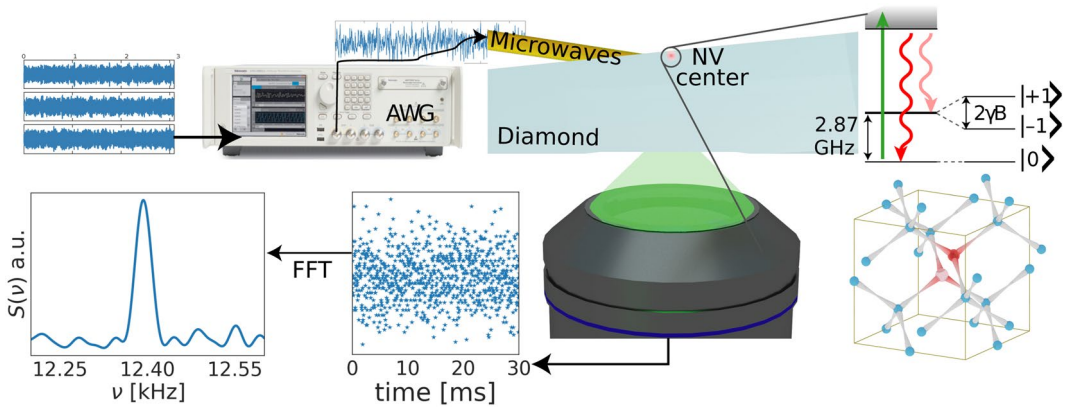


Figure 3. Experimental verification of the Hyperdyne method. Using an arbitrary waveform generator (AWG), the simulated magnetic field ($N_m = 1000$) was applied on a single NV center by a current carrying wire, with the setup of ref.[25]. Taking a Fourier transform of the summed photon counts, the M_z, diffusion independent signal can be clearly seen, producing a peak with 170 Hz linewidth (limited only by the 5.6 ms length of the simulated signal). A simulated signal with only statistical polarization produces no peak, and the diffusion limited signal would be over 10 kHz.

On the extreme nanometric scale (l.h.s. of Fig. 2), one may implement Hyperdyne NMR with a single NV center. However, the single NV center needs to be close to the surface for sufficient efficiency in the hyperpolarization cycle, which leads to the disadvantage that many of the polarized nuclei will diffuse outside the small NV detection region, and thus produce a much smaller net gain in the NMR sensitivity.

In the next two sections we first provide expressions for the signal to noise ratio for large numbers of detection events, either due to high detection efficiency or large number of phase coherent averages that apply to a standard Fast Fourier Transform (FFT) analysis and present the results of the experimental detection of simulated signals by means of an NV center. In the following section we will then describe Bayesian inference methods to improve signal detection from noisy measured data for situations in which signals are so noisy that standard FFT analysis is not able to extract frequency information from data. We will demonstrate that Bayesian inference methods are capable of extracting information from significantly more noisy signals and thus allow for orders of magnitude reduction in measurement time.

Verification and FFT signal analysis of hyperdyne. To experimentally verify the Hyperdyne protocol, the magnetic field produced by an ensemble of nuclear spins as calculated by atomistic simulations was inputed into an arbitrary waveform generator and applied to a single NV center by a current carrying wire (see ref.[25] and the methods section for experimental details) for $N_m = 1000$ runs as shown in Fig. 3. While in each individual run the number of photons detected in each measurement was typically 0 or 1, due to the summation of the N_m runs, a much better statistics of the photon count was achieved, even given the low detection probability. A measured signal due to the M_z polarization is clearly visible with 170 Hz linewidth, limited only by the 5.6 ms length of the detected signal. For comparison, with the chosen diffusion parameter the linewidth due to the statistical polarization would exceed 10 kHz.

We proceed with theoretically analysing the behaviour of the Hyperdyne signal. For shot noise limited detection,

$$SNR \propto \sqrt{N_{\mathrm{Phot}}}\, k\tau_m \propto \sqrt{N}\, \rho P_n \tau_m, \tag{2}$$

with $N_{\mathrm{Phot}} \propto V_s$ being the number of detected photons, τ_m the length of a single XY measurement, V_s the total detection volume, $k(\tau_m)$ the interaction strength (time) for an individual NV center, $N = N_m N_{NV}$ the number of independent measurements (which is the product of N_m runs with N_{NV} NV centers), ρ the nuclear spin concentration and P_n the average polarization. There are two regimes to be considered when aiming to maximize SNR in a given total experiment time here. Firstly, when $\tau_m < \min(T_2^{NV}, \pi/4k)$ it is most advantageous to increase τ_m while keeping N_m constant, i.e. increase the time over which the signal is accumulated coherently. In this case the total measurement time $T = N_m \tau_m$ scales as the first case of eq. (3). If however, $\tau_m = T_2^{NV}$ we cannot increase τ_m any further without suffering an exponential in τ_m loss in signal (for $\tau_m > \pi/4k$ we lose the ability to identify the phase). Hence we are reduced to increase N_m, that is averaging over independent runs. In this case the total measurement time $T = N_m \tau_m$ scales as the second case of eq. (3) benefiting more from an increase in polarization of the sample.

$$\frac{1}{T} \propto \begin{cases} \sqrt{V_s \rho_{NV}}\, \rho P_n & \text{if increasing } \tau_m < \min\left(T_2^{NV}, \dfrac{\pi}{4k}\right) \\ V_s \rho_{NV} \rho^2 P_n^2 & \text{else.} \end{cases} \tag{3}$$

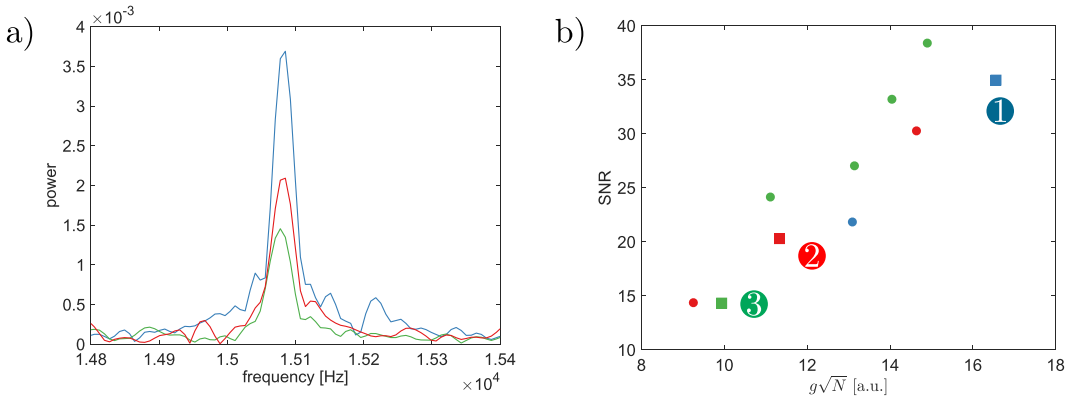


Figure 4. (**a**) The Fourier transform of the NV Hyperdyne signal with three different parameters for the diffusing nuclear spins. The SNR mainly depends on the signal amplitude within each XY measurement $g = k\tau_m$ and the number of measurements N. (**b**) Scaling of the SNR with $g\sqrt{N}$ for numerous parameter configurations, noting specifically the three parameters from (**a**), curve expected to be linear by Eq. 2. The parameters are $P_n = 0.1\%, \rho = 5\ M, N = 1600, \tau_m = 4.1\ \mu s$ (data set 1), $P_n = 0.5\%, \rho = 5\ M, N = 30, \tau_m = 4.1\ \mu s$, (data set 2) and $P_n = 0.05\%, \rho = 150\ mM, N = 400, \tau_m = 32.8\ \mu s$ (data set 3).

where T is the total measurement time for achieving a fixed SNR value, ρ_{NV} is the NV concentration, and enlarging V_s is assumed to be achieved by increasing the surface cross section, thereby scaling linearly with the number of NV centers.

Figure 4(a) shows the Fourier transform of the acquired M_z Qdyne signal by a 6.2 nm deep NV center for three scenarios with different polarization, molecular concentration and number of measurements N. All scenarios were produced by atomistic simulation of the detection process for diffusing nuclei at the density of water. One can see a difference in the SNR between the three scenarios, due to a difference in $g = k\tau_m$ and N. As shown in Fig. 4(b), the scaling of the SNR is proportional to $g\sqrt{N}$, as expected from Eq. 2.

As noted above, the statistical polarization can be allowed to be larger than the M_z polarization as it is reduced by the averaging of the signal over N_m runs. The statistical polarization does limit the accumulation time in the XY sequences for shallow NV centers, as the condition $\gamma_e B_{rms}\tau_m < \pi/2$ needs to be fulfilled to ensure that the M_z-signal is not fully randomized by the statistical polarization. As hyperpolarization enhances the M_z to statistical polarization ratio, a larger M_z signal can be accumulated by shallow NV centers, enabling the sensing of nano-scale volumes. It is important to note that the shot noise in the detection process scales as $\sqrt{N}$, as does the statistical polarization signal, which in turn implies that the fluctuations due to the statistical polarization signal are never larger than the shot noise (including the pre-factor due to $\gamma_e B_{rms}\tau_m < \pi/2$), and are typically negligible.

It is interesting to compare our scheme to microcoils. When scaling the diamond to the macroscopic regime (e.g. 1 μl), the expected sensitivity will be similar to that achieved with state of the art micro-coils. However, due to the ohmic contribution to the noise becoming dominant at small diameters[37], microcoil sensitivity per unit volume starts scaling as $1/\sqrt{d}$ instead of $1/d$ when $d < 100\ \mu$m, where d is the coil diameter, equivalent to $1/V_s^{1/43}$. Therefore, even for large micrometric samples NV detection may become superior to microcoil detection, even without combining with hyperpolarization.

Advanced signal analysis of hyperdyne: From FFT to hierarchical Bayesian models and Monte Carlo inference. The measured Hyperdyne photon count signal **D** is acquired by photo detectors with a detection scheme similar to that of[38] and suffers from several loss sources that make the acquired signal very noisy. On the one hand the detection is extremely lossy, leading to a very sparse time series of photon counts with less than a detection event per signal period. On the other hand each NV emits with a finite probability a photon in the $|-1\rangle$ state, leading to just a small net difference in detection probability p between $|0\rangle$-state ($p_{|0\rangle} \approx 4.0\%$) and $|-1\rangle$-state ($p_{|-1\rangle} \approx 2.5\%$). In the framework of Fourier NMR spectroscopy, this setting leads to rapidly decaying SNR. Of note, the detection efficiency can be significantly increased to almost 100% by using single-shot readout.

In this challenging, low SNR settings, approximating the parameters of an underlying, hidden model by Bayesian inference has shown great benefit in other experimental scenarios (e.g. in astro- or particle-physics[39,40] and recently in NV center measurements[41]). In[42,43] and more recently[25] it was mentioned, that Fourier analysis is not necessarily optimal in terms of precision and other estimation methods, such as maximum likelihood, can be used.

Similar to FFT the hierarchical Bayesian method operates on the raw signal vector **D** without any preprocessing or reconstruction, but at the same time reducing the measurement time by at least one order of magnitude in typical settings. It relies on a probabilistic graphical model (PGM) capturing the hierarchical nature of the Rabi oscillation, photon emission and detection. This parametric model allows to incorporate prior knowledge of the problem into the analysis of the sparse signal. By using Bayesian inference NMR spectroscopy can be interpreted as fitting the distribution of parameters of an underlying harmonic model. The fit is guided by measured data **D**

and an informed choice of priors of the parameters Θ. The priors which go into the population probability P in eq. (1) are determined by a normally distributed $g \sim \mathcal{N}_{\mu}(\mu = 4k\tau_m/\pi)$, the uniform oscillation frequency $\delta \sim \mathcal{U}_{a,b}(\delta_0 - a, \delta_0 + b)$ and an uniform free phase parameter $\phi \sim \mathcal{U}_{a,b}([0, 2\pi])$. Descending from P the measurement is modeled by $M \sim \mathcal{P}_{\lambda}(\lambda = p_{|-1\rangle} + (p_{|0\rangle} - p_{|-1\rangle})P)$, where $\mathcal{P}_{\lambda}$ is the Poisson distribution for the photon counts. It's rate parameter λ is determined by the parent emission process. The resulting distributions after the fit are called posteriors. An advantage of the hierarchical model is the ability to directly model the photon counts with a discrete probability distribution, instead of approximating the signal by a continuous distribution. The approximation via a continuous distribution is typically justified by the central limit theorem, which is applicable if $\dim(\mathbf{D}) \rightarrow \infty$. However in our case, where $\dim(\mathbf{D}) \approx \mathbf{10^5}$ and the assumption of a continuous model constitutes an approximation that would lead to loss of precision and model performance.

M is a vector of stochastic random variables (RVs) as it depends on parents in the PGM. The parents could either be constants or random according to a specified probability distribution. The value of the vector is determined by the measured photon counts. It's up to the inference mechanism to estimate the posterior model parameters $\Theta = g, \delta, \phi$ such, that the posterior distribution approximates the measured values best. The adjustment of the posteriors is done by drawing many samples from a proposal distribution using Markov Chain Monte Carlo (MCMC) and either keeping the current Θ with a certain probability if the likelihood of the measured data is increased, or rejecting the sample. The MCMC sampling takes the form of a Markov-Chain which means the position of step $n+1$ is dependent only upon the position of step n, and is otherwise independent of all other steps. The walk around the joint proposal distribution happens in a semi-random manner. The step-size and direction are decided according to specific rules of the sampling method, including randomness (the Monte-Carlo aspect) and gradient-seeking and momentum (Hamilton Monte Carlo[44]) for efficiency. Simpler algorithms like maximum likelihood (ML) or expectation maximization (EM) couldn't be directly applied, due to the complex nature of the likelihood function. If the MCMC algorithm has converged sufficiently well, the samples drawn approximate the respective posterior distributions of the RVs. The whole procedure can be seen as a stochastic simulation of the experiment and adjustment of the parameters until measured and simulated data is statistically equivalent. To implement the inference algorithm we relied on recent software techniques, which provide easy to use and flexible to program inference algorithms to model complex problems. Practically the performance of the sampling highly depends on it's initial starting value[45]. Therefore an as good as possible a posteriori (MAP) estimate is used as a starting point. Recently tools for probabilistic programming (PP), automatic differentiation frameworks and advances in MCMC methods made automatic Bayesian inference on PGMs easy to formulate and perform. The tool used in this work is called PyMC3[46]. The framework automatically derives a likelihood function for the model and repeats the sampling and evaluation for a a defined upper bound. This reduces implementation effort and make quick model changes possible.

The benefit of a Bayesian analysis can be seen in Fig. 5b where, in this specific setting, the inset demonstrates that the Bayesian analysis allows for an order of magnitude reduction in the minimal detectable concentration.

Micromolar range detection in the (sub)micron scale. Hyperdyne achieves excellent SNR with a relatively small number of measurements N_m. The key question is whether such a diamond-based setup can combine high nuclear polarization with M_z Qdyne to achieve NMR spectrometry with chemical shift resolution on the nano-micro scale.

We propose the following setup for nano-micron scale NMR (Fig. 2(b)) - an analyte with μM-mM concentration in a solution is placed on top of a nanostructured diamond for improved surface ratio, e.g. with nanoslits[47]. The walls of the ~0.3 μm wide nanoslits are assumed to be doped with NV centers to achieve a concentration of $10^{17}\,\mathrm{cm}^{-2}$. We assume that the NV doping includes a micron-scale depth detection layer and a 5–20 nm near the surface layer. The Hyperdyne sequence is then composed of N_m alternations of hyperpolarization and M_z Qdyne sequence. The hyperpolarization, driven by the shallow NV centers, significantly enhances the measured signal.

Since NV centers can be optically polarized to over 90% polarization with microsecond-long laser pulses[48], shallow NVs provide a unique resource for polarizing nuclear spins in nearby molecules. The polarization efficiency depends on $g_{tot}\tau_c$, where τ_c is the correlation time, and $g_{tot} = g\sqrt{N_I}$ is the total flip-flop coupling between the nuclear spins and the NV center, N_I the number of nuclear spins in the polarisation region, and g the average coupling to these nuclear spins. When $g_{tot}\tau_c < 1$, the typical scenario, the polarization efficiency does not depend on the analyte concentration[29].

As the distance between slits is 300 nm, and with the chosen NV concentration the average distance between NV centers is 22 nm, to calculate the achieved polarization, on needs to consider the polarization buildup in a 22 nm × 22 nm × 150 nm region for each NV. Assuming $g_{tot}\tau_c < 1$, a nuclear $T_1 \sim 2$ s, using robust polarization pulses[49] and experimentally verified polarization transfer rates[29], we obtain 0.5% polarization of the analytes in the nanoslit solution after 2 seconds of polarization, as shown in Fig. 5(a). the diffusion of the analyte is assumed to be around $10^{-11}\,\mathrm{m}^2/\mathrm{s}$, either due to large analytes (e.g. proteins) or a viscous solution. The polarization simulation takes into account the polarization rate, the nuclear relaxation process and the molecular diffusion.

For thermal polarization the duty cycle for the measurements is limited by the time required to build up the thermal polarization, on the order of several T_1 times. Unsurprisingly, as the nuclear T_1 is the limiting time also for the polarization buildup, replacing nuclear thermalization by NV-based DNP does not change the duty cycle of the NMR experiments.

The achieved NMR sensitivity now depends on the volume of material probed, as N_{NV} scales linearly with the volume (the solution is assumed to reside mainly in the nanoslits, but the diamond surface cross section can be enlarged). Figure 5(b) shows the detectable analyte concentration within 10 minutes of measurement time (taking into account the time for polarization and the experimental photon detection efficiency) when varying the probe size, for the achieved polarization of 0.5% in each hyperpolarization cycle, with spectral and Bayesian analysis. As a comparison, best

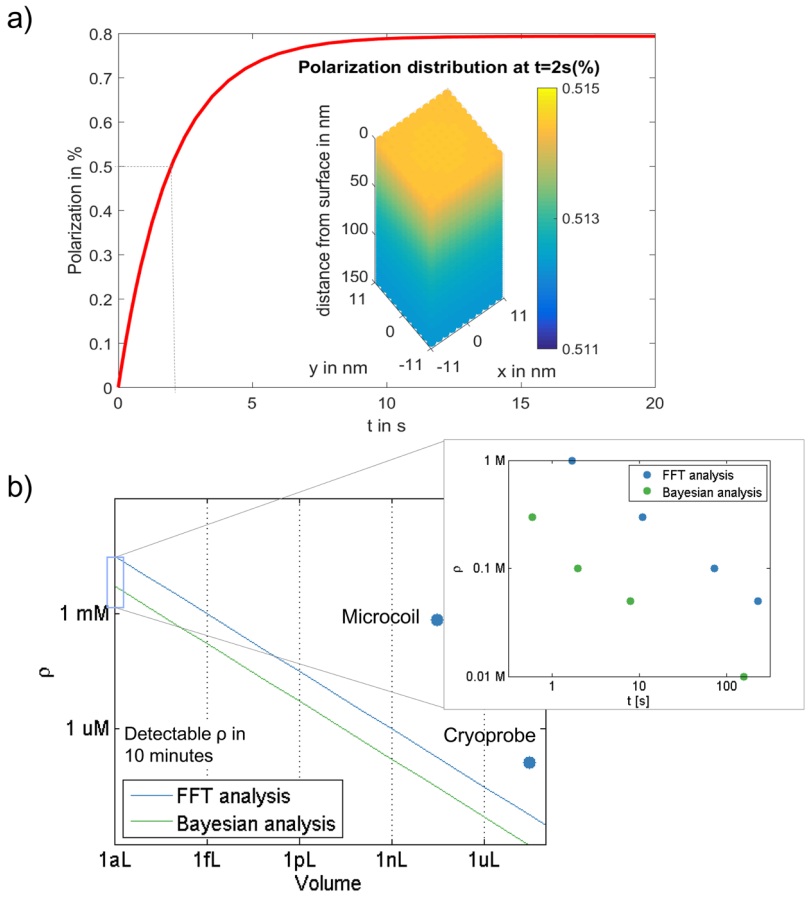


Figure 5. (**a**) Simulation of the polarization buildup for our setup, taking into account the polarization rate, molecular diffusion and nuclear relaxation of $T_1 = 2$ s. (**b**) The minimal detectable molecular concentration for different volumes using the $\sqrt{N}$ dependence (volume increased by increasing the surface cross-section). A SNR of 10 was chosen as the threshold. Also shown are the best achieved sensitivities for cryoprobes and microcoils[47]. The insert depicts the time required for detection (SNR > 10) of different concentrations for a volume of $(100\,nm)^3$, used for the calculation of the detectable minimal concentration within 10 minute time.

achieved sensitivity for microcoil and cryogenic probe NMR are noted[47]. For NMR spectroscopy we see that for a volume of less than 1 femtoliter (1 nanoliter), detection with a few Hz resolution of mM (μM) concentrations is feasible with Hyperdyne within 10 minutes, corresponding to 3×10^6 spins $\times \sqrt{\text{Hz}}$ (10^{18} spins $\times \sqrt{\text{Hz}}$), paving the way for applicable diamond-based NMR spectroscopy. Even with hyperpolarization, these regimes would not be possible with standard microcoils due to the $V^{1/4}$ scaling. Note that at very low concentrations, additional noise will be produced by the spatial location of the individual number of nuclear spins at the NV detection region.

Regarding the minimal linewidth detectable by the setup we note that due to the small width of the slits (300 nm) the nuclear spins are in close proximity of the NV center sensors and may be subject to shifts of the nuclear Larmor frequency due to the Z-Z coupling with the NV centers. This leads to a broadening in high-resolution NMR which we calculate to be in the range of $\gamma_e \Delta B \approx 1 - 2$ Hz. Here, the presence of NV centers on both sides of the slit improves the homogeneity of the signal, as the deviation of the Larmor becomes more homogeneous spatially, see Supplementary Information.

Resolution of chemical shifts. To further underline the practical relevance of the Hypdyne scheme, we show that it is capable of resolving chemical shifts and therefore well suited for detection, spectroscopy and fingerprinting of molecules and compounds. To this end we generated atomistic scale simulations of the NMR signal of a toluene solution of 0.2 M concentration at 0.25 T field, whose detection was simulated for parameters typical of near surface NV-centers and realistic detection rates, see Supplementary Information. The upper part of Fig. 6 shows the result of a Bayesian data analysis of such a signal which is capable of inferring the central frequencies of the two NMR resonances of Toluene in the signal. The two NMR resonances, exhibiting a chemical shift of 5 *Hz* relative to each other, are found in our simulation at $\omega_1 = 1.820$ *kHz* and 1.825 *kHz*. Our Bayesian analysis of the photon cout record reveals several pieces of information, a probability density of the estimated frequency positions and from it the estimated central frequency as well as the relative power of the two NMR peaks. Both pieces of information, position and relative strength, provide the foundation for fingerprinting molecules. The lower part of Fig. 6 shows the result of a classical FFT analysis of the same photon count signal. This comparison clearly

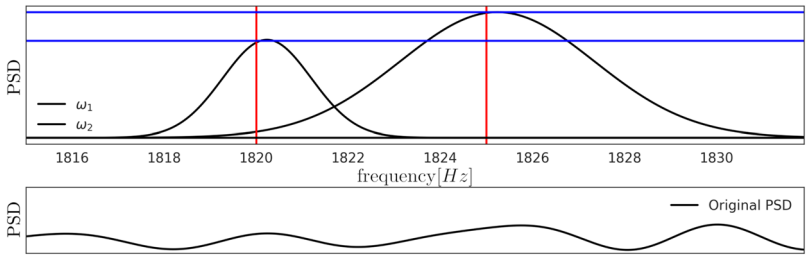


Figure 6. Comparison of detection results between Bayesian (upper part) and FFT (lower part) analysis of 160 *s* of simulated Toluene signal. The Bayesian analysis obtains the posterior densities of mean frequency positions, where the horizontal lines give the true value of the simulated signal. Further the heights of this peaks are scaled such that they correspond to the relative power contained in this resonance frequency.

shows that application of Bayesian inference, which is making use of a priori knowledge about the underlying model leading to a measurement signal as well as sensible priors for system parameters outperforms uninformed FFT. It should be noted, that the 320 *s* of signal time used in the analysis could be equally acquired by a bulk of NVs concurrently. Similar to the case for a signal frequency for longer signal times, the relevant peaks will also become visible with FFT analysis.

Discussion

The ability of NV centers to serve simultaneously as a hybrid quantum-classical detector and a source of hyperpolarization and to combine this with the analysis of the collected NMR signal with methods of signal processing based on Bayesian inference opens up new possibilities for (sub)micro scale NMR. It is interesting to note the uniqueness of the system - the NMR detection is based on individual electron spins, accumulating phase independently, very differently from other methods of high-field NMR detection (e.g. induction in tuned coils). This spin-based detection has similarities to the atomic-based magnetometry used in ZULF[10–13], which has shown radically higher sensitivity in the zero-field regime compared to NMR coils. The use of NV centers as the electron detectors enable to expand this approach both to higher magnetic fields where atomic magnetometers are no longer usable, as well as the sub-micron scale (for both ZULF and high field). The fact that these same electron spins (at least the shallow ones) can also be optically polarized and serve as a source for suprathermal dynamic nuclear polarization for the investigated nuclear spins is a fortuitous coincidence for the hybrid polarizer/micro-NMR system, and enables achieving remarkable sensitivities. The achieved polarization of the molecules will depend on the molecular relaxation time and diffusion, and can be optimized for specific molecules.

Regarding the analysis of the M_z Qdyne signal, the introduced heirachical Bayesian analysis was shown to dramatically improve the detection sensitivity even in the regime where the central-limit theorem, typically use for NMR spectra analysis, does not apply. It is worth exploring how well this analysis could also improve non-hyperpolarized Qdyne, as it could push the limits (concentration, time, volume) of the regimes where it is applicable. Further it would be interesting, if inferred parameter combinations from signal with chemical shifts make it possible to do reliable fingerprinting of chemical compounds.

Summary and Conclusions

In this work we have presented a blueprint for nanoscale NMR. Our approach builds on earlier work that demonstrates experimental feasibility of the required magnetic field detection scheme[25], on theoretical and experimental work that developed and demonstrated polarization transfer from color centers to liquids[28–30] and signal processing methods[39,45].

Methods

Simulation parameters. All simulations were performed using a 6.1 nm or 12.2 nm deep NV center, with the diffusion coefficient of $10^{-12}\,m^2/s$. For the simulation of the toluene molecule, a 12.2 nm deep NV was used with 0.2 M concentration at 0.25 T magnetic field, using XY8-8 sensing sequences for the signal accumulations and a delay time of 64 ns between the pulses.

Bayesian inference. In Bayesian statistics, a model of those aspects of the experiment that are relevant to the detected signal is built, and within this model parameters are considered as random variables. An estimation problem is then equivalent to the determination of the distribution of those parameters. For brevity of the manuscript, the model, parameters and algorithms are presented in detail in the Supplementary Information.

Experimental parameters. The experiment was performed with the setup presented in[25]. The amplitude of the RF signal was calibrated by fitting the accumulated phase due to the statistical polarization to that measured by a 6.2 nm deep NV center[50]. For each run, the NV phase in each XY measurement was accumulated over 5.6 μs, resulting in 1000 data points for the 5.6 ms long signal.

References

1. Findeisen, M. & Berger, S. *50 and more essential NMR experiments: a detailed guide*. (Wiley-VCH, Weinheim, 2014).
2. Badilita, V. *et al*. Microscale nuclear magnetic resonance: a tool for soft matter research. *Soft Matter* **8**, 10583–10597 (2012).
3. Webb, A. G. Radiofrequency microcoils in magnetic resonance. *Progress in Nuclear Magn. Reson. Spectrosc.* **31**, 1–42 (1997).

4. Zalesskiy, S. S., Danieli, E., Blumich, B. & Ananikov, V. P. Miniaturization of nmr systems: Desktop spectrometers, microcoil spectroscopy, and "nmr on a chip" for chemistry, biochemistry, and industry. *Chem. Rev.* **114**, 5641–5694 (2014).
5. Ardenkjær-Larsen, J. H. *et al*. Increase in signal-to-noise ratio of >10,000 times in liquid-state nmr. *Proceedings of the National Academy of Sciences* **100**, 10158–10163 (2003).
6. Grisi, M. *et al*. Nmr spectroscopy of single sub-nl ova with inductive ultra-compact single-chip probes. *Sci. reports* **7**, 44670 (2017).
7. Somorjai, G. A. & Li, Y. Impact of surface chemistry. *Proc. Natl. Acad. Sci.* **108**, 917–924 (2011).
8. Markley, J. L. *et al*. The future of nmr-based metabolomics. *Curr. Opinion Biotechnology* **43**, 34–40 (2017).
9. Spiess, H. W. 50th anniversary perspective: the importance of nmr spectroscopy to macromolecular science. *Macromolecules* **50**, 1761–1777 (2017).
10. Theis, T. *et al*. Parahydrogen-enhanced zero-field nuclear magnetic resonance. *Nat. Phys.* **7**, 571 (2011).
11. Theis, T. *et al*. Zero-field nmr enhanced by parahydrogen in reversible exchange. *J. Am. Chem. Soc.* **134**, 3987–3990 (2012).
12. Ledbetter, M. *et al*. Zero-field remote detection of nmr with a microfabricated atomic magnetometer. *Proc. Natl. Acad. Sci.* **105**, 2286–2290 (2008).
13. McDermott, R. *et al*. Liquid-state nmr and scalar couplings in microtesla magnetic fields. *Science* **295**, 2247–2249 (2002).
14. Wrachtrup, J., Von Borczyskowski, C., Bernard, J., Orrit, M. & Brown, R. Optical detection of magnetic resonance in a single molecule. *Nature* **363**, 244 (1993).
15. Gruber, A. *et al*. Scanning confocal optical microscopy and magnetic resonance on single defect centers. *Science* **276**, 2012–2014 (1997).
16. Maze, J. *et al*. Nanoscale magnetic sensing with an individual electronic spin in diamond. *Nature* **455**, 644 (2008).
17. Balasubramanian, G. *et al*. Nanoscale imaging magnetometry with diamond spins under ambient conditions. *Nature* **455**, 648 (2008).
18. Doherty, M. W. *et al*. The nitrogen-vacancy colour centre in diamond. *Phys. Rep.* **528**, 1–45 (2013).
19. Schirhagl, R., Chang, K., Loretz, M. & Degen, C. L. Nitrogen-vacancy centers in diamond: nanoscale sensors for physics and biology. *Annu. Rev. Phys. Chem.* **65**, 83–105 (2014).
20. Liu, G.-Q. & Pan, X.-Y. Quantum information processing with nitrogen–vacancy centers in diamond. *Chinese Physics B* **27**, 020304 (2018).
21. Staudacher, T. *et al*. Nuclear magnetic resonance spectroscopy on a (5-nanometer)^3 sample volume. *Science* **339**, 561–563 (2013).
22. Kong, X., Stark, A., Du, J., McGuinness, L. P. & Jelezko, F. Towards chemical structure resolution with nanoscale nuclear magnetic resonance spectroscopy. *Physical Review Applied* **4**, 024004 (2015).
23. Wu, Y., Jelezko, F., Plenio, M. B. & Weil, T. Diamond quantum devices in biology. *Angewandte Chemie International Edition* **55**, 6586–6598 (2016).
24. van Oort, E., Stroomer, P. & Glasbeek, M. Low-field optically detected magnetic resonance of a coupled triplet-doublet defect pair in diamond. *Phys. Rev. B* **42**, 8605 (1990).
25. Schmitt, S. *et al*. Submillihertz magnetic spectroscopy performed with a nanoscale quantum sensor. *Science* **356**, 832–837 (2017).
26. Boss, J. M., Cujia, K., Zopes, J. & Degen, C. L. Quantum sensing with arbitrary frequency resolution. *Science* **356**, 837–840 (2017).
27. Glenn, D. R. *et al*. High-resolution magnetic resonance spectroscopy using a solid-state spin sensor. *Nature* **555**, 351 (2018).
28. Chen, Q., Schwarz, I., Jelezko, F., Retzker, A. & Plenio, M. B. Resonance-inclined optical nuclear spin polarization of liquids in diamond structures. *Phys. Rev. B* **93**, 060408 (2016).
29. Fernández-Acebal, P. *et al*. Toward hyperpolarization of oil molecules via single nitrogen vacancy centers in diamond. *Nano Lett.* **18**, 1882–1887 (2018).
30. Abrams, D., Trusheim, M. E., Englund, D. R., Shattuck, M. D. & Meriles, C. A. Dynamic nuclear spin polarization of liquids and gases in contact with nanostructured diamond. *Nano letters* **14**, 2471–2478 (2014).
31. London, P. *et al*. Detecting and polarizing nuclear spins with double resonance on a single electron spin. *Phys. Rev. Lett.* **111**, 067601 (2013).
32. King, J. P. *et al*. Room-temperature *in situ* nuclear spin hyperpolarization from optically pumped nitrogen vacancy centres in diamond. *Nat. communications* **6**, 8965 (2015).
33. Álvarez, G. A. *et al*. Local and bulk 13 c hyperpolarization in nitrogen-vacancy-centred diamonds at variable fields and orientations. *Nat. communications* **6**, 8456 (2015).
34. Scheuer, J. *et al*. Optically induced dynamic nuclear spin polarisation in diamond. *New J. Phys.* **18**, 013040 (2016).
35. Scheuer, J. *et al*. Robust techniques for polarization and detection of nuclear spin ensembles. *Phys. Rev. B* **96**, 174436 (2017).
36. Bucher, D. B., Glenn, D. R., Park, H., Lukin, M. D. & Walsworth, R. L. Hyperpolarization-enhanced nmr spectroscopy with femtomole sensitivity using quantum defects in diamond. *E-print arXiv:1810.02408* (2018).
37. Peck, T. L., Magin, R. L. & Lauterbur, P. C. Design and analysis of microcoils for nmr microscopy. *J. Magn. Resonance, Series B* **108**, 114–124 (1995).
38. Gaebel, T. *et al*. Room-temperature coherent coupling of single spins in diamond. *Nat. Phys.* **2**, 408 (2006).
39. Hilbe, J. M., De Souza, R. S. & Ishida, E. E. *Bayesian models for astrophysical data: using R, JAGS, Python, and Stan*. (Cambridge University Press, 2017).
40. Feroz, F., Hobson, M. & Bridges, M. Multinest: an efficient and robust bayesian inference tool for cosmology and particle physics. *Mon. Not. R. Astron. Soc.* **398**, 1601–1614 (2009).
41. Hincks, I., Granade, C. & Cory, D. G. Statistical inference with quantum measurements: methodologies for nitrogen vacancy centers in diamond. *New J. Phys.* **20**, 013022 (2018).
42. Bretthorst, G. L. *Bayesian spectrum analysis and parameter estimation*, vol. 48 (Springer Science & Business Media, 2013).
43. Hoch, J. C. & Stern, A. S. *NMR data processing* (Wiley, 1996).
44. Hoffman, M. D. & Gelman, A. The no-u-turn sampler: adaptively setting path lengths in hamiltonian monte carlo. *J. Machine Learning Research* **15**, 1593–1623 (2014).
45. Flegal, J. M. & Jones, G. L. Implementing mcmc: estimating with confidence. *Handbook of Markov Chain Monte Carlo* 175–197 (2011).
46. Salvatier, J., Wiecki, T. V. & Fonnesbeck, C. Probabilistic programming in python using pymc3. *PeerJ Computer Science* **2**, e55 (2016).
47. Kehayias, P. *et al*. Solution nuclear magnetic resonance spectroscopy on a nanostructured diamond chip. *Nat. communications* **8**, 188 (2017).
48. Manson, N., Harrison, J. & Sellars, M. Nitrogen-vacancy center in diamond: Model of the electronic structure and associated dynamics. *Phys. Rev. B* **74**, 104303 (2006).
49. Schwartz, I. *et al*. Robust optical polarization of nuclear spin baths using hamiltonian engineering of nitrogen-vacancy center quantum dynamics. *Sci. Adv.* **4**, eaat8978 (2018).
50. Pham, L. M. *et al*. Nmr technique for determining the depth of shallow nitrogen-vacancy centers in diamond. *Phys. Rev. B* **93**, 045425 (2016).

Acknowledgements
The authors would like to thank Jochen Scheuer and Julen Simon Pedernales for discussions and support. This work was supported by the EU projects HYPERDIAMOND and AsteriQs, the QuantERA project NanoSpin, the BMBF project DiaPol, the ERC Synergy grant BioQ, the DFG CRC 1279, the Volkswagen Foundation grants A123229 and A129533 and a PhD fellowship of the Integrated Center for Quantum Science and Technology (IQST). The authors acknowledge support by the state of Baden-Württemberg through bwHPC and the German Research Foundation (DFG) through grant no INST 40/467-1 FUGG (JUSTUS cluster).

Author Contributions
M.B.P., I.S., B.T. initiated the project, B.T. carried out the simulation of the polarisation dynamics and with advice from I.S., M.B.P. and Q.C. provided the analytical aspects of the study. I.S. simulated the signal that were used in the experimental part of this project. J.R. developed and implemented the Bayesian inference approach with advice from M.B.P., I.S., S.S. and B.T. The experiments were carried out by S.S., L.P.G. and F.J. with advice from M.B.P., I.S., B.T. The manuscript was written by I.S., M.B.P. with input from all the authors. All authors discussed the research and read and commented on the manuscript.

Additional Information
Supplementary information accompanies this paper at https://doi.org/10.1038/s41598-019-43404-2.

Competing Interests: M.B.P. and F.J. hold contractual agreement as adviser to NVision Imaging. The other authors declare that they have no competing interests.

Publisher's note: Springer Nature remains neutral with regard to jurisdictional claims in published maps and institutional affiliations.

Open Access This article is licensed under a Creative Commons Attribution 4.0 International License, which permits use, sharing, adaptation, distribution and reproduction in any medium or format, as long as you give appropriate credit to the original author(s) and the source, provide a link to the Creative Commons license, and indicate if changes were made. The images or other third party material in this article are included in the article's Creative Commons license, unless indicated otherwise in a credit line to the material. If material is not included in the article's Creative Commons license and your intended use is not permitted by statutory regulation or exceeds the permitted use, you will need to obtain permission directly from the copyright holder. To view a copy of this license, visit http://creativecommons.org/licenses/by/4.0/.

© The Author(s) 2019

5 Conclusions and Outlook

NMR applications have fundamental limitations due to the minute nuclear magnetization of analytes. In this doctoral research I have tried to leverage the unique properties of nitrogen-vacancy centers in diamond to significantly enhance the sensitivity of magnetic resonance as well as increase the spatial resolution towards the nanoscale. A new theoretical approach was combined with proof of concept experiments for three main applications: optically hyperpolarized nanodiamonds, general hyperpolarization of molecules and NMR on the nanoscale.

Nanodiamonds are a promising agent as an in-vivo and in-vitro marker, as they can be functionalized, e.g. with antibodies, and therefore targeted to specific processes [9], and have excellent optical properties for fluorescent imaging [22]. Moreover, nanodiamonds are full of ^{13}C nuclear spins, opening up the possibility of generating a very strong MRI signal if they can be hyperpolarized. This will turn nanodiamonds into a truly multimodal imaging agent. Using our devised strategies for polarizing nanodiamonds, nanodiamonds could be optically polarized in macroscopic quantities. Nanodiamonds are currently being optimized for hyperpolarization [23], and are being optically hyperpolarized in experiments [24, 25]. Unfortunately, the polarization achieved with nano and microdiamonds is currently mostly limited due to the challenge of optically illuminating entire batch of nanodiamonds. Diamond has a very high refractive index, around 2.42, much higher than air or water (refractive index of 1, 1.33 respectively). Therefore, the light propagation in the nanodiamond powder undergoes Mie scattering during propagation, limiting the penetration of light to hundreds of micrometers. There is an ongoing experimental effort to improve the light penetration into the nanodiamond ensembles by e.g. using thin films or structuring the optical fiber providing the light to increase its surface area.

In future work, we envision the nanodiamond polarization techniques to be useful for polarizing various systems of interest, including microparticles or polycrystals of

organic molecules using photo-excited triplet states, as well as DNP in solid-state NMR, a burgeoning field of research.

In addition, the PROPI technique which we have developed to illuminate the nuclear spin bath dynamics surrounding a single NV center has been used for the initialization and readout of nuclear spin registers[26, 27]. I believe this technique will find applications in both optimization of DNP protocols on the nanoscale as well as quantum simulation and computation, where understanding the bath dynamics are of key importance to increase the coherence of the nuclear spins.

The techniques outlined in this thesis for hyperpolarization of molecules via optically-polarized NV centers have the potential to create substantial impact on magnetic resonance spectroscopy and imaging. While the experiments we performed were on the proof of concept level, there is ongoing progress in realization of the envisioned applications. External molecule hyperpolarization is an active field of research, with recent experiments demonstrating efficient hyperpolarization of nuclear spins in external molecules using PulsePol in NV ensembles [28, 29] as well as the combination of QDyne and hyperpolarization [29]. An ongoing effort which will significantly improve NV-based hyperpolarization of molecules is the improved creation of high coherence shallow NV centers[30, 31, 32, 33, 34, 35].

In addition to molecule polarization, the polarization of molecules across the diamond interface enables to obtain information of the dynamics on the surface in the nanometric scale, which cannot be viewed by other means. For example, in follow-up experiments we detected that the nuclear relaxation time of PDMS molecules at the diamond surface have a shorter relaxation time than bulk PDMS molecules, hinting at interesting dynamics at the surface, perhaps due to electron spins on the diamond surface due to dangling bonds. Similarly effects such as nanoscale viscosity, boundary layers and such can be detected by such means.

The PulsePol sequence, in addition to its use in external molecule hyperpolarization [28, 29], is being applied to a variety of applications utilizing its precise control over nuclear spins, including more efficient two-qubit gates [36], determination of precise nuclear spin location [37], and control of quantum memory in quantum dots [38]. In addition, the polarization Hamiltonian produced by PulsePol (flip-flop dynamics) is different than the effective dynamics produced by XY sensing sequences. This leads to potential non-classical effects which can be used for magnetic-inhomogeneity robust sensing sequences [39].

In future work, I believe that the efficiency PulsePol, given its pulsed nature, can be greatly optimized with various methods for production of optimized pulses, such as optimal control [40]. There is a substantial opportunity to use PulsePol for optimization of different hyperpolarization systems. For example, general DNP in solid-state NMR (i.e. with magic-angle spinning - MAS) is seeing significant ongoing progress [41]. Following improvements in MW hardware, pulse control of the microwave at high magnetic fields is now possible [42]. Similarly to NV center-based hyperpolarization, PulsePol could bring significant improvements to this wide field of research.

In addition, PulsePol can be applied for other hyperplarization techniques, even ones not relying on electron spins, such as parahydrogen-induced polarization (PHIP) and Signal amplification by reversible exchange (SABRE) [43]. These hyperpolarization techniques rely on transferring singlet order from a pair of ^1H nuclear spins to a nearby nuclear spin (e.g. ^{13}C) [44]. Recent experiments have shown that pulsed techniques, similar in essence to PulsePol but less robust and potentially less efficient (e.g. S2hM [44, 45]), can achieve very high polarization at high magnetic fields. As in the case of NV-based DNP, PulsePol can probably achieve a substantial improvement in the polarization transfer.

Finally, I believe that the combination of hyperpolarization and nanoscale or microscale sensing using NV centers in diamonds, as outlined in Ref. [21], can result in breakthrough applications. In this work we demonstrated theoretically that combining these techniques with Bayesian inference models can improve by more than an order of magnitude the amount of data needed for differentiation of two molecules on the nanoscale level. In extending this idea further, one could use sophisticated data analysis to obtain a finger-print nanoscale NMR spectrum specific to certain molecules, and be able to differentiate between them even with limited data. In future work we could combine this finger-printing method with hyperpolarization of specific molecules (e.g. glucose and its derivatives) and nanoscale/microscale NV sensing to significantly push the boundary on the volume for which such molecules can be detected. As a "holy grail" application, we envisage the detection of analytes from a few cells down to the single cell level.

Bibliography

[1] A. W. Overhauser, *Polarization of nuclei in metals*, Physical Review **92**, 411 (1953),
URL: http://dx.doi.org/10.1103/PhysRev.92.411

[2] J. H. Ardenkjær-Larsen, B. Fridlund, A. Gram, G. Hansson, L. Hansson, M. H. Lerche, R. Servin, M. Thaning, and K. Golman, *Increase in signal-to-noise ratio of> 10,000 times in liquid-state NMR*, Proceedings of the National Academy of Sciences **100**, 10158 (2003),
URL: http://dx.doi.org/10.1073/pnas.1733835100

[3] F. Jelezko, T. Gaebel, I. Popa, A. Gruber, and J. Wrachtrup, *Observation of Coherent Oscillations in a Single Electron Spin*, Physical Review Letters **92**, 076401 (2004),
URL: http://dx.doi.org/10.1103/PhysRevLett.92.076401

[4] F. Jelezko, T. Gaebel, I. Popa, M. Domhan, A. Gruber, and J. Wrachtrup, *Observation of Coherent Oscillation of a Single Nuclear Spin and Realization of a Two-Qubit Conditional Quantum Gate*, Physical Review Letters **93**, 130501 (2004),
URL: http://dx.doi.org/10.1103/PhysRevLett.93.130501

[5] F. Jelezko and J. Wrachtrup, *Single defect centers in diamond: A review*, physica status solidi (a) **203**, 3207 (2006),
URL: http://dx.doi.org/10.1002/pssa.200671403

[6] G. Waldherr, J. Beck, M. Steiner, P. Neumann, A. Gali, T. Frauenheim, F. Jelezko, and J. Wrachtrup, *Dark states of single nitrogen-vacancy centers in diamond unraveled by single shot NMR*, Physical review letters **106**, 157601

(2011),
URL: http://dx.doi.org/10.1103/PhysRevLett.106.157601

[7] P. London, J. Scheuer, J.-M. Cai, I. Schwarz, A. Retzker, M. B. Plenio, M. Katagiri, T. Teraji, S. Koizumi, J. Isoya, R. Fischer, L. P. McGuinness, B. Naydenov, and F. Jelezko, *Detecting and Polarizing Nuclear Spins with Double Resonance on a Single Electron Spin*, Physical Review Letters **111**, 067601 (2013),
URL: http://dx.doi.org/10.1103/PhysRevLett.111.067601

[8] E. Rej, T. Gaebel, T. Boele, D. E. J. Waddington, and D. J. Reilly, *Hyperpolarized nanodiamond with long spin-relaxation times*, Nature Communications **6**, 8459 (2015),
URL: http://dx.doi.org/10.1038/ncomms9459

[9] V. N. Mochalin, O. Shenderova, D. Ho, and Y. Gogotsi, *The properties and applications of nanodiamonds*, Nature nanotechnology **7**, 11 (2012)

[10] N. Aslam, M. Pfender, P. Neumann, R. Reuter, A. Zappe, F. F. de Oliveira, A. Denisenko, H. Sumiya, S. Onoda, J. Isoya, et al., *Nanoscale nuclear magnetic resonance with chemical resolution*, Science **357**, 67 (2017),
URL: http://dx.doi.org/10.1126/science.aam8697

[11] S. Schmitt, T. Gefen, F. M. Stürner, T. Unden, G. Wolff, C. Müller, J. Scheuer, B. Naydenov, M. Markham, S. Pezzagna, et al., *Submillihertz magnetic spectroscopy performed with a nanoscale quantum sensor*, Science **356**, 832 (2017),
URL: http://dx.doi.org/10.1126/science.aam5532

[12] A. Henstra, P. Dirksen, and W. T. Wenckebach, *Enhanced dynamic nuclear polarization by the integrated solid effect*, Physics Letters A **134**, 134 (1988),
URL: http://dx.doi.org/10.1016/0375-9601(88)90950-4

[13] Q. Chen, I. Schwarz, F. Jelezko, A. Retzker, and M. B. Plenio, *Optical hyperpolarization of ^{13}C nuclear spins in nanodiamond ensembles*, Physical Review B **92**, 184420 (2015),
URL: http://dx.doi.org/10.1103/PhysRevB.92.184420

[14] J. Scheuer, I. Schwartz, Q. Chen, D. Schulze-Sünninghausen, P. Carl, P. Höfer, A. Retzker, H. Sumiya, J. Isoya, B. Luy, M. B. Plenio, B. Naydenov, and

F. Jelezko, *Optically induced dynamic nuclear spin polarisation in diamond*, New Journal of Physics **18**, 013040 (2016),
URL: http://dx.doi.org/10.1088/1367-2630/18/1/013040

[15] J. Scheuer, I. Schwartz, S. Müller, Q. Chen, I. Dhand, M. B. Plenio, B. Naydenov, and F. Jelezko, *Robust techniques for polarization and detection of nuclear spin ensembles*, Physical Review B **96**, 174436 (2017),
URL: http://dx.doi.org/10.1103/PhysRevB.96.174436

[16] Q. Chen, I. Schwarz, F. Jelezko, A. Retzker, and M. B. Plenio, *Resonance-inclined nuclear spin polarization of liquids in diamond structures*, arxiv

[17] P. Fernández-Acebal, O. Rosolio, J. Scheuer, C. Müller, S. Müller, S. Schmitt, L. McGuinness, I. Schwarz, Q. Chen, A. Retzker, B. Naydenov, F. Jelezko, and M. B. Plenio, *Toward hyperpolarization of oil molecules via single nitrogen vacancy centers in diamond*, Nano letters **18**, 1882 (2018)

[18] I. Schwartz, J. Scheuer, B. Tratzmiller, S. Müller, Q. Chen, I. Dhand, Z.-Y. Wang, C. Müller, B. Naydenov, F. Jelezko, et al., *Robust optical polarization of nuclear spin baths using Hamiltonian engineering of nitrogen-vacancy center quantum dynamics*, Science advances **4**, eaat8978 (2018),
URL: http://dx.doi.org/10.1126/sciadv.aat8978

[19] D. Suter and G. A. Álvarez, *Colloquium: Protecting quantum information against environmental noise*, Reviews of Modern Physics **88**, 041001 (2016)

[20] Q. Chen, I. Schwarz, and M. B. Plenio, *Dissipatively stabilized quantum sensor based on indirect nuclear-nuclear interactions*, Physical Review Letters **119**, 010801 (2017)

[21] I. Schwartz, J. Rosskopf, S. Schmitt, B. Tratzmiller, Q. Chen, L. P. McGuinness, F. Jelezko, and M. B. Plenio, *Blueprint for nanoscale NMR*, Scientific Reports (2019),
URL: http://dx.doi.org/10.1038/s41598-019-43404-2

[22] C.-C. Fu, H.-Y. Lee, K. Chen, T.-S. Lim, H.-Y. Wu, P.-K. Lin, P.-K. Wei, P.-H. Tsao, H.-C. Chang, and W. Fann, *Characterization and application of single*

fluorescent nanodiamonds as cellular biomarkers, Proceedings of the National Academy of Sciences **104**, 727 (2007)

[23] Y. Mindarava, R. Blinder, Y. Liu, J. Scheuer, J. Lang, V. Agafonov, V. A. Davydov, C. Laube, W. Knolle, B. Abel, et al., *Synthesis and coherent properties of 13C-enriched sub-micron diamond particles with nitrogen vacancy color centers*, Carbon **165**, 395 (2020)

[24] A. Ajoy, K. Liu, R. Nazaryan, X. Lv, P. R. Zangara, B. Safvati, G. Wang, D. Arnold, G. Li, A. Lin, et al., *Orientation-independent room temperature optical 13C hyperpolarization in powdered diamond*, Science advances **4**, eaar5492 (2018)

[25] K. Miyanishi, T. F. Segawa, K. Takeda, I. Ohki, S. Onoda, T. Ohshima, H. Abe, H. Takashima, S. Takeuchi, A. I. Shames, et al., *Room temperature hyperpolarization of polycrystalline samples with optically polarized triplet electrons: Pentacene or Nitrogen-Vacancy center in diamond?*, Magnetic Resonance Discussions , 1 (2020)

[26] T. Unden, N. Tomek, T. Weggler, F. Frank, P. London, J. Zopes, C. Degen, N. Raatz, J. Meijer, H. Watanabe, K. M. Itoh, M. B. Plenio, B. Naydenov, and F. Jelezko, *Coherent control of solid state nuclear spin nano-ensembles*, npj Quantum Information **4**, 39 (2018),
URL: http://dx.doi.org/https://doi.org/10.1038/s41534-018-0089-8

[27] M. H. Metsch, K. Senkalla, B. Tratzmiller, J. Scheuer, M. Kern, J. Achard, A. Tallaire, M. B. Plenio, P. Siyushev, and F. Jelezko, *Initialization and Readout of Nuclear Spins via a Negatively Charged Silicon-Vacancy Center in Diamond*, Physical review letters **122**, 190503 (2019),
URL: http://dx.doi.org/10.1103/PhysRevLett.122.190503

[28] A. Healey, L. Hall, G. White, T. Teraji, M.-A. Sani, F. Separovic, J.-P. Tetienne, and L. Hollenberg, *Hyperpolarisation of external nuclear spins using nitrogen-vacancy centre ensembles*, arXiv preprint arXiv:2101.12325 (2021)

[29] T. U. et al., *Hyperpolarization and direct detection of external spins via nitrogen-vacancy center enesmble ensembles*, In preparation (2021)

[30] T. Yamamoto, T. Umeda, K. Watanabe, S. Onoda, M. L. Markham, D. J. Twitchen, B. Naydenov, L. P. McGuinness, T. Teraji, S. Koizumi, F. Dolde, H. Fedder, J. Honert, J. Wrachtrup, T. Ohshima, F. Jelezko, and J. Isoya, *Extending spin coherence times of diamond qubits by high-temperature annealing*, Physical Review B **88**, 075206 (2013),
URL: http://dx.doi.org/10.1103/PhysRevB.88.075206

[31] B. Naydenov, F. Reinhard, A. Lämmle, V. Richter, R. Kalish, U. F. S. D'Haenens-Johansson, M. Newton, F. Jelezko, and J. Wrachtrup, *Increasing the coherence time of single electron spins in diamond by high temperature annealing*, Applied Physics Letters **97**, 242511 (2010),
URL: http://dx.doi.org/10.1063/1.3527975

[32] A. T. Collins, A. Connor, C.-H. Ly, A. Shareef, and P. M. Spear, *High-temperature annealing of optical centers in type-I diamond*, Journal of Applied Physics **97**, 083517 (2005),
URL: http://dx.doi.org/10.1063/1.1866501

[33] G. Braunstein and R. Kalish, *Damage and lattice location studies in high-temperature ion-implanted diamond*, Applied Physics Letters **38**, 416 (1981),
URL: http://dx.doi.org/10.1063/1.92400

[34] J. Orwa, C. Santori, K. Fu, B. Gibson, D. Simpson, I. Aharonovich, A. Stacey, A. Cimmino, P. Balog, M. Markham, et al., *Engineering of nitrogen-vacancy color centers in high purity diamond by ion implantation and annealing*, Journal of applied physics **109**, 083530 (2011),
URL: http://dx.doi.org/10.1063/1.3573768

[35] F. F. De Oliveira, D. Antonov, Y. Wang, P. Neumann, S. A. Momenzadeh, T. Häußermann, A. Pasquarelli, A. Denisenko, and J. Wrachtrup, *Tailoring spin defects in diamond by lattice charging*, Nature Communications **8**, 15409 (2017),
URL: http://dx.doi.org/10.1038/ncomms15409

[36] B. Tratzmiller, J. F. Haase, Z. Wang, and M. B. Plenio, *Parallel selective nuclear-spin addressing for fast high-fidelity quantum gates*, Physical Review A **103**, 012607 (2021)

[37] K. Sasaki, K. M. Itoh, and E. Abe, *Determination of the position of a single nuclear spin from free nuclear precessions detected by a solid-state quantum sensor*, Physical Review B **98**, 121405 (2018)

[38] E. V. Denning, D. A. Gangloff, M. Atatüre, J. Mørk, and C. Le Gall, *Collective quantum memory activated by a driven central spin*, Physical review letters **123**, 140502 (2019)

[39] Y. Vaknin, B. Tratzmiller, T. Gefen, I. Schwartz, M. Plenio, and A. Retzker, *Robustness of the NV-NMR Spectrometer Setup to Magnetic Field Inhomogeneities*, Physical Review Letters **125**, 110502 (2020)

[40] X. Yang, Y. Ge, B. Zhang, and J. Li, *Robust Dynamical Decoupling for the Manipulation of a Spin Network via a Single Spin*, arXiv preprint arXiv:2101.03976 (2021)

[41] T. Maly, G. T. Debelouchina, V. S. Bajaj, K.-N. Hu, C.-G. Joo, M. L. Mak-Jurkauskas, J. R. Sirigiri, P. C. van der Wel, J. Herzfeld, R. J. Temkin, et al., *Dynamic nuclear polarization at high magnetic fields*, The Journal of chemical physics **128**, 02B611 (2008)

[42] G. Mathies, S. Jain, M. Reese, and R. G. Griffin, *Pulsed dynamic nuclear polarization with trityl radicals*, The journal of physical chemistry letters **7**, 111 (2016)

[43] S. B. Duckett and R. E. Mewis, *Application of para hydrogen induced polarization techniques in NMR spectroscopy and imaging*, Accounts of chemical research **45**, 1247 (2012)

[44] J. Eills, G. Stevanato, C. Bengs, S. Glöggler, S. J. Elliott, J. Alonso-Valdesueiro, G. Pileio, and M. H. Levitt, *Singlet order conversion and parahydrogen-induced hyperpolarization of 13C nuclei in near-equivalent spin systems*, Journal of Magnetic Resonance **274**, 163 (2017)

[45] G. Stevanato, J. Eills, C. Bengs, and G. Pileio, *A pulse sequence for singlet to heteronuclear magnetization transfer: S2hM*, Journal of Magnetic Resonance **277**, 169 (2017)

List of Publications

1. *Resonance-inclined nuclear spin polarization of liquids in diamond structures*
   Chen, Q. and Schwarz, I. and Jelezko, F. and Retzker, A. and Plenio, M. B.
   Physical Review B **93**, 060408 (2016)
   URL: https://doi.org/10.1103/PhysRevB.93.060408

2. *Robust optical polarisation of nuclear spin baths using Hamiltonian engineering of nitrogen-vacancy center quantum dynamics*
   I. Schwartz*, J. Scheuer*, B. Tratzmiller*, S. MÃ¼ller, Q. Chen, I. Dhand, Z. Wang, C. MÃ¼ller, B. Naydenov, F. Jelezko, M.B. Plenio
   Science Advances **4**, 8 eaat8978 (2018)
   URL: http://www.doi.org/10.1126/sciadv.aat8978
   * these authors contributed equally to the work

3. *Toward Hyperpolarization of Oil Molecules via Single Nitrogen Vacancy Centers in Diamond*
   P. FernÃ¡ndez-Acebal, O. Rosolio, J. Scheuer, C. MÃ¼ller, S. MÃ¼ller, S. Schmitt, L.P. McGuinness, I. Schwarz, Q. Chen, A. Retzker, B. Naydenov, F. Jelezko, M.B. Plenio
   Nano letters **18**, 3 1882-1887 (2018)
   URL: https://pubs.acs.org/doi/abs/10.1021/acs.nanolett.7b05175

4. *Optical hyperpolarization of ^{13}C nuclear spins in nanodiamond ensembles*
   Chen, Q. and Schwarz, I. and Jelezko, F. and Retzker, A. and Plenio, M. B.
   Physical Review B **92**, 184420 (2015)
   URL: https://doi.org/10.1103/PhysRevB.92.184420

5. *Robust techniques for polarization and detection of nuclear spin ensembles*
   J. Scheuer, I. Schwartz, S. Müller, Q. Chen, I. Dhand, M. B. Plenio, B. Nay-

denov, F. Jelezko
Physical Review B **96**, 174436 (2017)
URL: https://journals.aps.org/prb/abstract/10.1103/PhysRevB.96.174436

6. *Optically induced dynamic nuclear spin polarisation in diamond*
J. Scheuer, I. Schwartz, Q. Chen, D. Schulze-Sünninghausen, P. Carl, P. Höfer, A. Retzker, H. Sumiya, J. Isoya, B. Luy, M. B. Plenio, B. Naydenov, F. Jelezko
New Journal of Physics **18**, 013040 (2016)
URL: https://iopscience.iop.org/article/10.1088/1367-2630/18/1/013040

7. *Dissipatively stabilized quantum sensor based on indirect nuclear-nuclear interactions*
Chen, Q* and Schwarz, I* and Plenio, Martin B
Physical Review Letters **119.1**, 010801 (2017)
URL: https://doi.org/10.1103/PhysRevLett.119.010801
* these authors contributed equally to the work

8. *Blueprint for nanoscale NMR*
Schwartz, Ilai and Rosskopf, Joachim and Schmitt, Simon and Tratzmiller, Benedikt and Chen, Qiong and McGuinness, Liam P. and Jelezko, Fedor and Plenio, Martin B.
Scientific Reports **9.1** (2019)
URL: https://doi.org/10.1038/s41598-019-43404-2

9. *Submillihertz magnetic spectroscopy performed with a nanoscale quantum sensor*
S. Schmitt,T. Gefen, F. M. Stürner, T. Unden, G. Wolff, C. Müller, J. Scheuer, B. Naydenov, M. Markham, S. Pezzagna, J. Meijer, I. Schwarz, M. Plenio, A. Retzker, L. P. McGuinness, F. Jelezko
Science **356**, 6340 (2017)
URL: https://doi.org/10.1126/science.aam5532

Ilai Schwartz

Education

4/2015 – present **Ph.D. in Physics** at The Institute of Theoretical Physics, Universität Ulm

- Research focused on novel methods for using Nitrogen-vacancy centers in diamond to polarize nuclear spins, either in nanodiamonds (turning the nanodiamond into an MRI tracer) or in external molecules (using the diamond only as the polarizer)
- Collaborating with the Institute of Quantum Optics to build the first polarizer prototype demonstrating polarization in an NMR spectrometer

10/2009 – 12/2011 **M.Sc. in Physics** at The Hebrew University of Jerusalem
Graduated *Summa cum Laude*

Thesis: A Theoretical Study of Topics in Nano and Quantum Optics

10/2006 – 10/2009 **B.Sc. in Physics and Cognitive Studies** at The Hebrew University of Jerusalem
Graduated *Summa cum Laude*

Awards

- Co-coordinator and Principal Investigator in the EU Quantum Technologies Flagship project MetaboliQs (2018)
- Coordinator and Principal Investigator in the BMBF project POLCHIP (2018)
- Principal Investigator in the BMBF project DIAPOL (2018)
- Principal Investigator in the Horizon 2020 project HYPERDIAMOND (2016)
- Awarded the competitive AISEF (Austalia-Israel Scientific Exchange Foundation) Post-Graduate Fellowship (2011)
- Awarded the Sir Zelman Cowen Universities Fund Student Scholarship for research exchange with Sydney University (2011)
- Awarded the Rector's Prize (highest accolade) for first year of M.Sc (2010)
- Won Outstanding Poster Presentation Award in the 2010 Israel Physics Society conference, given to the top five posters in the conference (2010)
- Received the Hebrew University scholarship for exceptional research students (2009-2010)
- Awarded the Dean's Prize (second highest accolade) for second year of B.Sc. (2008)
- Awarded the Rector's Prize (highest accolade) for first year of B.Sc. (2007)
- Awarded "Amirim" Special Honors program full scholarship for entire B.Sc (2007-2009)

Publications

Publication review/summary: 10 papers in refereed international journals, 2 in preparation.

- Anders, J., Dreyer, F., Krüger, D., **Schwartz, I.**, Plenio, M. B., & Jelezko, F. (2021). Progress in miniaturization and low-field nuclear magnetic resonance. *Journal of Magnetic Resonance*, *322*, 106860.
- Mindarava, Y., Blinder, R., Laube, C., Knolle, W., Abel, B., Jentgens, C., Isoya, J., Scheuer, J., Lang, J., **Schwartz, I.**, Naydenov, B. And Jelezko F. 2020. “Efficient conversion of nitrogen to nitrogen-vacancy centers in diamond particles with high-temperature electron irradiation”. *Carbon*, 170, pp.182-190.
- Tratzmiller, B., Chen, Q., **Schwartz, I.**, Huelga, S. F., & Plenio, M. B. (2020). ”Limited-control metrology approaching the Heisenberg limit without entanglement preparation”. *Physical Review A*, 101(3), 032347.
- Aharon, Nati, **Ilai Schwartz**, and Alex Retzker. "Quantum control and sensing of nuclear spins by electron spins under power limitations." *Physical review letters* 122.12 (2019): 120403.
- Casanova, J., Wang, Z. Y., **Schwartz, I.**, & Plenio, M. B. (2018). “Shaped Pulses for Energy-Efficient High-Field NMR at the Nanoscale”. *Physical Review Applied*, 10(4), 044072.
- **Schwartz, I.**, Rosskopf, J., Schmitt, S., Tratzmiller, B., Chen, Q., McGuinness, L.P., Jelezko, F. and Plenio, M.B., “Blueprint for nanoscale NMR”. *Scientific Reports* 9, 6938 (2019).
- **Schwartz, I.**, Scheuer, J., Tratzmiller, B., Müller, S., Chen, Q., Dhand, I., Wang, Z.Y., Müller, C., Naydenov, B., Jelezko, F. and Plenio, M.B., 2018. “Robust optical polarization of nuclear spin baths using Hamiltonian engineering of nitrogen-vacancy center quantum dynamics”. *Science advances*, 4(8), p.eaat8978.

- Fernández-Acebal, P., Rosolio, O., Scheuer, J., Muller, C., Muller, S., Schmitt, S., McGuinness, L.P., **Schwarz, I.**, Chen, Q., Retzker, A., Naydenov, B., Jelezko, F. and Plenio M.B., 2018. “Toward hyperpolarization of oil molecules via single nitrogen vacancy centers in diamond”. *Nano letters*, 18(3), pp.1882-1887.
- Scheuer, J., **Schwartz, I.**, Müller, S., Chen, Q., Dhand, I., Plenio, M.B., Naydenov, B. and Jelezko, F., 2017. “Robust techniques for polarization and detection of nuclear spin ensembles”. *Physical Review B*, 96(17), p.174436.
- Chen, Q., I. **Schwarz (joint lead author)**, and Martin B. Plenio. "Dissipatively stabilized quantum sensor based on indirect nuclear-nuclear interactions." **Physical Review Letters** 119.1 (2017): 010801.
- Scheuer, Jochen, **Ilai Schwartz (theory lead)**, Qiong Chen, David Schulze-Sünninghausen, Patrick Carl, Peter Höfer, Alexander Retzker et al. "Optically induced dynamic nuclear spin polarisation in diamond." *New Journal of Physics* 18, no. 1 (2016): 013040.
- Simon Schmitt, Tuvia Gefen, Felix M Stürner, Thomas Unden, Gerhard Wolff, Christoph Müller, Jochen Scheuer, Boris Naydenov, Matthew Markham, Sebastien Pezzagna, Jan Meijer, Ilai Schwarz, Martin Plenio, Alex Retzker, Liam P McGuinness, Fedor Jelezko, "Submillihertz magnetic spectroscopy performed with a nanoscale quantum sensor." *Science* 356.6340 (2017): 832-837.
- Chen, Qiong, **Ilai Schwarz (joint lead author)**, Fedor Jelezko, Alex Retzker, and Martin B. Plenio. "Resonance-inclined optical nuclear spin polarization of liquids in diamond structures." *Physical Review B* 93, no. 6 (2016): 060408.
- Chen, Q., **I. Schwarz**, F. Jelezko, A. Retzker, and M. B. Plenio. "Optical hyperpolarization of ^{13}C nuclear spins in nanodiamond ensembles." *Physical Review B* 92, no. 18 (2015): 184420.
- P London, J Scheuer, J-M Cai, **Ilai Schwarz**, A Retzker, MB Plenio, M Katagiri, T Teraji, S Koizumi, J Isoya, R Fischer, LP McGuinness, B Naydenov, F Jelezko. "Detecting and polarizing nuclear spins with double resonance on a single electron spin". *Phys. Rev. Lett. Vol. 111, Issue 6 (2013)*
- **Ilai Schwarz** and Terry Rudolph. "Efficient entanglement-length measurements for photonic-cluster-state sources". *Phys. Rev. A, Vol. 85, Issue 5 (2012)*
- Dominic V. Else, **Ilai Schwarz**, Stephen D. Bartlett, and Andrew C. Doherty. "Symmetry-Protected Phases for Measurement-Based Quantum Computation". *Phys. Rev. Lett., Vol. 108, Issue 24, (2012)*
- **Ilai Schwarz**, Nitzan Livneh and Ronen Rapaport. "General closed-form condition for enhanced transmission in subwavelength metallic gratings in both TE and TM polarizations". *Optics Express, Vol. 20, Issue 1, pp. 426-439 (2012)*
- **Ilai Schwarz**, Moshe G. Harats, Nitzan Livneh, Shira Yochelis, Ayelet Strauss, Adiel Zimran, Uri Banin, Yossi Paltiel, and Ronen Rapaport. "Theory and experiments of Bragg cavity modes in passive and active metallic nanoslit array devices". *JOSA B, Vol. 29, Issue 2, pp. A127-A137 (2012)*
- Nitzan Livneh, Ayelet Strauss, **Ilai Schwarz**, Itamar Rosenberg, Adiel Zimran, Shira Yochelis, Gang Chen, Uri Banin, Yossi Paltiel and Ronen Rapaport. "Highly directional emission and photon beaming from nanocrystal quantum dots embedded in metallic nanoslit arrays". *Nano Letters*, *11 (4), pp 1630–1635 (2011)*
- Moshe G. Harats, **Ilai Schwarz**, Adiel Zimran, Uri Banin, Gang Chen and Ronen Rapaport. "Enhancement of two-photon processes in quantum dots embedded in subwavelength metallic gratings". *Optics Express, Vol. 19, Issue 2, pp. 1617-1625 (2011)*

Patents

Inventor of 6 international patent applications, including:

- Fedor Jelezko, Martin Plenio, J-M Cai, Alex Retzker., Boris Naydenov & **Ilai Schwarz,** (2014). Method for the hyperpolarisation of nuclear spin in a diamond via a long-range interaction, PCT/EP2014/056958
- **Ilai Schwartz**, Martin Plenio, Qiong Chen, Fedor Jelezko and Alex Retzker, (2015). Method for the hyperpolarization of nuclear spins, PCT/EP2015/061465
- **Ilai Schwartz**, Martin Plenio, Qiong Chen and Zhenyu Wang, (2016). Verfahren und Vorrichtung zur Hyperpolarisierung einer Materialprobe

Presentations

Presented at 5 seminars as an academic visitors in Germany, Israel, UK and Australia, and in 2 international conferences, including the 5th International Dynamic Nuclear Polarization (DNP) Symposium.

Professional Experience

3/2015 – present **Co-Founder and CTO** at NVision Imaging Technologies GmbH, Ulm, Germany

- Focusing on commercializing applications for increasing the MRI signal of target molecules >10,000-fold, in a fast and cost-efficient method
- Leading the research and development for the multiple company product lines

1/2014 – 3/2015 **Post-graduate research** at the Institute of Theoretical Physics, Universität Ulm, Germany

- Focusing on medical applications of Nitrogen-Vacancy centers in diamonds
- Developed the theory basis for hyperpolarization of nanodiamonds at room temperature

7/2012 – 12/2013 **Consultant** at McKinsey & Company

- Facilitated the change management initiative at a global chemicals company, transforming the communication process and employee involvement across the company
- Guided a Lean Manufacturing transformation for a global pharmaceutical company, improving flexibility and enabling the plant to achieve yearly targets
- Served as a start-up business mentor in TheHive Accelerator, as part of McKinsey's pro-bono initiative with Gvahim NGO

2/2012 – 6/2012 **Post-graduate research** at the Institute of Theoretical Physics, Universität Ulm, Germany

- Patented a novel application for polarization of nano-diamonds via Nitrogen-Vacancy centers, enabling the usage of nano-diamonds as molecular imaging tracers

6/2007 – 4/2009 **R&D project leader** at Gita Technologies (part time)

- Directed development of a yearlong information security software project, resulting in a top product in its market.
- Increased the efficiency of a client's computing process by 6,000% over the best known competitor's solution. Assisted in the multi-team implementation, leading to one of the company's key products, and the best solution on the market.

2/2002 – 4/2006 **Algorithm developer** at military intelligence

- Led a four-member team on a large-scale intelligence project. Coordinated timelines and collaboration with related specialized units.
- Specialized in statistical data analysis. Was chosen to participate in special "think tanks" which had to generate novel ideas and innovative solutions under a very tight schedule.